The Applicability of Aerodynamic Models to Tidal Turbines

Naomi Turner

A thesis submitted in partial fulfilment of the requirements of the Robert Gordon University for the degree of Doctor of Philosophy

April 2012

Abstract

For the tidal current power industry to progress, simple models for predicting the performance of tidal current turbines are needed. Currently the aerodynamic models developed for wind turbines are typically used to predict tidal turbine performance. There are a number of significant differences between wind and tidal turbines so these models will not provide a good representation of tidal turbine performance. The main aim of this project was to show the magnitude of the differences between wind and tidal turbine performance caused by dissimilarities in wind and tidal turbine operation.

Two main areas were investigated: the effects of energy extraction on flow speeds and the effect of the proximity of the boundaries. An analytical model was developed which allowed the effect of the number of turbines at a site on the performance of each turbine to be investigated. The magnitude of the change in performance was found to depend on the design and geometry of the turbines and the drag coefficient of the site. The model results indicated that, typically, there will be no noticeable reduction in the power generated by single or small farms of turbines, but installing large farms of turbines will cause significant reduction in the power generated per turbine. An analytical model was developed which allowed the effects of blockage on performance to be investigated. Applying the model to a single turbine in the Sound of Islay indicated that the performance of a realistically sized turbine in an actual tidal channel will differ from that predicted by an aerodynamic model. The effect of the proximity of the turbine to channel boundaries was investigated and performance was found to decrease as the free surface was approached.

In all of the areas investigated the performance tidal turbines has been found to differ significantly from the performance predicted by aerodynamic models. This implies that it is not appropriate to use aerodynamic models to predict tidal turbine performance.

Acknowledgements

I would like to thank to my supervisors Alan Owen, Mamdud Hossain and Pat Pollard for their help and support. Also with thanks to Graeme Budge, Martin Johnstone, Allan MacPherson, Steven Pirie and Bill Walker for their invaluable assistance with preparing for the experimental aspects of this project. Finally I would like to thank my friends and family for their support.

Contents

Figures

Tables

Nomenclature

A	projected area of either the actuator disc representing the turbine or the porous material, m^2
a	axial interference factor
a'	tangential interference factor
A_2	area of streamtube in far downstream plane, m^2
A_c	cross sectional area of channel, m^2
A_e	area of channel exit, m^2
A_{ref}	reference area used in drag calculation, m^2
A_t	cross sectional area of the channel at the point where the turbines are deployed, m^2
b	amplitude of sinusoidal sea level difference between the two ends of the channel, m
c	chord length, m
c_1	$\int_0^L \frac{1}{A} dx$
c_2	$\rho \int_0^L A\, dx$
C_2	pressure jump coefficient
c_3	$\frac{1}{2}\rho \int_0^L \frac{C_D w}{A^2} dx$
c_4, c_5	constants used to describe the variation of thrust force with free-stream velocity for constant tip speed ratio operation
c_6, c_7, c_8, c_9,	constants used to describe the variation of thrust force with free-stream velocity for constant rotational speed operation
C_{Dc}	drag coefficient of channel
C_{Dt}	drag coefficient of turbine blade
C_L	lift coefficient
C_P	power coefficient
$\mathcal{D}$	drag
f	force acting in the direction of flow per unit length of blade
$f(x)$	Probability density function of the Gaussian distribution
F	resistance force per unit mass of seawater
F^*	$\frac{Nc}{8\pi R}\frac{RW^2}{ru_\infty^2}(C_L \cos\phi + C_D \sin\phi)$
F_{fricf}	drag force due to natural friction
F_r	resistance force
F_t	drag force due to turbines
g	acceleration of gravity
h	depth of channel
h_t	time step used in extended model

k	resistance coefficient of porous material
L	length of channel
l	height of porous region
N	number of blades
n	number of turbines
n_s	number of sections the channel is divided into
P	power
P_{1o}	pressure at plane out turbine, outside the streamtube enclosing the turbine
P_2	pressure at plane far downstream of turbine
P_∞	pressure far upstream of turbine
P_d	pressure on downstream side of porous material
P_{max}	average maximum power extractable from the channel
P_u	pressure on upstream side of either the porous material or actuator disc
P_u	pressure on upstream side of actuator disc
$P_u + \Delta P$	pressure on downstream side of actuator disc
Q	Torque acting on entire rotor
q	torque per unit length of blade
Q^*	$\frac{Nc}{8\pi R}\frac{1}{\lambda}\frac{R^2W^2}{ru_\infty^2}(C_L\sin\phi - C_D\cos\phi)$
R	radius of turbine
r	radius of blade element
R_r	root radius of blade
T	thrust force acting on rotor, actuator disc or porous material
t	time
u	velocity of flow through actuator disc
u_{1o}	velocity at plane of turbine, outside the streamtube enclosing the turbine
u_{2o}	velocity at plane far downstream of turbine, outside streamtube enclosing the turbine
u_{2s}	velocity at plane far downstream of turbine, inside streamtube enclosing turbine
u_∞	free-stream velocity
u_c	velocity of flow in channel
$u_c(y)$	the velocity at a depth y
u_{ce}	flow velocity at channel exit
u_{c0}	the reference velocity at the reference depth, y_0
u_{cs}	the flow velocity at the surface of the channel
$\overline{u_{dc}}$	the depth averaged velocity
$\dot{V}$	volume flow rate
$\dot{V}_{max}$	maximum volume flux through the channel in its undisturbed state
W	resultant velocity of flow past blade element

w	width of channel
x	along channel coordinate
y	vertical coordinate
y_0	y position of base of porous region
y_L	y position of top of porous region
z	channel width
α	angle of attack
α_m	permeability of the porous medium
β	twist angle of turbine blade
γ	coefficient which varies over the range 0.2 to 0.24
Δm	thickness of porous medium
ΔP	pressure change across actuator disc or porous material
Δr	change in radius between blade elements
Δy	distance by which the free surface has deflected at the far downstream plane
θ	open area ratio of porous material (open area/total area)
λ	tip speed ratio
μ	laminar fluid viscosity
ρ	fluid density
ς_0	sea level difference between two basins
φ	angle between resultant velocity and plane of rotation
ω	frequency of the sine wave used to represent the change in the difference of elevation between the ends of the channel over time
Ω	angular velocity of turbine blades

Chapter 1 Introduction

This project has investigated whether the aerodynamic models developed for wind turbines can accurately predict the performance of tidal turbines. Whilst many designs for tidal turbines strongly resemble wind turbines, there are a number of significant differences between wind and tidal turbine operation. When these differences are considered, it would suggest that aerodynamic models are unlikely to be able to accurately predict tidal turbine performance. In order to demonstrate whether or not the differences between wind and tidal turbines have a significant effect on their performance, the magnitudes of the differences in performance caused by a number of the differences between wind and tidal turbine operation have been investigated. The models developed have been applied to a case study of the Isle of May in order to demonstrate if the effects are significant for an actual channel.

Concerns about climate change and security of energy supply have led to a growing interest in the generation of energy from renewable sources (1). Of the renewable energy sources, tidal power is unique since the movement of the tides is predictable decades in advance. This is a major advantage over wind power which can only be predicted a few hours in advance (2) and wave power which can only be predicted a few days in advance (3). Tidal current power is thought to have less environmental impact than tidal barrage schemes (4). It also has a number of other advantages, such as minimal visual impact (5).

Currently marine renewables, including wave, tidal power and offshore wind, are economically less favourable than land based technologies (6). This is due to the challenges of working in a marine environment (7). The tidal current energy industry is at an early stage of development. A large number of concepts for extracting energy from tidal currents have been proposed but only a few have progressed past laboratory scale model tests to an advanced demonstration phase. If tidal current technology is

to become economically competitive with other renewable energy technologies, further technological development is needed.

The development of tidal current technology requires accurate performance prediction models for tidal turbines. Performance prediction models are powerful tools in the development of tidal turbines since they allow design parameters to be optimised more rapidly and at a lower cost than scale model testing. Tidal and wind turbines extract energy from a moving stream of fluid in a similar manner and many tidal turbines bear a strong resemblance to wind turbines. This has resulted tidal turbines typically being modelled using the aerodynamic models developed for wind turbines.

Aerodynamic models may not accurately represent tidal turbines since there are a number of fundamental differences between wind and tidal turbine operation. The differences between wind and tidal turbines include the Reynolds number of the flow, the possibility of cavitation occurring, different stall characteristics, the presence of a free surface, the effects of wave motion and the extent to which the flow is constrained (8). For some tidal turbines the geometry of the turbine also differs from that of a wind turbine (9). This project aims to establish if aerodynamic models are applicable to tidal turbines. This will be achieved by investigating the extent to which the differences between wind and tidal turbine operation cause the performance of tidal turbines to differ from the performance predicted by the aerodynamic models.

The next section gives a review of models which can be applied to turbines. Firstly the models developed for wind turbines are described. This is followed by a discussion of models which have been developed specifically for tidal turbines. Finally numerical solution techniques are discussed. Numerical methods are used to solve a wide variety of problems involving fluid flows and so their use in predicting tidal turbine performance has been investigated.

1.1 Aerodynamic models

Many analytical models have been developed to predict the performance of wind turbines. These models vary both in complexity and in accuracy and mostly fall into two main categories: Streamtube models and Vortex models (10). Streamtube models can usually only accurately predict time averaged quantities but they require much less computational time than vortex models and so are cheaper to implement (11). Vortex models are more complex and much more expensive to implement but they can predict the instantaneous forces with better accuracy than a streamtube model (12). Lifting line models are a type of vortex model. Streamtube and vortex models have been developed for both horizontal and vertical axis turbines. Other types of model which can be applied to wind turbines include acceleration potential models (13). These models were developed to model the flight performance of helicopter rotors but can also be applied to lightly loaded wind turbine rotors. The use of acceleration potential models to predict turbine performance is much less widespread than the used of streamtube and vortex models so acceleration potential models will not be considered in more detail here.

1.1.1 Vortex models

In vortex models the blade elements are represented by one or more bound vortices. Helmholtz theorems of vorticity and Kelvin's theorem (14) are used to determine the strength of the shed vortices. Knowledge of the strength of the shed vortices can be used to establish the induced velocities in the flow field and the forces acting on the turbine blades. The strength of the bound vortex and the local flow velocity can be related in several ways and it is the manner in which these quantities are related that determines the accuracy and complexity of the model.

There are two main types of vortex models: prescribed-wake and free-wake (10). In prescribed wake vortex models the geometry of the wake of

the turbine is assumed to be known. The wake is typically assumed to be rigid and helical. Wake equations derived from previous wake studies can also be used (15). In free-wake models the exact path taken by the trailing vortices is found by an iterative method. The free-wake method requires a great deal of computer time (16).

A number of different vortex models for vertical axis wind turbines have been proposed. The early models were 2D vortex models and include work by Fanucci and Walters (17), Larsen (18), Wilson (19), and Holmes (20). In 1979 Strickland extended these concepts to form a model that could be used to model 3D cases such as the Darrieus turbine (12). VDART, is the simplest vortex model for the Darrieus turbine. VDART is both more accurate and much more complex than even the most advanced streamtube model (11). More recent vortex models include FEVDTM by Ponta and Jacovkis (21) and the VPM2D model by Wang et al (22). FEVDTM is the most complex and accurate of the vortex models. The VPM2D model is much simpler than FEVDTM, more accurate than VDART and only slightly less accurate than FEVDTM (22). Vortex models give much more accurate predictions of instantaneous forces than streamtube models, however it must be noted that the forces predicted by vortex models still differ from experimental results to some extent.

1.1.2 Streamtube models

Streamtube models are momentum models. The most basic momentum model is actuator disc theory which is used to derive the maximum amount of energy which can be converted from the wind: the Betz limit (16). More complex streamtube models are based on Glauert's Blade element theory (23) where the change in fluid momentum is equated to the streamwise forces acting on the aerofoil blades. This type of model is also referred to as a blade element momentum (BEM) model. In order to calculate the aerodynamic forces acting on the blades, the blades are divided into elements. The blade elements used to model a vertical axis

turbine are created by taking horizontal slices though the rotor and for a horizontal axis turbine the elements are radial.

In streamtube models the rotor is represented as an actuator disc. An actuator disc is an infinitely thin disc which offers no resistance to the flow passing through it. There is a step change in pressure between the upstream face of the disc and the downstream face of the disc, but the velocity is continuous through the disc (15). The load acting on the actuator disc is uniform across it, as is the velocity of the flow passing through it. It is also assumed that far upstream and downstream of the actuator disc the pressure is uniform, both inside and outside the streamtube enclosing the actuator disc. For a horizontal axis turbine the actuator disc is a flat, circular disc and for a straight bladed vertical axis turbine it is a cylinder. In early streamtube models the actuator disc is enclosed by a single streamtube. Using only one streamtube requires the assumption that the velocity is constant over the whole of the area swept by the rotor (15). In order to take into account differences in flow velocity across the rotor more recent models use multiple streamtubes (16), which are typically considered in isolation.

Momentum models can only accurately predict the performance of lightly loaded turbines. If the turbine is heavily loaded, momentum theory predicts flow reversal in the wake. Flow reversal does not actually occur in the wake of a heavily loaded rotor, instead the vortex structure of the wake breaks down and the wake becomes turbulent (10).

As well as inducing a momentum change in the axial direction, horizontal axis turbines also induce a momentum change in the tangential direction. This change in tangential momentum is taken into account through the use of a tangential induction factor as well as an axial induction factor. Multiple streamtube BEM models for horizontal axis turbines are presented in most texts on wind energy systems (for example (10), (13), (15), (16)). Corrections for heavily loaded rotors, tip losses and blade root losses are often also included.

Models for vertical axis turbines are more complex than those for horizontal axis turbines since the flow passes through the area swept by the turbine blades twice. A large number of streamtube models have been developed for vertical axis turbines. The first streamtube model for a vertical axis turbine was proposed by Templin in 1974 (24). In this model the turbine and the flow through it is represented by a single actuator disc enclosed by a single streamtube. Strickland (25) developed a multiple streamtube model to provide a better representation of the flow field through the rotor. This model allows the effects of wind shear to be taken into account. The next generation of models used two actuator discs so that they could also take into account the differences between the upwind and downwind halves of the rotor. Much of the work on double-multiple-streamtube models had been carried out by Parashivoiu (11) who developed three generations of computer codes: CARDAA (26), CARDAAV (27) and CARDAAX (28). The most advanced of these is able to take into account variations with azimuth angle and the expansion of the streamtubes as they pass through the rotor. The more recent streamtube models provide a more accurate representation of the flow field than the early models which increases the accuracy of the model results.

1.1.3 Applying aerodynamic models to tidal turbines

A review of the types of aerodynamic model used to predict the performance of tidal turbines found that BEM models were commonly used, particularly to model horizontal axis turbines (29), (8), (30). Despite the ability of vortex models to predict instantaneous forces with greater accuracy, they are less commonly used than BEM models. This is because BEM models can predict time averaged quantities with a high level of accuracy in a fraction of the computational time required by vortex models.

Whilst the BEM model is commonly used to predict the performance of tidal turbines they have a number of limitations which restrict the accuracy with which they can predict their behaviour. These are:

- the extent of the flow in which the rotor operates is assumed to be infinite
- the flow is assumed to be steady
- the flow is assumed to be inviscid, except when calculating the forces acting on the blade elements

A number of models have been developed specifically for tidal turbines. These models are mainly based on the BEM model and extend this model in order to overcome one of the limitations listed above. Typically this allows the model to take into account one of the differences between wind and tidal turbine operation, allowing it to predict tidal turbine performance with greater accuracy. These models are described in more detail in the following section.

1.2 Models developed for tidal turbines

Models have been developed which take into account a number of the differences between wind and tidal turbines. These include the effect of waves, cavitation, stall, differences in geometry, the effects of blockage and the effects of energy extraction on the available resource.

The effect of waves on tidal turbine performance has been investigated by a number of authors. This has included both experimental investigation and analytical modelling. The experiments carried out by Barltrop et al (31) in the wave/ towing tank at Strathclyde university have shown that waves have little effect on the mean axial thrust force acting on a horizontal axis rotor. The torque acting on the rotor was found to be increased slightly by the application of waves. This means that whilst it is important to consider the effects of waves in the structural design of the turbine, they will have little effect on its performance. Whelan et al (32)

carried out experiments to investigate the effects of inertia on horizontal axis turbines. In these experiments the turbine was placed in a water flume and the wave motion simulated by moving the turbine backwards and forwards in an approximately sinusoidal motion. These experiments demonstrated that the inertia effects due to waves are also small. Barltrop et al (31) has proposed an alteration to the standard BEM model which allows it to take into account the effects of waves. The agreement between the model and experimental results is reasonable. It is, however, worth noting that the effect of waves on the torque acting on the rotor was not large and there was little effect on the thrust force. Thus reasonable agreement between the model and experimental results may not imply that it can accurately capture the how the turbine performance is affected by waves, since the variation will be small.

Cavitation occurs when the local pressure on the blade falls below the vapour pressure of seawater (8). Cavitation can have a detrimental effect on the surface of the turbine blades and affect performance so ideally turbines should be designed either to avoid cavitation or to be able to withstand the effects of cavitation (7). Much information is available on the cavitation of marine propellers (for example (33), (34)) and this can be used as the knowledge base from which to start the investigation of the cavitation of tidal turbines. Batten et al have modelled the cavitation behaviour of the NACA 63-2xx and 63-8xx aerofoil sections, both of which are suitable for tidal turbines. Cavitation was also observed in experiments carried out by the same authors (35). They concluded that careful design of blade angles and tip speeds should allow cavitation to be prevented in full size turbines. It was also observed that a significant amount of cavitation can be tolerated by marine propellers without a significant loss of performance. Thus cavitation is an important factor to consider in the design of turbines, but it should not affect the performance of well designed turbines.

Stall is another area where the information available about marine propellers can, to some extent, be transferred to tidal turbines.

Experiments by Myers and Bahaj (36) demonstrated that, for rotating turbine blades, flow separation was delayed which lead to lift forces which were greater than those predicted by 2D measurements or conventional theory. Subsequent modelling work by members of the same research group used a modified approach to calculate the aerofoil section coefficients (37), (38). Coefficients well below the stall angle were predicted using XFoil, a 2D panel code. These values were extrapolated up to the stall delay angle using the method proposed by Snel et al (39) and beyond the stall delay angle using Viterna and Corrigan's methodology for post stall predictions (40). This methodology allows the stall behaviour of tidal turbines to be more accurately represented in performance prediction models without having to change the models themselves, just the manner in which the blade section lift and drag coefficients are obtained.

Whilst the three-bladed horizontal axis turbine has become the industry standard for wind energy, there is much more variation in the designs of tidal turbines which are currently being developed. The characteristics of tidal currents vary from site to site so, for the tidal current industry, a standard turbine may not emerge. Robinson et al are developing models for tidal turbines with different geometries to conventional wind turbines (9). In particular the work focuses on the modelling of ducted turbines.

The effects of blockage on tidal turbine performance have been investigated by Whelan et al (41) (42). In this work an extension to a BEM model was proposed to allow it to take into account blockage effects. This model cannot take into account the position of the turbine relative to the boundaries; it only considers the area of the turbines relative to the area of the channel. Akwensivie (43) carried out a CFD investigation of the geometry of the wake of a turbine at two different depths. The performance of the turbine was not studied, but the depth was found to impact the geometry of the wake, which implies that performance changes with surface proximity.

A number of models have also been proposed which aim to quantify the effects of energy extraction on the flow at a site (44). Extracting energy has the potential to change the flow speed and surface elevation at sections of the site. The models use both numerical (45) and analytical approaches (4,46-53). In these models the turbines are represented as additional drag terms. Draper et al (54) have proposed an actuator disc model which can be used in a numerical two-dimensional depth averaged shallow flow models. This allows a link to be made between the energy extraction and a tidal device. The actuator disc model has been developed so that it takes into account the effects of blockage. The work does not use blade element theory and so it does not consider actual devices. Instead the turbine is assumed to be operating at maximum efficiency (disc velocity equal to 1/3 of free-stream velocity) and the power generated is calculated from the thrust force acting on the disc multiplied by the velocity of the flow through the disc.

1.3 Numerical modelling

In the previous sections a number of analytical models for turbines were discussed. In these models the flow in the majority of the flow field is considered to be inviscid and viscous effects are only taken into account when calculating the forces acting on the blade elements. This section describes the equations and solution techniques necessary to take into account viscous effects over the whole flow field. If viscous effects are not taken into account over the whole flow field, the effects of the proximity of the boundaries cannot be studied. Viscous effects also cause the mixing of the wake with the flow outside the wake. The distance over which this occurs is an area of importance for the design of farms of turbines. Since viscous effects need to be taken into account over the entire flow field to model some of the aspects of tidal turbine behaviour, numerical methods, such as Computational fluid dynamics (CFD), are a valuable tool in the study of tidal turbine performance.

Use of the Navier Stokes equations allows viscous effects to be taken into account. Combining the Navier Stokes equations with the conservation of mass equation provides a complete mathematical description of the flow of incompressible Newtonian fluids. There are few instances for which an exact mathematical solution for the Navier Stokes equations can be obtained since, despite being mathematically well posed, they are non-linear second order partial differential equations (55). A number of numerical solution techniques have been developed which allow approximate solutions to be found for a much greater variety of problems than can be solved exactly.

All numerical solution techniques consist of a number of components. These include the mathematical model, the discretisation method, the solution method and the convergence criteria (56). The mathematical model is the set of partial differential equations (in this case the Navier Stokes equations) and the boundary conditions used to describe the flow. An approximate solution to the mathematical model can be found using discrete values at a number of locations in space and time to provide a representation of the flow field. This allows the flow field to be described using a set of algebraic equations instead of the differential equation. The method used to approximate the differential equations by a system of algebraic equations for variables at a discrete set of points is called the discretisation method. There are many different discretisation methods including the finite difference, finite volume and finite element methods (57). Once the algebraic equations have been generated, a method needs to be selected that can be used to solve them. Typically the solution method is iterative since the equations are non-linear. The convergence criteria determine when the iterative solution is stopped.

Numerical solutions include three types of systematic error: modelling errors, discretisation errors and iteration errors (56). The accuracy of the solution will depend on the magnitude of these errors. Errors may also be introduced by the setting of the boundary conditions, development of the solution algorithms or in programming.

Modelling errors are the difference between the exact solution of the mathematical model and the actual flow. The extent of the modelling error can be obtained by comparing the numerical solution, with known discretisation and iteration errors, with experimental data. This can be problematic since numerical solution methods are often applied to situations where it would be too difficult or costly to obtain experimental results. For cases such as this an indication of whether the model provides a reasonable representation of the actual flow can be obtained by modelling a simplified version of the case for which a solution is known. This does not provide conclusive proof that the mathematical model is a good representation of the flow but it does typically demonstrate that some of the features of the model provide a reasonable representation of the flow. Care should also be taken to thoroughly assess the limitations of any experimental data sets that the numerical solutions are to be compared with. Particular care should be taken when interpreting the results of scale model experiments as in many cases the model used will be a distorted model since it is frequently not possible to satisfy all the similarity requirements at once.

The discretisation error is the difference between the exact solution of the differential equations of the model and the exact solution of the algebraic system of equations obtained by discretising the differential equation. The discretisation error can be reduced by refining the grid. As the grid size is reduced, the computational time is increased. The largest grid size for which the discretisation error is deemed to be acceptably small can be found by running the same model on successively smaller grids.

1.3.1 Turbulence models

Tidal flows are turbulent. A number of numerical approaches have been developed to deal with turbulent flows. For most situations it is not necessary to know all the details of a flow: knowledge of mean quantities is sufficient. This allows the Navier-Stokes equations to be solved in a

time averaged form, resulting in a significant reduction in computational cost. These methods are referred to as Reynolds averaged Navier-Stokes (RANS) methods. The time averaged Navier-Stokes equations contain unknown stresses and heat fluxes, called Reynolds stresses, which need to be expressed in terms of the basic flow variables to allow the equations to be solved. In RANS methods, turbulence models are used to express the Reynolds stresses in terms of the basic flow variables (58).

Turbulence models are often categorised according to the number of differential equations that they use in addition to the RANS equations (59). The models can also be classified according to whether or not they contain non-linear terms. Linear turbulence models assume that the turbulent shear stress is directly proportional to the strain, a theory attributed to Boussinesq. Boussinesq proposed that, in analogy to laminar flow, the Reynolds stresses can be expressed in terms of an eddy viscosity and a velocity gradient (60).

Non-linear models include explicit algebraic Reynolds stress models (EARSM) and full Reynolds stress models (RSM). EARSM models can be implemented as two-equation models but RSM models require the solution of additional turbulence models. RSM models are not widely used, due to their complexity; however they represent the most complete approximation level in a RANS framework (61).

The choice of a turbulence model is very important since subtle differences in turbulence models can have a significant effect on the predicted results (62). For example, the performance of a tidal turbine depends on the lift and drag forces acting on the blades. Stall of an aerofoil is not always caused by the separation of the boundary layer from the surface of the aerofoil; stall can also be caused by flow reversals in the wake of the main aerofoil (63). The growth of the wake and the extent to which flow reversal occurs is determined by the turbulent mixing in the wake, so the lift and drag forces acting on the turbine and hence the power generated, depend heavily on the turbulence.

A number of different researchers have carried out CFD studies of tidal turbine performance. The turbulence models used in these studies have varied. In the work by Sun et al (64) and the work by Edinburgh Designs (29) the k-ε turbulence model was used. No justification was given for this choice of turbulence model. In his review of turbulence models for the flow past aircraft Tulapurkara (58) states:

“The calculations based on the k-ε do not give satisfactory results when the streamlines are curved and when the flow is subjected to severe adverse pressure gradients”

This suggests that the k-ε model may not be the most suitable turbulence model for modelling tidal turbines. Harrison et al (65) uses the SST k-ω model. The SST k-ω model combines aspect of the k-ω and k-ε turbulence models. The SST k-ω model has been demonstrated to perform well in situations with adverse pressure gradients and separated flows whilst avoiding the free stream dependency of the original k-ω model (63). This makes it a more suitable choice for modelling tidal turbines than the k-ε model.

1.4 Summary

A number of differences have been identified between wind energy and tidal stream energy. Models have been developed which aim to extend the basic aerodynamic models to better represent the conditions encountered in tidal flows. The effects of the boundaries and the alteration of flow speeds caused by the presence of turbines have been identified as the areas requiring further investigation. Wave effects will not be considered as these have been shown to have very little effect on tidal turbine performance. Alternative turbine geometries will also not be considered as many of the tidal turbine concepts which have been proposed are sufficiently similar to conventional wind turbines to merit the development

of models which can accurately represent these turbines, before going on the develop models which can take into account alternative geometries.

Whilst an extension to BEM theory has already been proposed which takes into account the effects of blockage, the effect of the boundaries on turbine performance was thought to merit further investigation. The blockage model has not been used to study the magnitude of the expected performance change for realistically sized turbines in actual tidal channels. Without this application, it is not possible to determine whether blockage will have a significant effect on performance. In addition the blockage model is not able to take into account the position of the turbine in the flow. Since the position of the turbine relative to the surface has been shown to affect the wake generated by the turbine, surface proximity is also likely to have an effect on turbine performance and so the effects of boundary proximity will also be investigated.

Since turbine performance is highly dependent on flow speed, the effect of turbines on the flow speed has the potential to significantly alter the amount of energy which a turbine can extract. Previous work has focussed on setting limits for the amount of energy which can be extracted and not on modelling how a given number of actual turbines will modify the flow speed at a site or the effect that the alteration in flow speed will have on the power generated by the turbines.

Modelling will be carried out using both analytical models based on blade element theory and numerical models. Blade element theory has been selected as the analytical modelling technique since it has been shown to accurately predict time averaged quantities and the simplicity of this modelling technique allows it to be readily adapted to take into account the conditions being studied. Numerical modelling will be used to investigate the effects of surface proximity. For the effects of surface proximity to be studied, viscous effects need to be taken into account over the entire flow field, so a numerical modelling technique needs to be used.

Chapter 2 The representation, design and operation of turbines

This chapter considers how turbines are represented in analytical, numerical and experimental investigations. When modelling the effect of tidal turbines on the available resource, a simplified model of a turbine is used: the ideal turbine. A similar approach is taken in small scale experimental investigations of turbine behaviour. In these experiments a turbine simulator, a porous disc, is used to represent the turbine. The porous disc has also been used in numerical simulations in order to simplify the case to be modelled, reducing both the time taken to develop the model and the computational time. Understanding the validity of these analytical, numerical and experimental results requires knowledge of the difference between the ideal model predictions and actual turbine performance. The analytical models of turbine performance developed in the subsequent chapters are for real turbines. For these models to be used to generate results, they require the parameters of a turbine to be defined. Two different turbines are proposed for use in these models and the characteristics of these turbines under different types of operation are investigated.

2.1 Real and ideal turbines

Chapter 1 introduced the concept of an actuator disc. In the actuator disc representation of the turbine the power generated is considered to be the rate at which kinetic energy is extracted from the flow. The power generated by an actuator disc is calculated by multiplying the force exerted on the disc (caused by the pressure change across the disc) by the flow velocity through the disc:

$$Power = Tu$$

Equation 1

Where:

T is the force acting on the disc
u is the speed of the flow through the disc

In blade element momentum theory the force exerted on the actuator disc is related to the forces acting on the blade elements. The axial force acting on a blade element is given by Equation 2. It can be seen from this equation that both the lift force and drag force acting on the blades contribute to the axial force. The torque acting on a blade element is given by Equation 3. It can be seen from this equation that the drag force reduces the torque acting on the blade. The shaft power generated by the turbine is given by Equation 4 and is a function of the torque. This means that estimating the power from the axial force applied to the fluid will overestimate the power since the drag force contributes to the axial force but reduces the torque, reducing the shaft power. The discrepancy between the power extracted from the flow and the shaft power depends both on the turbine design and the conditions under which it is being operated.

$$f = 0.5\rho W^2 Nc(C_L \cos\phi + C_{Dt} \sin\phi)$$
Equation 2

$$q = 0.5\rho W^2 Nc(C_L \sin\phi - C_{Dt} \cos\phi)r$$
Equation 3

$$shaft\ power = Q\Omega$$
Equation 4

The actuator disc representation of the turbine is referred to as an ideal turbine. This type of model is used when the general effects of energy extraction, rather than the performance of a particular turbine, are being studied. The amount by which the ideal turbine model over-predicts the power generated depends on the turbine being modelled, so the ideal turbine model provides more insight into the general effects of turbines than if an actual turbine model was used in the same study.

The blade element model allows the performance of actual turbines to be studied. It is used when the performance of a particular turbine is being modelled. Blade element momentum models also over-predict the power generated since they do not take into account the drag on the supporting structure or the efficiency with which the mechanical energy is converted into electrical energy.

The dimensionless quantity typically used to describe wind turbine performance is the power coefficient. The power coefficient is the ratio of the power generated by the turbine to the power that would pass through the cross section of the swept area of the turbine in the absence of the turbine (Equation 5).

$$C_P = \frac{power}{0.5\rho u_\infty^3 A}$$

Equation 5

2.2 Turbine simulators

For the performance of a scale model turbine to be directly comparable with the performance of a full size turbine there must be similarity between the blade Reynolds numbers of the full size and model turbines. For most test facilities, if the turbine is scaled so that the ratio of device height to water depth is representative of that of anticipated for the full scale device, the turbine would have to rotate at a very high rate in order to maintain blade Reynolds number similarity. Operating the model turbine at these rotational speeds would lead to swirl and pressure gradients in the wake which are not present in the wake of a full scale turbine. It is also impractical from an engineering perspective to produce a model turbine which can rotate at these very high speeds (66). This difficulty was also encountered during the early work on the effect of wind turbine wake interaction. Instead of attempting to fit a large number of rotating models in a wind tunnel, experiments were carried out using arrays of perforated discs (67)(68,69). Perforated discs have also been

used to represent tidal turbines. In addition to being used in scale model experiments (41,42,66,70,71), porous discs have also been used to represent tidal turbines in CFD analysis (64,65).

A porous material, such as a perforated disc, extracts energy from a flow in a similar manner to a turbine. Unlike a turbine, which converts most of the energy it extracts into mechanical motion, a porous material converts the energy to small-scale turbulence downstream of the disc. Since the turbulence induced by the disc differs from that induced by a turbine and the swirl angle of the flow from the disc is zero, the near wake of a turbine simulator will differ from that of a rotating turbine (71). The far wake region of a turbine simulator has, however, been shown to be very similar to that of a rotating turbine with the same thrust coefficient (69). This allows porous discs to be used to represent turbines, provided that the properties of the near wake are not of interest.

The pressure drop across a porous material is given by Equation 6. The pressure change across the material can be integrated over the area of the material to give the thrust force acting on the material. If the thrust force is uniform over the material (this occurs when u is uniform), then the force acting on the material is given by Equation 7.

$$\Delta P = P_u - P_d = \frac{1}{2}\rho k u^2$$

Equation 6

Where:

P_u = pressure on upstream side of porous material

P_d = pressure on downstream side of porous material

k = resistance coefficient of porous material

u = the normal component of the velocity of the flow through the screen

$$F = \frac{1}{2}\rho A k u^2$$

Equation 7

Where:

A = area of material

The turbine simulator is assumed to be an ideal turbine: the power generated by the turbine simulator is equal to the rate at which energy is extracted from the flow. This assumption has been made because it is not possible to comment on the difference between the energy extracted from the flow and the energy converted to a useable form, since none of the energy extracted is converted into a useable form. The rate at which energy is extracted from the flow is given by Equation 8. The rate at which energy is extracted is termed the power generated since the turbine simulator is assumed to be equivalent to an ideal turbine. Substituting Equation 8 into Equation 5 and simplifying gives an expression for the power coefficient of the turbine simulator (Equation 9).

$$power = \frac{1}{2}\rho A k u^3$$

Equation 8

$$C_P = \frac{k u^3}{u_\infty^3}$$

Equation 9

The resistance coefficient of the material is dependant on both the solidity of the material and the Reynolds number of the flow through it. A number of authors have developed empirical relationships between the solidity of the material and the resistance coefficient (42,65,72,73). Of these relationships, the one found to be most applicable to the range of solidities and Reynolds numbers of the materials used to represent tidal turbines is that of Taylor (42,73):

$$\theta^2 = \frac{1}{1+k}$$

Equation 10

Where:

θ is the open area ratio of the material (open area/total area)

This equation can be used to estimate the open area ratio needed to represent a turbine operating with a given interference factor. However the equation is only an approximation and so for experiments which use turbine simulators the force acting on the simulator should always be measured and not calculated from Equation 7 using a k value calculated from Equation 10.

2.3 BEM model

In chapters 3 and 4 new models are developed which need input from a performance prediction model for a wind turbine. The model selected for use in the development of the new models in chapters 3 and 4 is a BEM model. A BEM model was used since this type of model can accurately predict time averaged quantities whilst still being simple enough to be readily adapted. The BEM model used is one of the blade element momentum models for a horizontal axis turbine presented by Sharpe in (10). It is a basic BEM model and does not include corrections for tip loss, hub loss or high induction. The angles and velocities used in the model are defined in Figure 2. 1. A flow chart showing calculation procedure for the model is shown in Figure 2.2.

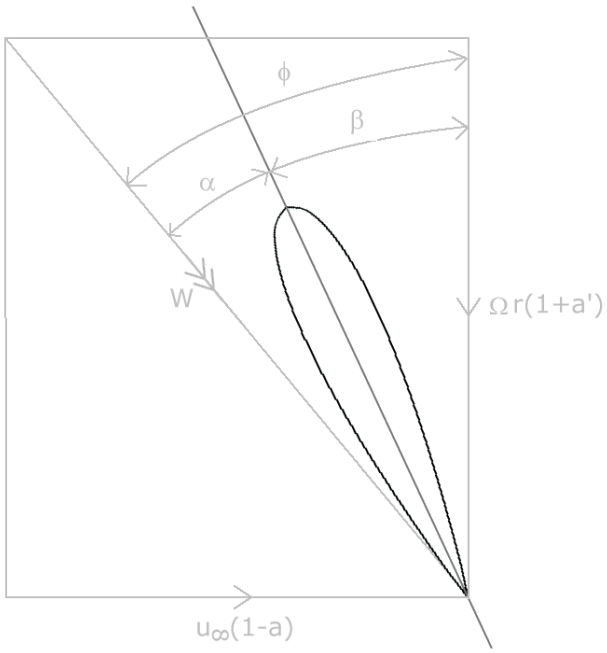

Figure 2. 1 - Angles and velocities relative to blade element

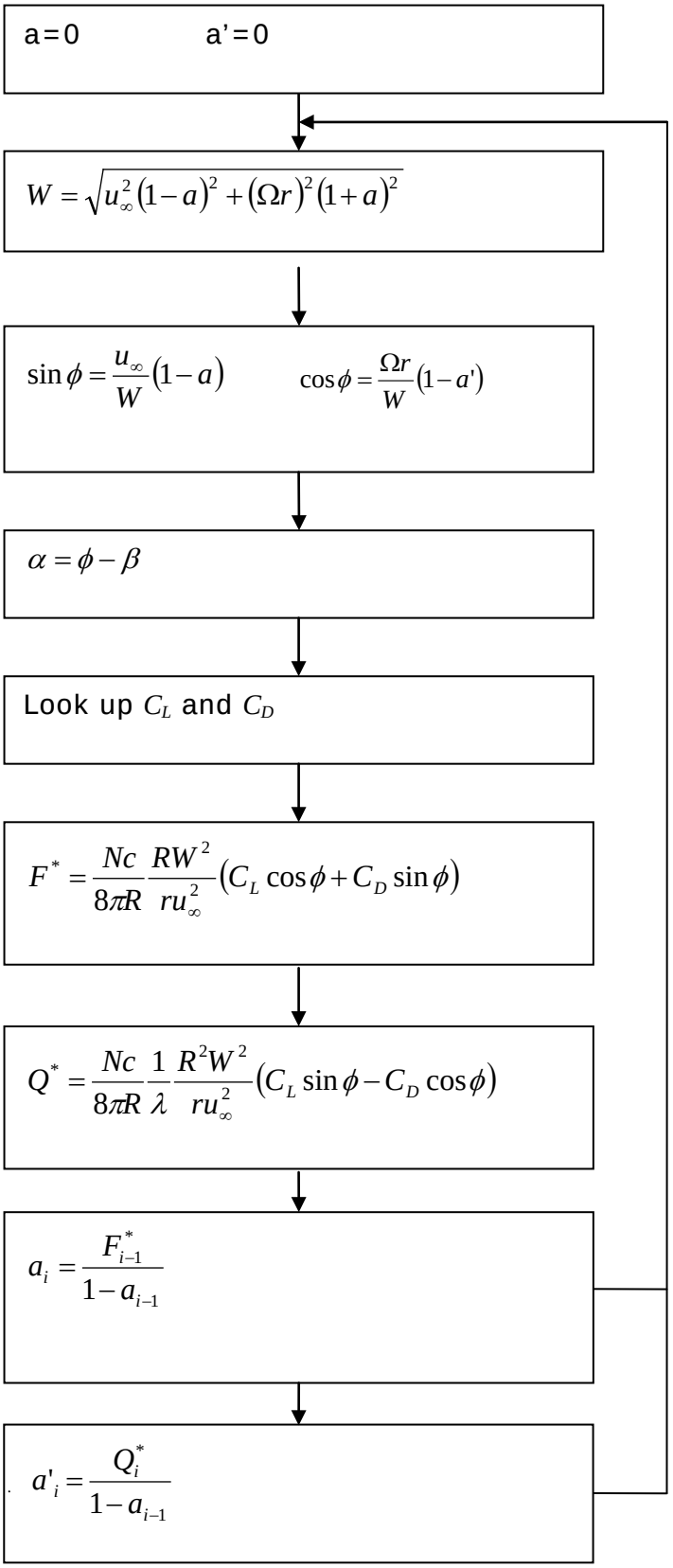

Figure 2.2 - Flow chart showing calculation procedure for blade element momentum model

Once the values for the axial and tangential interference factors have converged the torque acting per unit length of blade can be calculated using Equation 11. The torque acting on the complete rotor is given by Equation 12 and the power coefficient by Equation 13. The torque acting on the rotor and the power coefficient were only calculated for cases where convergence was reached for each blade element.

$$q = 0.5\rho W^2 Nc\left(C_L \cos\phi - C_D \sin\phi\right)r$$

Equation 11

$$Q = \int_{Rr}^{R} q dr$$

Equation 12

Where:

Rr is the root radius of the blades

$$C_p = \frac{Q\Omega}{0.5\rho u_\infty^2 A}$$

Equation 13

Where A is the area of the turbine actuator disc

This model has been applied to a turbine of the dimensions modelled and tested by Batten et al (38). Each blade was represented by 10 elements. In Figure 2. 3 the output of this model for a hub pitch angle of 20^o is plotted with results from Batten et al's model presented in (21). In (21) Batten et al plot the results from their model with experimental data. This figure is reproduced below in Figure 2. 4. It can be seen from this figure that the agreement between Batten et al's model results and experimental result is generally very good, with the model slightly over-predicting power coefficient at tip speed ratios greater than around 7. From Figure 2. 3 it can be seen that there is good agreement between the model results and the results from Batten et al's model for tip speed ratios below 6. For tip speed ratios above 6 the model over-predicts the power coefficient

slightly. This difference is likely to be due to a number of factors including errors in the aerofoil lift and drag coefficient data used and the simplicity of the model. The coefficient data used was estimated from graphs of lift and drag coefficient variation with angle of attack presented in (38). These graphs apply to a single, unspecified, Reynolds number but the data has been used for the whole range of Reynolds numbers which will introduce errors. The model would also be more accurate if it included corrections for tip loss, hub loss and high induction. The agreement between the model and the verification model output was felt to be sufficiently good for the model to be used as a starting point for the new models developed in chapters 3 and 4.

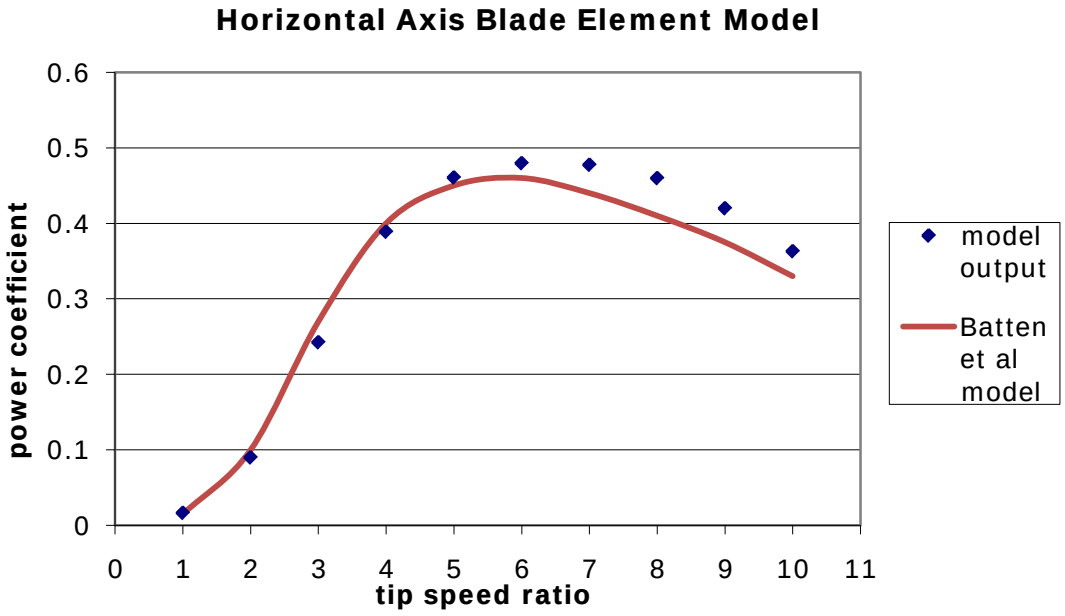

Figure 2. 3 - Model results plotted with results from Batten et al model

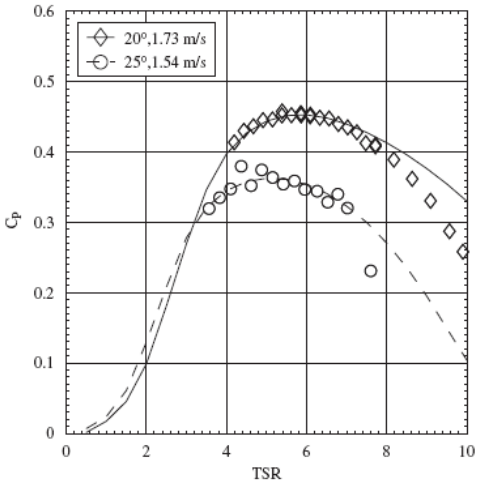

Fig. 5. Cavitation tunnel power coefficient (C_P) measurements versus theoretical results.

Figure 2. 4- Batten et al model results plotted with experimental data (74)

2.4 Turbine design

The optimum design for a turbine will depend on the distribution of flow speeds at the site where it is to be installed and its mode of operation (13). Design procedures have been proposed which allow the geometry of a blade to be optimised for a given tip speed ratio (10,13,75). These procedures allow the taper, chord length and aerofoil section of the blade to be designed. If the turbine is operated at a tip speed ratio other than that for which the blade was optimised, the performance of the turbine will no longer be optimal. Compromises also need to be made between the performance and the manufacturability of the blade since the optimum blade shape will be difficult to manufacture (75). Typically an iterative procedure is used to design turbine blades so as to optimise the performance of turbine for the flow speed variation at a given site. It should, however, be noted that the improvements gained by optimising blade shape are not large: Walker et al state that the best possible wind turbine blade will only be 10% more aerodynamically efficient than a plank of wood (16).

This work is not concerned with designing a new turbine, but for the models developed in chapters 3 and 4 the calculations cannot be carried out for a generic turbine and the design of a specific turbine needs to be defined. So that the results remain as general as possible, two different designs of turbine have been developed for use in these calculations. The first design has blades with a constant twist angle and taper. The second design is more optimised than the first design and has tapered blades with a twist angle that varies along the length of the blade. Both the turbines use NACA 0018 section blades. Whilst a thicker and more advanced aerofoil, such as some of the NACA 6-series sections, might give better performance and structural performance, the NACA 0018 section has been selected because coefficient data for the symmetrical sections is more readily available. The lift and drag coefficient data for the NACA 0018 section is taken from Shiedahl and Klimas (76). This data set was selected since it gives the coefficients over a 180^{o} angle of attack range and for Reynolds numbers applicable to those encountered by turbine blades. Graphs of the variation of the lift and drag coefficients of the NACA 0018 section with angle of attack are shown in Figure 2.5The data set for the NACA 0018 profile is one of seven data sets for symmetrical aerofoils which were obtained by experiment and modelling. These data sets were originally produced for the aerodynamic analysis of vertical axis wind turbines.

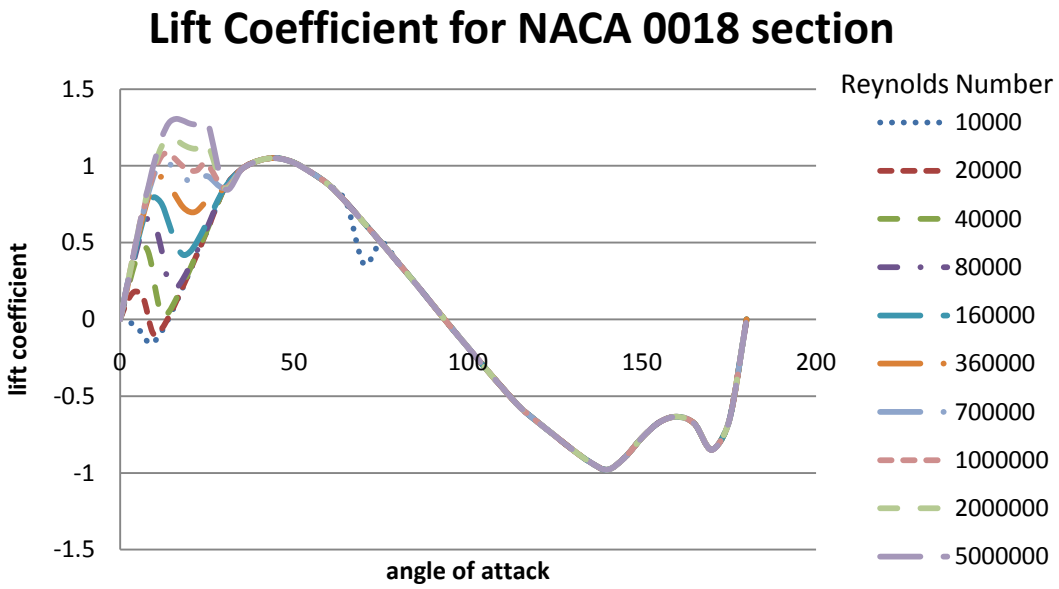

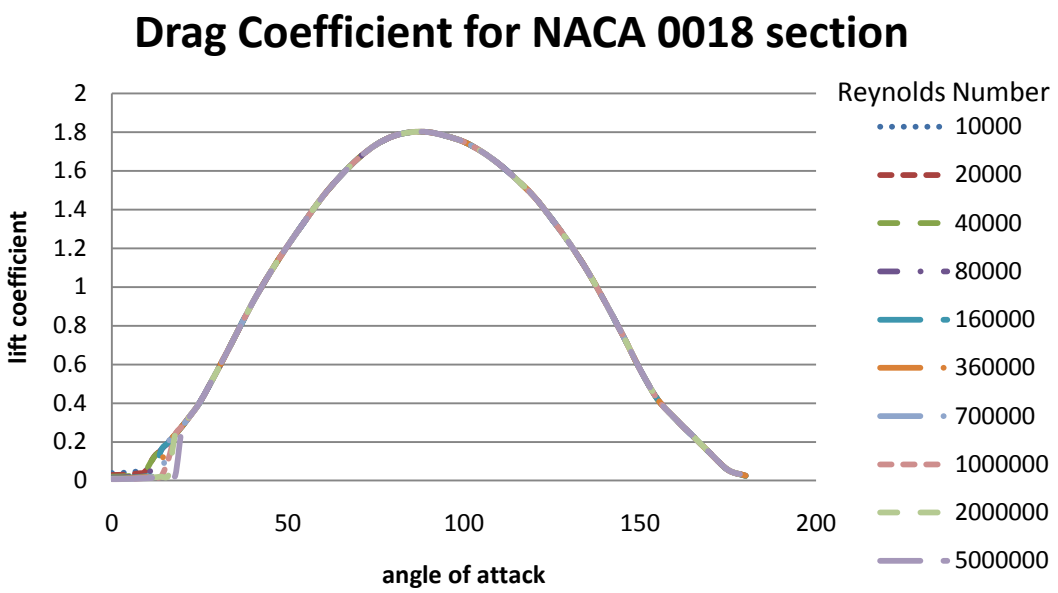

Figure 2.5- Variation of lift and drag coefficients with angle of attack for NACA 0018 section

The turbine geometry is presented in tables showing the variation of the chord length and blade twist angle with the position along the blade. When defining the variation of chord length the chord length is defined at a number of radii along the blade. The symbol r is used to denote the local radius and the symbol c is used to denote the local chord length (Figure 2.6).

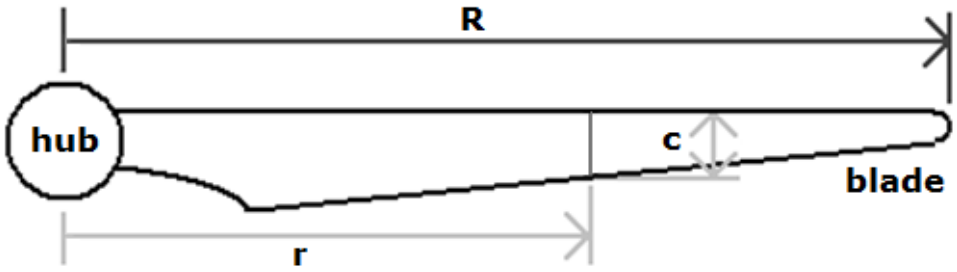

Figure 2.6 - Definition of parameters used to define blade geometry

The parameters of the turbine with blades with a constant twist angle and taper are given in Table 2.1. This turbine will hereafter be known as Turbine A. This turbine performs best at a tip speed ratio of 5 and a hub pitch angle of 5^{o}.

Table 2.1- Variation of chord length with radius for Turbine A

r/R	c/R
0.1	0.1791
0.2	0.1050
0.3	0.0599
0.4	0.0373
0.5	0.0251
0.6	0.0179
0.7	0.0134
0.8	0.0104
0.9	0.0083
1.0	0.0067

The parameters of the turbine which has tapered blades and a twist angle that varies along the length of the blade are given in Table 2.2. This turbine is hereafter known as turbine B. Turbine B has the same variation of chord length with radius as turbine A. The performance of turbine B is maximum for a tip speed ratio of 5 and a hub pitch angle of 8^{o}.

Table 2.2- Variation of chord length and blade twist angle with radius for Turbine B

r/R	c/R	β/R
0.1	0.1791	2.6573
0.2	0.1050	2.5588
0.3	0.0599	1.8150
0.4	0.0373	1.1961
0.5	0.0251	0.7379
0.6	0.0179	0.3978
0.7	0.0134	0.1392
0.8	0.0104	-0.0625
0.9	0.0083	-0.2236
1	0.0067	-0.3548

Curves showing the variation of power coefficient with tip speed ratio for a range of diameters of turbines A and B are shown in Figure 2.7 and Figure 2.8. Another dimensionless parameter used to describe turbine performance is the thrust coefficient. The thrust coefficient is calculated using Equation 14. Figure 2.9 and Figure 2.10 show how the thrust coefficient of a range of diameters of turbines A and B vary with tip speed ratio.

$$C_T = \frac{T}{0.5\rho u_\infty^2 A}$$

Equation 14

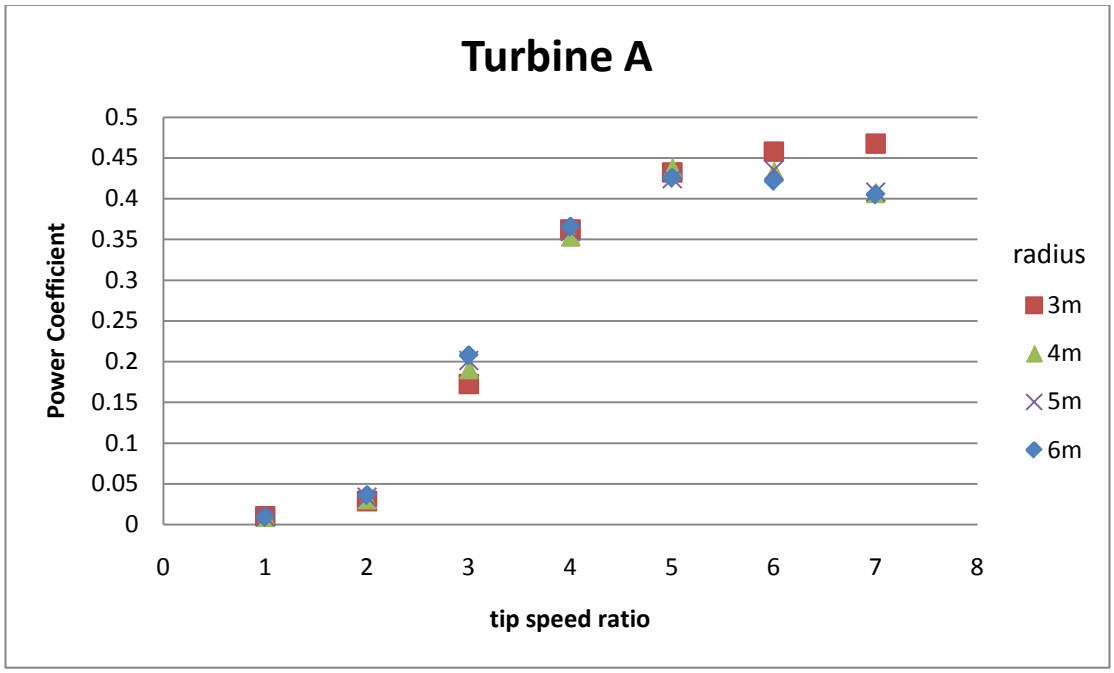

Figure 2.7- Power coefficient- tip speed ratio performance curve for turbine A

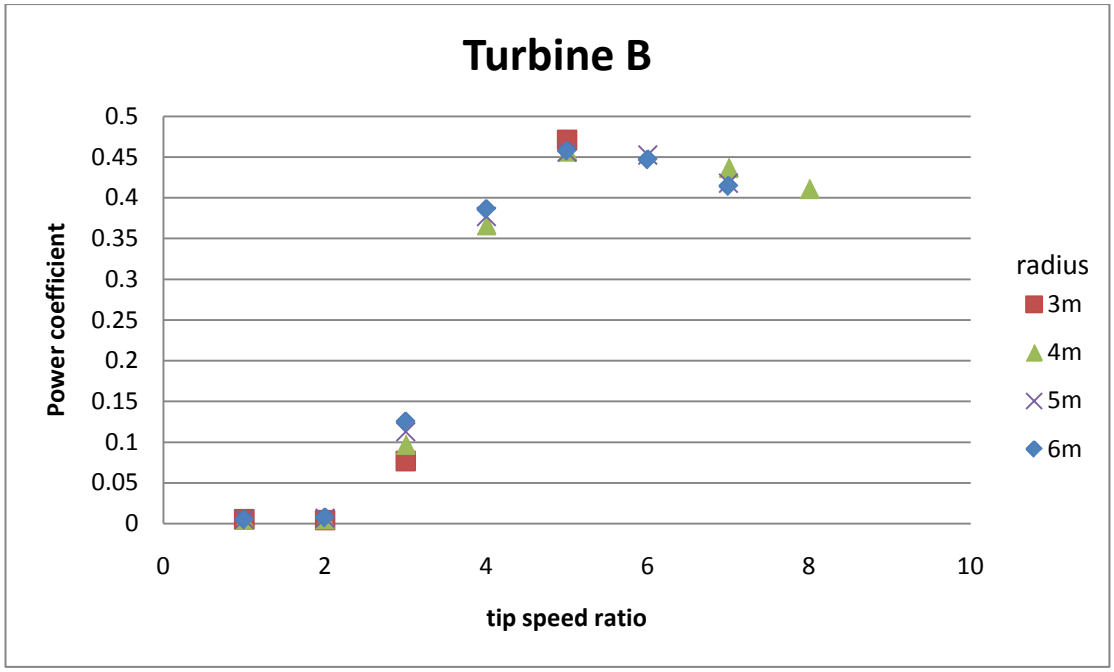

Figure 2.8- Power coefficient- tip speed ratio performance curve for turbine B

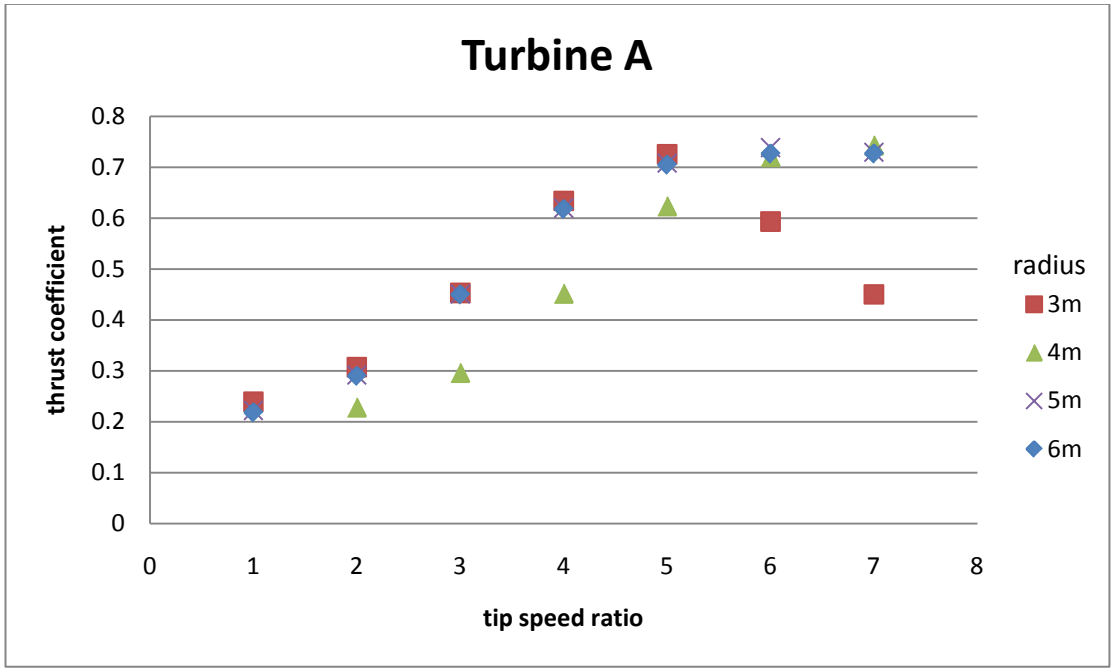

Figure 2.9- Thrust coefficient- tip speed ratio performance curve for turbine A

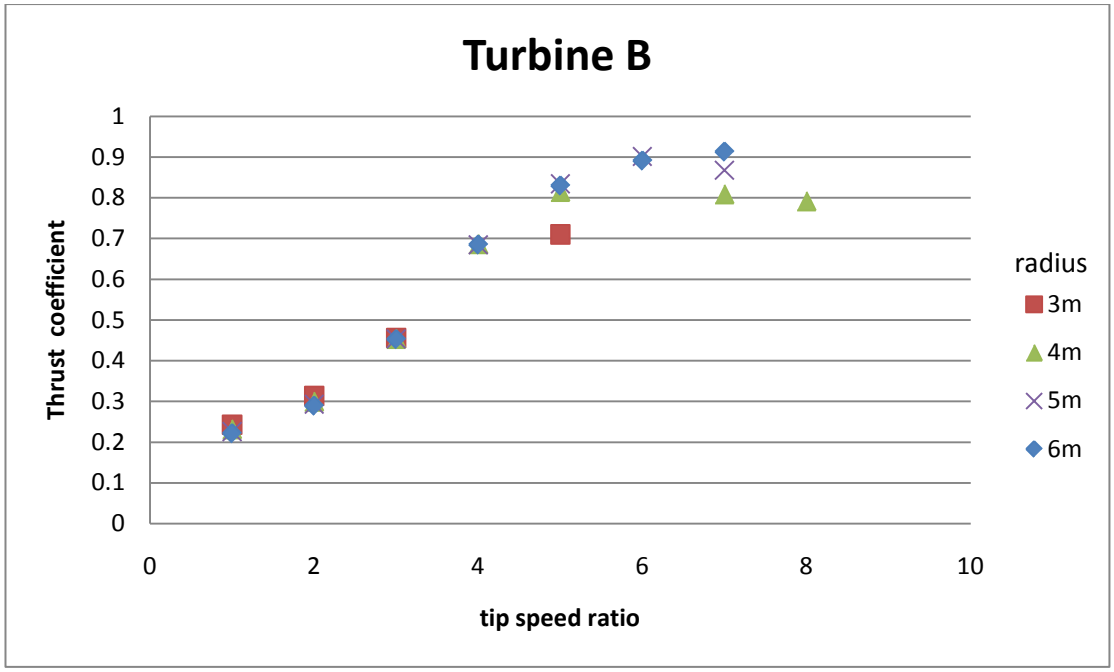

Figure 2.10- Thrust coefficient- tip speed ratio performance curve for turbine B

2.5 Turbine operation

Turbines can either be operated at a fixed or variable rotational speed (77). If the rotational speed of the turbine is held constant, the tip speed ratio at which the turbine operates will vary as the speed of the flow at the site varies. For a turbine with fixed pitch blades, this means that the turbine will not always be operating at the optimal tip speed ratio. The efficiency of a turbine operating at a constant rotational speed can be maintained by altering the pitch of the blades as the flow speed changes in order to keep the blades at the optimum angle of attack. For fixed pitch turbines even though the efficiency of the turbine is reduced at speeds above the optimum tip speed ratio, the power generated can remain high since it is proportional to the cube of the flow speed (78). Most turbines operate at constant speed (16) with either fixed or variable pitch blades. The electricity delivered to the grid by a turbine has to be of constant frequency. If the turbine connects to a generator through a constant ratio gearbox, the turbine must rotate at a constant speed in order to generate electricity of a constant frequency. Variable speed turbines use power

electronics to ensure that the power generated is of the required form (75).

2.6 Turbine performance

The manner in which the power generated by the turbine and the thrust force acting on the turbine vary with upstream flow speed depends on the mode of operation, design and geometry of the turbine. The variation of thrust force and power generated are significant for estimating the resource available at a site and the power which could be generated by the turbine at a site. The variation with upstream flow speed of thrust force, power coefficient and power generated has been calculated for turbines A and B. The turbines were modelled for constant tip speed ratio operation and constant rotational speed operation. For the constant rotational speed operation the turbines were assumed to have fixed pitch blades. Variable pitch operation was not considered due to the increased complexity of the models required to model this type of turbine. Using the BEM model described in section 2.3, the performance of the turbines was investigated for flow speeds between 0.1 and 3 m/s and for turbines of radius of 3 to 6m. The maximum flow speed of 3 m/s is representative of the Sound of Islay which is used as a case study in chapters 3 and 4.

For the constant tip speed ratio operation of the turbines a tip speed ratio of 5 was selected, since performance is optimised at this tip speed ratio. Figure 2.11 and Figure 2.12 show the variation of power coefficient with free stream velocity for the constant tip speed ratio operation of turbines A and B. These graphs show that the power coefficient of the turbine has little dependence on the flow speed or the turbine radius once flow speed is above a certain threshold. As the free stream velocity decreases the rotational speed of the turbine must also decrease if the tip speed ratio of the turbine is to remain constant. The reduction in free stream velocity and rotational speed reduces the blade Reynolds number of the blade elements. At low Reynolds numbers the lift force acting on the blade elements is low and the drag force is high so the overall torque acting on

the blade element is low (or in some cases negative). The rotational speed of the blade element increases with radius. For the smaller diameter turbines a larger percentage of the blade will be operating at Reynolds numbers where the torque generated is small or negative and so the reduction in power coefficient at low upstream flow speeds is greater for the smaller diameter turbines.

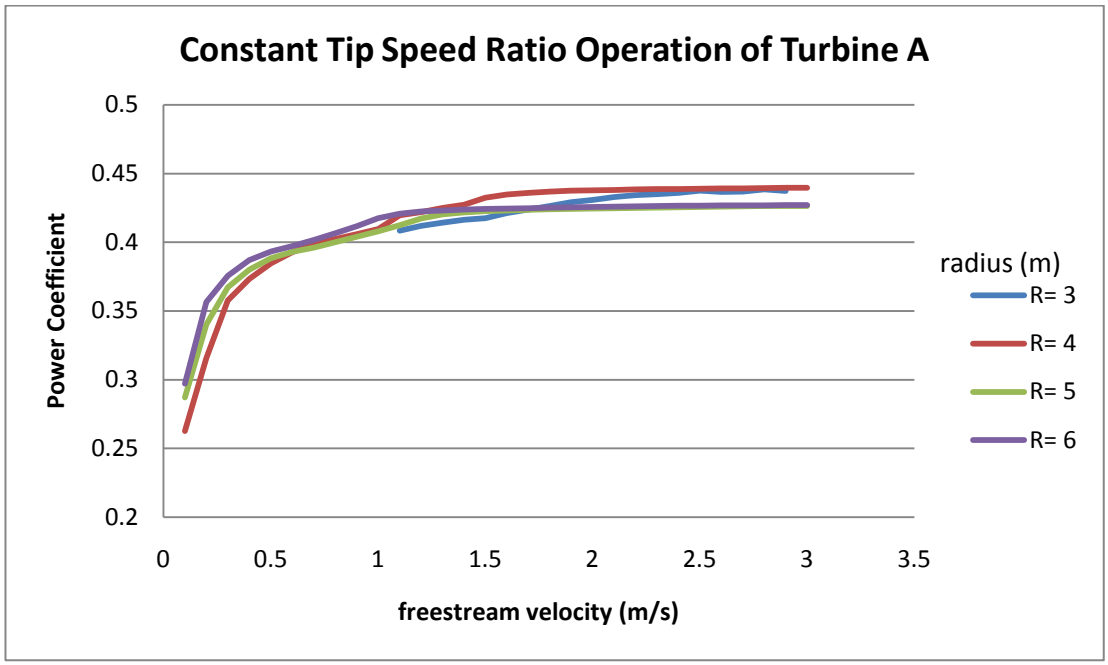

Figure 2.11 - Variation of power coefficient with free-stream velocity for the constant tip speed ratio operation of Turbine A

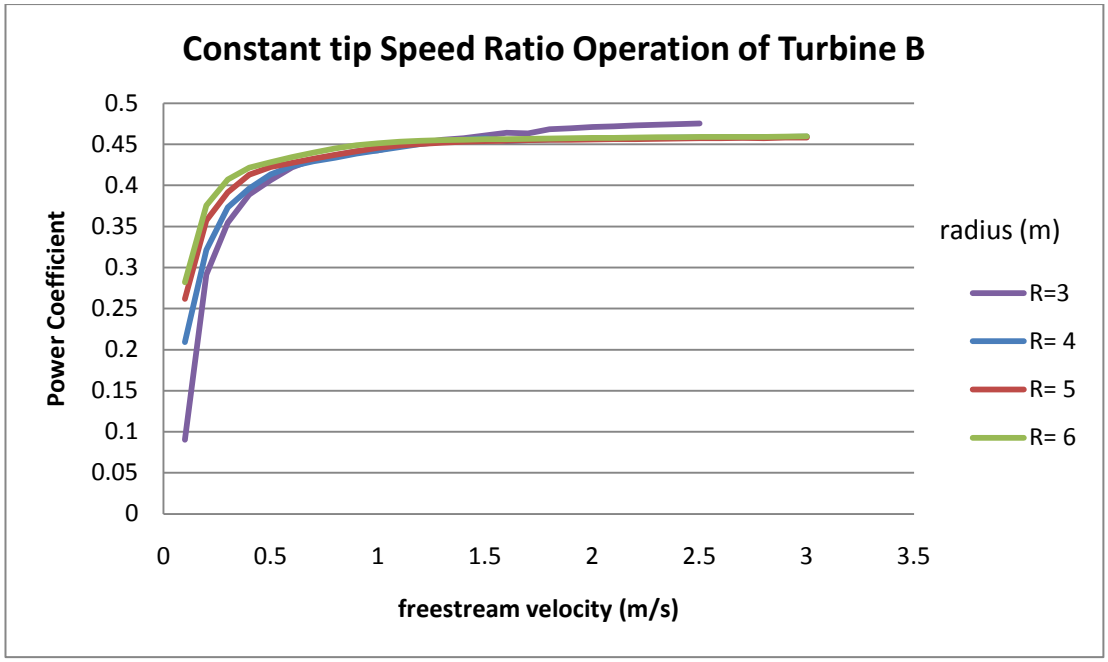

Figure 2.12 - Variation of power coefficient with free-stream velocity for the constant tip speed ration operation of Turbine B

For the fixed pitch constant rotational speed operation of the turbine, the rotational speed was selected to give the optimum tip speed ratio at the mean flow speed (1.65m/s). Figure 2.13 and Figure 2.14 show the variation of power coefficient with free-stream velocity for the constant rotational speed operation of turbines A and B with fixed pitch blades. As expected, the variation of power coefficient with free stream velocity is much greater for constant rotational speed operation than it is for constant tip speed ratio. For the constant rotational speed operation of Turbine A there is very little variation in power coefficient with turbine radius. For Turbine B there is more variation in power coefficient with radius. Keeping the rotational speed constant helps to keep the blade Reynolds numbers outside the range where the torque acting on the blades is low or negative so there is less variation with turbine radius.

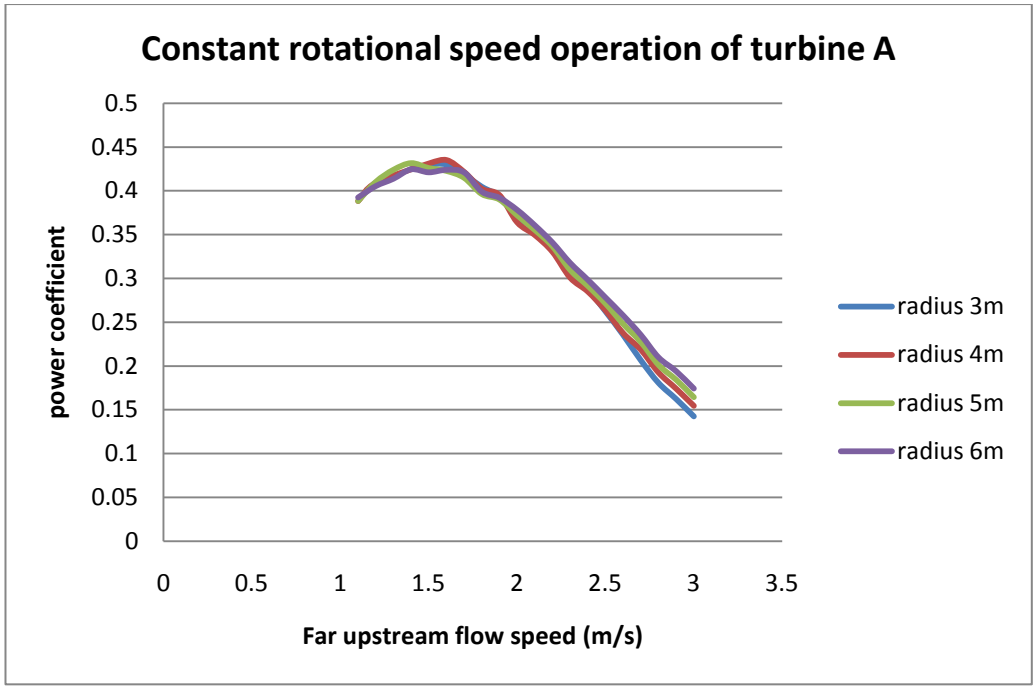

Figure 2.13- Variation of power coefficient with free-stream velocity for constant rotational speed operation of Turbine A

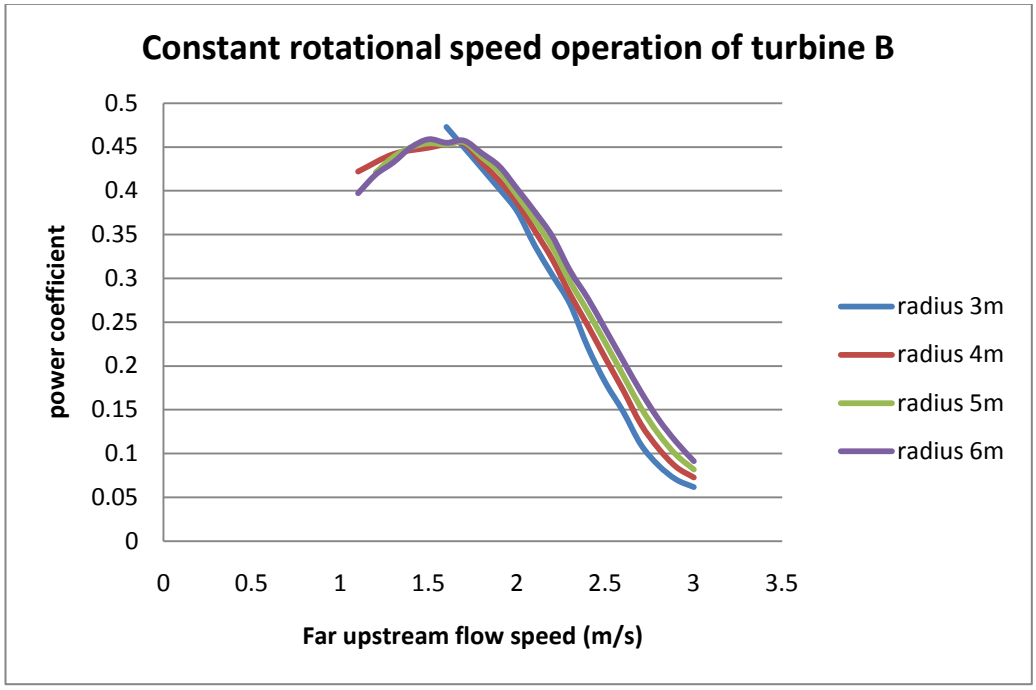

Figure 2.14- Variation of power coefficient with free-stream velocity for the constant rotational speed operation of Turbine B

Relationships between the free stream flow speed and the thrust acting on the turbine and the power generated by the turbine are needed. These relationships are used in the model developed in Chapter 3. The

relationships were obtained by using the BEM model to calculate the thrust and power at a range of free-stream velocities and fitting polynomial trend lines to the resulting data points. Caution must be taken when using polynomial trend lines as a good fit over the range of the data does not necessarily correspond to a good fit outside the range of the data. In order to establish which order of polynomial should be used to model the data, the coefficient of determination, R^2, value has been calculated for each trendline. R^2 values provide a measure of the goodness of the fit of the regression line to the data. An R^2 value of 1 indicates that the trendline provides a perfect fit to the data.

2.6.1 Variation of power generated with free-stream velocity

The variation of power generated with free-stream velocity for the constant tip speed ratio operation of the turbines was found to differ greatly from that for the constant rotational speed operation. The same trends were demonstrated by both designs of turbine. Figure 2.15 and Figure 2.16 show the variation of power generated with free-stream velocity for the constant tip speed ratio and constant rotational speed operation of Turbine B. Above a free stream velocity of 2.5 there were some problems with the model converging for the 3m turbine. The missing data points in Figure 2.16 were also points for which the BEM model did not converge properly. For the constant rotational speed operation there is a peak in the power generated whilst for the constant tip speed ratio operation the power generated continues to increase with increased flow speed. For the constant rotational speed operation of the turbine, the turbine only operates at its optimum tip speed ratio for one value of the free-stream velocity. At flow speeds above the value which gives the optimum tip speed ratio the power in the flow increases, but the power coefficient of the turbine decreases, allowing an increase in flow speed to result in a decrease in the amount of power generated.

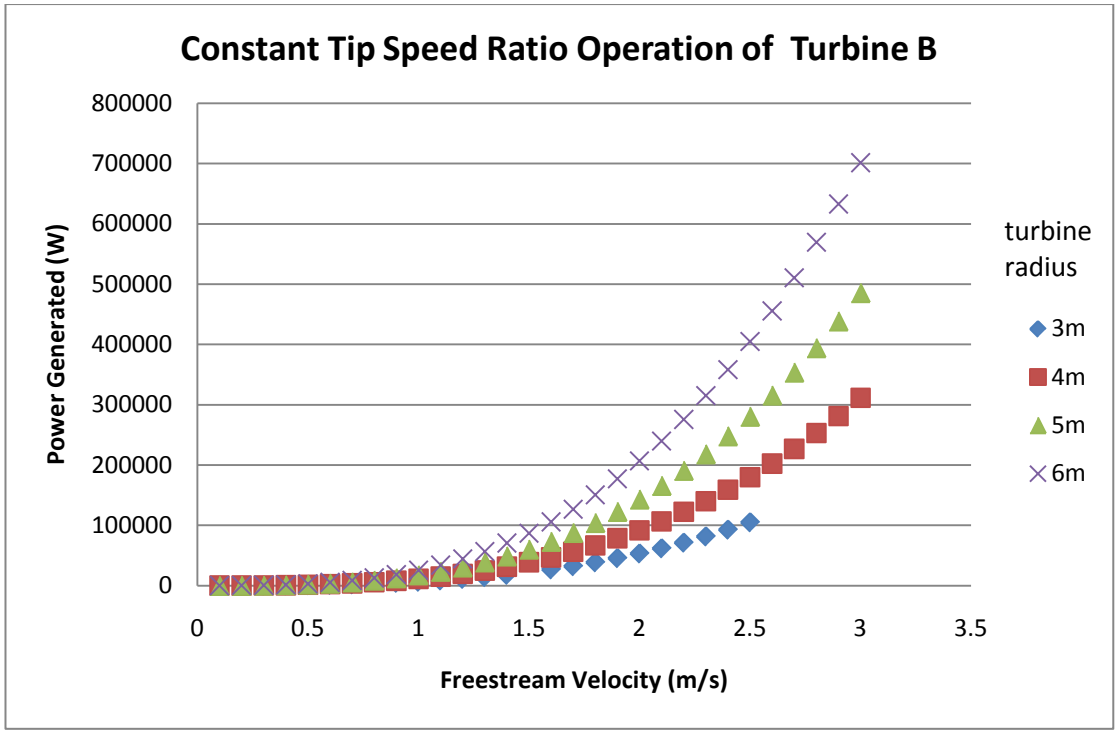

Figure 2.15 - Variation of power generated with free-stream velocity for the constant tip speed ratio operation of Turbine B

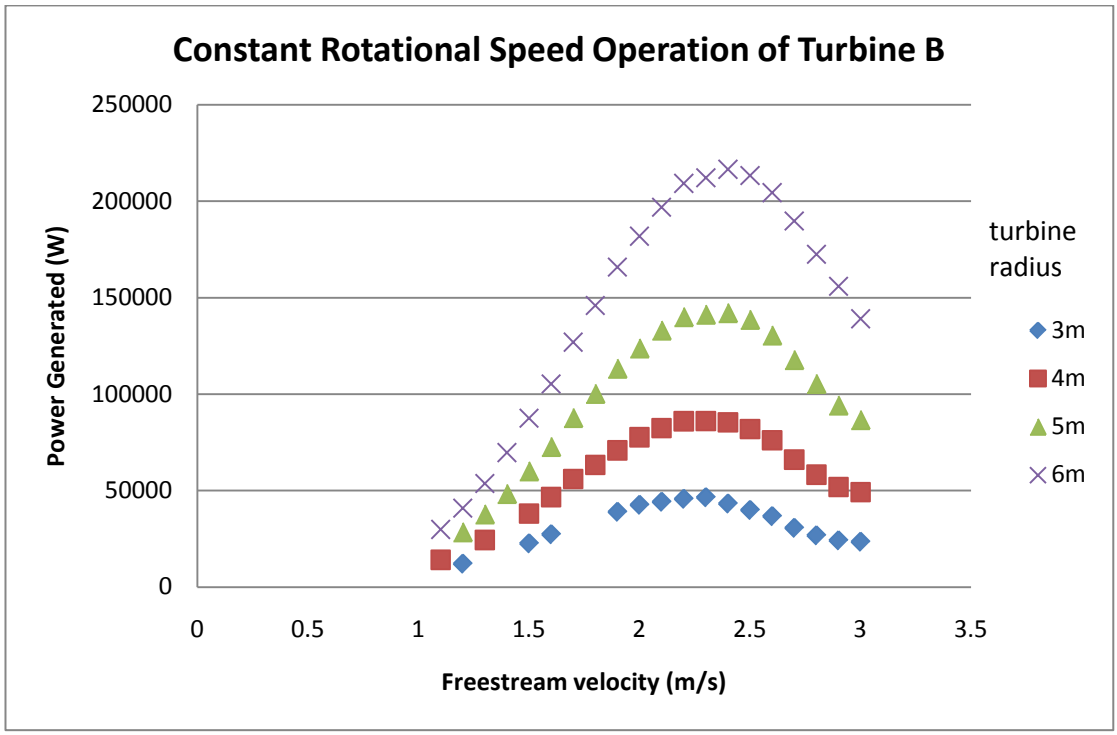

Figure 2.16- Variation of power generated with free-stream velocity for the constant rotational speed operation of turbine B

A third order polynomial trendline was applied to the data form the turbines found to give the best fit to the variation of power generated with free-stream velocity for the constant tip speed ratio operation of the turbines. The trendline equations are given in Table 2.3. Table 2.3 also gives the R^2 values of the trendlines. These indicate that a third order polynomial provides an excellent fit for the constant rotational speed data.

Table 2.3- Trendline equations for constant tip speed ratio operation

design	radius	equation	R^2
A	3m	$P = 6233.6u_\infty^3 + 194.42u_\infty^2 - 951.68u_\infty$	1.0000
	4m	$P = 11006u_\infty^3 + 406.85u_\infty^2 - 920.14u_\infty$	1.0000
	5m	$P = 16773u_\infty^3 + 82.263u_\infty^2 - 637.61u_\infty$	1.0000
	6m	$P = 24155u_\infty^3 + 129.17u_\infty^2 - 656.85u_\infty$	1.0000
B	3m	$P = 7024u_\infty^3 - 773.75u_\infty^2 + 26.441u_\infty$	1.0000
	4m	$P = 11609u_\infty^3 - 146.08u_\infty^2 - 251.21u_\infty$	1.0000
	5m	$P = 18082u_\infty^3 - 232.35u_\infty^2 - 308.69u_\infty$	1.0000
	6m	$P = 26146u_\infty^3 - 497.13u_\infty^2 - 149.17u_\infty$	1.0000

Third to sixth order polynomial fits were applied to the data sets. None of these fits provided a perfect fit for the data but most provide a reasonable fit. The sixth order trendline was selected as it provided the most accurate fit to the data within the range of flow speeds covered by the data. The trendline equations and R^2 values are given in Table 2.4.

Table 2.4- Trendline equations for constant rotational speed operation

design	radius	equation	R^2
A	3m	$P = 9902.1u_\infty^6 - 103103\ u_\infty^5 + 418521\ u_\infty^4 - 838617\ u_\infty^3 + 850590\ u_\infty^2 - 340954\ u_\infty$	0.9994
	4m	$P = 1258\ u_\infty^6 - 10665\ u_\infty^5 + 29580\ u_\infty^4 - 39697\ u_\infty^3 + 62010\ u_\infty^2 - 34370\ u_\infty$	0.9994
	5m	$P = 4792.5\ u_\infty^6 - 44249\ u_\infty^5 + 148140\ u_\infty^4 - 236571\ u_\infty^3 + 232890\ u_\infty^2 - 91672\ u_\infty$	0.9997
	6m	$P = 3976.2\ u_\infty^6 - 31778\ u_\infty^5 + 76918\ u_\infty^4 - 55533\ u_\infty^3 + 46281\ u_\infty^2 - 19421\ u_\infty$	0.9997
B	3m	$P = 7551.5\ u_\infty^6 - 64441\ u_\infty^5 + 203389\ u_\infty^4 - 302720\ u_\infty^3 + 231209\ u_\infty^2 - 68031\ u_\infty$	0.9978
	4m	$P = 11684\ u_\infty^6 - 99462\ u_\infty^5 + 309189\ u_\infty^4 - 445872\ u_\infty^3 + 332069\ u_\infty^2 - 97828\ u_\infty$	0.9993
	5m	$P = 15796\ u_\infty^6 - 135968\ u_\infty^5 + 426931\ u_\infty^4 - 625076\ u_\infty^3 + 485403\ u_\infty^2 - 153843\ u_\infty$	0.9997
	6m	$P = 13456\ u_\infty^6 - 106177\ u_\infty^5 + 275312\ u_\infty^4 - 265897\ u_\infty^3 + 115983\ u_\infty^2 - 11397\ u_\infty$	0.9998

2.6.2 Variation of thrust force acting on turbine with free-stream velocity

The variation of thrust force acting on the turbine with free-stream velocity for constant tip speed operation also differs from that for constant rotational speed operation. Figure 2.17 and Figure 2.18 show the variation of the thrust force acting on the turbine with free-stream velocity for the constant tip speed ratio and constant rotational speed operation of Turbine B. The curves for turbine A show the same trends as those for turbine B.

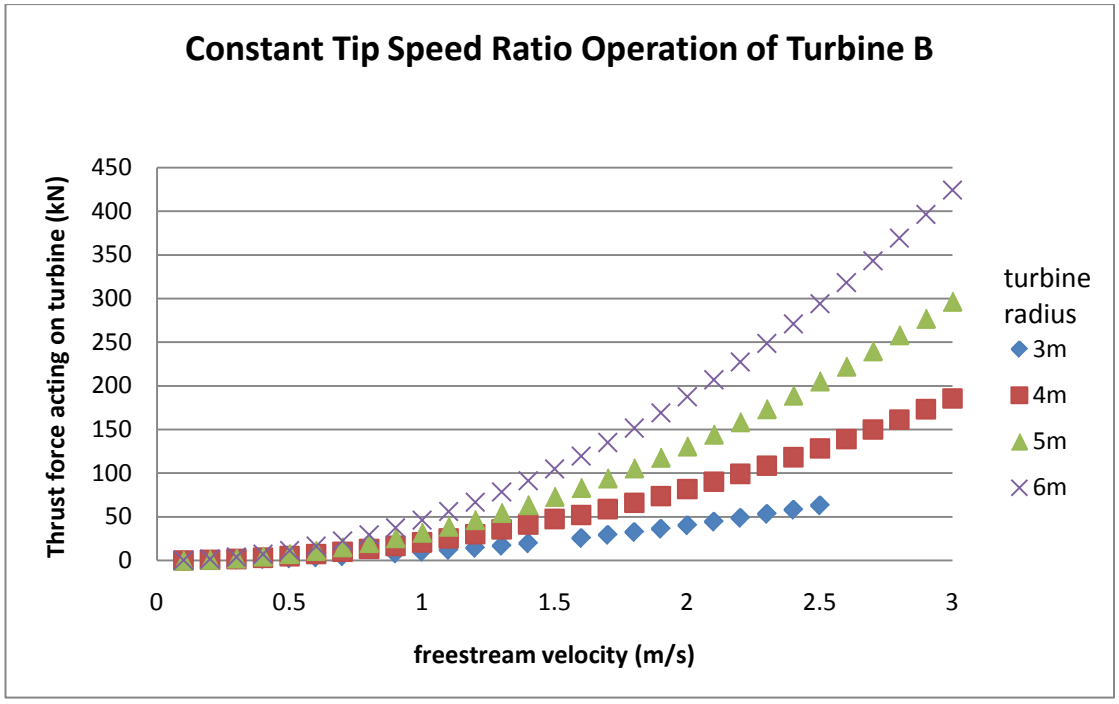

Figure 2.17- Variation of thrust force acting on turbine with free-stream velocity for the constant tip speed ratio operation of Turbine B

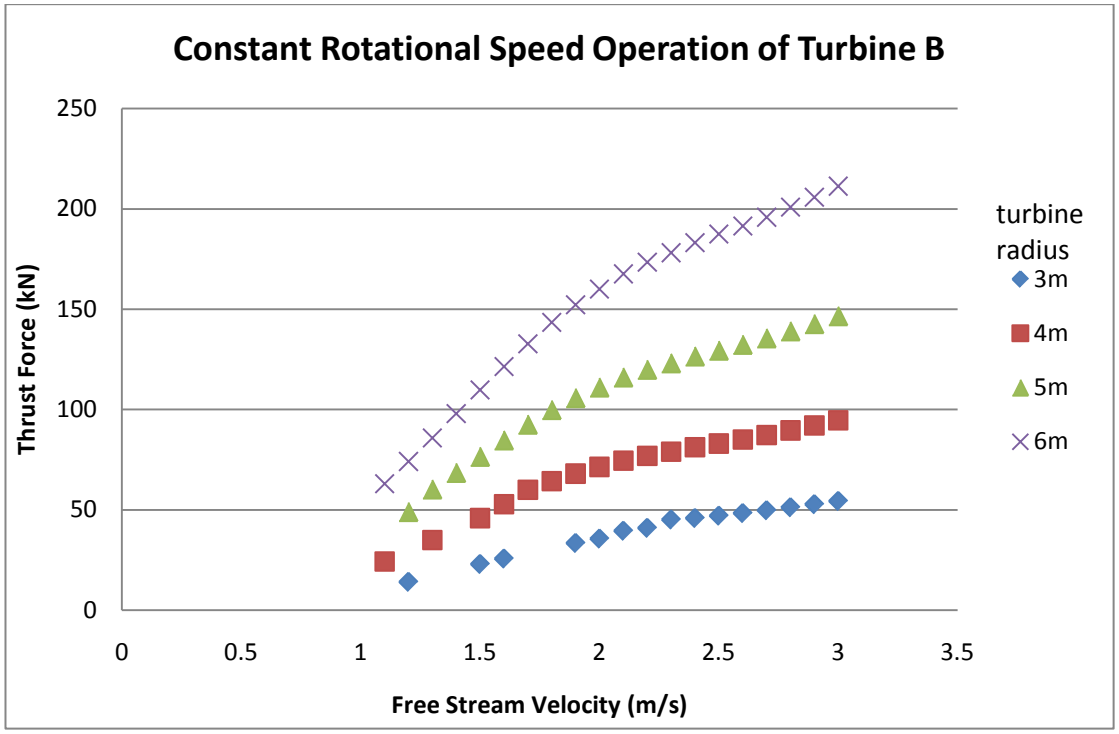

Figure 2.18- Variation of thrust force acting on turbine with free-stream velocity for the constant rotational speed operation of Turbine B

A second order polynomial was applied to the data from the turbines. The trendline equations and R^2 values are given in Table 2.5. It can be seen

from this table that the second order polynomials provided a very good fit to the data.

Table 2.5- Trendlines for constant tip speed ratio operation

Design	radius	equation	R^2
A	3	$T\ (kN) = 10.515u_\infty^2 - 0.5354u_\infty$	1.0000
	4	$T\ (kN) = 18.414u_\infty^2 - 0.6538u_\infty$	1.0000
	5	$T\ (kN) = 28.289u_\infty^2 - 0.9826u_\infty$	1.0000
	6	$T\ (kN) = 40.435u_\infty^2 - 1.2094u_\infty$	1.0000
B	3	$T\ (kN) = 10.204u_\infty^2 - 0.3449u_\infty$	1.0000
	4	$T\ (kN) = 20.539u_\infty^2 + 0.065u_\infty$	0.9999
	5	$T\ (kN) = 33.339u_\infty^2 - 1.1874u_\infty$	1.0000
	6	$T\ (kN) = 47.624u_\infty^2 - 1.4256u_\infty$	1.0000

For the constant rotational speed operation of the turbine, second order polynomials did not fit the data well. Third to sixth order polynomials were fitted to the data. None of these gave the very good fits shown by the constant tip speed ratio operation trendlines but they all had R^2 values of at least 0.998. In order to select which order trendline to use, the trendline equations were used to calculate the thrust force acting on the turbine at low flow speeds, outside the data range. The fourth order fits were found to give the best agreement for these flow speeds. The trendline equations and R^2 values are given in Table 2.6.

Table 2.6- Trend lines for constant rotational speed operation

design	radius	equation	R^2
A	3m	$T\ (kN) = 1.5827u_\infty^4 - 14.111u_\infty^3 + 40.048u_\infty^2 - 17.975u_\infty$	0.9993
	4m	$T\ (kN) = 3.3853u_\infty^4 - 28.087u_\infty^3 + 75.486u_\infty^2 - 33.643u_\infty$	0.9999
	5m	$T\ (kN) = 3.9273u_\infty^4 - 34.928u_\infty^3 + 99.207u_\infty^2 - 40.636u_\infty$	0.9999
	6m	$T\ (kN) = 6.2073u_\infty^4 - 54.302u_\infty^3 + 152.66u_\infty^2 - 66.638u_\infty$	0.9999
B	3m	$T\ (kN) = 1.4305u_\infty^4 - 13.654u_\infty^3 + 40.756u_\infty^2 - 20.033u_\infty$	0.9971
	4m	$T\ (kN) = 8.2057u_\infty^4 - 60.711u_\infty^3 + 143.71u_\infty^2 - 74.653u_\infty$	0.9983
	5m	$T\ (kN) = 11.514u_\infty^4 - 84.762u_\infty^3 + 198.54u_\infty^2 - 94.592u_\infty$	0.9998
	6m	$T\ (kN) = 13.138u_\infty^4 - 99.179u_\infty^3 + 236.92u_\infty^2 - 102.53u_\infty$	0.9997

2.6.3 Turbine cut-in speeds

The data sets used to generate the trendlines did not cover many of the low flow speeds frequently encountered in tidal channels. In order to establish if the trendlines provide a good representation of the expected power and thrust values for this range, thrust and power values were calculated using the trendline equations for a range of low flow speeds. For a number of low flow speeds the equations predicted negative values of power. Since the turbine will not be operated if power had to be put in to make it turn, using these equations to predict the power generated at low flow speeds will lead to errors. In particular the negative values of power predicted at low flow speeds reduce the value calculated for the average power generated by the turbines. Instead the equations will be used once the flow speed is greater than the speed for which the trendline equation stops predicting negative power and the power generated will be assumed to be zero below this flow speed. This is actually closer to the operation pattern which would be used for a turbine than if the turbine was assumed to generate power from a low speed. It is uneconomical to operate turbines at low flow speeds so instead the turbine remains stationary until the flow speed reaches a certain level: the cut in speed (16). The value selected for the power cut in speed does not actually

affect the flow speeds at the sites since it is the thrust force acting on the turbines rather than the power generated by the turbines which contributes to the resistance to the flow and hence the flow speed.

The trendline equations also predicted negative values of thrust force for low flow speeds. Thus a cut in speed is also needed for the thrust equations. It is the thrust force that contributes to the resistance to the flow in a channel and hence affects how the presence of the turbines affects the flow speeds in the channel. Negative values for the thrust force would indicate that the presence of the turbines was reducing the resistance to the flow in the channel and so are unrealistic. The thrust cut in speed can either be selected as the value above which all thrust values are positive, or it can be selected to be the same as the power cut in speed. The power cut in speed should always be greater than or equal to the thrust cut in speed since the turbine cannot generate power if the thrust force is zero. This is shown by Equation 1 which states that the power generated by an ideal turbine is equal to the product of the thrust force acting on the turbine and the flow speed through the turbine. The flow speeds at and above which the thrust and power values are positive are given in Table 2.7. It can be seen from this table that there is significant variation of the cut in speeds of the turbines. In order to make the results from the different turbines more comparable a single cut in speed for power and thrust has been chosen. The cut in speed is 0.8m/s and applies to all the turbines except for the constant rotational speed operation of a 3m turbine of design A. For this turbine a power and thrust cut in speed of 1.1m/s was used. The 0.8m/s value was chosen because it covered the majority of the turbines but was still low enough for speeds above this value to regularly occur in tidal flows.

Table 2.7- Thrust and power cut in speeds

design	radius	constant rotational speed operation		constant tip speed ratio operation	
		thrust cut in speed (m/s)	power cut in speed (m/s)	thrust cut in speed (m/s)	power cut in speed (m/s)
A	3m	0.1	1.1	0.1	0.4
	4m	0.2	0.8	0.05	0.3
	5m	0.2	0.8	0.15	0.2
	6m	0.2	0.6	0.05	0.2
B	3m	0.65	0.7	0.05	0.05
	4m	0.75	0.7	0.05	0.2
	5m	0.65	0.8	0.1	0.15
	6m	0.6	0.15	0.05	0.1

2.6.4 Other factors affecting performance

The equations developed in the previous sections describe the power generated by and thrust force acting on turbines in pristine condition operating in uniform speed flows. The conditions encountered in a marine environment are likely to cause the turbine behaviour to differ from the predicted behaviour. In particular the blades of tidal turbines will be subject to biofouling. Orme et al studied the effects of biofouling on turbine performance (79). They simulated fouling on aerofoil section using small cones and studied the effects of a number of levels of fouling on the lift and drag coefficients of the section. The ratio of lift to drag coefficient decreased significantly as the level of fouling was increased, leading to large loss in the efficiency of the turbine. They noted that it was unknown if the fouling will attach itself to tidal turbine blades and that further investigation was needed. To date, little additional progress has been made in this field, as was recognised by Mueller and Wallace (80) and Rourke et al (81) who identified biofouling as a priority area of research needed to advance the tidal current power industry. Until more is known about the level of fouling which occurs on different designs of tidal turbine

installed at a number of sites, it is not possible to quantify the effects biofouling will have on performance.

2.7 Summary

A number of different ways of representing turbines have been proposed. The different ways of representing turbines are based on different assumptions and the most suitable representation depends on the application. In the ideal representation of the turbine all of the energy extracted from the flow is assumed to be converted to a useful form. The porous disc representation of the turbine is also based on this assumption. The ideal turbine model is suitable for situations where the general effects of tidal turbines on the flow are being investigated. If the performance of a specific turbine is to be investigated, the real turbine representation, which takes into account losses due to drag on the turbine blades, needs to be used. None of these representations take into account the drag force acting on the supporting structure or losses in the gearbox and generator.

Turbines are typically operated at a constant rotational speed although constant tip speed ratio is also possible. Case studies of two turbines showed that constant tip speed ratio operation gives a more uniform power coefficient over the tidal cycle than fixed pitch constant rotational speed operation. The thrust force acting on the turbines was found to be a function of free stream velocity squared for constant tip speed ratio operation. The relationship between free stream velocity and thrust force was more ambiguous for a fixed pitch turbine operating at constant rotational speed. Increasing the order of the polynomial equation fitted to the data increased the goodness of fit within the data range but did not always provide the best fit for flow speeds lower than those in the data range. This is demonstrated in Figure 2.19 which shows how 2^{nd} to 6^{th} order polynomial trendlines fit the model predictions of the variation of thrust force with free-stream velocity for the constant rotational speed operation of a 3m radius turbine of design B. The variation of the goodness of fit of the polynomials to the data can be seen more clearly in

Figure 2.20. The fit of the polynomials at speeds below the model data range is shown in Figure 2.21. At low flow speeds the polynomial fits tended to predict negative values of thrust force and power. This necessitates the use of a cut in speed, below which the power or thrust generated is zero.

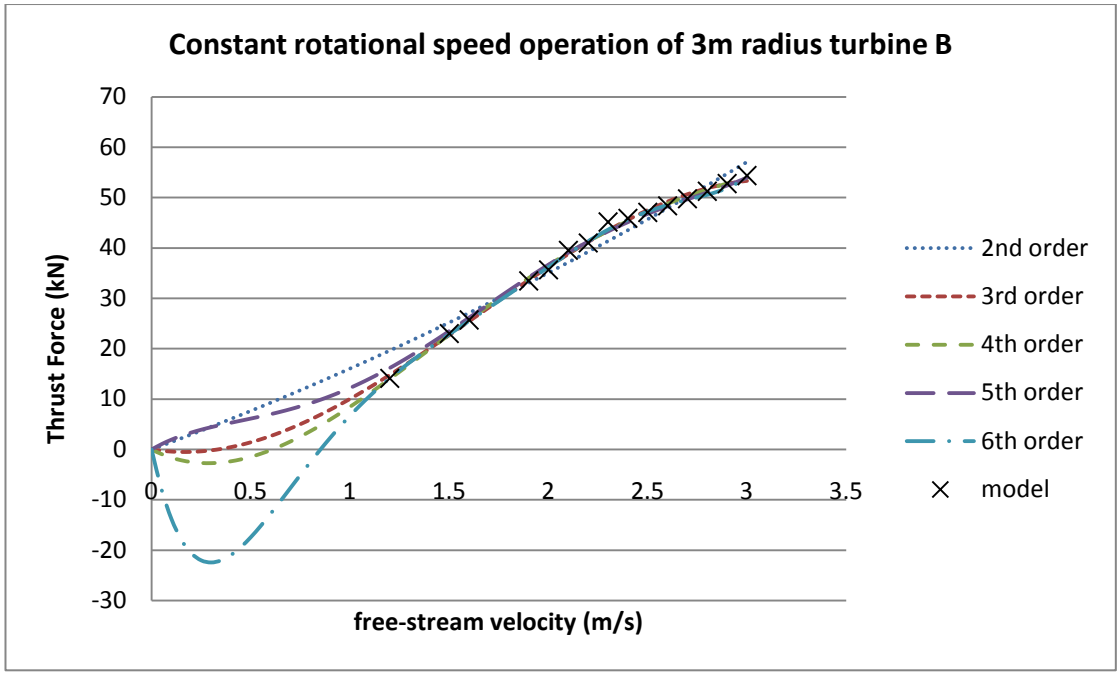

Figure 2.19- Fit of polynomial trend lines

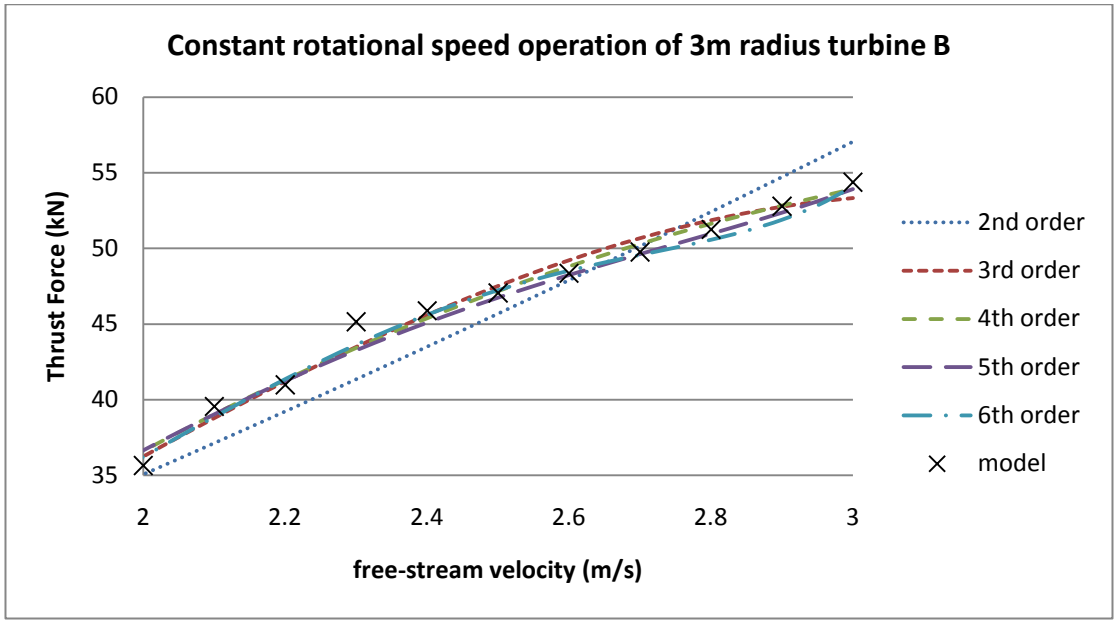

Figure 2.20- Fit of polynomials over upper part of the data range

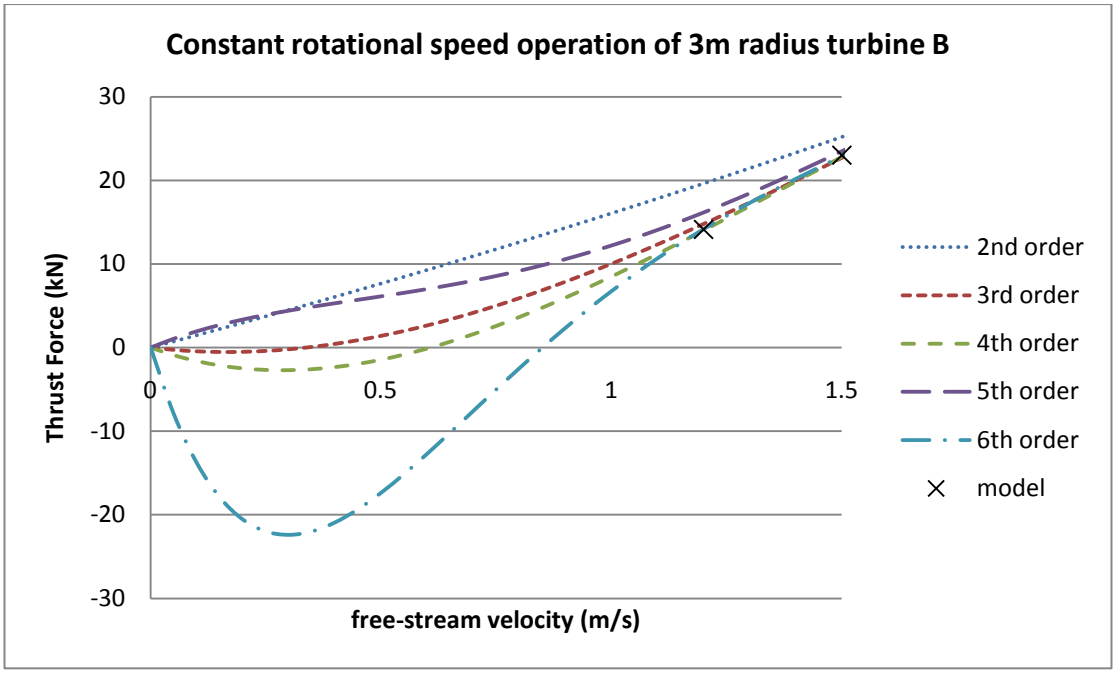

Figure 2.21- Fit of polynomials a speeds lower than the data range

The models used to predict how the power generated and thrust force acting on the turbines did not take into account a number of effects, such as biofouling, which will affect the performance of the turbines when installed in actual ocean sites. Little is known about the magnitude of these effects so it was not possible to account for them in the models. Once further information from sea trials is available, it should be used to modify the models, to enable them to more accurately model the performance of marine turbines.

Chapter 3 The effect of energy extraction on the available tidal current resource

For the performance of a turbine to be modelled, the speed of the undisturbed flow needs to be known. This makes resource estimation models a topic of interest for those involved in designing tidal turbines. If the variation of the flow speed throughout the tidal cycle can be predicted with reasonable accuracy, not only can the power generated by a turbine at the site be predicted, the design of the turbine can be optimised so as to maximise the power it can generate for the flow conditions.

Resource prediction is an area in which the differences between wind and tidal power have been shown to be significant. Initially the available resource was estimated using the farm model developed for wind farm design (82,83). In the farm method it is assumed that the amount of energy in the flow is limitless and the power generated is simply a function of the number of turbines and their efficiency, geometry and spacing. Whilst this approach is valid for wind turbines which only skim a tiny proportion of the earth's atmospheric boundary layer, for tidal turbines it can predict the extraction of more energy than actually passes through the site, since a farm of tidal turbines is likely to skim a significant proportion of the flow (84). In order to overcome the limitations of the farm method, the flux method for assessing the tidal stream resource was developed by Black and Veatch and Owen (85). The flux method defines the resource as the total kinetic energy flux entering the upstream cross-section of the site multiplied by a significant impact factor. The significant impact factor of a site is the fraction of the total flux that can be extracted without the extraction having a significant impact. The significant impact factor is site specific.

A further difference between wind and tidal power is that extracting energy from a tidal current causes a reduction in the flow speed of the whole channel (49). This effect is best understood using an analogy (86). In an electronic circuit consisting of a constant voltage source and a

resistor, the current flowing through the circuit depends on the resistance of the resistor. If the resistance of the resistor is increased, the current decreases. In a tidal channel the flow is caused by a head difference between the ends of the channel, this is equivalent to the voltage source. Installing turbines in the channel increases the resistance to the flow, this is equivalent to increasing the resistance of the resistor. The volume flow rate through the channel is equivalent to the current in the circuit, so installing turbines in the channel reduces the volume flow rate and, hence, the flow speed in all parts of the channel. This reduction in flow speed alters the kinetic energy flux passing through the channel. Due to this effect, there is some debate as to whether the kinetic energy flux in the undisturbed channel provides any indication of the amount of energy that could be extracted at that site (48,50,86). A number of analytical and numerical models have been developed by a variety of authors to investigate the effect of energy extraction on the available resource at a site.

3.1 Numerical models of the effects of energy extraction on the available tidal current resource

In numerical models a grid or mesh is applied to the site and finite difference methods are used to calculate velocity, temperature and salinity at points on the grid. The models can either be 2D or 3D. In 2D models the quantities are vertically averaged and this type of model is also referred to as a 2DH model. In the numerical models tidal turbines are represented as an additional bed friction source term which varies with velocity squared (54).

Numerical models have been applied to a number of sites around the world including Portland Bill (45), Cobscook Bay (87,88), the Ria de Muros (89), the Espinheiro Channel (90), the Bay of Fundy (53), the inland marine waters of Washington State (91) and Johnstone Strait (4). The size of grid elements used in these models varies, often with a smaller

grid size used in regions of interest. The smallest size of element used was 50m (45) with the elements in most models typically ranging from 200-300m in the areas of interest. Given the size of elements used, a tidal power farm could easily fit within one or two elements. This means that, whilst very good at giving an overall picture of the flow at a site, numerical models do not have the resolution to accurately predict the flow experienced by individual turbines. Thus numerical models cannot be used to predict the performance of turbines, they can only be used to estimate how energy extraction will affect average velocities, taken over large areas.

3.2 Analytical models of the effects of energy extraction on the available tidal current resource

The analytical models vary in complexity from simple one-dimensional models of uniform channels in which flow accelerations are neglected (49,92,93) to more complex models that consider quasi-steady flows and channels with longitudinally varying cross sections. Of these more complex models, Blanchfield's model (47) applies to the flow in a bay linking a channel to the open ocean and the model of Garrett and Cummins applies to a channel connecting two large bodies of water (50). Blanchfield's model has been applied to the Masset Sound and Garrett and Cummins' model has been applied to Johnstone Strait. Garrett and Cummins have also extended their model to consider the relative efficiency of full and partial fences of turbines (51,52).

More recently models have been developed which aim to allow more realistic conditions to be modelled. These include a model of a split channel (94), a model which allows turbine non-linearities to be taken into account (46) and a model which uses actuator disc theory to represent the turbines (95). The model of the split channel enables the investigation of the effect of energy extraction on more complex channel geometries

such as a channel where turbines are installed on one side of an island and the channel on the other side is left free for navigation. The model which allows turbine non-linearities to be taken into account allows the rated and cut in speeds of the turbines to be taken into account. This allows the resistance to the flow caused by the turbines to be represented in a more realistic manner. The model which uses actuator disc theory to represent the turbines also allows the resistance to the flow caused by the turbines to be represented in a more realistic manner. This model uses ideal turbine assumptions and so still does not describe the performance of actual turbines.

3.3 The significance of resource assessment models that take into account the effects of energy extraction

The results from these models suggest that installing turbines at a site will lead to a significant change in flow velocity. It should be noted however, that the results from these models have not been verified using experimental data. Comparison of the output of one of the analytical models with the output of one of the numerical models has shown the results to be in reasonably good agreement (4). The numerical model was verified against measured water elevations and current speeds in the undisturbed state. As yet, there are no large scale tidal stream turbine farms, so the effects of large scale energy extraction on the resource cannot be experimentally verified. This means that whilst there has been shown to be agreement between one of the analytical models and one of the numerical models, this does not actually imply that they are accurately predicting the effects of large scale energy extraction on the resource.

Assuming that the models are correctly predicting the effects of energy extraction on the resource, the method for estimating the flow speeds used in the design of turbines needs to be revised. If the performance of the turbines is to be optimised, the modified flow velocity needs to be

used in the design rather than the flow velocity at the undisturbed site. The analytical models outlined above are interested in defining the maximum power that could be extracted in the channel, they do not however indicate the requirements of the turbines needed to extract this power. The analytical models also assume that the turbines are ideal. The power generated by actual turbines will be less than the theoretical limit since real turbines dissipate energy through friction and the generation of turbulence.

If performance prediction models are to accurately predict the power generated at a site, they need to be able to take into account the effect of the turbines on the flow speed at the site. The existing analytical models are unable to do this since they model the turbines as an additional drag term or an actuator disc and assume that all the energy extracted from the flow by this drag term or actuator disc is converted into a useable form. For the effect of the turbines on the flow to be taken into account when designing turbines a new model was required. The new model, developed by the author, combines elements of the BEM model with elements of a model of energy extraction in an open channel developed by Garrett and Cummins (50). More detail on the model developed by Garrett and Cummins is given in section 3.4. The new model, referred to as the extended model, is described in section 3.5.

3.4 Garret and Cummins' model

Garrett and Cummins have developed a model of the flow in a channel connecting two large basins which allows the maximum extractable power to be estimated (50). In this model the following assumptions were made (51):

- The water levels in the basins at either end of the channel are unchanged by any changes in the channel flow caused by the presence of turbines

- The volume flux of the flow in the channel is independent of the along channel position
- The speed of the current varies only with the position along the channel, it does not vary across the cross-section of the channel
- The cross sectional area of the channel does not vary with time
- The cross sectional area of the channel is the same at both ends of the channel and does not vary with time
- The current enters the channel from all directions but leaves the channel as a jet surrounded by stagnant water with the same elevation as the water in the downstream basin
- The turbines form a fence covering the entire cross section of the channel

The equation of motion in a channel is given by Equation 15 (51)

$$\frac{\partial u_c}{\partial t} + u_c \frac{\partial u_c}{\partial x} = -F$$

Equation 15

Where:

x is the along channel coordinate

u_c is the current speed (function of time and x)

F is the resistance force per unit mass of seawater (from natural friction and the presence of turbines)

These assumptions listed above, in particular the assumption that the flux $A_c u$ along the channel is independent of x, allow Equation 16 to be integrated along the channel to give:

$$c_1 \frac{d\dot{V}}{dt} - g\varsigma_0 = -\int_0^L F dx - \frac{1}{2} u_e |u_e|$$

Equation 16

Where:

x is the along channel coordinate

ς_0 is the sea level difference between the two basins

$\dot{V}$ is the volume flow rate in the channel

F is the resistance force per unit mass of seawater (from natural friction and the presence of the turbines)

u_e is the flow velocity at the channel exit

$$c_1 = \int_0^L \frac{1}{A_c} dx$$

Equation 17

A_c is the cross sectional area of the channel (it is a function of x)

This model produces the general result that the maximum average extractable power is given by:

$$\overline{P_{max}} = \gamma \rho g b \dot{V}_{max}$$

Equation 18

Where:

γ is a coefficient which varies over the range 0.20 to 0.24

ρ is the density of the water in the channel

g is the acceleration of gravity

b is the amplitude of the sinusoidal sea level difference between the two ends of the channel

$\dot{V}_{max}$ is the maximum volume flux through the channel in its undisturbed state

3.5 Extended model

In Equation 16 the resistance force was given per unit mass of sea water within the channel (96). The resistance force, F_r, is related to the resistance force per unit mass, F, by Equation 19.

$$F_r = \left(\rho \int_0^L A_c dx \right) F = c_2 F$$

Equation 19

The resistance force, F_r, is the sum of the drag force due to natural friction and the drag force due to the turbines. This allows Equation 16 to be written as:

$$c_1 \frac{d\dot{V}}{dt} - g\varsigma_0 = -\frac{1}{c_2}\int_0^L (F_{frict} + F_t)dx - \frac{1}{2}u_{ce}|u_{ce}|$$

Equation 20

Where:

F_{frict} is the resistance force due to natural friction

F_t is the resistance force due to the turbines

Drag force is typically calculated using Equation 21. For a channel, the reference area used in Equation 21 is normally taken to be the area given by multiplying the width of the channel by the length of the channel. An alternative is to use the wetted perimeter of the channel multiplied by the length of the channel. In this model the area shall be defined using the width of the channel. This definition of area has been selected so as to allow direct comparison with the drag coefficient values for channels quoted by Salter (86).

$$\mathfrak{D} = \frac{1}{2}\rho {u_c}^2 C_{Dc} A_{ref}$$

Equation 21

Using this definition of the drag coefficient allows the drag force due to natural friction to be written as:

$$F_{frict} = \int_0^L \frac{1}{2} C_{Dc} \rho {u_c}^2 w \, dx$$

Equation 22

Where:

w is the width of the channel

The volume flow rate in the channel is independent of the position along the channel. The volume flow rate in the channel is given by Equation 23.

The volume flow rate in the channel is a function of time, the flow speed is a function of time and position and the cross sectional area is a function of position.

$$\dot{V}(t) = u_c(x,t)A_c(x)$$

Equation 23

Equation 23 allows Equation 22 to be expressed in terms of the volume flow rate:

$$F_{frict} = \left(\dot{V}\left|\dot{V}\right|\right)\frac{1}{2}\rho\int_0^L \frac{C_{Dc}w}{A_c^2}\,dx$$

Equation 24

Defining a channel dependent constant, c_3:

$$c_3 = \frac{1}{2}\rho\int_0^L \frac{C_{Dc}w}{A_c^2}\,dx$$

Equation 25

Equation 25 allows Equation 24 to be simplified to:

$$F_{frict} = c_3\left(\dot{V}\left|\dot{V}\right|\right)$$

Equation 26

For the turbine drag term to be evaluated, an expression for the variation of the drag force of the turbine with flow speed needs to be obtained. The variation the drag force exerted on the flow by the turbines with flow speed can be investigated using a modified BEM model. The use of the BEM model requires the parameters of the turbine to be specified, so at this point the model ceases to be generic. In Chapter 2 the variation of drag force with flow speed was investigated for the two example turbines, turbine A and turbine B. For the constant tip speed ratio operation of both turbines, the thrust force was related to the free stream velocity by a second order polynomial. This allows the drag force for a single turbine of

either design operating at a constant tip speed ratio to be described by Equation 27. The values of c_4 and c_5 for fixed pitch turbines of design A and B and radius of 3m to 6m operating at constant tip speed ratio are given in Table 3.1.

$F_{1turb} = c_4 u_c + c_5 {u_c}^2$ (constant tip speed ratio operation)

Equation 27

Table 3.1- Polynomial Constants for Constant Tip Speed Ratio Operation

radius (m)	Thrust (kN)							
	turbine A				turbine B			
	c_4	c_5	R^2	cut in speed	c_4	c_5	R^2	cut in speed
3	-0.5354	10.515	1	0.1	-0.3449	10.204	1	0.05
4	-0.6538	18.414	1	0.05	0.065	20.539	0.9999	0.05
5	-0.9826	28.289	1	0.15	-1.1874	33.339	1	0.1
6	-1.2094	40.435	1	0.05	-1.4256	47.624	1	0.05

For operation at a constant rotational speed it was found that a fourth order polynomial gave a better representation of the variation of thrust force with free stream velocity. This allows the drag force for a single turbine of either design operating at a constant rotational speed to be described by Equation 28. The values of c_4 and c_5 for turbines of design A and B and radius of 3m to 6m operating at constant rotational speed are given in Table 3. 2.

$F_{1turb}\,(kN) = c_4 u_c + c_5 {u_c}^2 + c_6 {u_c}^3 + c_7 {u_c}^4$ (Constant rotational speed)

Equation 28

Where:

F_{1turb} is the drag force due to a single turbine

Table 3. 2- Polynomial constants for constant rotational speed operation

radius (m)	turbine design	c_4	c_5	c_6	c_7
3	A	-17.975	40.048	-14.111	1.5827
4	A	-33.643	75.486	-28.087	3.3853
5	A	-40.636	99.207	-34.928	3.9273
6	A	-66.638	152.66	-54.302	6.2073
3	B	-20.033	40.756	-13.654	1.4305
4	B	-74.653	143.71	-60.711	8.2057
5	B	-94.592	198.54	-84.762	11.514
6	B	-102.53	236.92	-99.179	13.138

Equation 23 allows Equation 27 and Equation 28 to be written in terms of the volume flow rate in the channel:

$$F_{1turb} = \frac{c_4 \dot{V}}{A_t} + \frac{c_5 \dot{V}|\dot{V}|}{A_t^2}$$

Equation 29 (constant tip speed ratio operation)

$$F_{1turb} = \frac{c_4 \dot{V}}{\mathrm{A_t}} + \frac{\mathrm{c_5} \dot{V}|\dot{V}|}{\mathrm{A_t^2}} + \frac{c_6 \dot{V}|\dot{V}|^2}{\mathrm{A_t^3}} + \frac{c_7 \dot{V}|\dot{V}|^3}{\mathrm{A_t^4}}$$

Equation 30 (constant rotational speed operation)

Typically more than one turbine would be deployed in the channel. The integral of F_t over the channel is equal to the sum of the resistance force of all the turbines. If all the turbines are deployed in the same section, the resistance due to the turbines for constant tip speed ratio operation is given by Equation 31 and the resistance due to the turbines for constant rotational speed operation is given by Equation 32. If the turbines are deployed in different sections of the channel the resistance is given by Equation 33 for constant tip speed ratio operation and
Equation 34 for constant rotational speed operation.

$$F_{turb} = n\left(\frac{c_4\dot{V}}{A_t} + \frac{c_5\dot{V}|\dot{V}|}{A_t^2}\right)$$

Equation 31 (constant tip speed ratio operation)

Where:

n is the number of turbines

A_t is the area of the section of the channel where the turbines are deployed

$$F_{turb} = n\left(\frac{c_4\dot{V}}{\mathrm{A_t}} + \frac{\mathrm{c_5}\dot{V}|\dot{V}|}{\mathrm{A_t^2}} + \frac{c_6\dot{V}|\dot{V}|^2}{\mathrm{A_t^3}} + \frac{c_7\dot{V}|\dot{V}|^3}{\mathrm{A_t^4}}\right)$$

Equation 32 (constant rotational speed operation)

$$F_{turb} = n_1\left(\frac{c_4\dot{V}}{A_{t1}} + \frac{c_5\dot{V}|\dot{V}|}{A_{t1}^2}\right) + n_2\left(\frac{c_4\dot{V}}{A_{t2}} + \frac{c_5\dot{V}|\dot{V}|}{A_{t2}^2}\right) + \cdots + n_i\left(\frac{c_4\dot{V}}{A_{ti}} + \frac{c_5\dot{V}|\dot{V}|}{A_{ti}^2}\right)$$

Equation 33 (constant tip speed ratio operation)

$$F_{turb} = n_1\left(\frac{c_4\dot{V}}{\mathrm{A_{t1}}} + \frac{\mathrm{c_5}\dot{V}|\dot{V}|}{\mathrm{A_{t1}^2}} + \frac{c_6\dot{V}|\dot{V}|^2}{\mathrm{A_{t1}^3}} + \frac{c_7\dot{V}|\dot{V}|^3}{\mathrm{A_{t1}^4}}\right)$$
$$+n_2\left(\frac{c_4\dot{V}}{\mathrm{A_2}} + \frac{\mathrm{c_5}\dot{V}|\dot{V}|}{\mathrm{A_{t2}^2}} + \frac{c_6\dot{V}|\dot{V}|^2}{\mathrm{A_{t2}^3}} + \frac{c_7\dot{V}|\dot{V}|^3}{\mathrm{A_{t2}^4}}\right) + \cdots$$
$$+ n_i\left(\frac{c_4\dot{V}}{\mathrm{A_{ti}}} + \frac{\mathrm{c_5}\dot{V}|\dot{V}|}{\mathrm{A_{ti}^2}} + \frac{c_6\dot{V}|\dot{V}|^2}{\mathrm{A_{ti}^3}} + \frac{c_7\dot{V}|\dot{V}|^3}{\mathrm{A_{ti}^4}}\right)$$

Equation 34 (constant rotational speed operation)

In Equation 31, Equation 32, Equation 33 and Equation 34 it has been assumed that the force applied by the turbines is linearly proportional to the number of turbines. This assumption is only valid if blockage does not have a significant effect on the thrust force applied by the turbines.

The final term in Equation 16 (losses due to exit separation) can also be expressed in terms of the volume flow rate in the channel:

$$\frac{1}{2}u_{ce}|u_{ce}| = \frac{\dot{V}|\dot{V}|}{2A_e^2}$$

Equation 35

The elevation difference between the ends of the channel is assumed to vary in a sinusoidal manner. This allows ς to be expressed as a function of time (Equation 36).

$$\varsigma_0 = b\ \cos \omega t$$

Equation 36

Where:

b is the amplitude of the sine wave (the maximum sea level difference between the basins)

ω is the frequency of the sine wave

The amplitude of the sine wave will vary over the spring neap cycle. In order to gain an understanding of how the turbines affect the flow over the entire spring neap cycle the model would need to be run for the amplitude of each 12 hour 25 minute period of the neap spring cycle.

Substituting Equation 26, Equation 35 and Equation 36 into Equation 20 yields an equation for d$\dot{V}$/dt in terms of $\dot{V}$:

$$\frac{d\dot{V}}{dt} = \frac{gb\cos\omega t - \frac{1}{c_2}\int_0^L \left(c_3 \dot{V}\left|\dot{V}\right| + F_{turb}\right)dx - \frac{\dot{V}\left|\dot{V}\right|}{2A_e^2}}{c_1}$$

Equation 37

The $c_3\dot{V}\left|\dot{V}\right|$ and F_{turb} terms of Equation 37 are the sum of the friction force and turbine drag force over the entire length of the channel. As such, they are not functions of x, allowing Equation 37 to be written as:

$$\frac{d\dot{V}}{dt} = \frac{gb\cos\omega t - \frac{L}{c_2}\left(c_3 \dot{V}\left|\dot{V}\right| + F_{turb}\right) - \frac{\dot{V}\left|\dot{V}\right|}{2A_e^2}}{c_1}$$

Equation 38

This equation is a first order non-linear differential equation and so it needs to be solved numerically. The values for the constants, c_1, c_2 and c_3, can be estimated by splitting the channel into a number of sections. The area of the channel at each section is evaluated and this area is assumed to apply to the channel until the next section. This allows c_1, c_2 and c_3 to be approximated by:

$$c_1 = \sum_{1}^{n_s} \frac{1}{A_c} \Delta x$$

Equation 39

$$c_2 = \rho \sum_{1}^{n_s} A_c \Delta x$$

Equation 40

$$c_3 = \frac{1}{2} \rho \sum_{1}^{n_s} \frac{C_D w}{A_c^2} \Delta x$$

Equation 41

Euler's method has been used to solve Equation 37. Whilst there a number of more accurate numerical solution methods, Euler's method has been chosen because of its simplicity. There is a large degree of uncertainty in the values of a number of the parameters used in Equation 37 so the solution of this equation will never be highly accurate, even if a more accurate numerical solution method was used.

Euler's method (97) allows y(x) to be found from equations of the form $\frac{dy}{dx} = f(x, y)$. $\frac{dy}{dx}$ is the gradient of the function. If an initial condition relating x and y at a point is known, the values of x_0 and y_0 can be used to evaluate the gradient at that point. The gradient can be used to estimate the y value at an x value which lies a short distance, h, along the x axis from x_0. If this process is repeated using the estimated values, a whole series of approximate values of y can be generated. This process can be expressed mathematically as:

$$y_{i+1} = y_i + h_t f(x_i, y_i)$$

Equation 42

In order to solve Equation 37 an initial condition and a time step need to be selected. The initial condition is supplied by the assumption that when there is no difference in elevation between the water levels at the ends of the channel there is no flow through the channel. This yields the condition that $\dot{V}$=0 at $t = \frac{\pi}{2\omega}$. This assumption is not true, however it has been found that the initial condition only effects the results from t=0 to the period of the sine wave used to represent the change in the difference in elevation between the ends of the channel, the results from subsequent cycles are identical regardless of the initial condition. If the drag force applied by the turbines is non-zero, more care needs to be taken in the selection of the initial condition than if the turbine drag is zero. Selecting an initial $\dot{V}$ value which is too large will result in $\dot{V} \rightarrow \infty$ as t increases. Setting the initial value of $\dot{V}$ to 0 always yields a solution and so this condition will be used despite the limitations of the assumption used to obtain this value. Calculations were carried out using both a 1s and a 10s time step. The results for the different time steps were almost identical, so 10s is an acceptable step size.

A flow chart showing the calculation procedure to find the variation in volume flow rate in the channel over the tidal cycle is shown in Figure 3.1. In this flow chart h_t is the time step size.

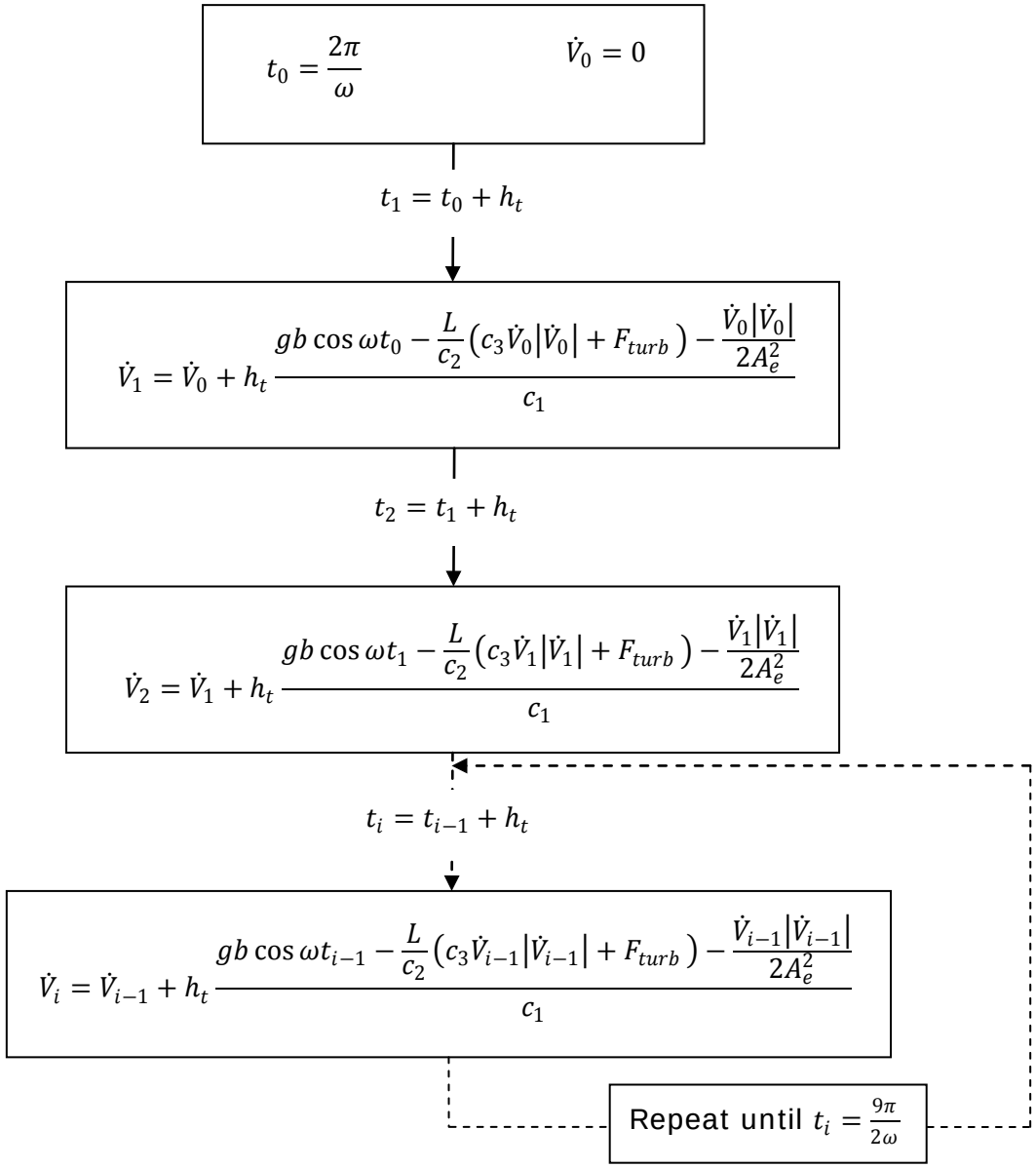

Figure 3.1- Flow chart showing calculation procedure for extended model

The power generated by the turbines at each time step is calculated from the volume flow rate. The relationship between the power generated and the volume flow rate for turbines installed in multiple sections of the channel is given in Equation 43. The values of the constants for the different diameters, and modes of operation of turbines A and B are shown in Table 3.3.

$$P\ (\mathrm{W}) = n_1\left(\frac{c_8\dot{V}}{\mathrm{A_{t1}}} + \frac{\mathrm{c_9}\dot{V}|\dot{V}|}{\mathrm{A_{t1}^2}} + \frac{c_{10}\dot{V}|\dot{V}|^2}{\mathrm{A_{t1}^3}} + \frac{c_{11}\dot{V}|\dot{V}|^3}{\mathrm{A_{t1}^4}} + \frac{c_{12}\dot{V}|\dot{V}|^4}{\mathrm{A_{t1}^5}}\frac{c_{13}\dot{V}|\dot{V}|^5}{\mathrm{A_{t1}^6}}\right)$$
$$+ n_2\left(\frac{c_8\dot{V}}{\mathrm{A_{t2}}} + \frac{\mathrm{c_9}\dot{V}|\dot{V}|}{\mathrm{A_{t2}^2}} + \frac{c_{10}\dot{V}|\dot{V}|^2}{\mathrm{A_{t2}^3}} + \frac{c_{11}\dot{V}|\dot{V}|^3}{\mathrm{A_{t2}^4}} + \frac{c_{12}\dot{V}|\dot{V}|^4}{\mathrm{A_{t2}^5}}\frac{c_{13}\dot{V}|\dot{V}|^5}{\mathrm{A_{t2}^6}}\right) + \cdots$$
$$+ n_i\left(\frac{c_8\dot{V}}{\mathrm{A_{ti}}} + \frac{\mathrm{c_9}\dot{V}|\dot{V}|}{\mathrm{A_{ti}^2}} + \frac{c_{10}\dot{V}|\dot{V}|^2}{\mathrm{A_{ti}^3}} + \frac{c_{11}\dot{V}|\dot{V}|^3}{\mathrm{A_{ti}^4}} + \frac{c_{12}\dot{V}|\dot{V}|^4}{\mathrm{A_{ti}^5}}\frac{c_{13}\dot{V}|\dot{V}|^5}{\mathrm{A_{ti}^6}}\right)$$

Equation 43

Table 3.3- Polynomial constants for the Power generated by the turbines

		radius	c_8	c_9	c_{10}	c_{11}	c_{12}	c_{13}	cut in speed
constant tip speed ratio	Turbine A	3	-951.68	194.42	6233.6	0	0	0	0.4
		4	-920.14	406.85	11006	0	0	0	0.3
		5	-637.61	82.263	16773	0	0	0	0.2
		6	-656.85	129.17	24155	0	0	0	0.2
	Turbine B	3	26.441	-773.75	7024	0	0	0	0.05
		4	-251.21	-146.08	11609	0	0	0	0.2
		5	-308.69	-232.35	18082	0	0	0	0.15
		6	-149.17	-497.13	26146	0	0	0	0.1
constant rotational speed	Turbine A	3	-340954	850590	-838617	418521	-103103	9902.1	1.1
		4	-34370	62010	-39697	29580	-10665	1258	0.8
		5	-91672	232890	-236571	148140	-44249	4792.5	0.8
		6	-19421	46281	-55533	76918	-31778	3976.2	0.6
	Turbine B	3	-68031	231209	-302720	203389	-64441	7551.5	0.7
		4	-97828	332069	-445872	309189	-99462	11684	0.7
		5	-153843	485403	-625076	426931	-135968	15796	0.8
		6	-11397	115983	-265897	275312	-106177	13456	0.15

3.5.1 Results from the extended model

A number of interesting results can be obtained by applying the extended model to the simple case of a uniform rectangular section channel:

L= 20km

w= 1km

h=20m

b= 2m

$\omega_{cycle} = \pi/21600$ (cycle period = 12 hours)

A range of drag coefficients were used in the calculations. These were chosen to be representative of actual tidal channels. The minimum drag coefficient used in the calculations was 0.006. Measured values drag coefficient for different areas in the Menai Strait between Anglesey and the Welsh mainland (98) were found to vary between 0.006 and 0.02. Since aerofoils at zero angle of attack typically have drag coefficients of around 0.005, it was felt that the drag coefficient of a tidal channel was unlikely to be below the minimum measured value in the Menai Strait. In his discussion of the selection of a friction coefficient for the Pentland Firth Salter cites an estimate of $C_{Dc} = 0.04$ made by Bryden (99). This value has been taken as the upper limit of the drag coefficient for which the flow in the rectangular channel was investigated.

Initially the channel was modelled with no turbines. This allowed the effect of drag coefficient on phase angle and maximum volume flow rate to be investigated. The model was then used to investigate the effect of turbines on the flow in the channel.

3.5.1.1 Rectangular channel with no artificial energy extraction

Changing the drag coefficient of the channel affects both the volume flow rate and the time between maximum head difference and maximum flow speed. In Figure 3.2 the variation of volume flow rate with time is plotted over the tidal cycle for a range of drag coefficients. It can be seen from this graph that as the drag coefficient is increased the peak volume flow rate is reduced and the time at which the peak volume flow rate occurs is shifted towards the left.

In Figure 3.3 the variation of volume flow rate is plotted with the variation of elevation difference between the ends of the channel. The volume flow

rate has been divided by the maximum volume flow rate for each value of the drag coefficient and the head difference has been divided by the maximum head difference in order to allow the curves to be plotted on the same scale. It can be seen from Figure 3.3 that the higher the drag coefficient smaller the time between maximum head difference and maximum volume flow rate.

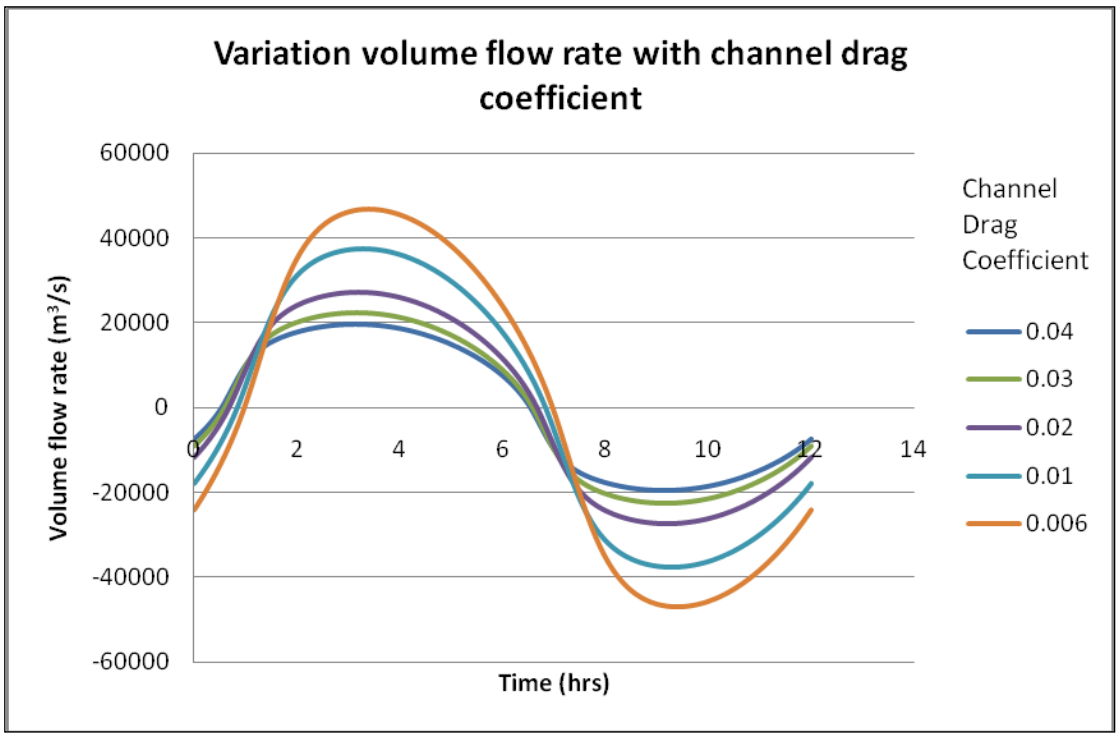

Figure 3.2- Effect of drag coefficient on volume flow rate over the tidal cycle

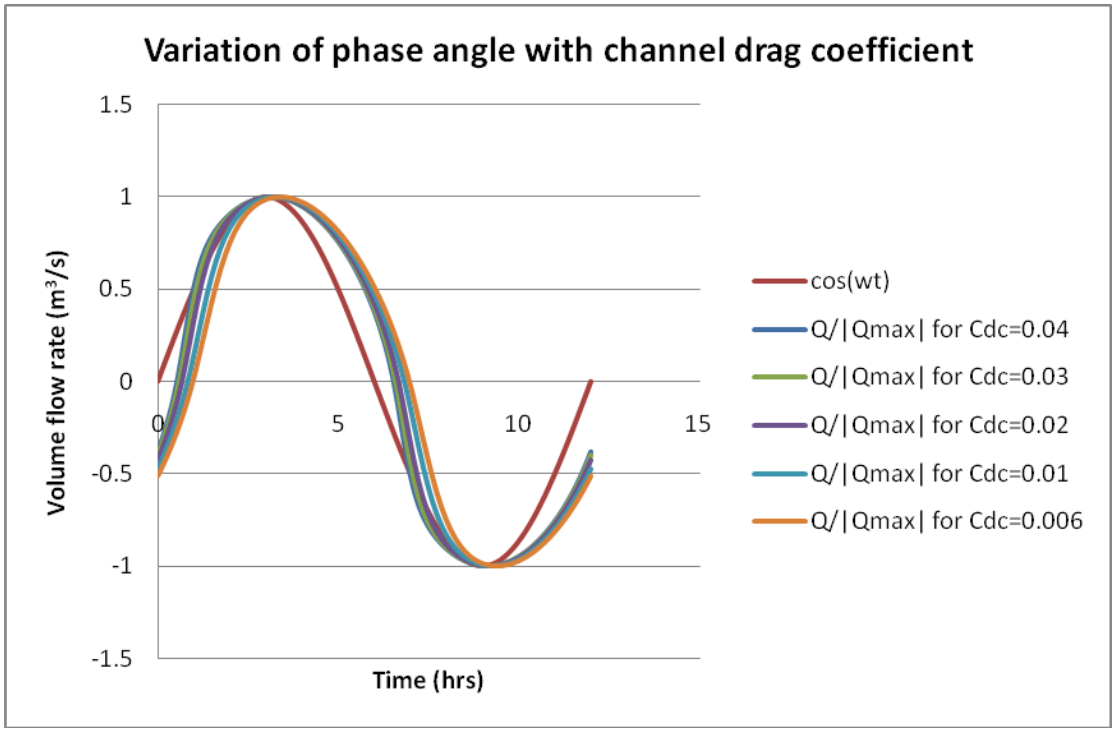

Figure 3.3- Effect of drag coefficient of phase angle

The dependence of the peak volume flow rate and phase angle between the maximum flow speed and maximum head difference on channel drag coefficient is of great value when applying the model to actual tidal channels. Typically the drag coefficient of the channel will not be known and it is a quantity which is difficult to measure. The peak volume flow rate can be estimated from measurements taken using acoustic Doppler current profilers (ADCPs) and the phase difference can be estimated from the voltage induced in cross channel telephone cables (99). Curves showing the variation of peak volume flow rate with drag coefficient and the variation of phase angle with drag coefficient can be generated by modelling the channel in its undisturbed state for a range of drag coefficient values. For example, Figure 3.4 and Figure 3.5 show the variation of the peak volume flow rate and phase lag with channel drag coefficient for the rectangular channel considered above. The average drag coefficient of the channel can then be estimated using the estimates of phase angle or peak flow rate and the relevant curve.

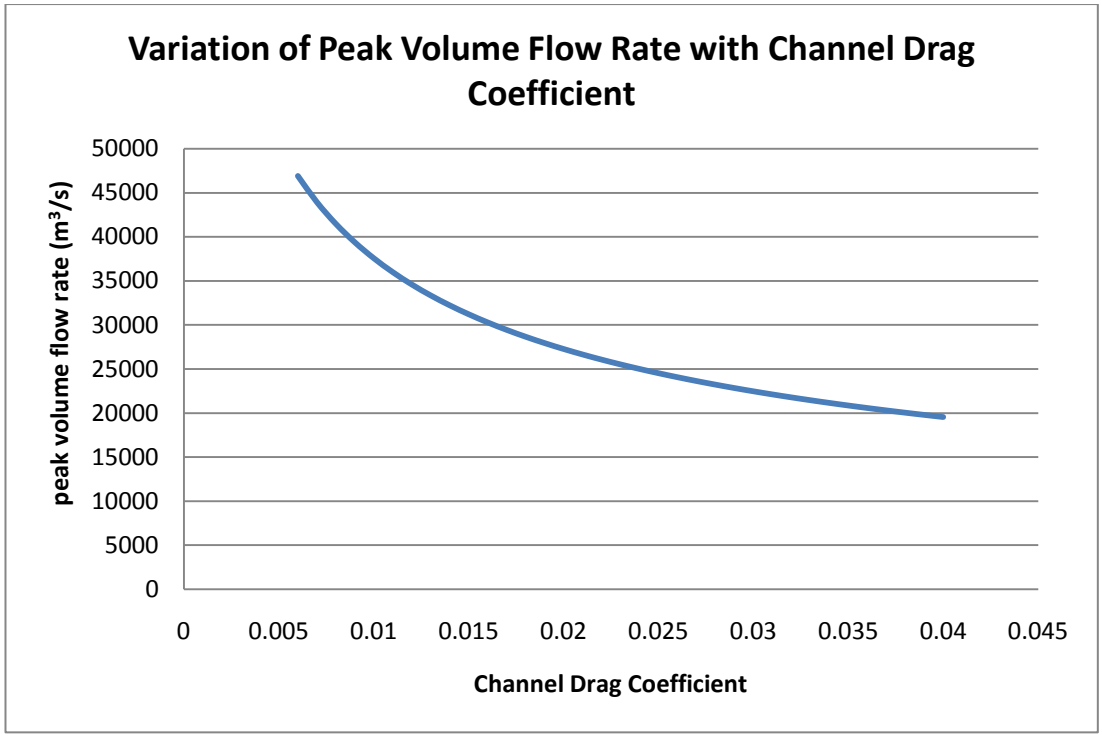

Figure 3.4- Variation of peak volume flow rate with channel drag coefficient for rectangular channel

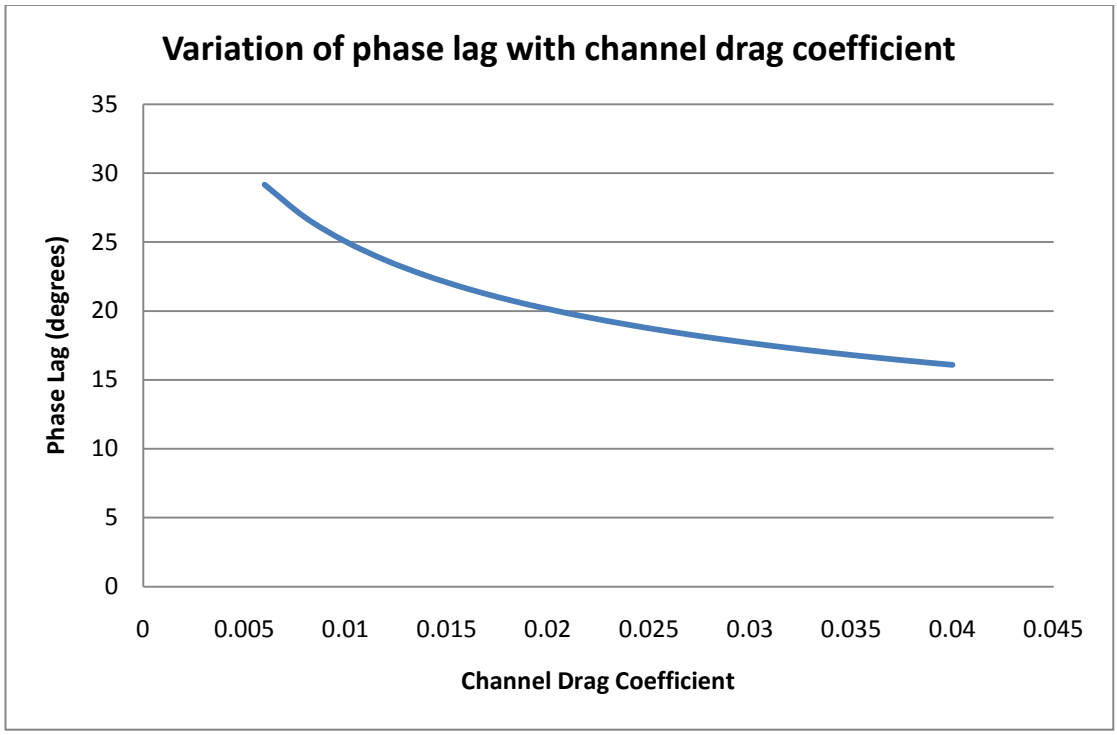

Figure 3.5- Variation of phase lag between zero head difference and zero flow velocity with channel drag coefficient for rectangular channel

The effect of channel geometry on peak volume flow rate was also investigated. Both the effect of changing the channel width and the effect of changing the channel length were investigated in order to establish whether there was a link between the constants c_1 and c_2 and the peak volume flow rate through the channel. Figure 3.6 shows the variation of peak volume flow rate with c_1 and Figure 3.7 shows the variation of peak volume flow rate with c_2. It can be seen from these graphs that channels with the same c_1 or c_2 values will not have the same peak volume flow rate unless they also have the same width, length and depth. Peak volume flow rate is determined by channel geometry and cannot be established through the knowledge of c_1 or c_2.

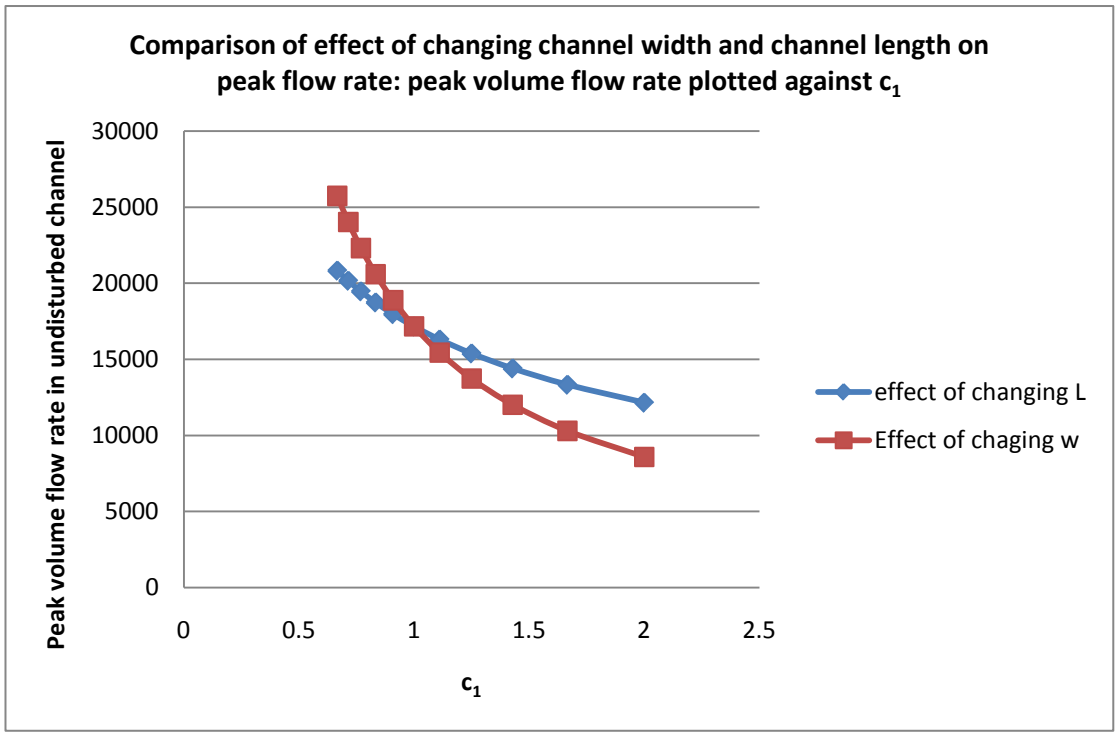

Figure 3.6- Effect of length and width changes on peak volume flow rate: Q_{max} vs c_1

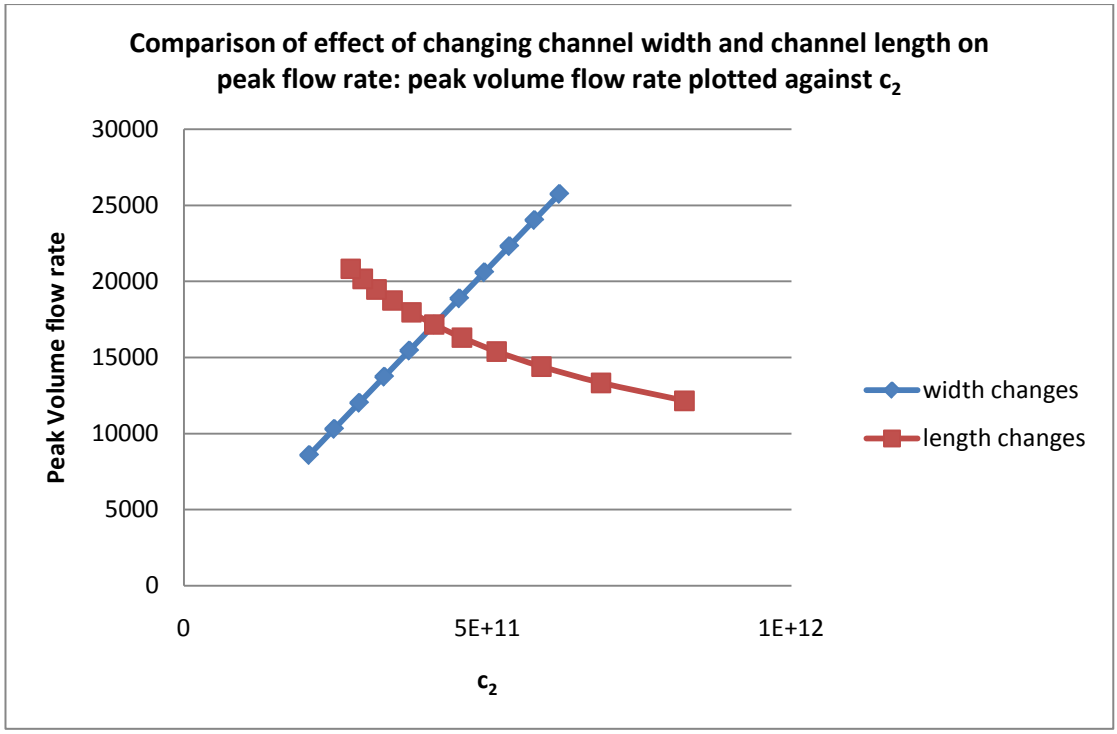

Figure 3.7- Effect of length and width changes on peak volume flow rate: Q_{max} vs c_2

3.5.1.2 Effect of turbines on the flow in a rectangular channel

The effect of extracting energy from the channel was investigated for turbines A and B operating at both a constant tip speed ratio and a constant rotational speed. The investigation looked at how the number of turbines affected the changes to the flow induced by the turbines and also at the effect of the number of turbines on the power generated. A cut in speed of 0.8m/s was used for both the power and thrust for all turbines and modes of operation except for the constant rotational speed operation of a 3m diameter turbine of design A for which a cut in speed of 1.1m/s was used for both power and thrust. The justification for the choice of these cut in speed is given in section 2.6.3.

All the designs and modes of operation of turbine were found to show similar trends for the variation of flow and power quantities with the

number of turbines installed. This allows the effect of the number of turbines on the power and flow quantities to be presented for a single design and mode of operation of turbine. Results are presented for the constant rotational speed operation of turbine B. Whilst the trends shown by the different turbines and modes of operation are the same, the magnitude of the flow and power quantities for a given number of turbines varies with the design and mode of operation of the turbines. The differences in the magnitude of the power and flow quantities for the other designs and modes of operation are considered by comparing the flow and power quantities for 1000 turbines of all designs and modes of operation. In the channel with a drag coefficient of 0.04, the flow speed did not reach the cut in speed of the 3m diameter turbine of design A and so this case is not included in the comparison tables.

The variation of peak volume flow rate with the number of turbines is shown in Figure 3.8. It can be seen from this graph that as the number of turbines installed in the channel is increased, the peak volume flow rate in the channel is reduced. This demonstrates that installing turbines in a channel reduces the flow speed in the channel. The amount by which the peak volume flow rate is reduced for a given number of turbines depends both on the turbine geometry and the channel drag coefficient. The greatest change in peak volume flow rate for a given number of turbines occurs for the largest diameter of turbine in the channel with the smallest drag coefficient. As the diameter of the turbine is reduced or the magnitude of the channel drag coefficient is increased, the change in peak volume flow rate is reduced.

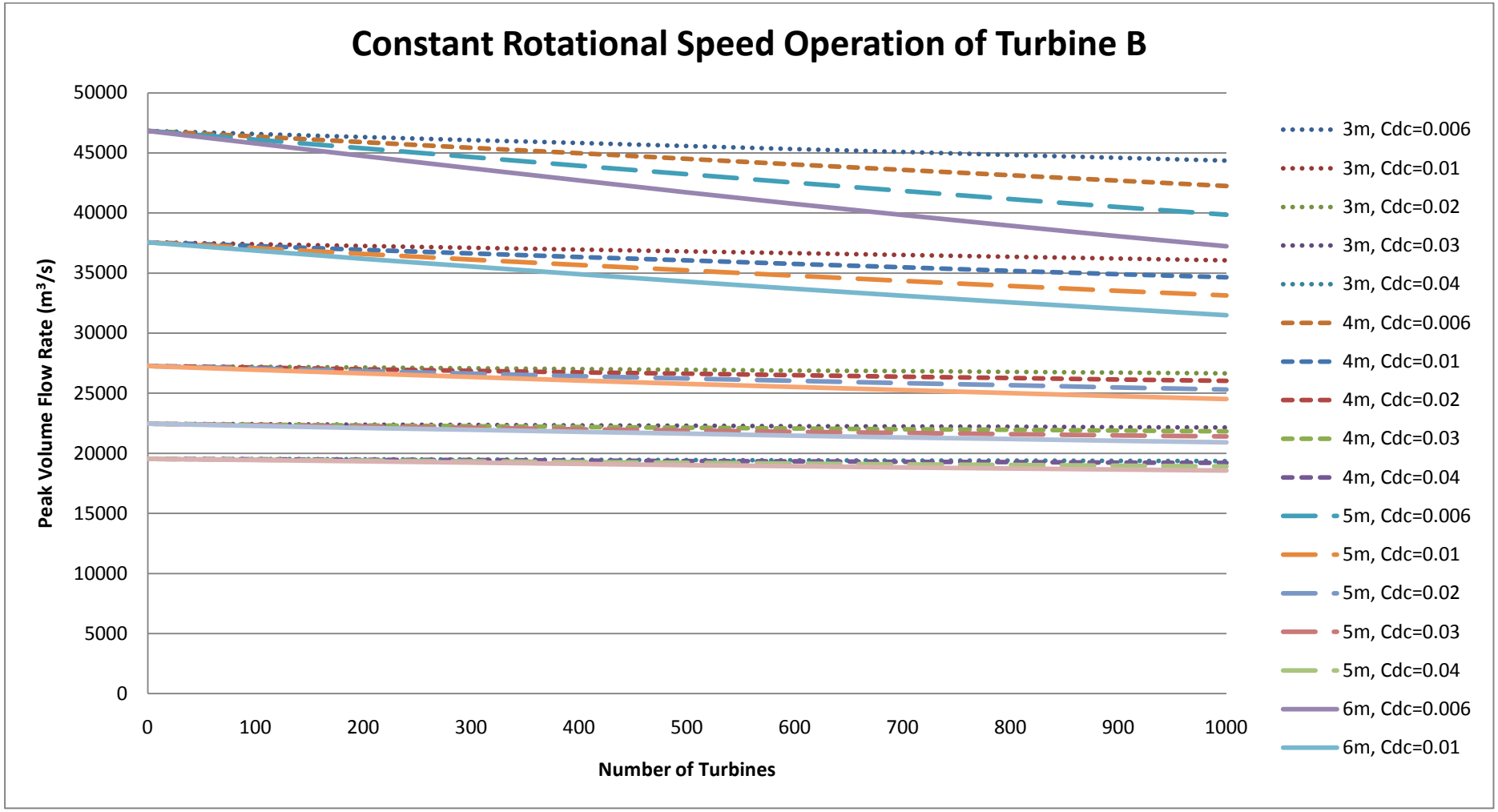

Figure 3.8- Effect of number of turbines on peak volume flow rate for the constant rotational speed operation of Turbine B

Table 3.4 gives the percentage difference between the peak volume flow rate for a channel with 1000 turbines of design B operated at constant rotational speed and 1000 turbines of the other designs and modes of operation. The percentage difference was calculated using Equation 44 with the two turbines being compared having equal radius. It can be seen from Table 3.4 that the variation in peak volume flow rate with turbine design and mode of operation is not large for a given geometry and channel drag coefficient.

$$\%\ \text{difference} = \left(\frac{\dot{V}_{max}\ \text{for other turbine} - \dot{V}_{max}\ \text{for const. rot. speed operation of B}}{\dot{V}_{max}\ \text{for const. rot. speed operation of B}} \right) \times 100$$

Equation 44

Graphs of the number of turbines against peak volume flow rate do not allow the relative effects of the turbines on channels with different drag coefficients to be seen. This can be achieved by plotting the number of turbines against percentage decrease in peak volume flow. Figure 3.9 shows the effect of the number of turbines on the % decrease in peak volume flow rate for the constant tip speed ratio operation of a 4m radius turbine of design B. In Figure 3.10 the percentage decrease in peak volume flow rate is plotted against blockage instead of number of turbines. It can be seen from these graphs that the larger the drag coefficient of the channel, the lower the % decrease in peak volume flow rate for the same number of turbines. This effect has been previously predicted by Salter (99) who observed that if a large amount of energy is being dissipated as bed friction then installing the first few tidal stream systems at this site will have very little effect. The dependence of the number of turbines needed to cause a certain percentage reduction in peak flow speed on channel drag coefficient is significant since this means that the different numbers of turbines would have to be installed at different sites in order to keep the reduction in peak volume flow rate at an acceptable level.

Table 3.4- Comparison of effect of 1000 turbines of both types, all geometries and all modes of operation on the peak volume flow rate

Turbine	Mode of Operation	Radius (m)	C_{Dc}=0.006	C_{Dc}=0.01	C_{Dc}=0.02	C_{Dc}=0.03	C_{Dc}=0.04
			% difference in Peak Volume Flow Rate (comparison with the constant rotational speed operation of the same diameter of turbine B in channel with same C_{Dc})				
A	constant rotational speed	3	0.02	-0.05	-0.11	-0.07	
		4	0.90	0.98	0.50	0.11	-0.16
		5	1.79	1.85	1.16	0.60	0.20
		6	2.80	2.69	1.97	1.42	1.04
	constant tip speed ratio	3	-0.99	-0.20	-0.01	-0.11	-0.21
		4	-0.57	0.80	0.70	0.14	-0.29
		5	0.26	1.77	1.50	0.74	0.14
		6	1.50	2.78	2.30	1.40	0.70
B	constant tip speed ratio	3	-0.86	-0.12	0.02	-0.09	-0.20
		4	-1.88	-0.15	0.13	-0.27	-0.62
		5	-2.08	0.06	0.51	0.05	-0.39
		6	-1.51	0.52	0.94	0.43	-0.05

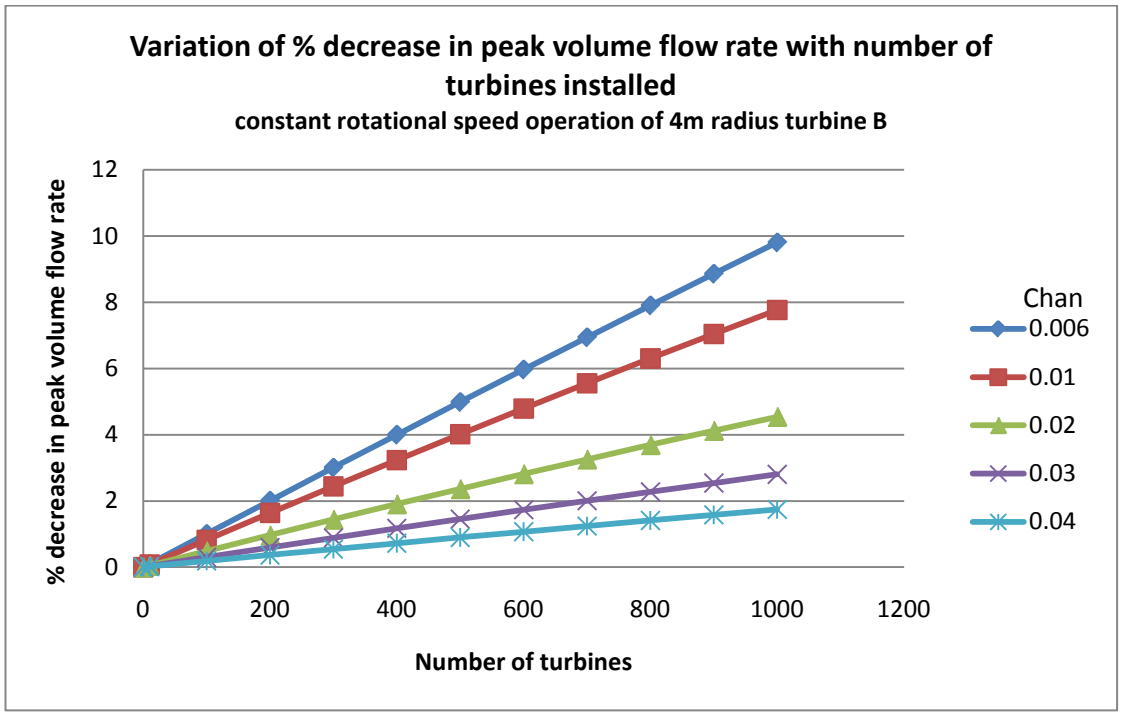

Figure 3.9- Effect of number of turbines on % decrease in peak volume flow rate for the constant rotational speed ratio of a 4m radius turbine B

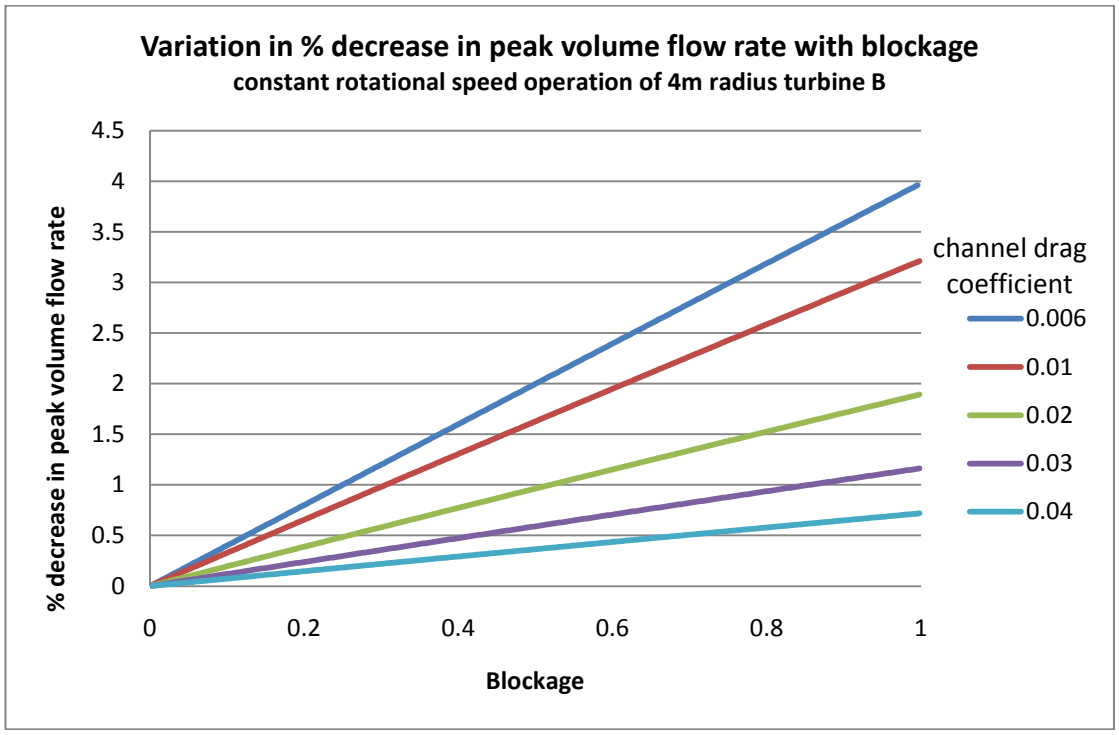

Figure 3.10- Variation in % decrease in peak volume flow rate with blockage for the constant rotational speed operation of a 4m radius turbine B

Table 3.5 shows the percentage reduction in peak volume flow rate for 1000 turbines of all designs in channels with a range of drag coefficients. It can be seen from this table that the largest differences in percentage reduction in peak volume flow rate are between different diameters of turbine and different channel drag coefficient. For a given turbine diameter in a given channel, the effects of changing the turbine design or mode of operation on the percentage reduction in peak volume flow rate are small. This implies that, whilst it is important to model a particular turbine if the effect of that turbine on a site is to be established, it is reasonable to assume that the trends shown in Figure 3.9 also indicate how the peak volume flow rate will be affected by turbines of different designs to the example turbines presented here.

Figure 3.11 is an example of a plot showing how the number of turbines affects the volume flow rate in the channel over the tidal cycle. It can be seen from the graph that as well as a reduction in the peak volume flow

rate, increasing the number of turbines also causes a slight decrease in the phase difference between zero flow and zero head difference between the ends of the channel. This change in phase difference is not large and so is unlikely to be considered significant when considering the effects of tidal stream device deployment at a site.

Table 3.5- % decrease in peak volume flow rate for 1000 turbines of all designs and modes of operation in channels with a range of drag coefficients

radius	turbine	mode of operation	C_{Dc}=0.006	C_{Dc}=0.01	C_{Dc}=0.02	C_{Dc}=0.03	C_{Dc}=0.04
			% decrease Peak Volume Flow Rate (m^3/s)				
3m	A	constant λ	6.25	4.17	2.25	1.53	1.16
		constant Ω	5.29	4.02	2.34	1.49	
	B	constant λ	6.13	4.09	2.21	1.51	1.14
		constant Ω	5.31	3.97	2.23	1.42	0.95
4m	A	constant λ	10.32	7.03	3.88	2.67	2.03
		constant Ω	8.99	6.86	4.06	2.70	1.90
	B	constant λ	11.50	7.91	4.42	3.07	2.35
		constant Ω	9.81	7.77	4.54	2.80	1.74
5m	A	constant λ	14.69	10.24	5.78	4.02	3.07
		constant Ω	13.39	10.17	6.10	4.15	3.01
	B	constant λ	16.69	11.75	6.71	4.68	3.58
		constant Ω	14.91	11.80	7.18	4.72	3.21
6m	A	constant λ	19.32	13.79	8.00	5.62	4.32
		constant Ω	18.29	13.87	8.30	5.60	4.00
	B	constant λ	21.71	15.69	9.23	6.52	5.03
		constant Ω	20.51	16.12	10.07	6.92	4.99

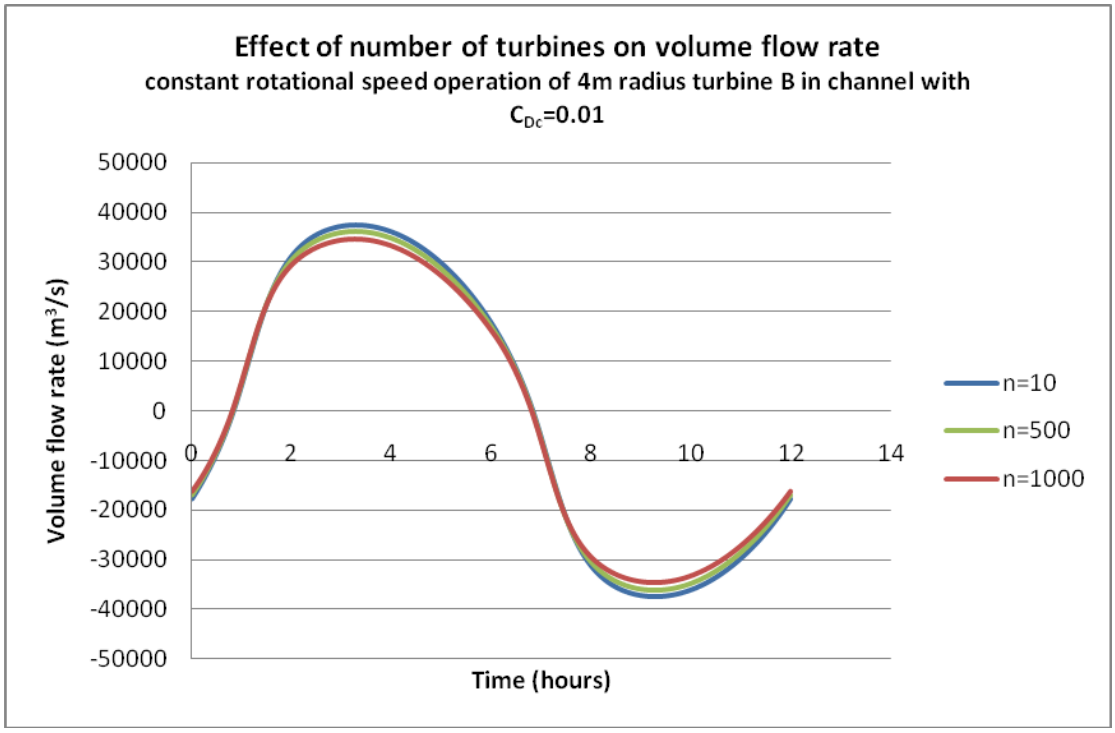

Figure 3.11- Effect of number of turbines on variation of volume flow rate with time for the constant rotational speed operation of a 4m radius turbine of design B in a channel with $C_D = 0.01$

The power generated by 10-1000 turbines was considered. Figure 3.12 shows the effect of the number of turbines on the peak power generated for a range of channel drag coefficients and Figure 3.13 shows the effect of the number of turbines on the peak power generated for a range of turbine radii. It can be seen from these graphs that as the number of turbines is increased the peak power generated also increases. The amount of power generated by a given number of turbines increased with increased turbine radius and decreased with increased channel drag coefficient. The increase in the power generated with the number of turbines is not linear: the amount of power generated per turbine added decreases as the number of turbines is increased. This is more apparent in Figure 3.13 than Figure 3.12. It is expected that once a certain number of turbines are installed the peak power generated will be reduced by the addition of further turbines but this number of turbines does not lie within the range considered.

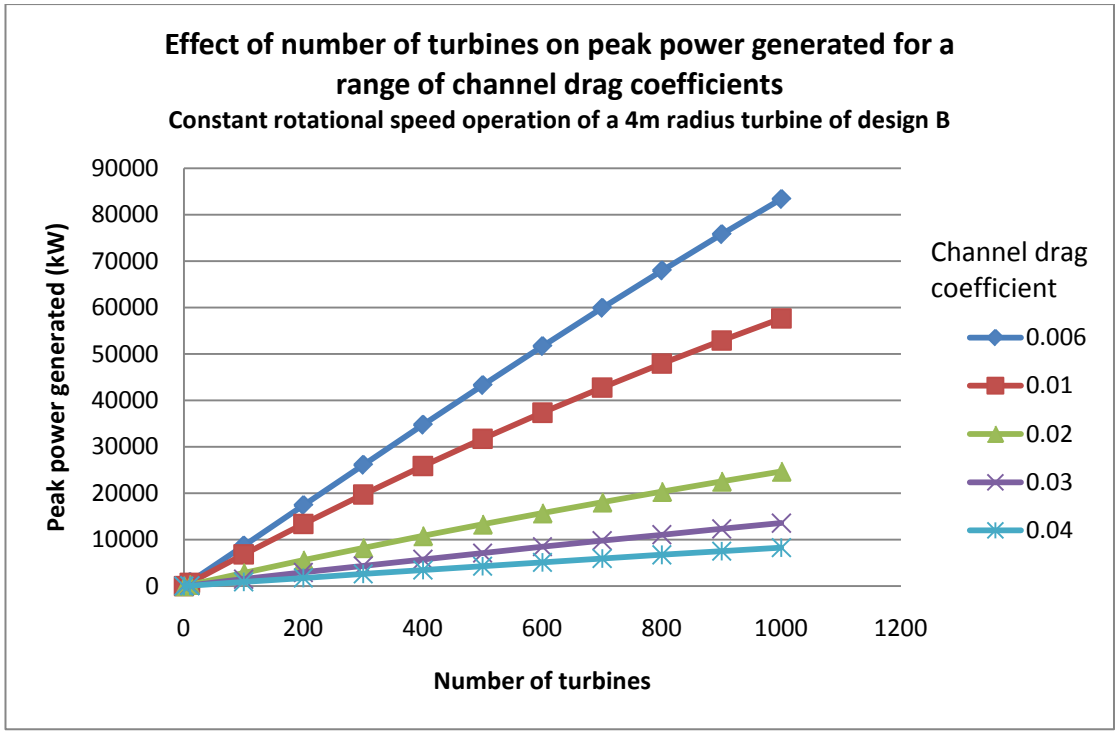

Figure 3.12- Effect of number of turbines on peak power generated for a range of channel drag coefficients

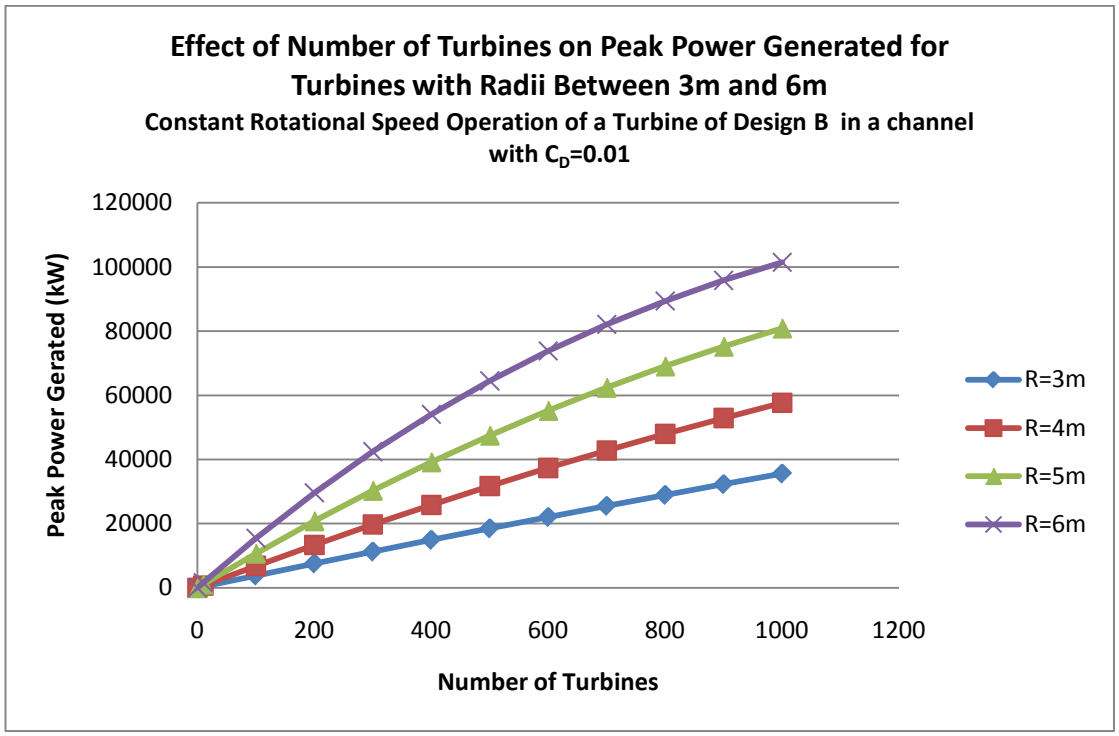

Figure 3.13- Effect of number of turbines on peak power generated for a range of turbine radii

Figure 3.12 and Figure 3.13 showed that the power generated was not directly proportional to the number of turbines. This effect can be seen more clearly by considering how the power generated per turbine varies with the number of turbines installed. Figure 3.14 shows how the peak power generated per turbine varies with the number of turbines for a range of channel drag coefficients and Figure 3.15 shows how the peak power generated per turbine varies with the number of turbines for a range of turbine radii. The reduction in peak power generated per turbine increases as the radius of the turbine is increased and reduces as the channel drag coefficient is increased. The reduction in peak power generated per turbine as the number of turbines is increased is a result of the effect of the turbines on the peak volume flow rate. The peak volume flow rate depends on the total resistance to the flow. Increasing channel drag coefficient and turbine radius increase the total resistance to the flow and so reduce the peak volume flow rate. The power generated by a turbine is a function of the flow speed, so reducing the peak volume flow rate, which reduces the peak flow speed, reduces the power generated by each turbine. For cases where the turbines have less effect on the peak volume flow rate, such as turbines installed in high drag coefficient channels or small radius turbines, the reduction in peak power generated per turbine with increasing numbers of turbines is smaller. This explains why some of the curves in Figure 3.12 and Figure 3.13 appear to be much straighter than others.

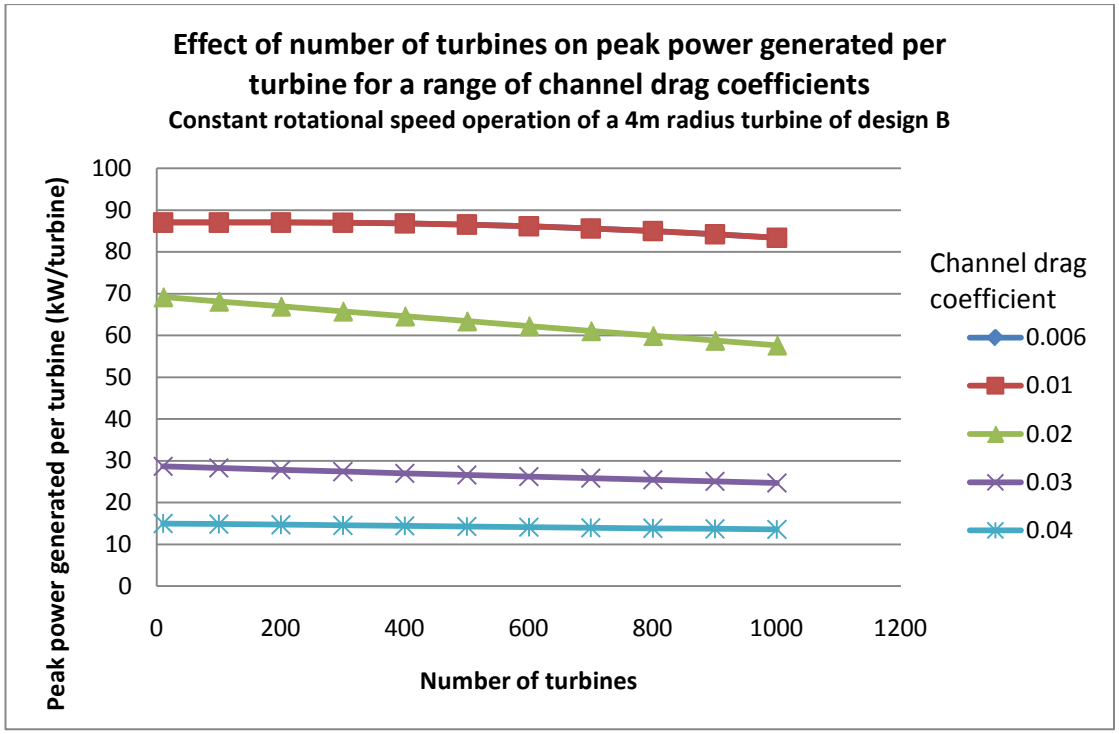

Figure 3.14- Effect of number of turbines on peak power generated per turbine for a range of channel drag coefficients

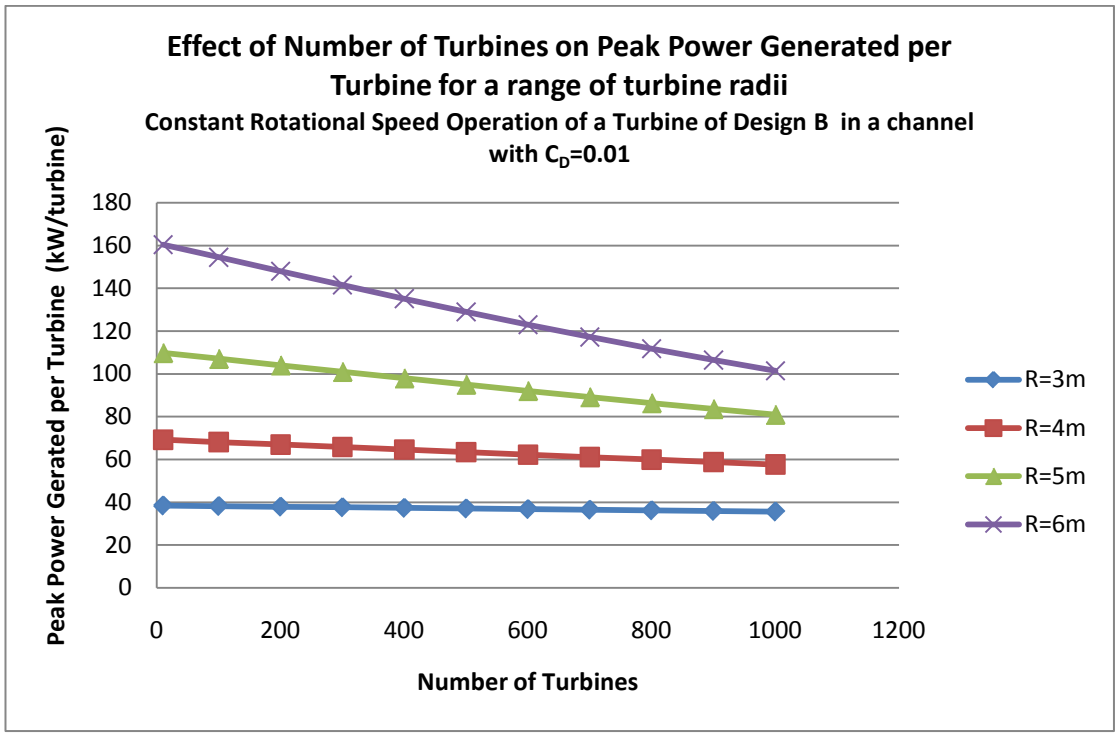

Figure 3.15- Effect of number of turbines on peak power generated per turbine for a number of radii of turbines

Table 3.6 gives the peak power generated per turbine for 1000 turbines of all designs, geometries and modes of operation in channels with a range of drag coefficients. It can be seen from this table that the peak power generated per turbine is much more dependent on the turbine design and mode of operation than the flow quantities are. The different designs and modes of operation of turbine present similar resistance to the flow, but vary greatly in the efficiency with which they convert the energy extracted from the flow into useful work. The significant differences in the power generated by the different designs and modes of operation of turbine suggests that the magnitude of the peak power generated by a turbine needs to be calculated for that specific turbine and cannot be estimated from results calculated for other turbines.

Table 3.6- Peak power generated per turbine for 1000 turbines

radius	turbine	mode of operation	C_{Dc}=0.006	C_{Dc}=0.01	C_{Dc}=0.02	C_{Dc}=0.03	C_{Dc}=0.04
			Peak power generated per turbine for 1000 turbines (kW/turbine)				
3m	A	constant λ	64.83	35.26	13.83	7.62	4.88
		constant Ω	51	33.55	13.53	2.57	
	B	constant λ	70.96	38.59	15.31	8.59	5.63
		constant Ω	45.71	35.62	16.44	9.57	6.23
4m	A	constant λ	101.86	58.22	24.26	13.86	9.14
		constant Ω	83.37	55.46	24.35	12.39	6.38
	B	constant λ	102.25	57.66	25.11	14.53	8.30
		constant Ω	83.39	59.20	24.70	13.56	9.71
5m	A	constant λ	132.85	79.52	34.87	20.42	13.72
		constant Ω	120.11	78.08	34.82	18.51	10.06
	B	constant λ	132.86	81.18	34.40	21.59	14.62
		constant Ω	123.44	80.93	36.44	18.01	9.88
6m	A	constant λ	162.22	101.80	47.05	28.22	19.23
		constant Ω	154.45	100.55	45.58	25.52	15.84
	B	constant λ	159.25	101.45	48.61	29.55	20.32
		constant Ω	158.00	102.32	43.98	24.87	16.52

Turbine performance is typically plotted in terms of the power coefficient of the turbine, rather than the power generated by the turbine. For the constant rotational speed operation of the turbines the maximum power coefficient did not always occur at the point in the tidal cycle when the maximum amount of power was being generated. Figure 3.16 shows the variation of maximum power coefficient with blockage for the constant rotational speed operation of a 4m radius turbine B for a range of channel drag coefficients and Figure 3.17 shows the variation of the power coefficient at the peak power with blockage for the same turbine and mode of operation for a range of channel drag coefficients. It can be seen from these graphs that for most of the channel drag coefficients the maximum power coefficient and the power coefficient at peak power remain constant or decrease slightly as the blockage increases. The power coefficient at the peak power for the channels with drag coefficients of 0.006 and 0.01 increased with increased blockage. This suggests that the turbine was poorly tuned for these channels and so altering the flow speed in the channels actually improved the performance of the turbine. This effect can also be seen in Figure 3.18 which shows how the power coefficient at peak power varies with blockage for a range of diameters of turbines in a channel with a channel drag coefficient of 0.01. In Figure 3.18 the power coefficient at peak power increases with blockage for all of the diameters of turbine. Figure 3.19 shows the variation of maximum power coefficient with blockage for the constant rotational speed operation of turbines of design B with a range of radii in a channel with channel drag coefficient equal to 0.01. As for the channel with a channel drag coefficient of 0.01 in Figure 3.16, the peak power coefficient did not vary as the blockage was increased.

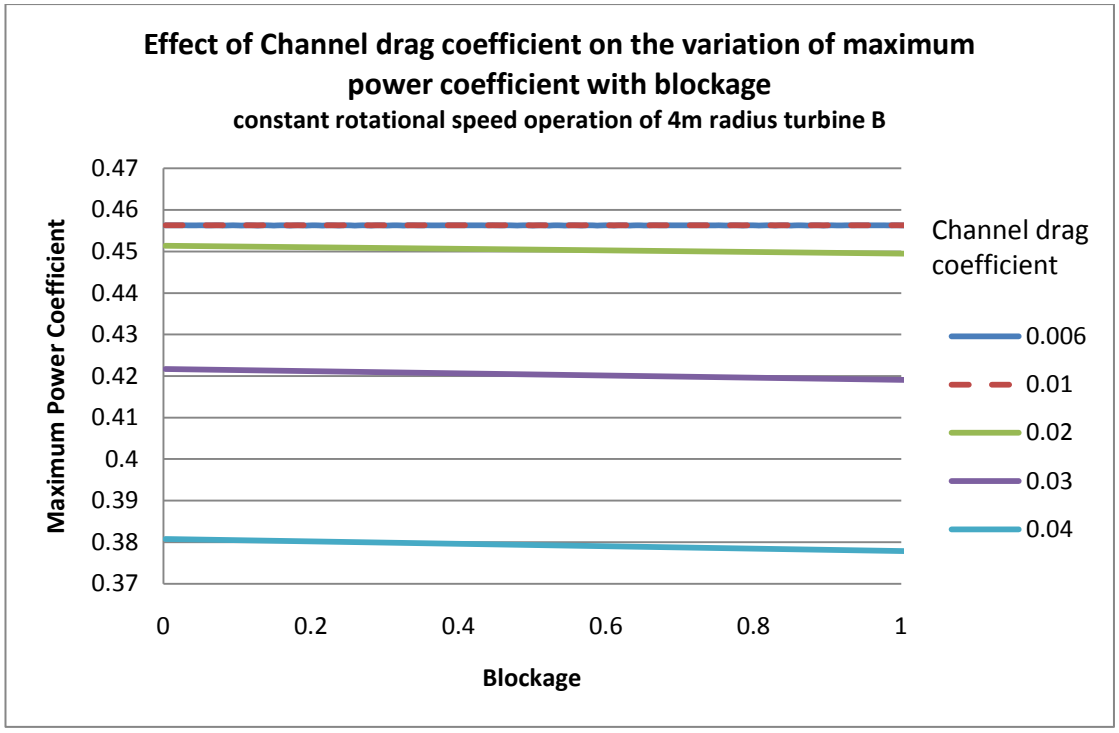

Figure 3.16- Effect of channel drag coefficient on the variation of maximum power coefficient with blockage for the constant rotational speed operation of a 4m radius turbine B

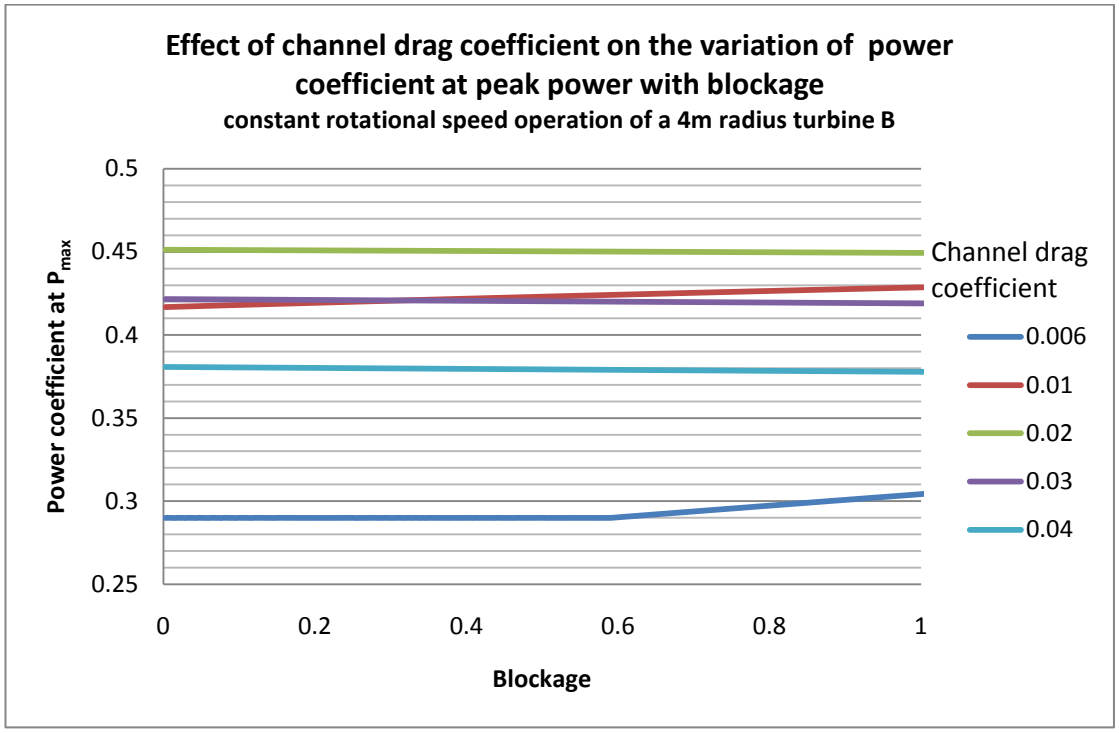

Figure 3.17- Effect of channel drag coefficient on the variation of power coefficient at peak power with blockage for the constant rotational speed operation of a 4m radius turbine B

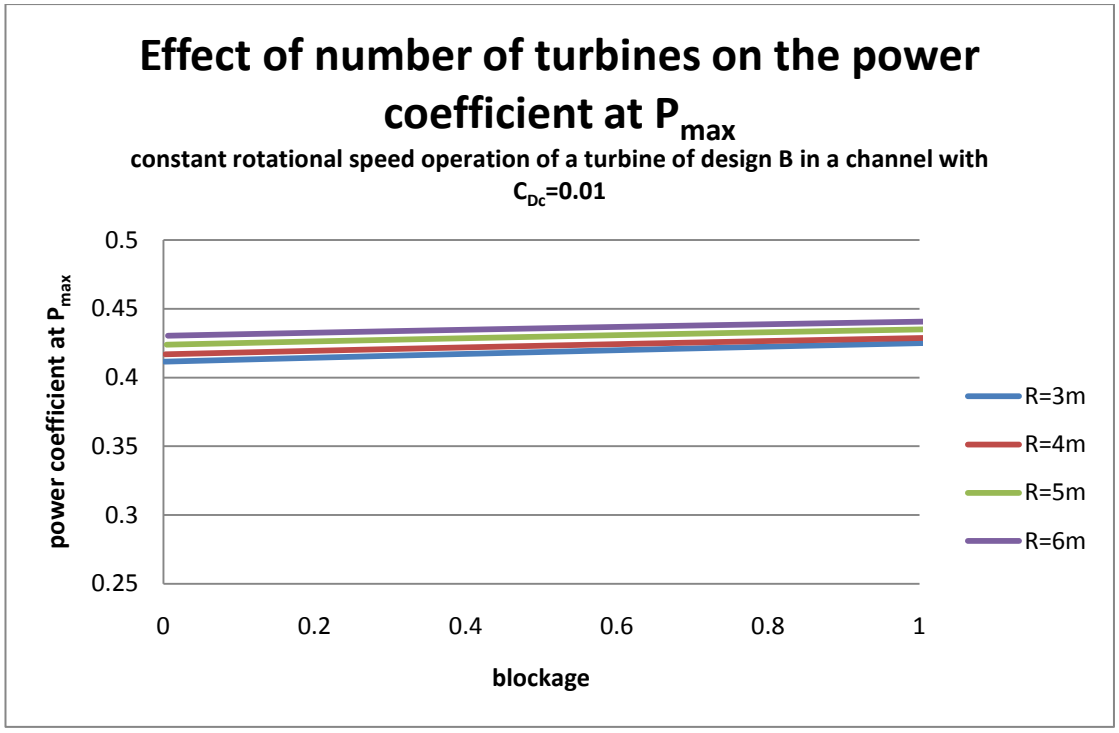

Figure 3.18- Variation of power coefficient at peak power with blockage for a range of turbine radii for the constant rotational speed operation of a turbine of design B in a channel with a drag coefficient of 0.01

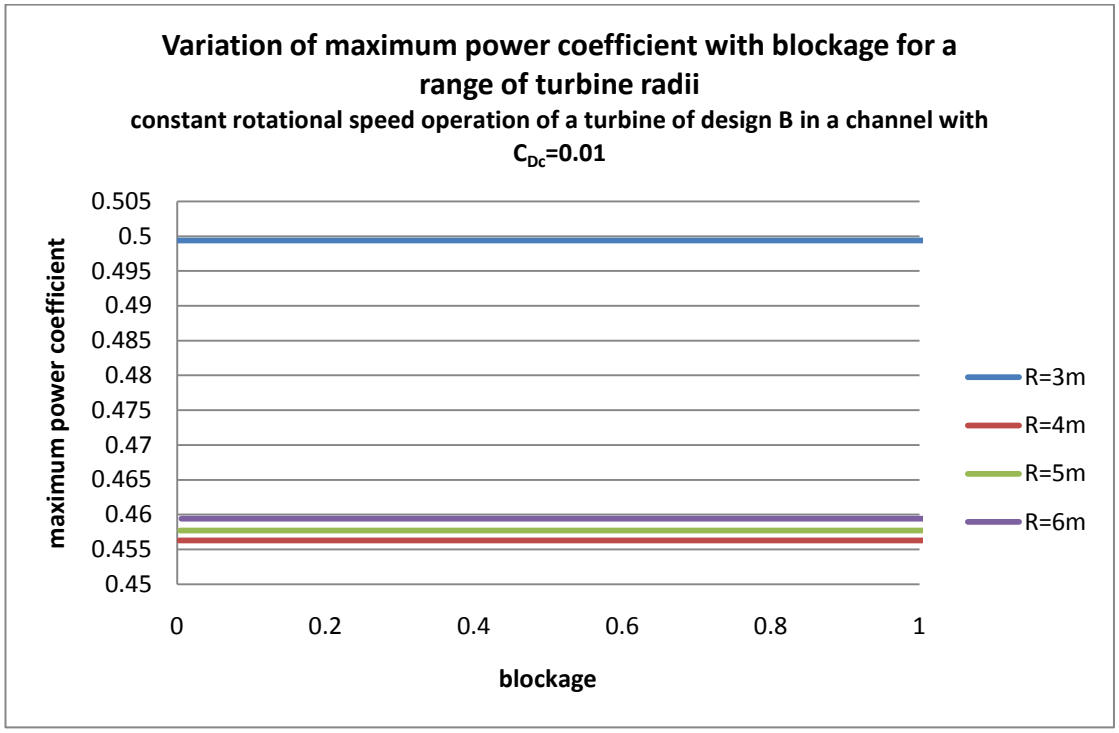

Figure 3.19- Variation maximum power coefficient with blockage for a range of turbine radii for the constant rotational speed operation of a turbine of design B in a channel with a drag coefficient of 0.01

Unlike the other variables studied so far, the trends in the variation of maximum power coefficient and power coefficient at peak power are not the same for the different modes of operation of the turbines. For the constant rotational speed operation of the turbines the trends in the variation of power coefficient are the same as those shown in Figure 3.16Figure 3.19. For the constant tip speed ratio operation of the turbines the variation of peak power coefficient with blockage for of turbine B is shown in Figure 3.20 for a 4m radius turbine in channels with a range of drag coefficients and in Figure 3.21 for a channel with a drag coefficient of 0.01 and a range of turbine radii. The trends shown in these figures are the same as those for the other radii and designs of turbines operated at a constant tip speed ratio. For the constant tip speed ratio operation of the turbines the maximum power coefficient is the same as the power coefficient at peak power. It can be seen from Figure 3.20 and Figure 3.21 that there is a slight decrease in the maximum power coefficient as the percentage of the channel cross section occupied by turbines increases.

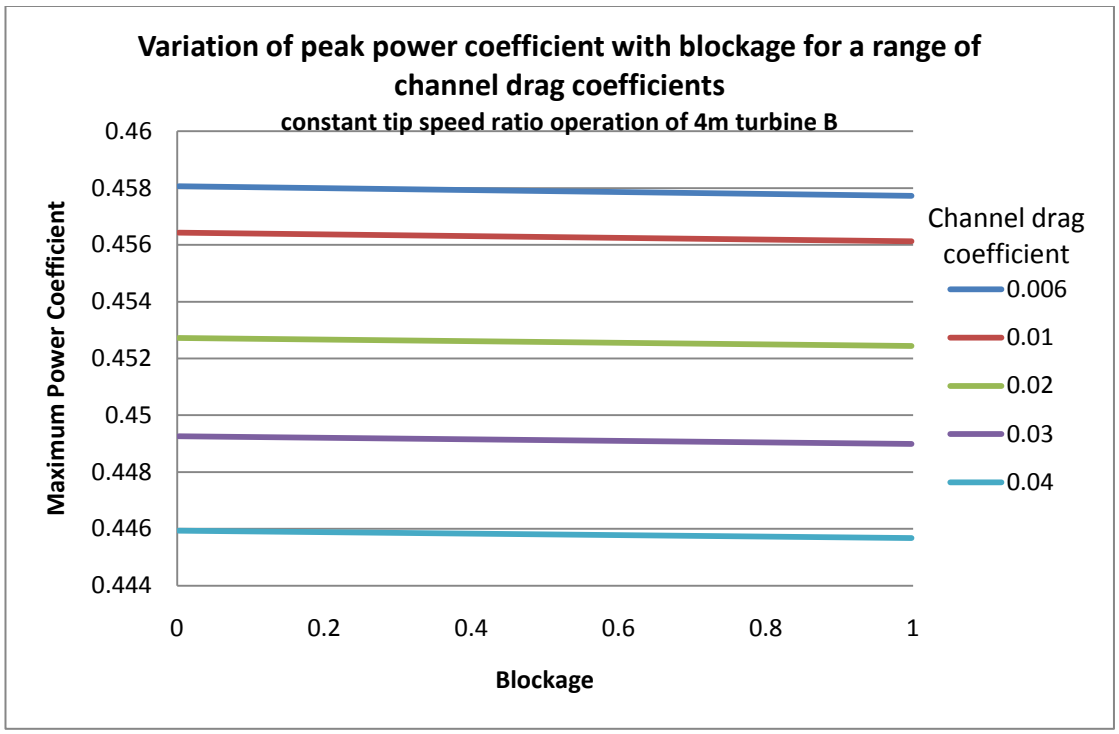

Figure 3.20- Variation of peak power coefficient with blockage for a range of channel drag coefficients

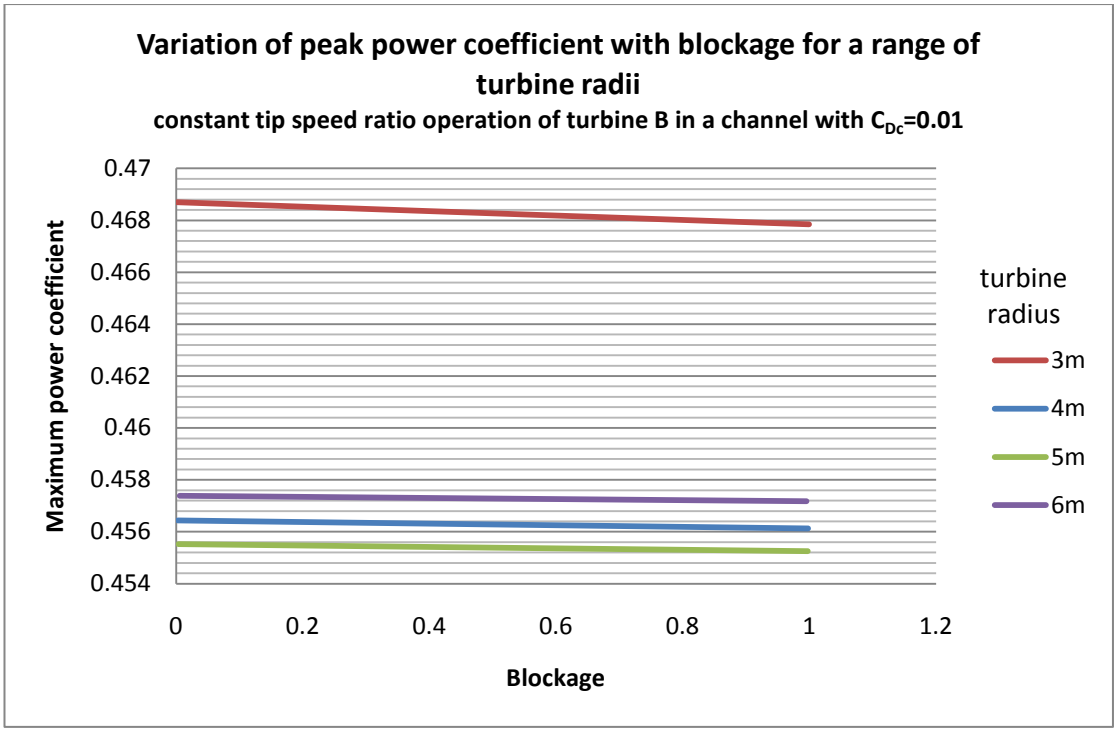

Figure 3.21- Variation of peak power coefficients with blockage for a range of turbine radii

Comparisons of the maximum power coefficient for 1 and 1000 turbines of the different designs, radii and modes of operation are given in Table 3.7. Table 3.8 compares the power coefficient at peak power for 1 and 1000 turbines of the different designs, radii and modes of operation. It can be seen from these tables that any changes in power coefficient between when 1 turbine is installed and when 1000 turbines are installed are very small. This is a contrast to when the power generated per turbine was considered, Figure 3.14 and Figure 3.15 both show significant reductions in the power generated per turbine for 1 turbine and 1000 turbines. This is because increasing the number of turbines reduces the flow speed in the channel so, despite small or no changes in power coefficient, the power generated is significantly less. This suggests that it may be more appropriate to use the actual power generated rather than the power coefficient to consider the effect of the number of turbines installed in a channel on their performance.

Table 3.7- Comparisons of the maximum power coefficient of 1 and 1000 turbines

Mode of operation	Turbine	Radius	C_{Dc}=0.006		C_{Dc}=0.01		C_{Dc}=0.02		C_{Dc}=0.03		C_{Dc}=0.04	
			$(C_P)_{max}$									
			n=1	n=1000	n=1	n=1000	n=1	n=1000	n=1	n=1000	n=1	n=1000
constant λ	A	3	0.435	0.434	0.430	0.428	0.415	0.414	0.400	0.399	0.385	0.383
		4	0.439	0.438	0.437	0.436	0.431	0.429	0.424	0.423	0.417	0.415
		5	0.426	0.425	0.424	0.423	0.420	0.419	0.417	0.416	0.413	0.412
		6	0.426	0.426	0.426	0.425	0.423	0.422	0.420	0.419	0.418	0.417
	B	3	0.474	0.473	0.469	0.468	0.458	0.457	0.450	0.449	0.443	0.443
		4	0.458	0.457	0.456	0.456	0.453	0.452	0.449	0.449	0.446	0.445
		5	0.457	0.456	0.456	0.455	0.452	0.451	0.449	0.449	0.447	0.446
		6	0.459	0.457	0.457	0.456	0.455	0.454	0.453	0.452	0.451	0.450
constant Ω	A	3	0.434	0.434	0.434	0.434	0.417	0.406	0.174	0.134		
		4	0.439	0.439	0.439	0.439	0.438	0.433	0.391	0.378	0.305	0.289
		5	0.429	0.429	0.429	0.429	0.428	0.423	0.394	0.378	0.324	0.302
		6	0.425	0.425	0.425	0.425	0.422	0.413	0.393	0.379	0.354	0.340
	B	3	0.499	0.499	0.499	0.499	0.499	0.499	0.499	0.499	0.489	0.487
		4	0.456	0.456	0.456	0.456	0.451	0.446	0.422	0.415	0.381	0.374
		5	0.458	0.458	0.458	0.458	0.447	0.433	0.396	0.375	0.322	0.298
		6	0.459	0.459	0.459	0.459	0.445	0.422	0.401	0.385	0.373	0.366

Table 3.8- Comparisons of the power coefficient at peak power for 1 and 1000 turbines

Mode of operation	Turbine	Radius	C_{Dc}=0.006		C_{Dc}=0.01		C_{Dc}=0.02		C_{Dc}=0.03		C_{Dc}=0.04	
			C_P at P_{max}									
			n=1	n=1000	n=1	n=1000	n=1	n=1000	n=1	n=1000	n=1	n=1000
constant λ	A	3	0.435	0.434	0.430	0.428	0.415	0.414	0.400	0.399	0.385	0.383
		4	0.439	0.438	0.437	0.436	0.431	0.429	0.424	0.423	0.417	0.415
		5	0.426	0.425	0.424	0.423	0.420	0.419	0.417	0.416	0.413	0.412
		6	0.426	0.426	0.426	0.425	0.423	0.422	0.420	0.419	0.418	0.417
	B	3	0.474	0.473	0.469	0.468	0.458	0.457	0.450	0.449	0.443	0.443
		4	0.458	0.457	0.456	0.456	0.453	0.452	0.449	0.449	0.446	0.445
		5	0.457	0.456	0.456	0.455	0.452	0.451	0.449	0.449	0.447	0.446
		6	0.459	0.457	0.457	0.456	0.455	0.454	0.453	0.452	0.451	0.450
constant Ω	A	3	0.302	0.331	0.394	0.406	0.417	0.406	0.174	0.134		
		4	0.297	0.343	0.392	0.413	0.438	0.433	0.391	0.378	0.305	0.289
		5	0.305	0.367	0.391	0.414	0.428	0.423	0.394	0.378	0.324	0.302
		6	0.312	0.390	0.395	0.421	0.422	0.413	0.393	0.379	0.354	0.340
	B	3	0.293	0.297	0.412	0.430	0.490	0.492	0.499	0.499	0.489	0.487
		4	0.290	0.352	0.417	0.442	0.451	0.446	0.422	0.415	0.381	0.374
		5	0.288	0.398	0.424	0.454	0.447	0.433	0.396	0.375	0.322	0.298
		6	0.298	0.433	0.431	0.459	0.445	0.422	0.401	0.385	0.373	0.366

Increasing the number of turbines installed in a channel increases the resistance to the flow and hence reduces the flow speed. This means that as more turbines are installed, the percentage of the tidal cycle which is spent below the cut in speed of the turbines is increased. This increase in time spent below the cut in speed results in a reduction in the power captured which is not shown by the peak power graphs. The energy captured per tidal cycle provides a better measure of how the number of turbines is affecting the amount of power generated than the peak power generated.

The variation of the energy captured per turbine per tidal cycle with the number of turbines installed in the channel is shown in Figure 3.22 for a number of different radii of turbine. Figure 3.23 shows how the drag coefficient of the channel affects the variation of the energy captured per turbine per tidal cycle with the number of turbines installed in the channel.

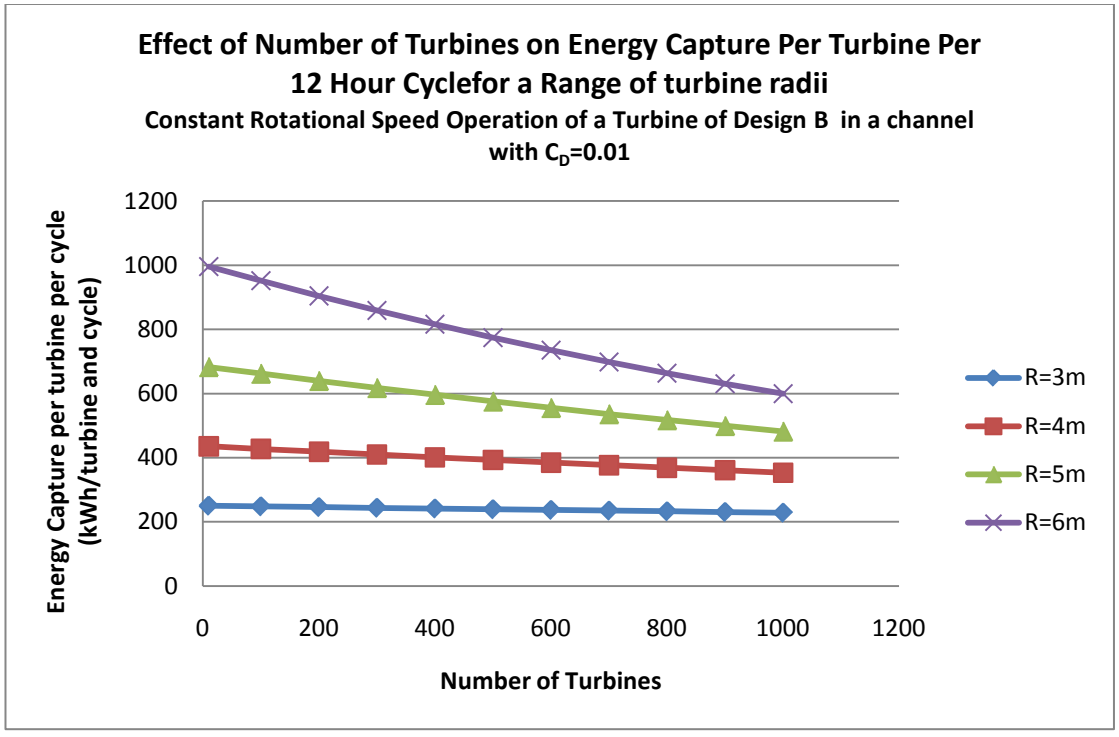

Figure 3.22- Effect of number of turbines on the energy capture per turbine per 12 hour cycle for a range of turbine radii

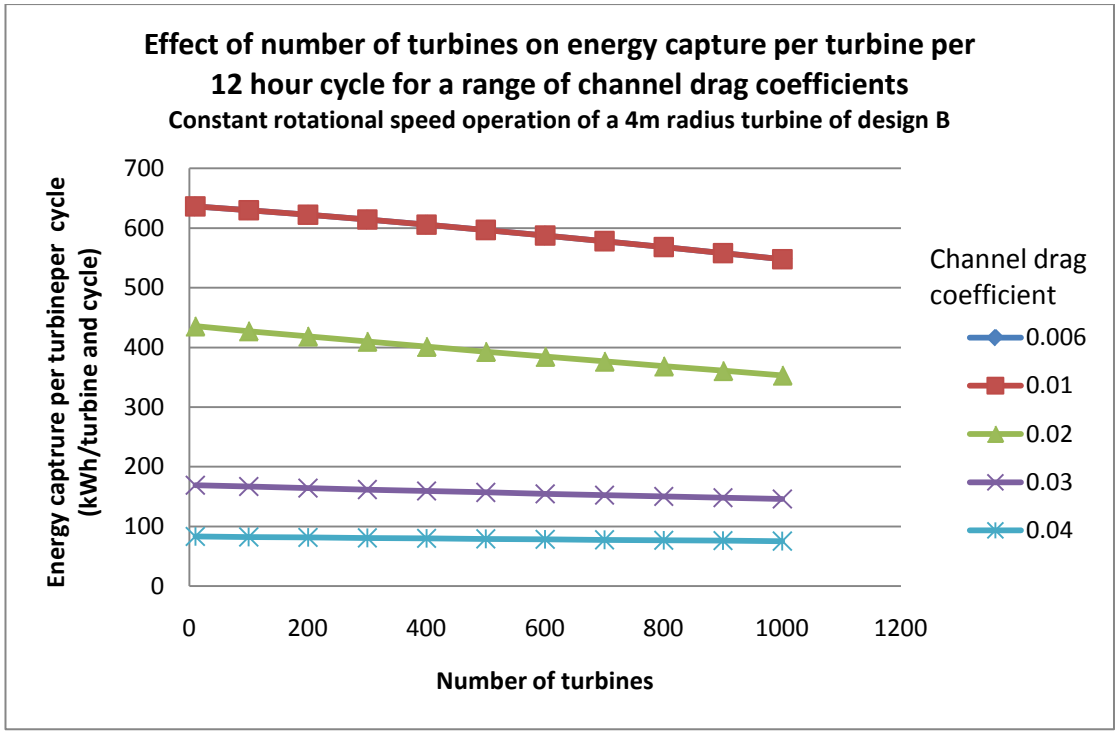

Figure 3.23- Effect of number of turbines on the energy capture per turbine per 12 hour cycle for a range of channel drag coefficients

Figure 3.14, Figure 3.15, Figure 3.22 and Figure 3.23 all show how the performance of the turbines varies with the number of turbines installed. The difference between these graphs is that in Figure 3.14 and Figure 3.15 the quantity used to measure the performance was the peak power and in Figure 3.22 and Figure 3.23 the quantity used to measure performance was the energy capture per turbine per tidal cycle. It is not obvious from the comparison of Figure 3.22 with Figure 3.14 and the comparison of Figure 3.23 with Figure 3.15 whether the use of different performance measures changes the manner in which the performance measure varies with number of turbines. In order to see more clearly if changing the performance measure changes how the performance varies with number of turbines each data set has been divided by the maximum value of that data set in order to allow them to be plotted together. The effect of the choice of performance measure on the rate of change of performance with number of turbines is shown in Figure 3.24 for a range of turbine radii and in Figure 3.25 for a range of channel drag coefficients. It can be seen from these graphs that the choice of performance measure does affect the rate at which the performance measure changes with the

number of turbines installed. For many of the cases shown in this graph the difference between the rate of change of performance with number of turbines is very similar for both performance measures. The variation in rate of change of performance increased as either the drag coefficient was decreased or the turbine radius was increased. Thus the variation in rate of change of performance with number of turbines was greatest for the cases where the turbines caused the greatest change in peak volume flow rate. This demonstrates that it is important to choose the measure by which the effect of number of turbines on performance is quantified with care as selection of the wrong quantity may indicate that performance is less affected by the number of turbines than it actually is.

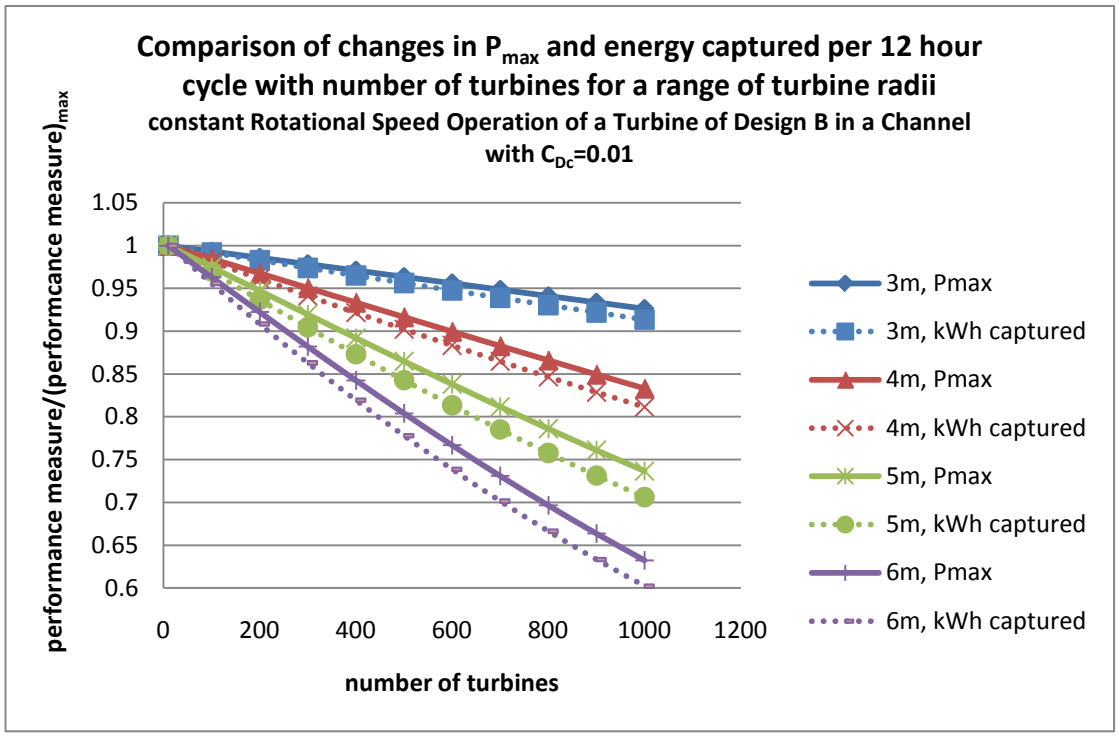

Figure 3.24- Comparison of changes in P_{max} and kWh captured per 12 hour cycle with number of turbines for a range of turbine radii

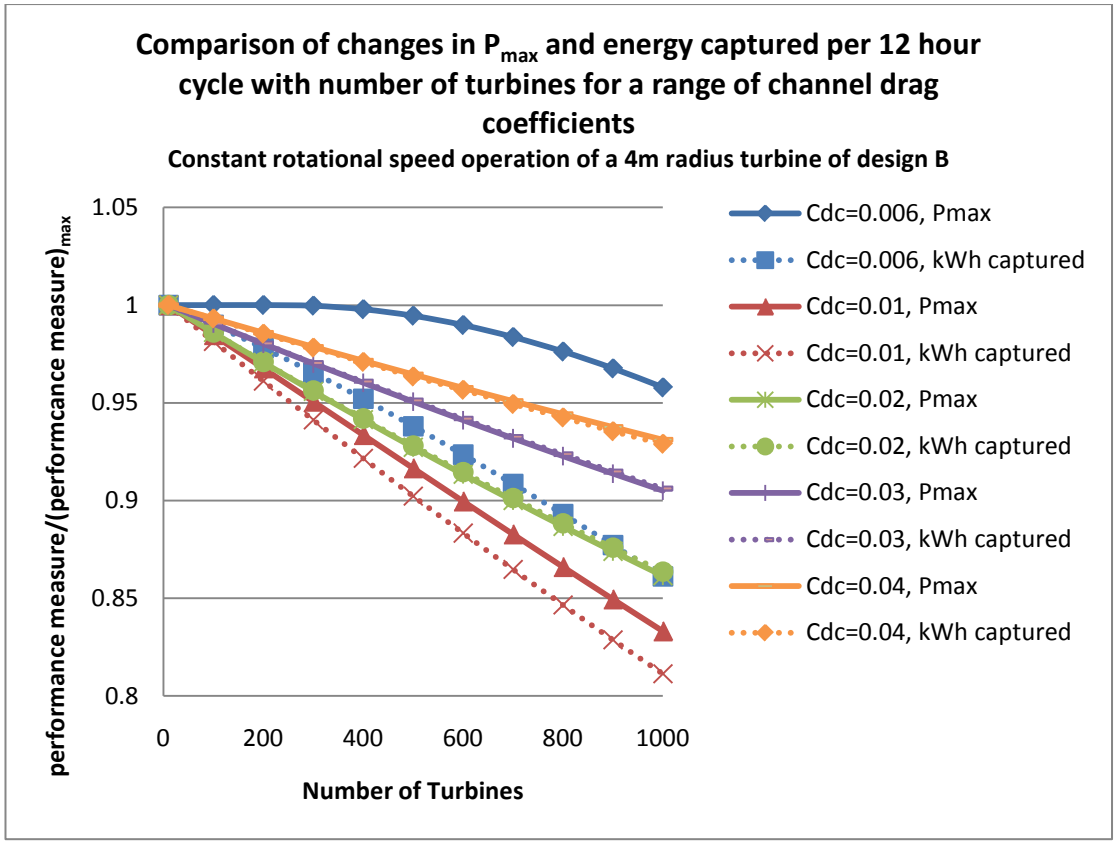

Figure 3.25- Comparison of changes in P_{max} and kWh captured per 12 hour cycle with number of turbines for a range of channel drag coefficients

A better metric for studying how the number of turbines affects their performance over the tidal cycle is the utilisation factor. The utilisation factor is a dimensionless quantity calculated using Equation 45.

$$utilisation\ factor = \frac{average\ energy}{peak\ energy}$$

Equation 45

The variation of utilisation factor as the blockage is increased is shown in Figure 3.26 for a number of radii of turbines and Figure 3.27 for a range of channel drag coefficients. It can be seen from these graphs that the utilisation factor typically decreases as the number of turbines installed in the channel increases. As the drag coefficient of the channel increases the rate of decrease of the utilisation factor with number of turbines installed decreases. For channel drag coefficients of 0.02, 0.03 and 0.04 there is

little or no decrease in utilisation factor. The percentage decrease in peak volume flow rate decreases as the drag coefficient increases, so there is less of a change in flow speed for the higher drag coefficients. This makes the change in utilisation factor less pronounced.

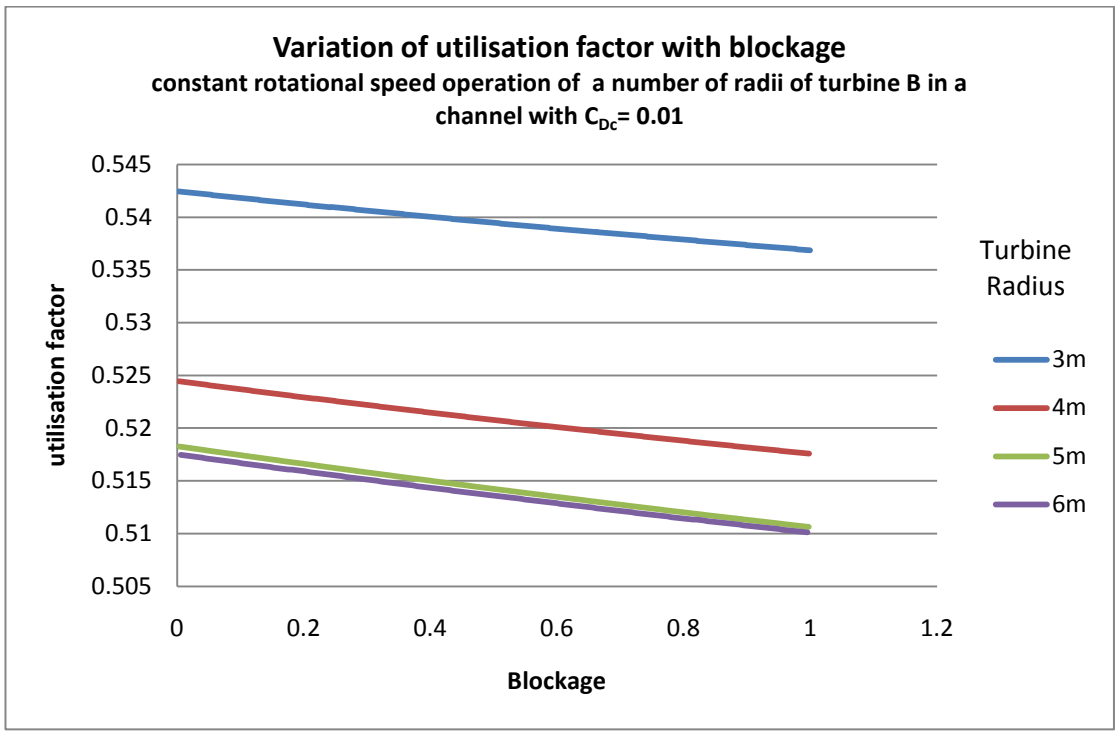

Figure 3.26- Variation of utilisation factor with blockage for the constant rotational speed operation of a range of radii of turbine B in a channel with $C_{Dc} = 0.01$

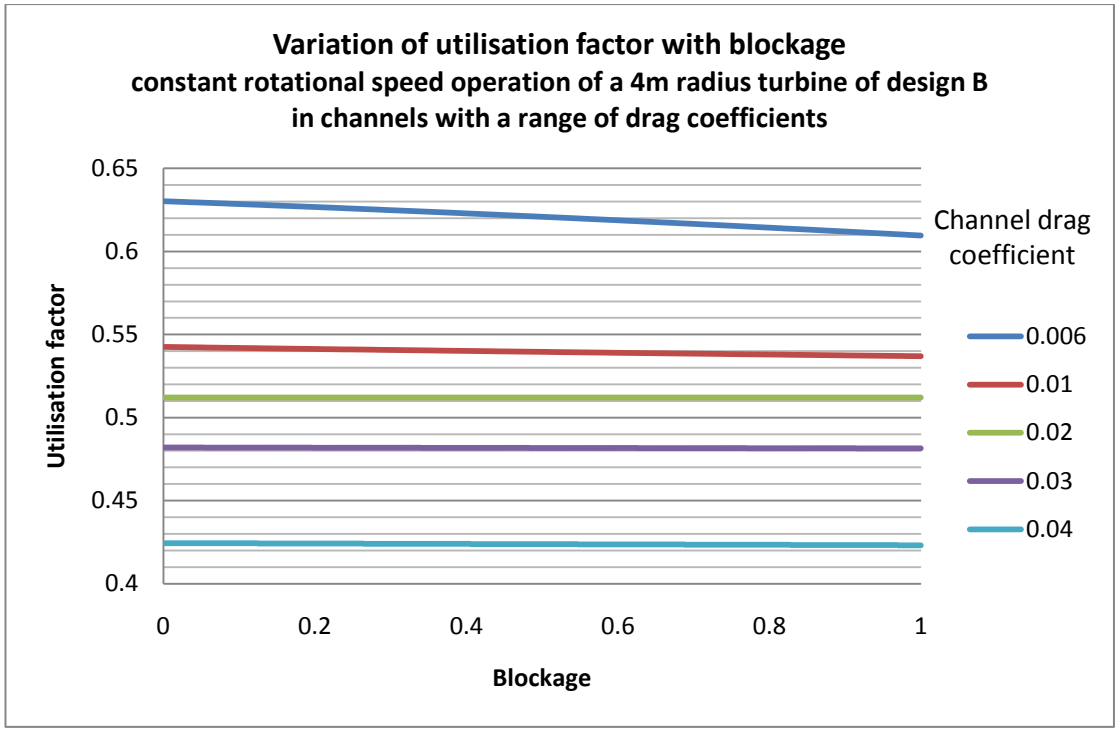

Figure 3.27-Variation of utilisation factor with blockage for the constant rotational speed operation of a 4m radius turbine of design B in channels with a range of drag coefficients

The results from the extended model have indicated that increasing the number of turbines in a channel reduces the amount of power generated by each turbine. In order to see if this effect is significant, the results from the extended model have been compared with the power generated by a turbine at the flow speeds found in the channel in its undisturbed state. Many of the cases considered show a large decrease in the amount of power generated.

The percentage decrease in power generated or energy captured was calculated using Equation 46.

$$percentage\ decrease = \left(\frac{decrease}{energy\ capture\ from\ undisturbed\ channel\ model}\right) \times 100$$

Equation 46

Figure 3.28 shows how the percentage decrease in the energy captured over a 12 hour cycle varies with the number of turbines for a range of turbine radii operating in a channel with C_{DC}=0.01. As the drag coefficient of the channel is increased, the percentage decrease in energy capture generally decreases. This is because the reduction in flow speed caused by a given number of turbines is less for a high friction channel than it is for a lower friction channel. Since the reduction in flow speed is lower, the difference between the energy capture predicted by the model and the energy capture calculated from the flow speeds in the undisturbed channel will be less. The exception to the trend is the C_{Dc}=0.006 data series which mostly lies between the C_{Dc}= 0.01 and 0.02 data series. Plots for the other turbines do not show the same variation, although some show other channel drag coefficients which do not follow the trend. These differences may be due to the tuning of the turbines. The efficiency of each turbine varies with the flow speed so in some cases the changes in flow speed may actually result in an increase in the performance for part of the cycle. In Figure 3.29 the percentage decrease in the energy captured over a 12 hour cycle has been plotted against blockage instead of number of turbines. It should be noted that a blockage of over 1 can be achieved if turbines are installed in more than one section of the channel.

Figure 3.30 shows how the percentage decrease in the energy captured over a 12 hour cycle varies with the number of turbines for a 4m turbine in channels with a range of drag coefficients. In Figure 3. 31 the percentage decrease in energy capture has been plotted against blockage. The percentage decrease in energy capture is greatest for the 6m radius turbine and it decreases as the radius of the turbine is reduced. This is again due to the fact that increasing the radius of the turbine increases the reduction in flow speed caused by the presence of the turbines. The other designs of turbine and modes of operation show similar trends.

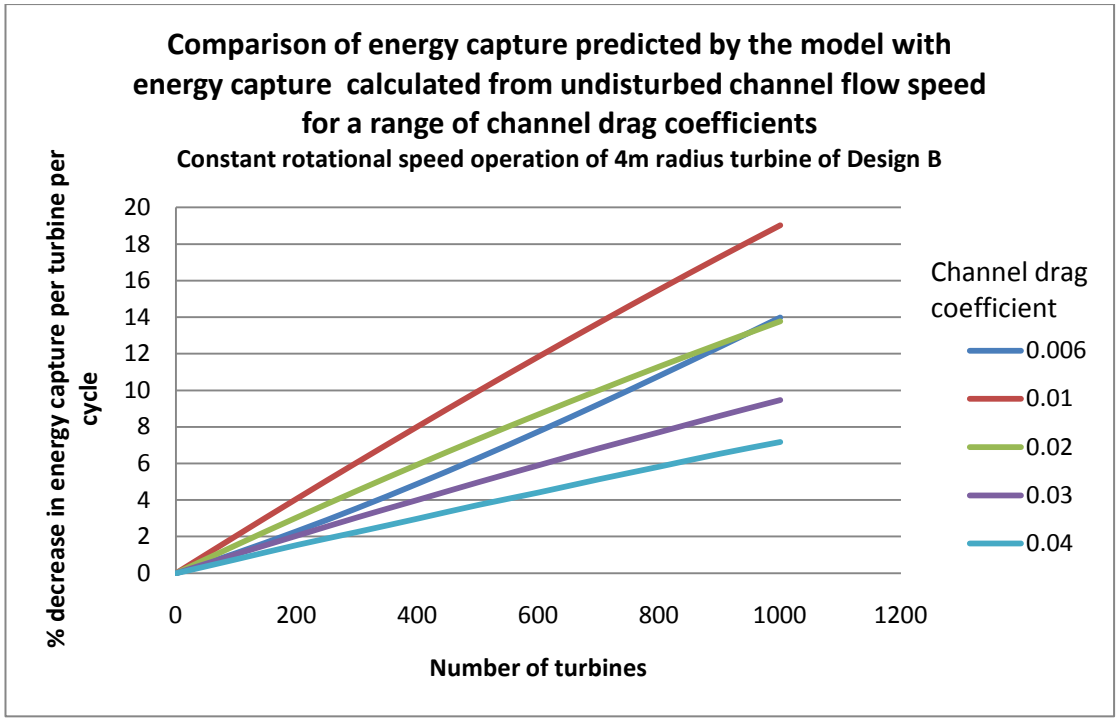

Figure 3.28- Comparison of energy capture predicted by the model with energy capture calculated using the undisturbed channel flow speeds for a range of channel drag coefficients

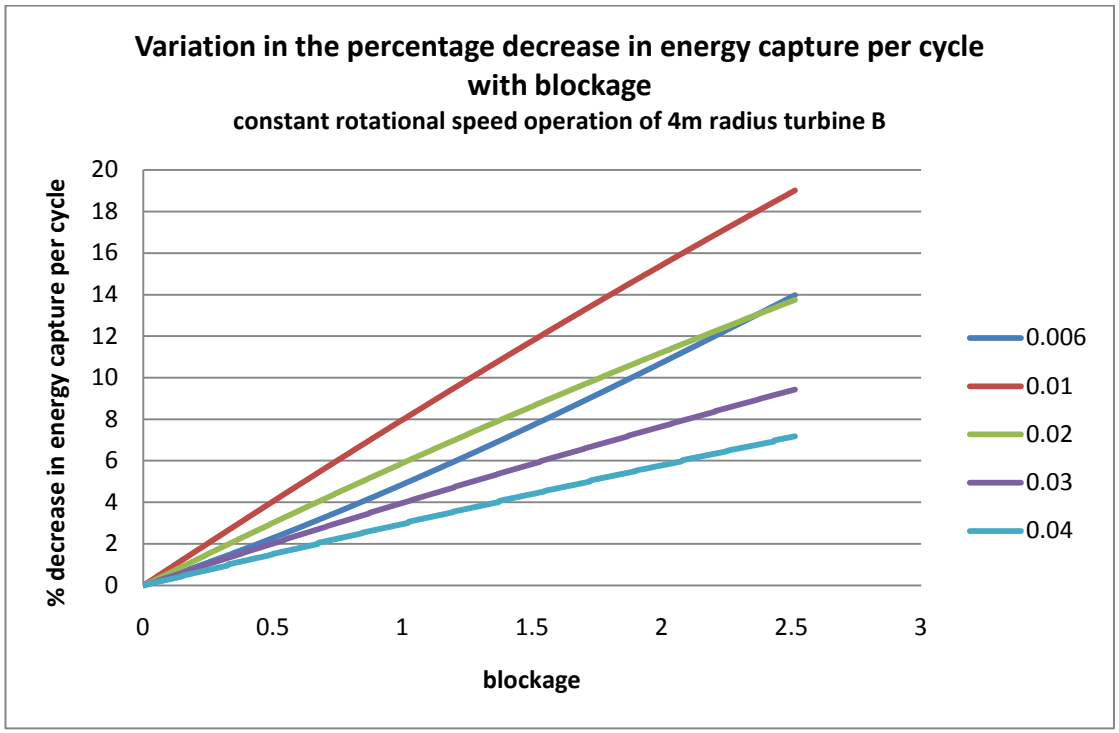

Figure 3.29- Variation in the percentage decrease in energy capture per cycle with blockage constant rotational speed operation of 4m radius turbine B

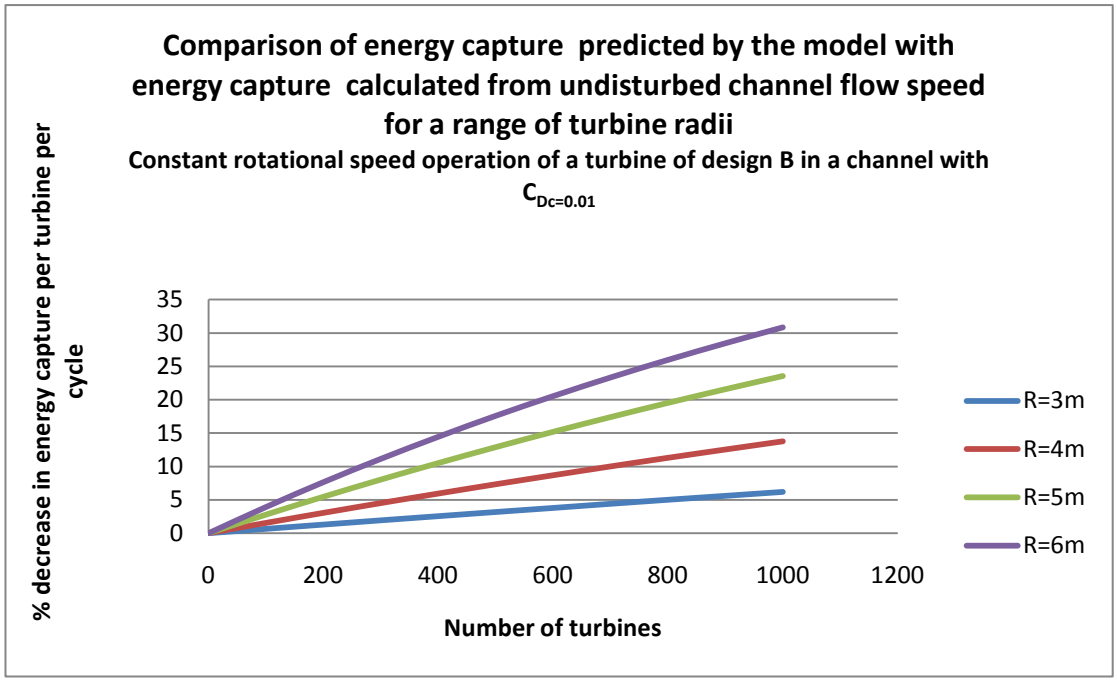

Figure 3.30- Comparison of energy capture predicted by the model with energy capture calculated using the undisturbed channel flow speeds for the constant tip speed ratio operation turbine of design A in a channel with $C_{Dc}=0.01$

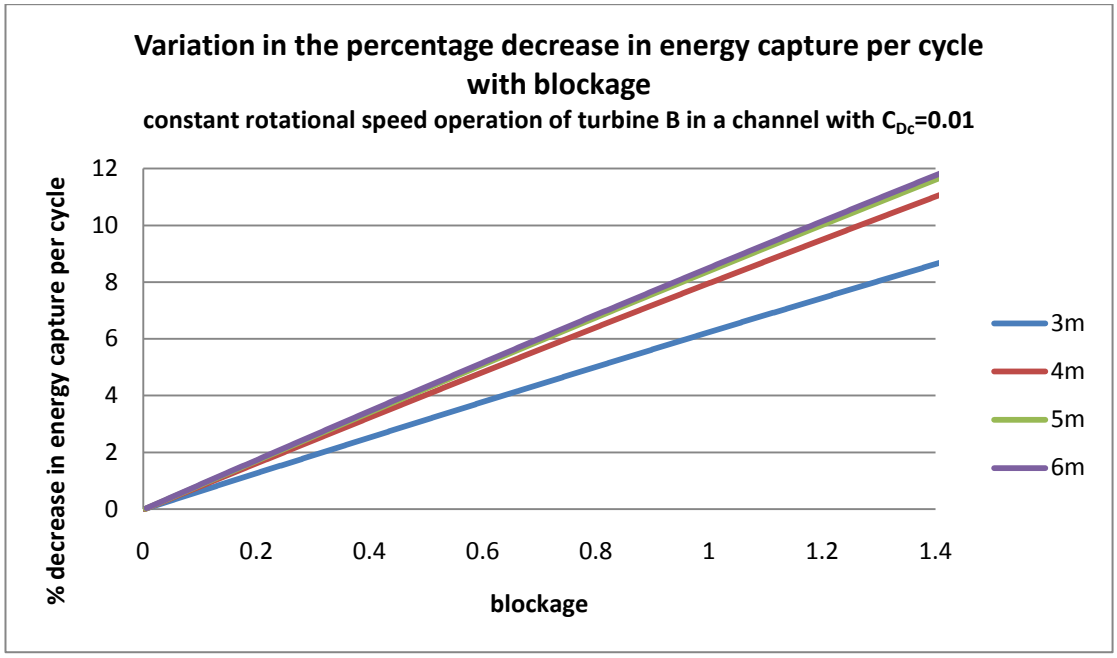

Figure 3. 31- Variation in the percentage decrease in energy capture per cycle with blockage for the constant rotational speed operation of turbine B in a channel with $C_{Dc}=0.01$

Table 3.9 gives the percentage decrease in energy capture over a 12 hour cycle for 1000 turbines of all diameters and both designs and modes of operation for a range of channel drag coefficients. The percentage decrease in energy capture is less for the constant rotational speed operation of the turbines than it is for the constant tip speed ratio operation. This can be explained by considering Figure 2.15 and Figure 2.16 of Chapter 2. For constant rotational speed operation there is a peak in the power generated whereas for constant tip speed ratio operation the power increases with the cube flow velocity. Whilst reducing the peak flow speed increases the time spent below the cut in speed, for a turbine operated at constant rotational speed it can also increase the time spent at flow speeds near the peak of the power curve. Thus the extent of the reduction in power for a turbine operated at constant rotational speed will depend on how well the performance of the turbine has been optimised for the undisturbed flow speeds at the site.

Table 3.9- Percentage decrease in energy capture over 12 hour tidal cycle for 1000 turbines

Channel drag coefficient	Turbine radius (m)	Constant tip speed ratio operation		Constant rotational speed operation	
		Turbine A	Turbine B	Turbine A	Turbine B
		% decrease in energy capture over 12 hour tidal cycle for 1000 turbines			
0.006	3	16.9	16.8	6.9	0.0
	4	27.0	29.7	12.9	4.2
	5	36.8	41.0	21.8	13.8
	6	46.2	50.7	31.7	26.8
0.01	3	12.3	12.0	9.1	7.5
	4	19.8	22.0	15.0	16.8
	5	27.8	31.4	23.1	26.5
	6	36.1	69.3	32.0	37.0
0.02	3	7.0	6.7	12.1	6.2
	4	11.6	13.0	13.6	13.8
	5	16.8	19.2	19.6	23.5
	6	22.7	25.8	25.2	30.8
0.03	3	5.2	4.9	38.6	4.4
	4	8.7	9.8	12.1	9.5
	5	12.7	14.7	17.4	19.3
	6	17.5	20.0	19.7	22.5
0.04	3	3.8	3.5		3.2
	4	6.3	7.0	10.6	7.0
	5	9.2	10.5	15.2	16.2
	6	12.6	43.9	15.1	15.9

3.5.2 Case Study: Sound of Islay

The sound of Islay is the channel between the islands of Islay and Jura which lie off the West coast of Scotland (Figure 3.32). This area is an ideal

region for initial commercial tidal stream power development as it has an energetic tidal stream resource and it is also closer to regions of demand than much of Scotland's tidal stream resource.

Figure 3.32 - Sound of Islay

The extended model has been applied to the Sound of Islay in order to investigate whether the effects of energy extraction on the flow in the channel will have a noticeable effect on the performance of a farm of turbines installed in the channel. In order to apply the extended model to the sound of Islay, information on the channel geometry, head difference across the channel and channel drag coefficient is needed.

3.5.2.1 Channel geometry

In order to calculate the constants c_1, c_2 and c_3, the cross sectional area of the channel needs to be found at a number of sections along the length of the channel. The Admiralty chart of the Sound of Islay was used to generate channel profiles at a number of sections from Rubha a' Mhail (north end of channel) to Mc Arthur's Head (south end of channel). When generating profiles they should ideally be perpendicular to the shoreline on both sides of the channel. For the Sound of Islay in most locations this is approximately the East-West direction. For the final four sections it was felt that East-West lines were not sufficiently close to being perpendicular to the shorelines on the sides of the channels. Instead these sections were

drawn so as to be perpendicular to the shoreline on both sides of the channel. The positions of the sections are shown in Figure 3.33.

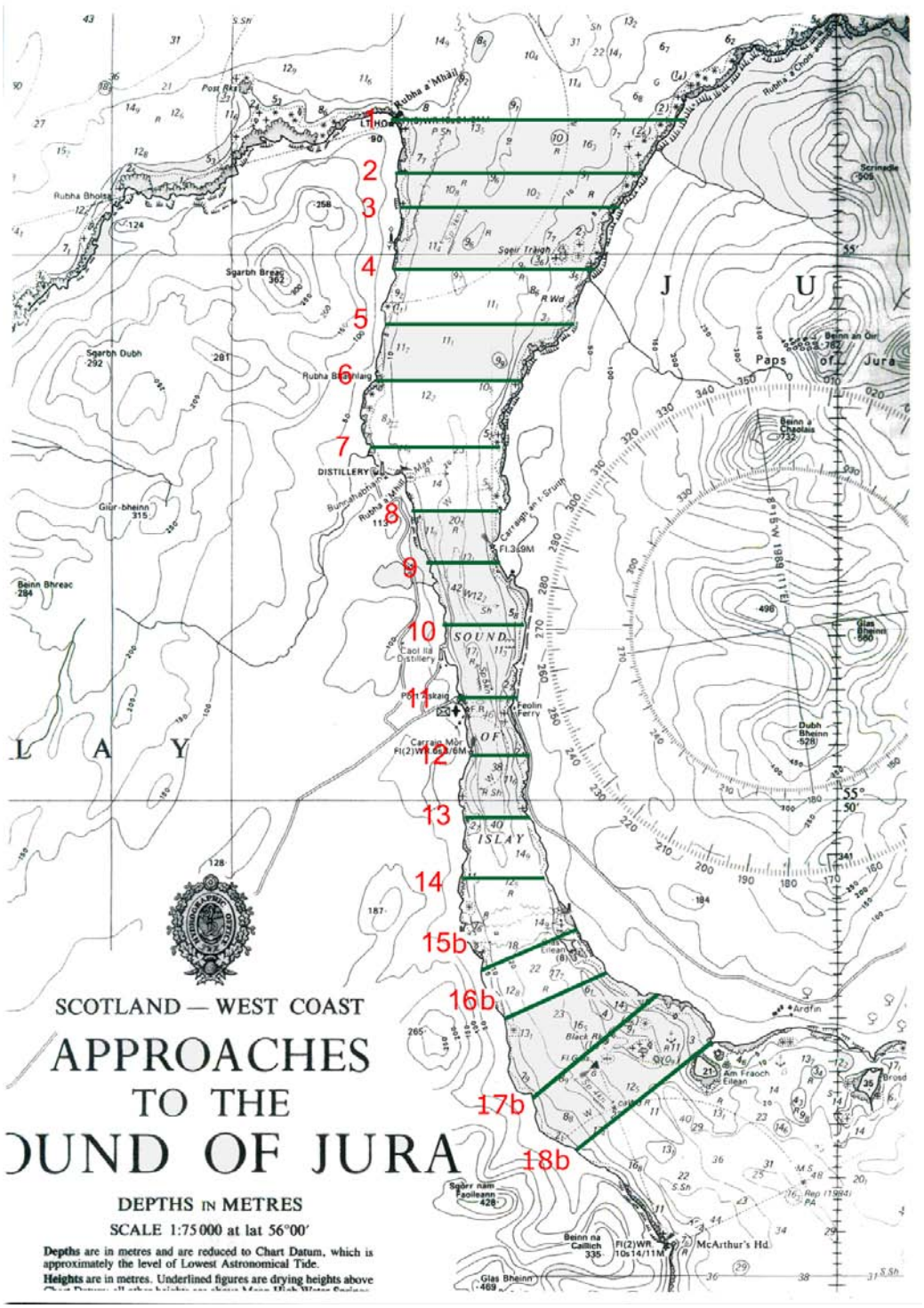

Figure 3.33- Positions of sections taken across Sound of Islay

A total of 18 Sections were used. These were mainly spaced at 1030m intervals. At each section the distance from the shoreline to the point at which each depth contour and spot depth crossed the section were

measured. The resulting points were plotted in a drawing program and the area of the resulting shape calculated. The average depth of the channel at each section was calculated by dividing the area by the width of the section. The position of Section 18b was selected to ensure the ends of the channel had roughly equal cross sectional areas. This was necessary because the model assumes that the cross sectional areas of the entrance and exit of the channel are equal. The distance to the next section, cross sectional area and width of each section is given in Table 3.10.

Table 3.10- Section spacings, areas and widths

section	Δx [m]	A [m^2]	w [m]
1	1030	44058	4837.5
2	550	36040	4112.5
3	1030	35099	3550
4	1030	25300	3325
5	1030	26148	3025
6	1030	27185	2562.5
7	1030	25716	2175
8	1030	18656	1425
9	1030	19531	1225
10	1030	23813	1337.5
11	1030	21685	900
12	1030	24031	1025
13	1030	21380	1175
14	1150	24138	1712.5
15b	1030	23875	1750
16b	1030	27301	1937.5
17b	1325	37350	2750
18b		40286	2950

Using the values in Table 3.10 and equations 39-41, values for c_1, c_2 and c_3/C_Dwere calculated. c_1 was found to be 0.67975, c_2 was found to be 4.8591×10^{11} and c_3/C_D was found to be 26.974.

3.5.2.2 Head difference between ends of channel

Total tide was used to find the water level at Rubha a' Mhail and Port Askaig. The data for these locations is calculated from water levels at Oban. High and low water levels over a period of two months were used to find the spring and neap high water levels and the average water level. The spring head difference was estimated to be 1.42m.

3.5.2.3 Channel drag coefficient

In order to apply the extended model to the sound of Islay, a value for the average drag coefficient is needed. This will be found from the peak volume flow rate of the channel. In the absence of more accurate data, the peak volume flow rate will be estimated from peak spring current speeds which are given for a number of locations on the chart of the sound of Islay.

The velocities given on the chart are surface current velocities. Due to frictional effects, the flow speed in the channel decreases as the side walls and bed are approached. If the peak volume flow rate is to be estimated from the surface current velocities, a relationship between the average velocity in a channel section and the peak surface velocity of the section is needed.

The vertical variation of flow speed is typically described using a power law relationship(100). There is some uncertainty as to the form of the power law relationship and both $1/10^{th}$ (100) and $1/7^{th}$ (101) power law relationships have been used. The exact form of the power law relationship will depend on the seabed roughness and so will vary from site to site. Since there is no data available describing the vertical variation of current velocity for the Sound of Islay, a $1/7^{th}$ power law

relationship has been selected. The 1/7th power law was selected as it has been found to approximate the velocity variation in some studies (101) and is also used for some wind farm sites.

The 1/7th power law relationship is given by:

$$u_c(y) = u_{c0}\left(\frac{y}{y_0}\right)^{\frac{1}{7}}$$

Equation 47

Where:

$u_c(y)$ is the velocity at a depth y

u_{c0} is the reference velocity at the reference depth y_0

The depth averaged velocity is given by:

$$\overline{u_{dc}} = \frac{\int_0^h u_c\, dy}{\int_0^h dy}$$

Equation 48

Where:

$\overline{u_{dc}}$ is the depth averaged velocity

h is the depth of the channel

Substituting Equation 47 into Equation 48 gives:

$$\overline{u_{dc}} = \frac{\int_0^h u_{cs}\left(\frac{y}{h}\right)^{\frac{1}{7}} dy}{\int_0^h dy} = \frac{u_{cs}\left(\frac{1}{h}\right)^{\frac{1}{7}}\int_0^h y^{\frac{1}{7}} dy}{\int_0^h dy} = \frac{u_{cs}\left(\frac{1}{h}\right)^{\frac{1}{7}}\int_0^h y^{\frac{1}{7}} dy}{\int_0^h dy} = \frac{u_{cs}\left(\frac{1}{h}\right)^{\frac{1}{7}}\left[\frac{y^{\frac{8}{7}}}{\frac{8}{7}}\right]_0^h}{[y]_0^h} = \frac{7}{8}u_{cs}$$

Equation 49

Where:

u_{cs} is the flow velocity at the surface of the channel

A Gaussian distribution has been chosen to represent the variation of flow speed across the channel. It was thought that, without data to define the variation in flow speed across the channel exactly, this distribution would provide an acceptable approximation of the flow variation. The Gaussian distribution is given by Equation 50 and is plotted in Figure 3.34.

$$f(x) = \frac{1}{\sqrt{2\pi}\sigma} e^{\frac{-(x-\mu)^2}{2\sigma^2}}$$

Equation 50

$f(x)$ is the probability density function of the Gaussian distribution

σ is the standard deviation

μ is the mean value of x

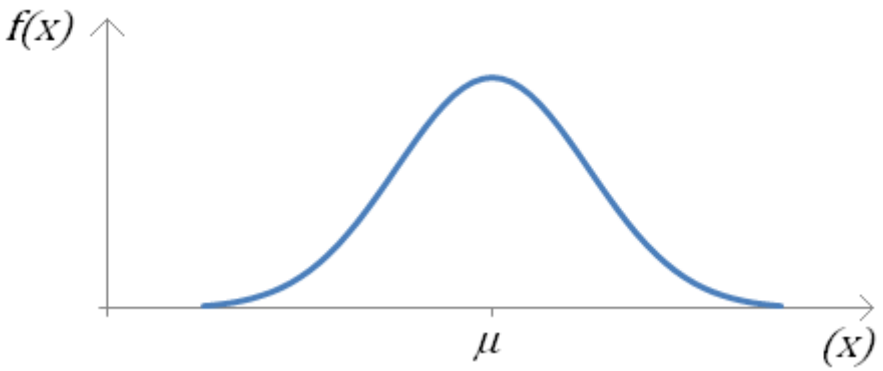

Figure 3.34- Gaussian distribution

It is being assumed that the Gaussian distribution represents the variation in velocity across the channel in the manner shown in Figure 3.35. In this μ is assumed to be equal to $\frac{w}{2}$. Since the probability that x lies in the interval between μ-3σ and μ-3σ is 0.9973, w has been approximated as 6σ.

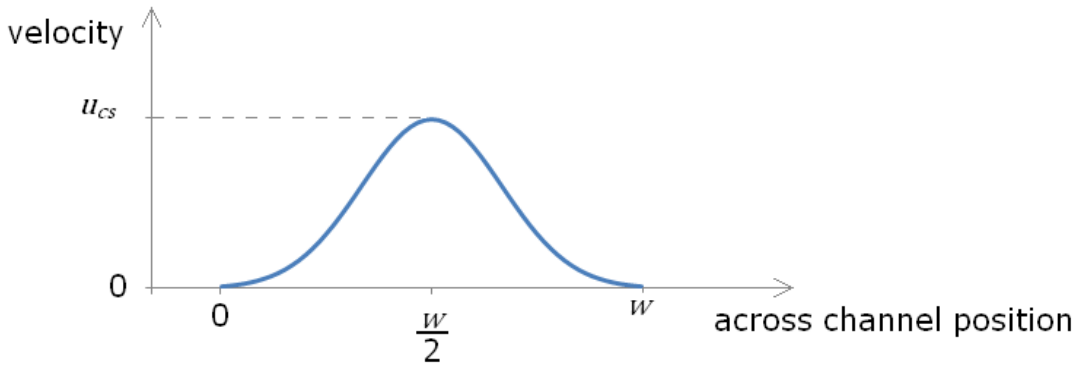

Figure 3.35- variation in flow speed across the channel

The average velocity is given by:

$$average\ velocity = \frac{\int_0^w \frac{1}{\sqrt{2\pi}\frac{w}{6}} e^{\frac{-\left(x-\frac{w}{2}\right)^2}{2\left(\frac{w}{6}\right)^2}} dx}{\int_0^w dx} = \frac{\frac{1}{2}\left[1 + erf\left(\frac{x-\frac{w}{2}}{\frac{w}{6}\sqrt{2\pi}}\right)\right]_0^w}{w} = \frac{1.819}{2w}$$

Equation 51

Since the maximum velocity is given by:

$$maximum\ velocity = \frac{6}{w\sqrt{2\pi}}$$

Equation 52

This allows a function for the average velocity in terms of the maximum velocity to be written:

$$\overline{u_{wc}} = 0.952 u_{cs}$$

Equation 53

Where:

$\overline{u_{wc}}$ is average velocity across the width of the channel

u_{cs} is the surface velocity in the centre of the channel

This allows the peak volume flow rate to be calculated for the sections for which surface current speeds have been stated on the admiralty chart. Surface current speeds are stated at 5 locations between the entrance and exit of the channel. New sections were defined at these points with the section perpendicular to the arrows indicating the direction of the flow and passing through the midpoint of these arrows. The sections have been labelled with the number of the closest section with the addition of a following letter. The depth and width averaged flow speeds and peak volume flow rates are given in Table 3.11.

Table 3.11- Depth and width averaged flow speeds and peak volume flow rates for Sound of Islay

Section	flow speed	width	average depth	cross sectional area	depth averaged flow speed	Depth and width averaged flow speed	Depth and width averaged $\dot{V}$
3b	1.54	3300	8.19	27011	1.35	1.29	34725
7b	2.31	1650	12.61	20812	2.03	1.93	40134
11b	2.57	913	24.21	22093	2.25	2.14	47338
15c	2.57	1713	13.62	23326	2.25	2.14	49980
17c	2.06	3050	11.83	36067	1.80	1.71	61823

Using the values from Table 3.11, the maximum, minimum and average peak volume flow rates were calculated. Table 3.12 gives the maximum, minimum and average estimates of the peak volume flow rate.

Table 3.12- maximum, minimum and average estimates of the peak volume flow rate

	Peak volume flow rate
Maximum	0.002666
Average	0.005075
Minimum	0.009605

The variation of peak volume flow rate with average drag coefficient for the Sound of Islay is plotted in Figure 3.36. Also plotted in Figure 3.36 are the maximum, minimum and average estimates of the peak volume flow rate for the Sound of Islay. This allows the average drag coefficient of the channel to be found for each estimate of peak volume flow rate. Table 3.13 gives the drag coefficient for each estimate of peak volume flow rate. All three estimates of drag coefficient will be used in the subsequent modelling work. It is thought that the value from the minimum and maximum peak volume flow rate will provide the upper and lower bounds within which the actual drag coefficient of the channel is expected to fall. The drag coefficient calculated from the average estimate of the peak

volume flow rate is thought to be closer to the actual value than the upper and lower bounds.

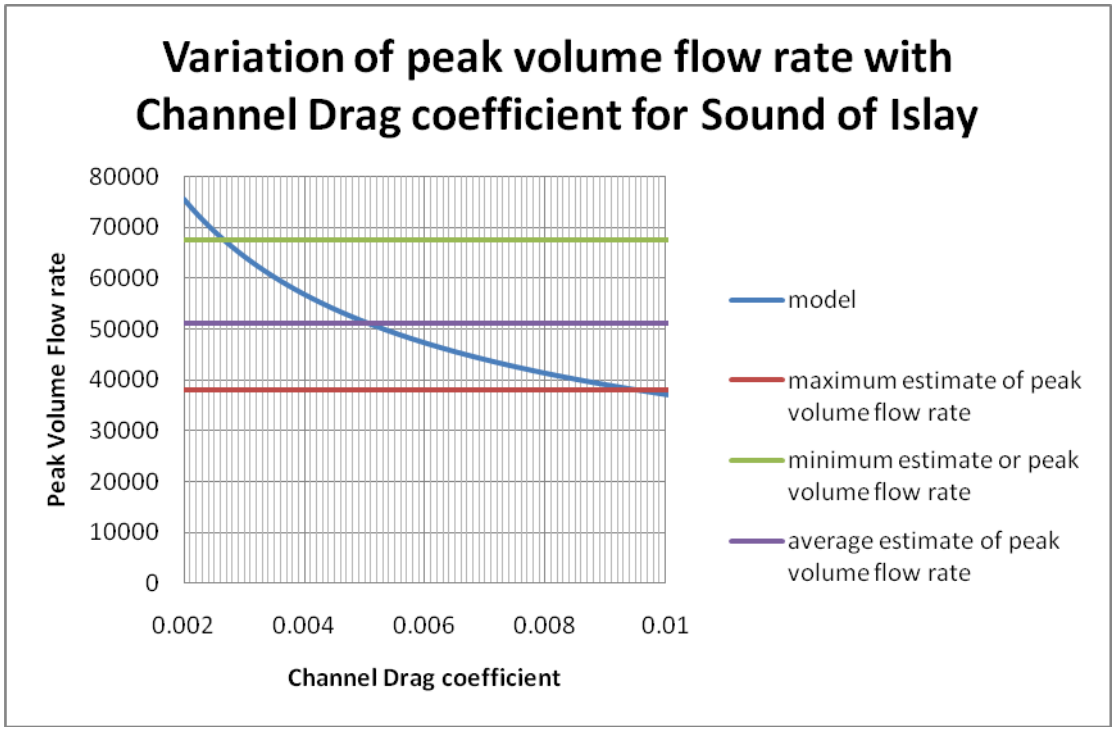

Figure 3.36-variation of peak volume flow rate with average channel drag coefficient for the Sound of Islay

Table 3.13- channel drag coefficient for the maximum, average and minimum estimates of the peak volume flow rate for the Sound of Islay

Estimate of peak volume flow rate	Channel drag Coefficient
Maximum	0.002666
Average	0.005075
Minimum	0.009605

3.5.2.4 Modelling the effects of energy extraction on the available resource in the Sound of Islay

The effects of energy extraction on the available tidal current resource in the Sound of Islay have been modelled for a number of different

scenarios. Since the cross section of the channel is not uniform, the power generated by the turbines and their effect on the flow will depend on their positioning as well as the number installed. The effects of installing turbines in a single section of the channel were modelled and compared for the different sections. Modelling was also carried out to establish the effects of installing turbines in multiple sections of the channel.

Turbines in narrowest section

Initially the effect of installing turbines in the narrowest section of the channel was investigated. The narrowest section is section 11, which has a width of 900m and an average depth of 24m. Table 3.14 gives the maximum number of turbines of each radius that could be installed without the blockage exceeding 1. In reality the maximum number of turbines that could be installed in this section would be lower since horizontal axis turbines have circular swept areas which do not tessellate. In practice much lower levels of blockage would be needed as sufficient space needs to be left for the passage of vessels and marine wildlife.

Table 3.14- Maximum number of turbines of each diameter that could be installed in section 11

Radius (m)	Maximum number of turbines
3	766
4	431
5	276
6	191

Figure 3.37, Figure 3.38, Figure 3.39 and Figure 3.40 show how increasing the number of turbines installed in section 11 affects the percentage decrease in the peak volume flow rate. For the designs and modes of operation of turbine considered, the maximum percentage decrease in peak volume flow rate was below 10%, even when the swept area of the turbines was equal to the cross sectional area of the channel. This suggests that very large number of turbines could be installed in the

Sound of Islay before they had a significant impact on the site. However, without extensive monitoring data, it will not be possible to say whether reductions in peak volume flow rate of this magnitude will have significant effects on physical processes (such as sediment transfer) or on the local ecosystem.

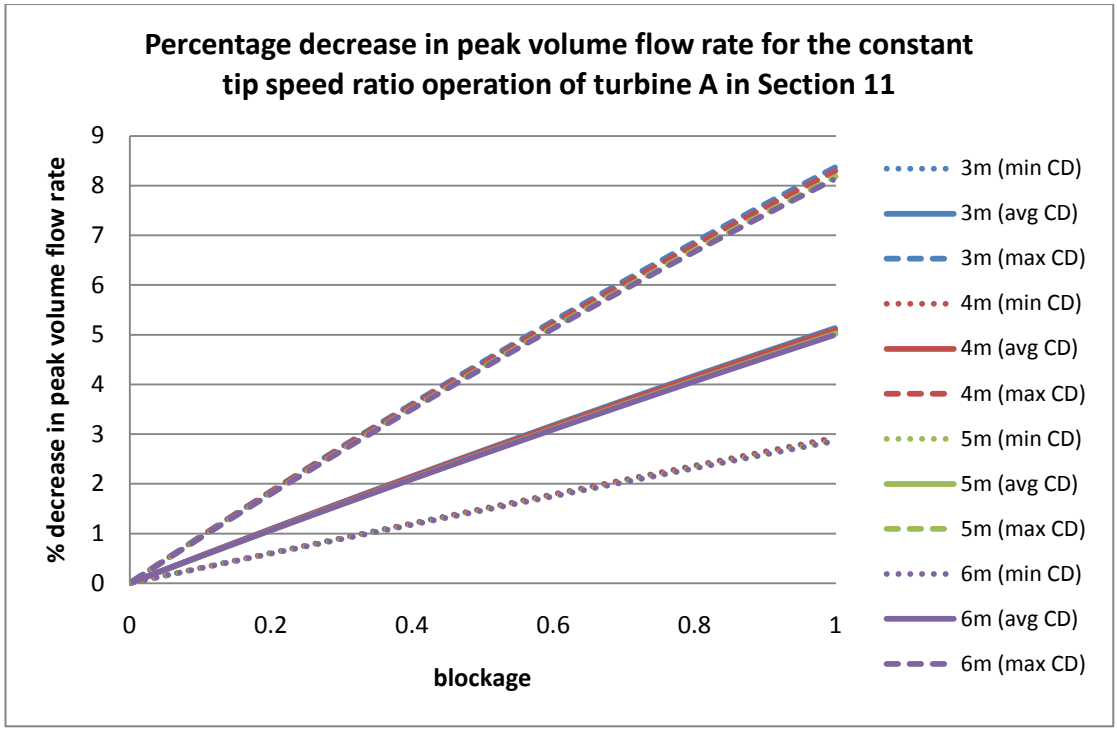

Figure 3.37- Percentage decrease in peak volume flow rate for the constant tip speed ratio operation of turbine A in section 11

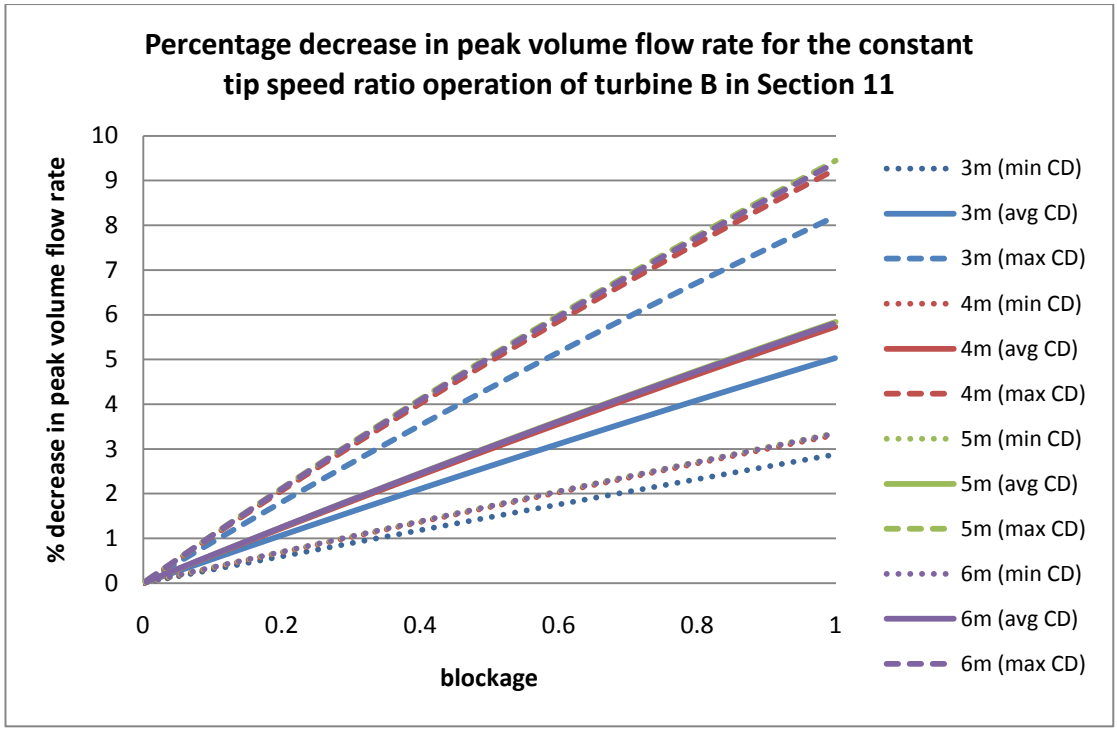

Figure 3.38- Percentage decrease in peak volume flow rate for the constant tip speed ratio operation of turbine B in Section 11

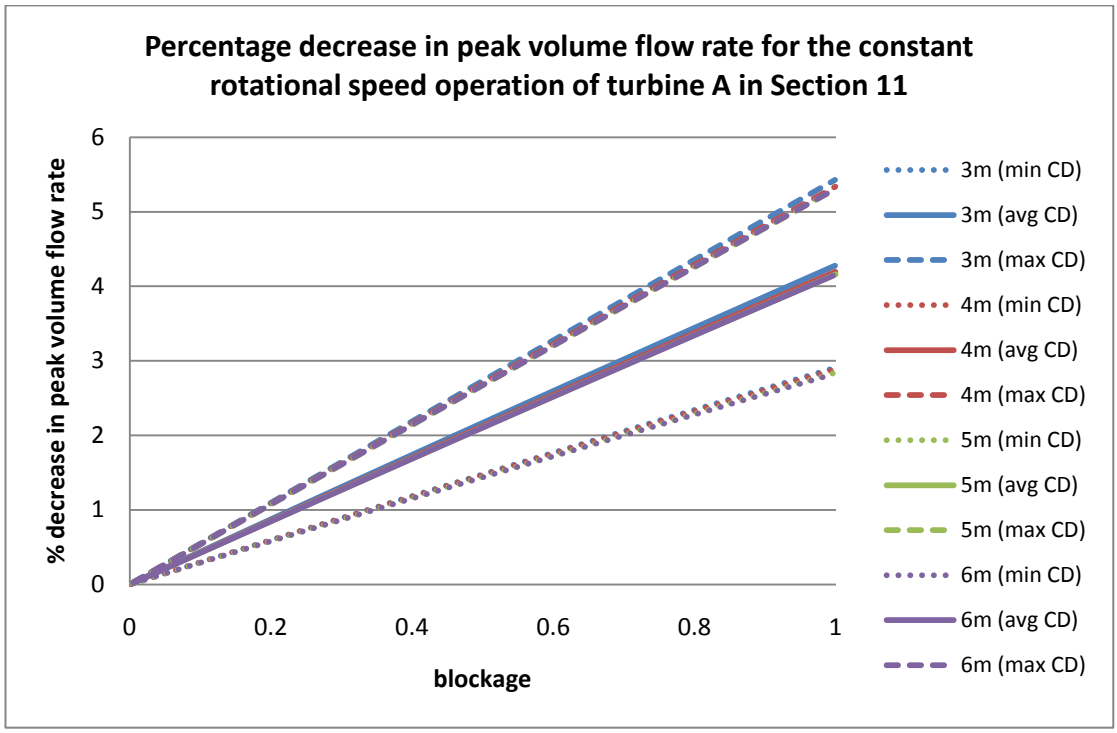

Figure 3.39- Percentage decrease in peak volume flow rate for the constant rotational speed operation of turbine A in section 11

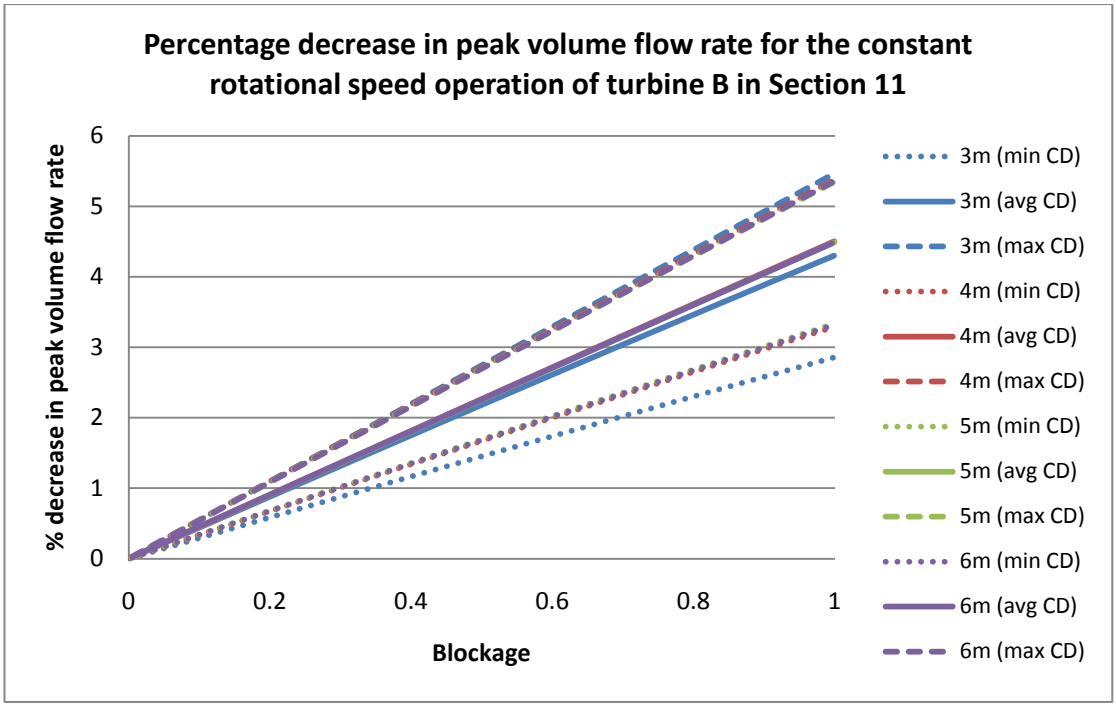

Figure 3.40- Percentage decrease in peak volume flow rate for the constant rotational speed operation of turbine B in Section 11

Figure 3.41, Figure 3.42, Figure 3.43 and Figure 3.44 show how increasing the number of turbines installed in section 11 affects the percentage decrease in the peak power generated per turbine. In the percentage decrease calculations the peak power per turbine is compared with the peak power generated by a single turbine installed in the channel. Whilst there is a significant decrease in the peak power generated per turbine for the constant rotational speed operation of turbines A and B, there is a much smaller or, in some cases no, decrease in peak power generated per turbine for the constant rotational speed operation of the turbines. This is due to the tuning of the turbines and highlights the need to ensure that the turbines are appropriately tuned to the flow conditions in the channel. If a turbine is appropriately tuned for the undisturbed flow conditions in the channel then reduction in the flow speeds in the channel caused by installing turbines in the channel will reduce the power generated by the turbine. It is, therefore, important that the effect of the turbines on the flow speeds is taken into account when tuning turbines for a particular channel.

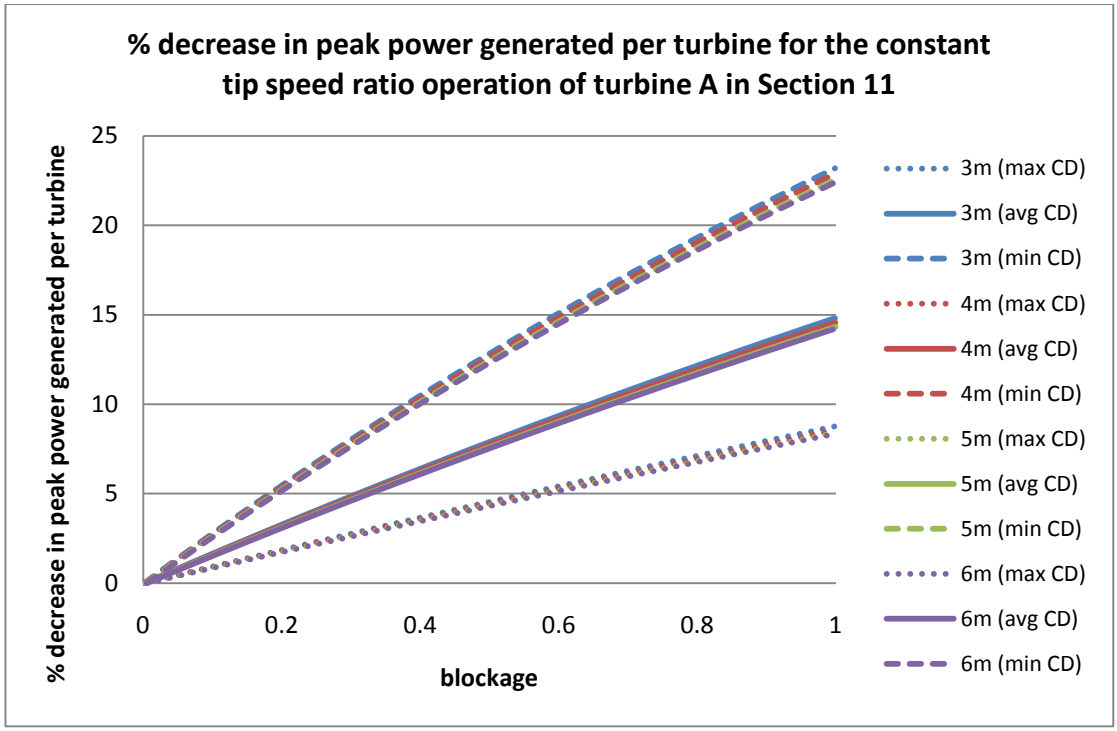

Figure 3.41- Percentage decrease in peak power generated per turbine for the constant tip speed ratio operation of turbine A in section 11

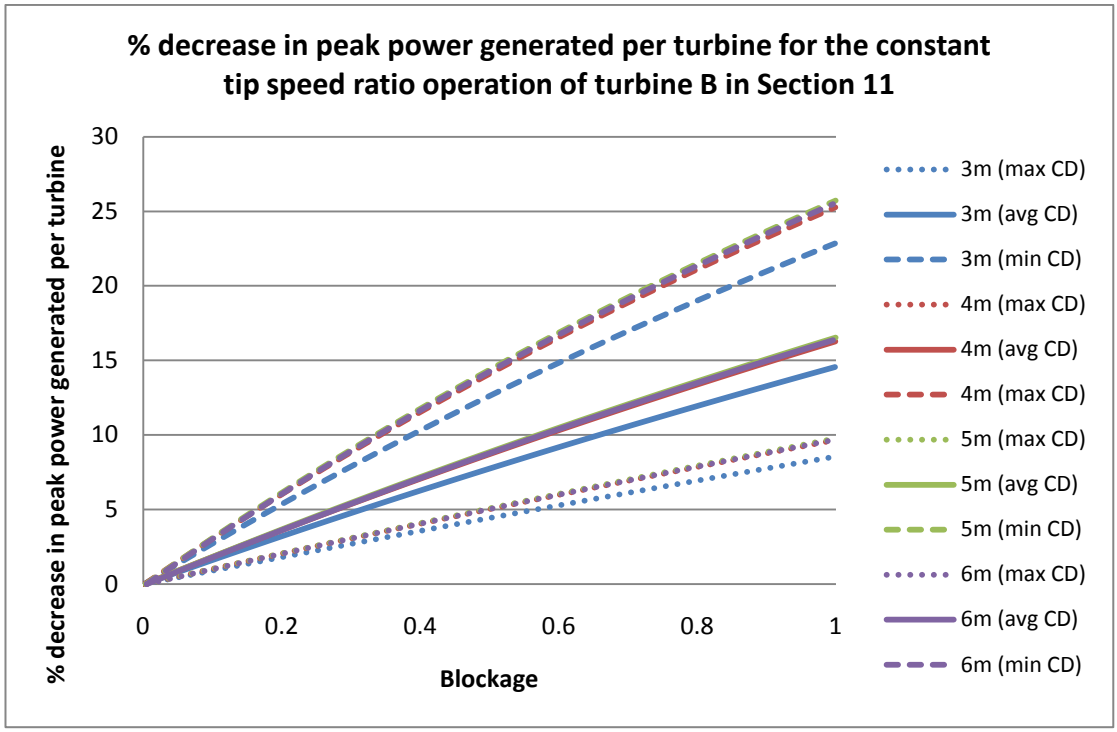

Figure 3.42- Percentage decrease in peak power generated per turbine for the constant tip speed ratio operation of turbine B in section 11

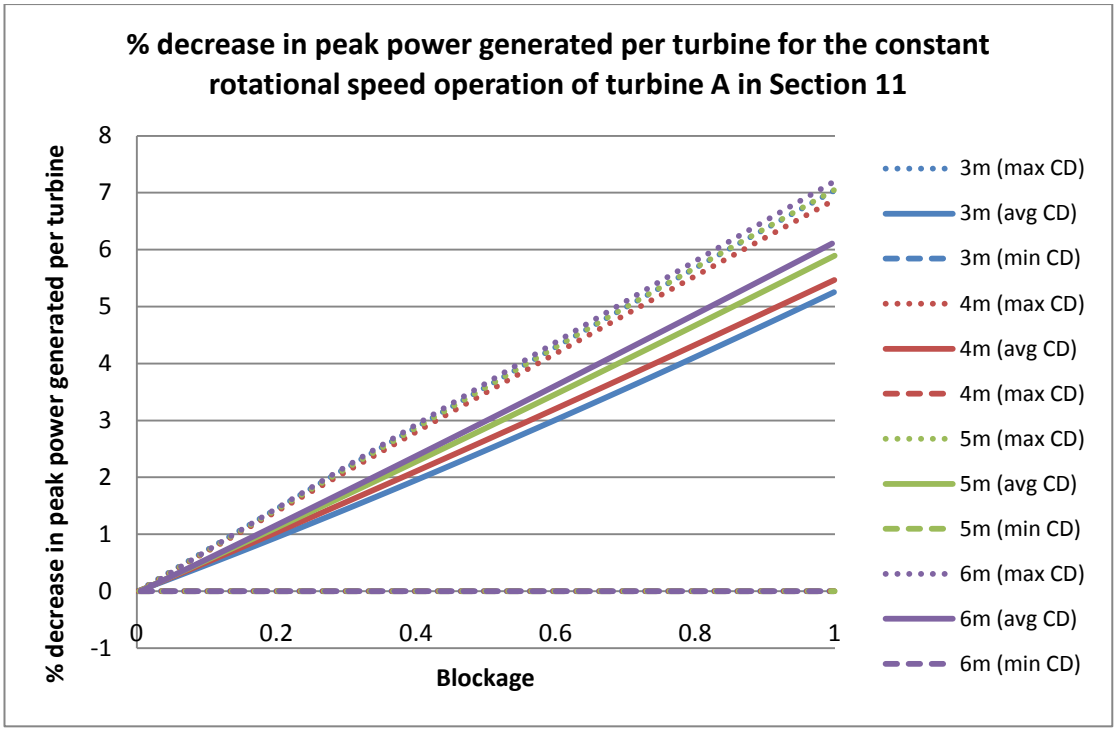

Figure 3.43- Percentage decrease in peak power generated per turbine for the constant rotational speed operation of turbine A in section 11

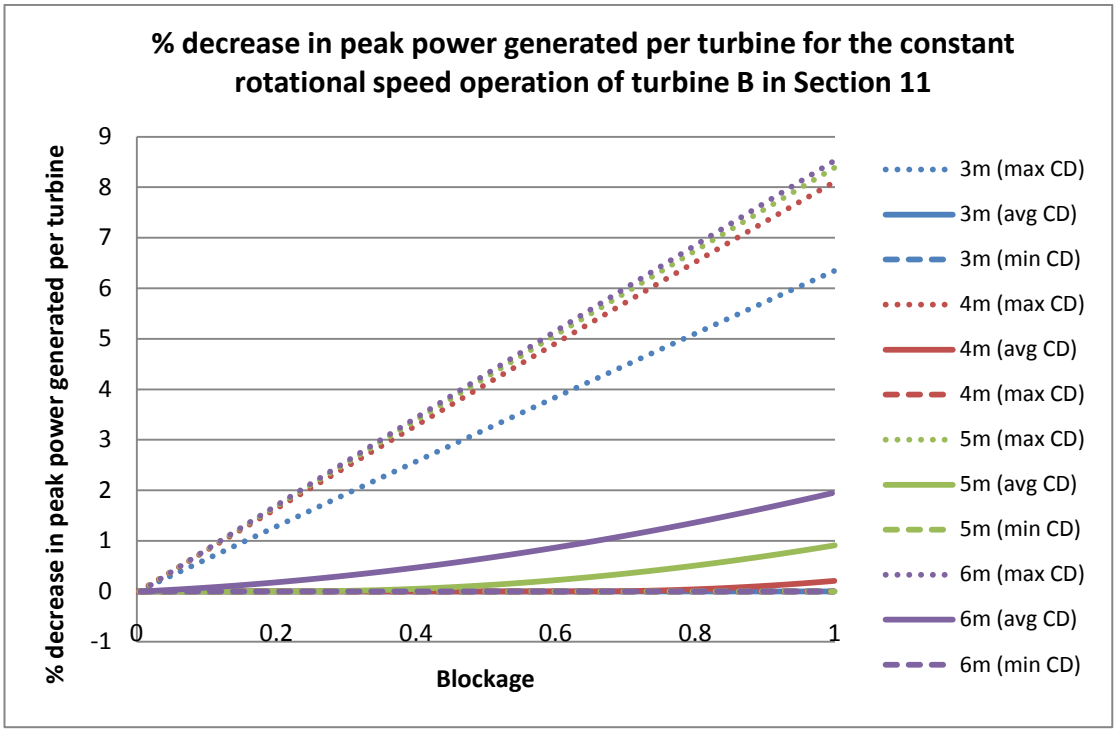

Figure 3.44- Percentage decrease in peak power generated per turbine for the constant rotational speed operation of turbine B in section 11

Figure 3.45, Figure 3.46, Figure 3.47 and Figure 3.48 show how increasing the number of turbines installed in section 11 affects the utilisation factor. It can be seen from these graphs that for the constant tip speed ratio operation of the turbines, increasing the number of turbines installed in the section actually results in a slight increase in the utilisation factor. This is because the reduction in peak volume flow rate, and hence peak power generated, has a greater effect on the utilisation factor than the reduction in average power generated caused by the increased time spent below the cut in speed of the turbine. For the constant rotational speed operation of the turbines, increasing the number of turbines typically results in a small reduction in the utilisation factor, except for when the maximum peak volume flow rate value of the channel drag coefficient is used. How well the turbines are tuned to the channel changes with changing flow conditions for the constant rotational speed operation of the turbines but does not change for the constant tip speed ratio of the turbines. This explains the different trends in the utilisation factor for the two modes of operation of the turbine. This again highlights the need to ensure that the turbines are appropriately tuned for the flow conditions in the channel.

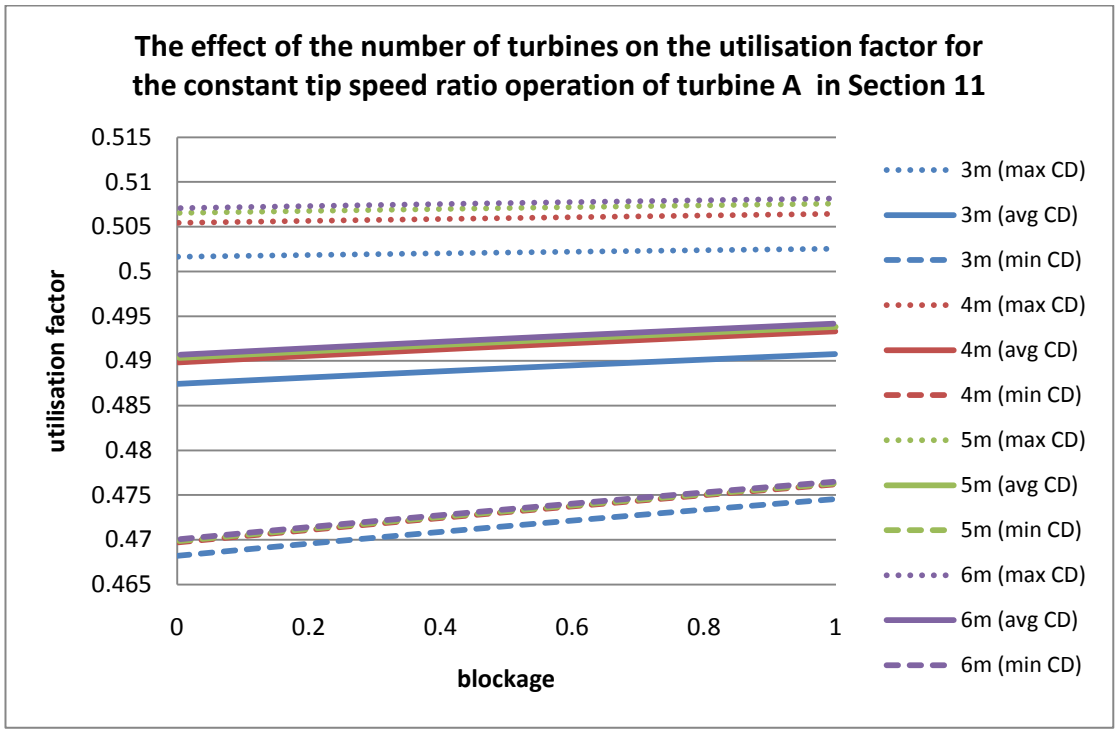

Figure 3.45- The effect of the number of turbines on the utilisation factor for the constant tip speed ratio operation of turbine A in section 11

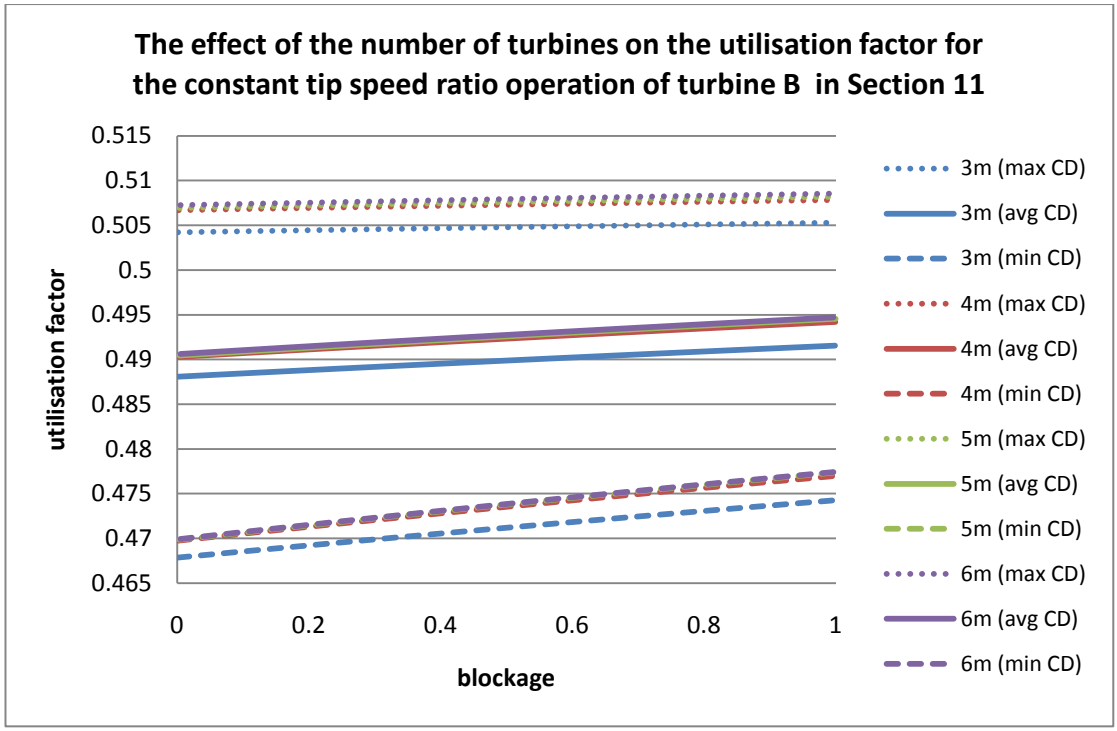

Figure 3.46- The effect of the number of turbines on the utilisation factor for the constant tip speed ratio operation of turbine B in section 11

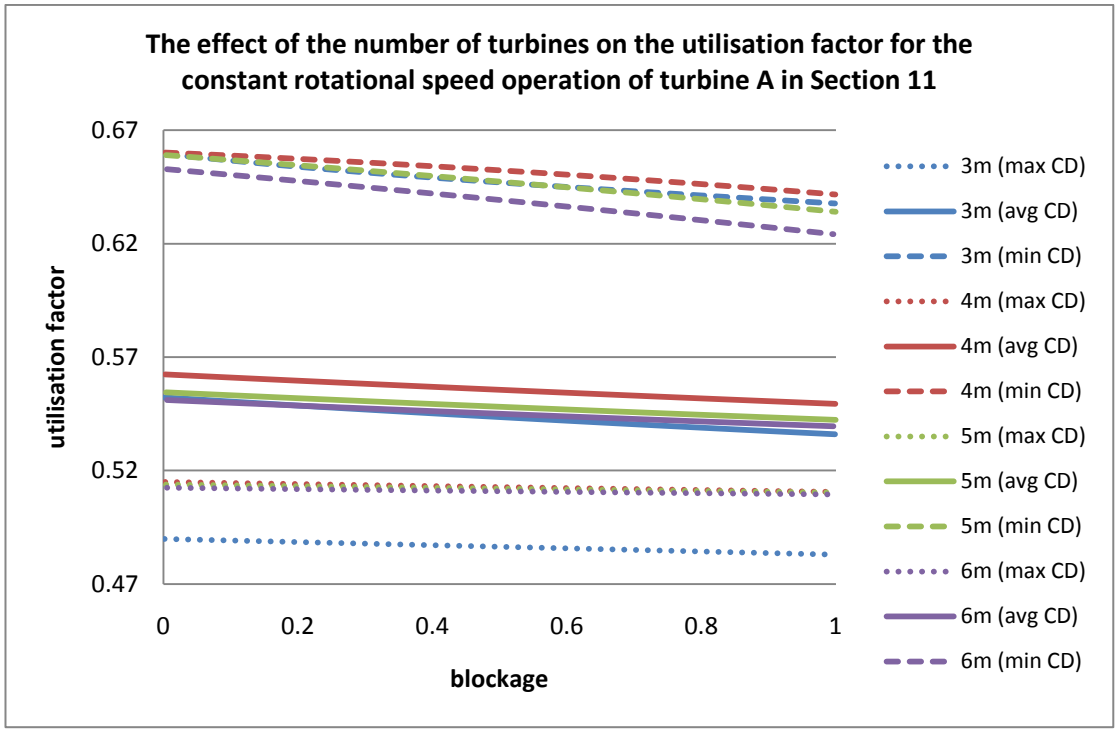

Figure 3.47- The effect of the number of turbines on the utilisation factor for the constant rotational speed operation of turbine A in section 11

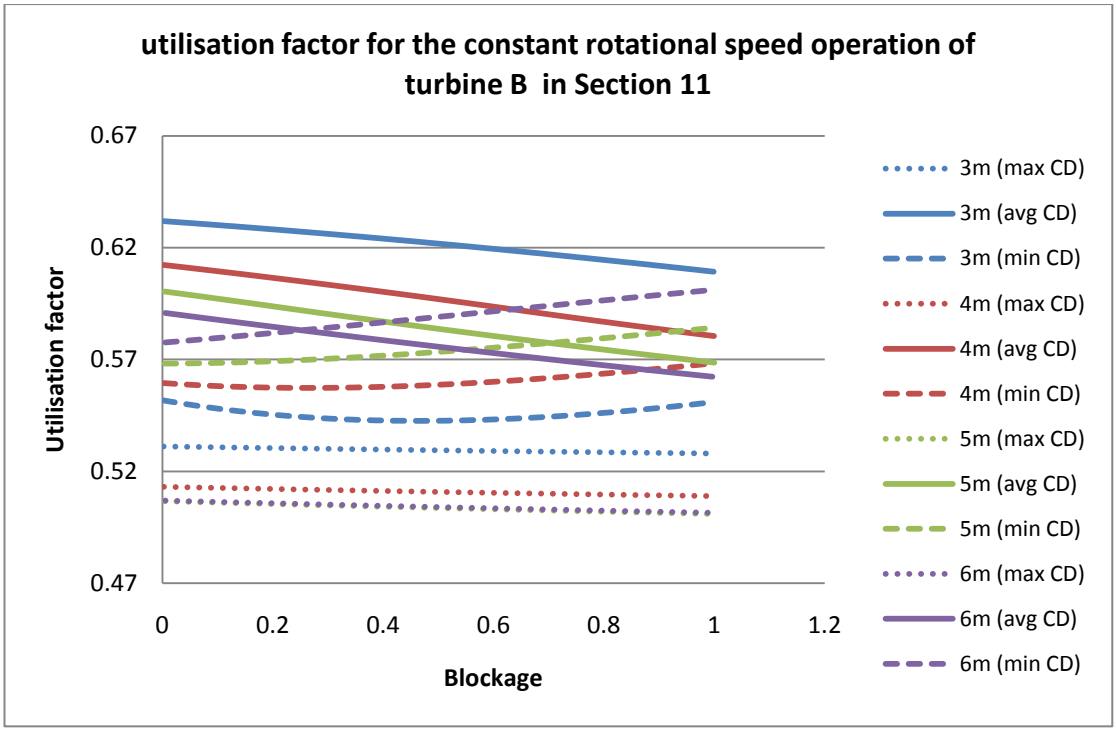

Figure 3.48- The effect of the number of turbines on the utilisation factor for the constant rotational speed operation of turbine B in section 11

The energy capture per tidal cycle of the different designs, radii and modes of operation of turbine was calculated using the flow speeds in the channel in its undisturbed state. This allows the effect of the reduction in the flow speeds in the channel, caused by extracting energy, on the amount of energy captured by the turbines to be investigated. The percentage decrease in energy capture per turbine per tidal cycle was calculated using:

$$\%\ decrease = \frac{(energy\ capture\ in\ undisturbed\ channel - energy\ capture)}{energy\ capture\ in\ undisturbed\ channel} \times 100$$

Equation 54

Figure 3.49, Figure 3.50, Figure 3.51 and Figure 3.52 show the effect of the number of turbines installed in section 11 of the channel on the percentage decrease in energy capture per turbine per tidal cycle. Figure 3.49 and Figure 3.50 show that there is a considerable decrease in energy capture per turbine per tidal cycle for the constant tip speed ratio

operation of the turbines for high values of blockage. For the constant rotational speed operation of the turbines the percentage decrease in energy capture is less than for the constant tip speed ratio operation. This is again due to the tuning of the turbines in this section. For the constant rotational speed operation of turbine B in the channel with the maximum peak volume flow rate drag coefficient (minimum value of C_{DC}) the energy capture is typically increases above the energy capture calculated from undisturbed channel.

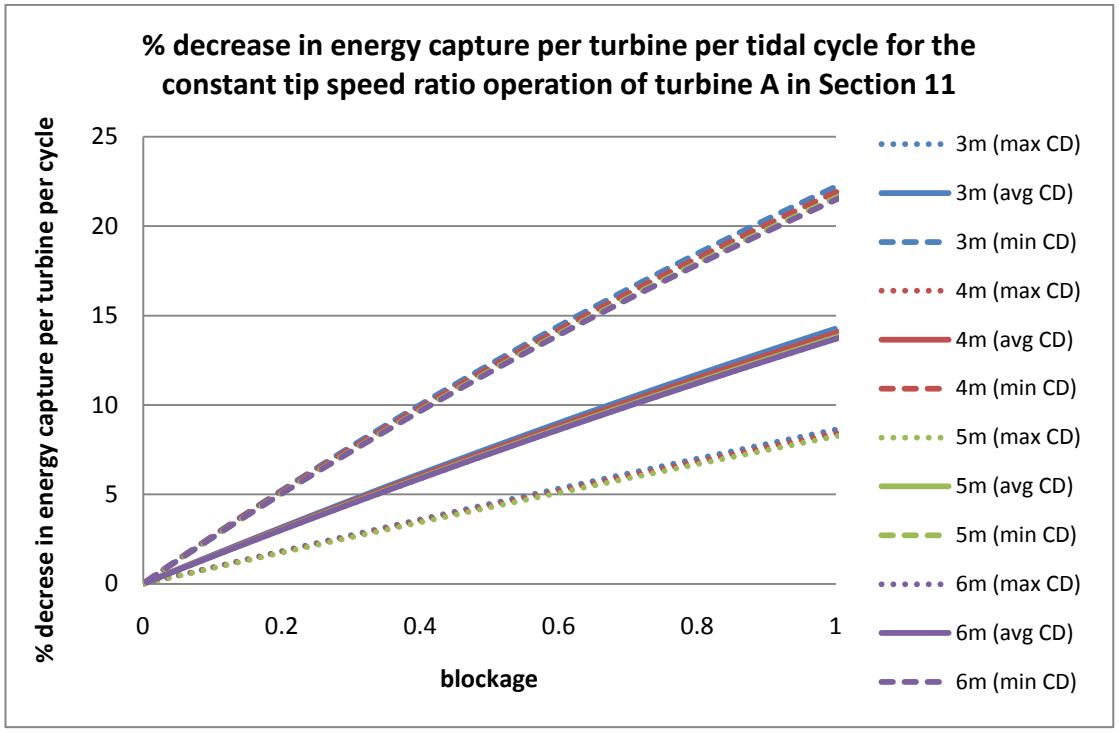

Figure 3.49- Effect of number of turbines on the percentage decrease in energy capture per turbine per tidal cycle for the constant tip speed ratio operation of turbine A in Section 11

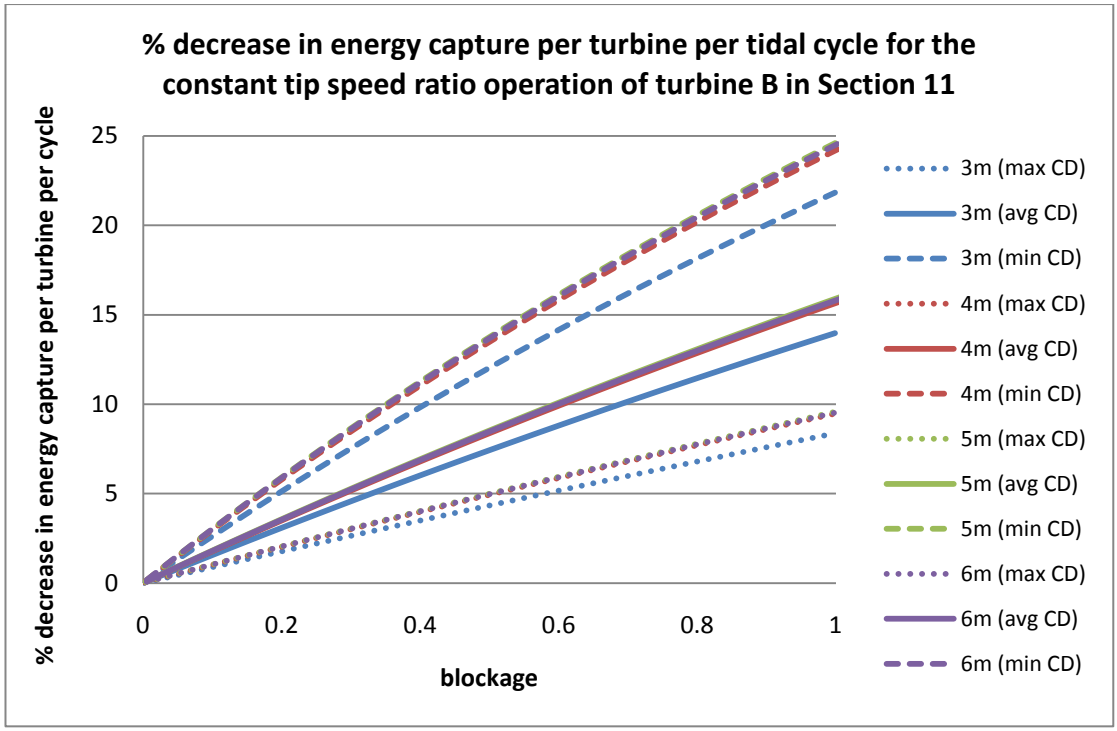

Figure 3.50-Effect of number of turbines on the percentage decrease in energy capture per turbine per tidal cycle for the constant tip speed ratio operation of turbine B in Section 11

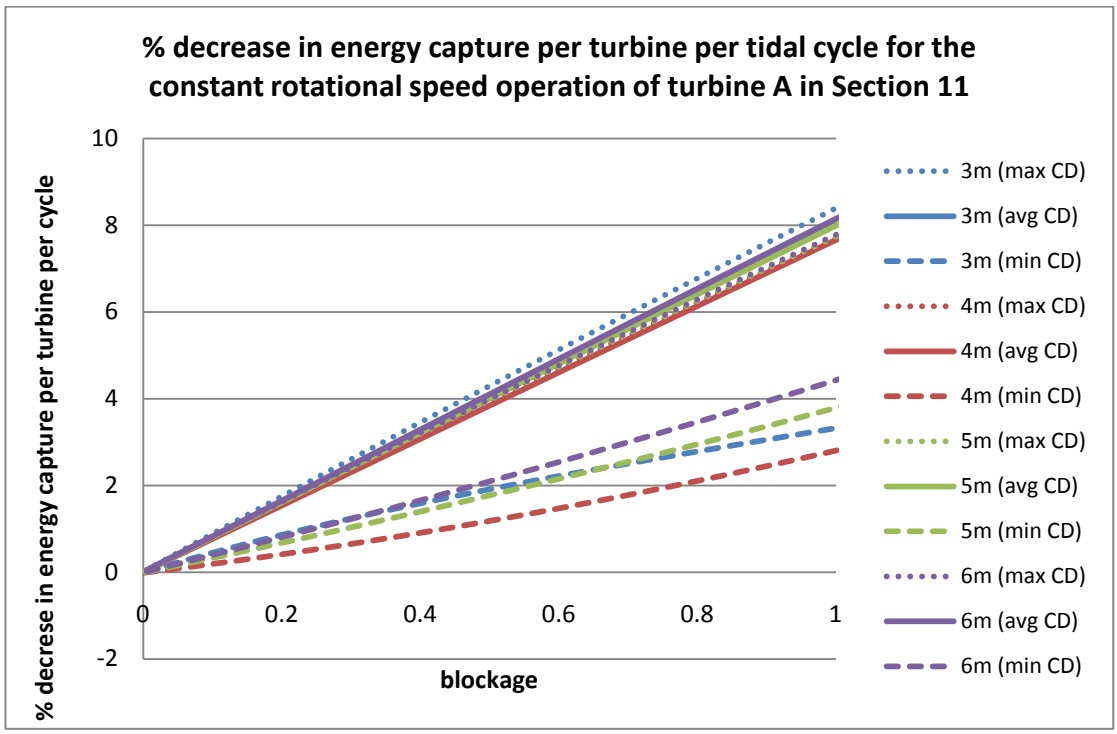

Figure 3.51- Effect of number of turbines on the percentage decrease in energy capture per turbine per tidal cycle for the constant rotational speed operation of turbine A in Section 11

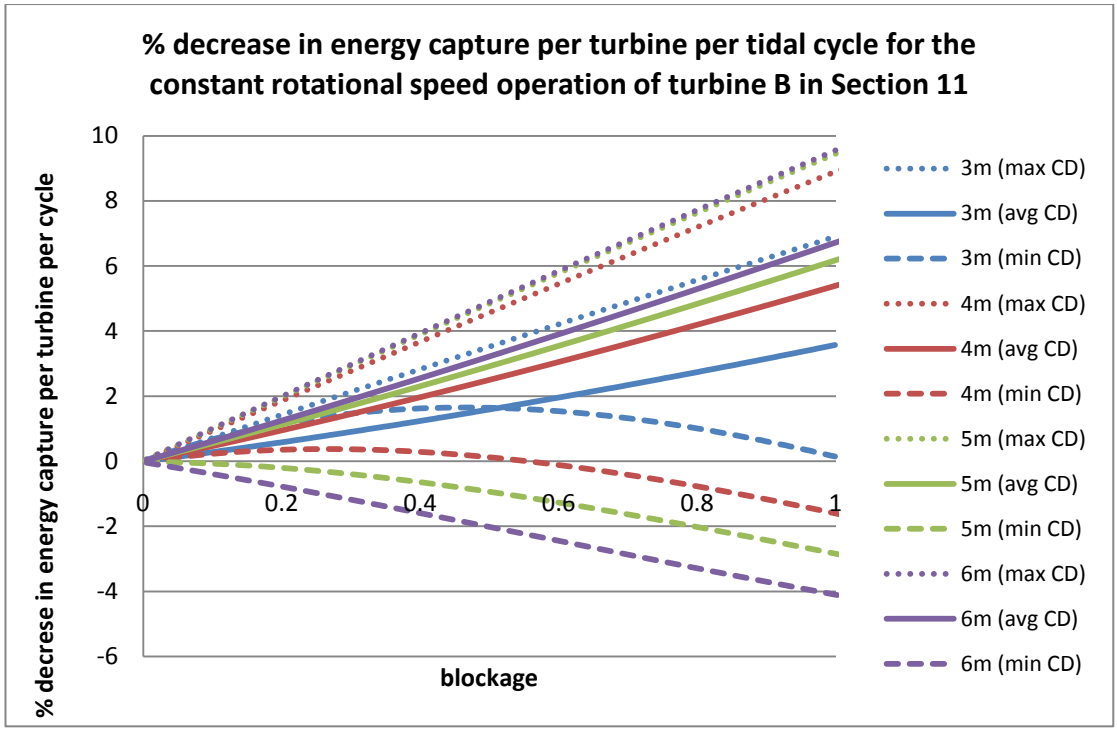

Figure 3.52-Effect of number of turbines on the percentage decrease in energy capture per turbine per tidal cycle for the constant rotational speed operation of turbine B in Section 11

From Figure 3.49, Figure 3.50, Figure 3.51 and Figure 3.52 it can be seen that, for section 11, whether the overestimation of energy capture is significant will depend on the number of turbines installed in the section and their design and mode of operation. For the constant tip speed operation of either design of turbine blockage of 0.5-0.6 or higher will result in at least a 5% decrease in the energy capture when compared with energy capture calculated from the undisturbed flow speeds in the channel. For the channel drag coefficient calculated from the average estimate of peak volume flow rate and the channel drag coefficient calculated from the maximum estimate of the peak volume flow rate a 5% decrease in energy capture is achieved at much blockage values of approximately 0.3 and 0.2 respectively.

Turbines in section with smallest area

Section 8 of the channel has the smallest area. The average depth of this section is only 13m, so section 11, the narrowest section, may be a more suitable site for installing tidal turbines. Table 3. 15 gives the maximum

number of turbines of each radius that could be installed in section 8 without the blockage exceeding 1. Once again it should be noted that it would not be possible to install this number of horizontal axis turbines in the section without the swept areas overlapping.

Table 3. 15- Maximum number of turbines of each diameter that could be installed in section 8

Radius (m)	Maximum number of turbines
3	659
4	371
5	237
6	164

Figure 3.53, Figure 3.54, Figure 3.55 and Figure 3.56 show how increasing the number of turbines installed in section 8 affects the percentage decrease in the peak volume flow rate. It can be seen from these figures that the percentage decreases in peak volume flow rate for section 8 show the same trends and are of similar magnitude to the percentage decreases in peak volume flow rate for section 11. Whether the percentage decrease in peak volume flow rate is greater in section 8 or section 11 depends on the turbine, mode of operation and the value taken for channel drag coefficient.

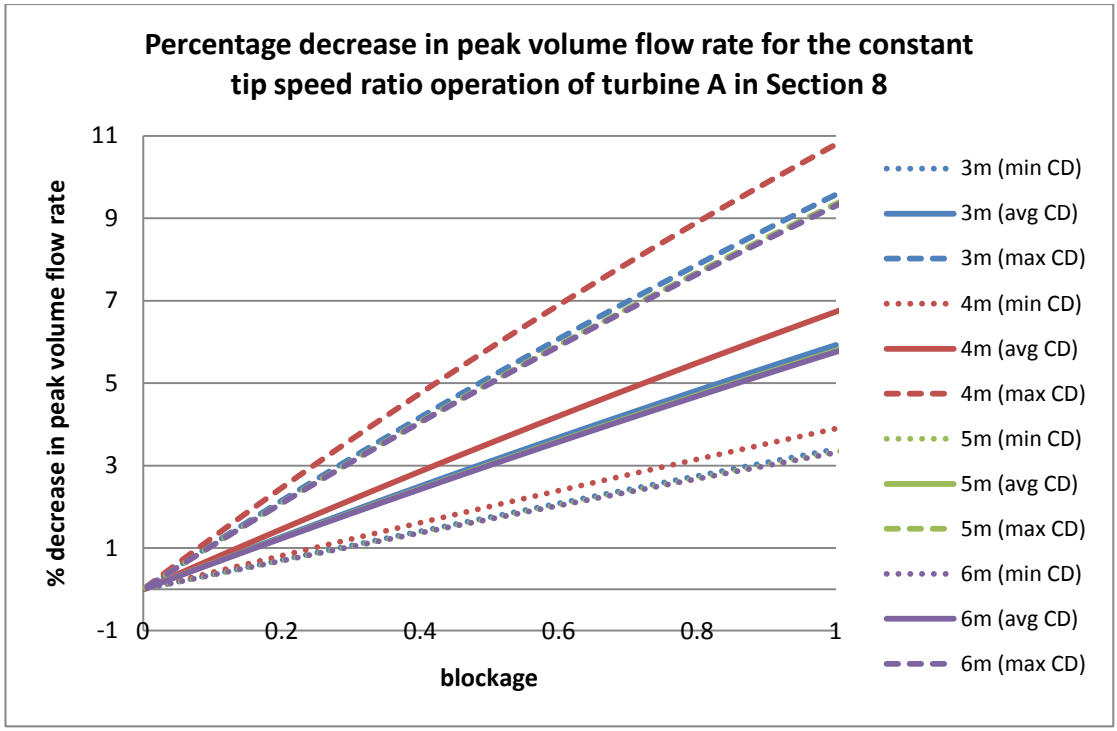

Figure 3.53- Percentage decrease in peak volume flow rate for the constant tip speed ratio operation of turbine A in section 8

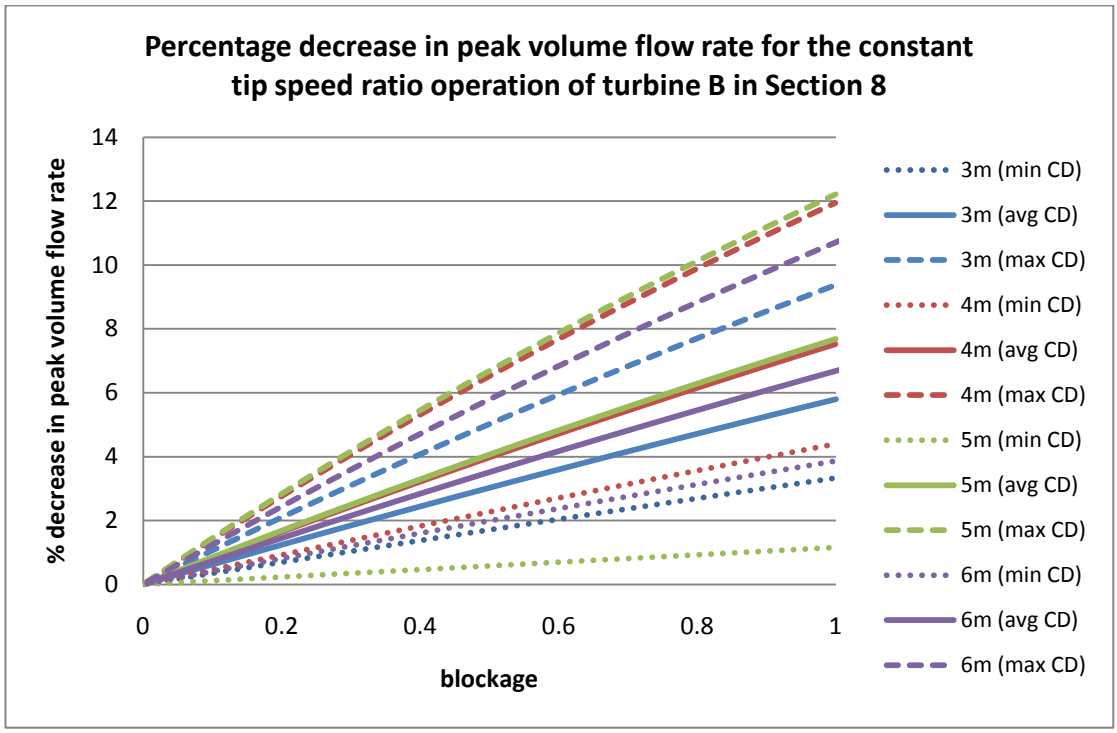

Figure 3.54- Percentage decrease in peak volume flow rate for the constant tip speed ratio operation of turbine B in section 8

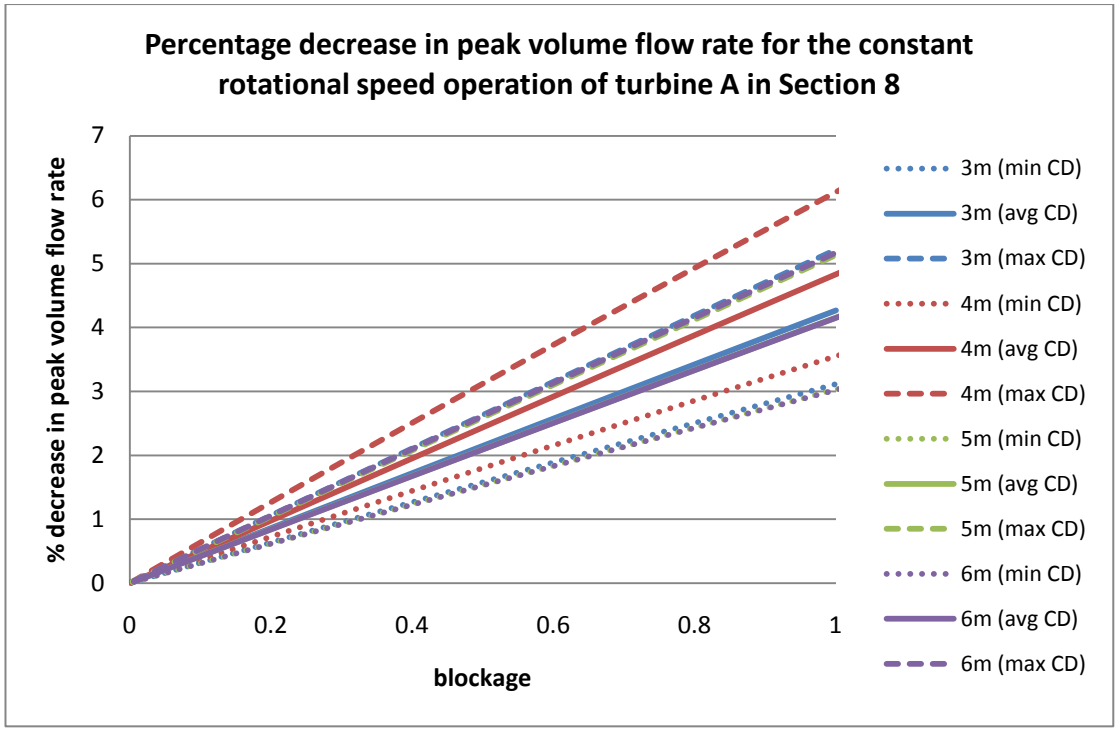

Figure 3.55- Percentage decrease in peak volume flow rate for the constant rotational speed operation of turbine A in section 8

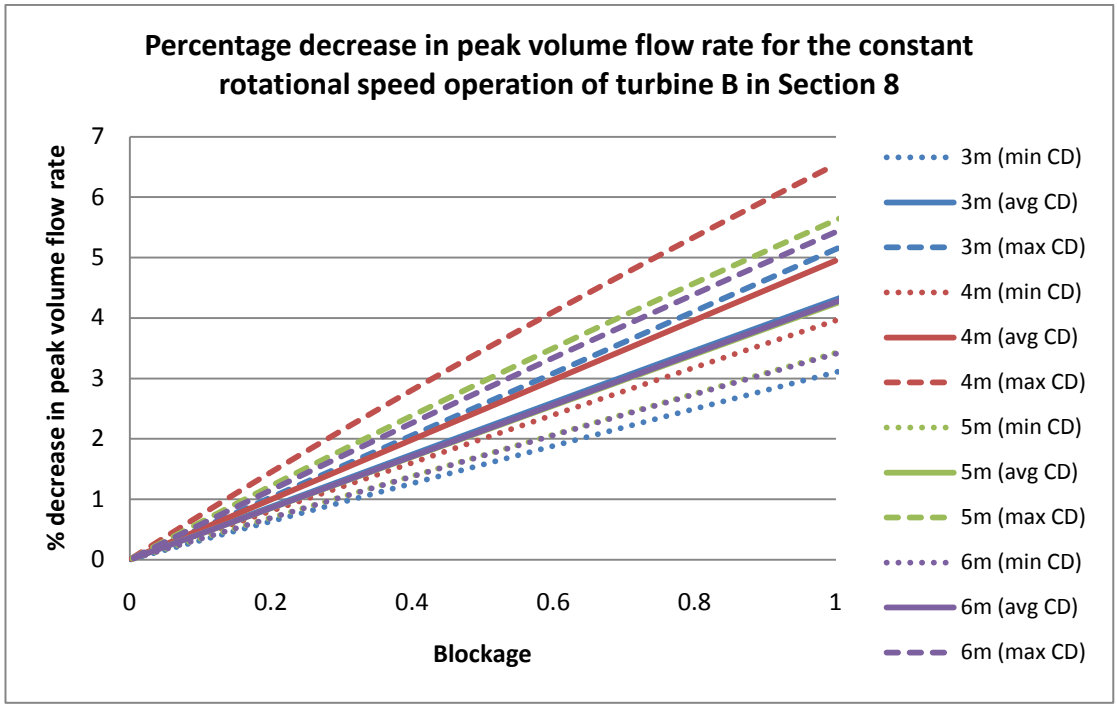

Figure 3.56- Percentage decrease in peak volume flow rate for the constant rotational speed operation of turbine B in section 8

Figure 3.57, Figure 3.58, Figure 3.59 and Figure 3.60 show the effect of increasing the number of turbines installed in the channel on the

percentage decrease in the peak power generated per turbine. As for the narrowest section, in the percentage decrease calculations the peak power per turbine is compared with the peak power generated by a single turbine installed in the channel. It can be seen from these graphs that the percentage decrease in peak power generated is typically much larger in section 8 than it is in section 11, particularly for the constant rotational speed operation of the turbines in the channel with the minimum drag coefficient (drag coefficient calculated from the maximum estimate of peak volume flow rate). In the minimum drag coefficient channel, the installation of turbines has a greater effect on the flow speeds than in the maximum drag coefficient channel. For the constant rotational speed operation of the turbines, when the performance of the turbines is optimised for one particular value of the channel flow speed, small changes in speed have the potential to have a large impact on the performance of the turbines. Looking back at the performance curves for the constant rotational speed of the turbines, Figures 2.14 and 2.15, it can be seen that some changes in flow speed result in much smaller changes in power coefficient (near the peak of the curves). This explains why the reduction in peak power generated is typically much greater in section 8 than section 11, despite the percentage decrease in peak volume flow rate being similar for the two sections.

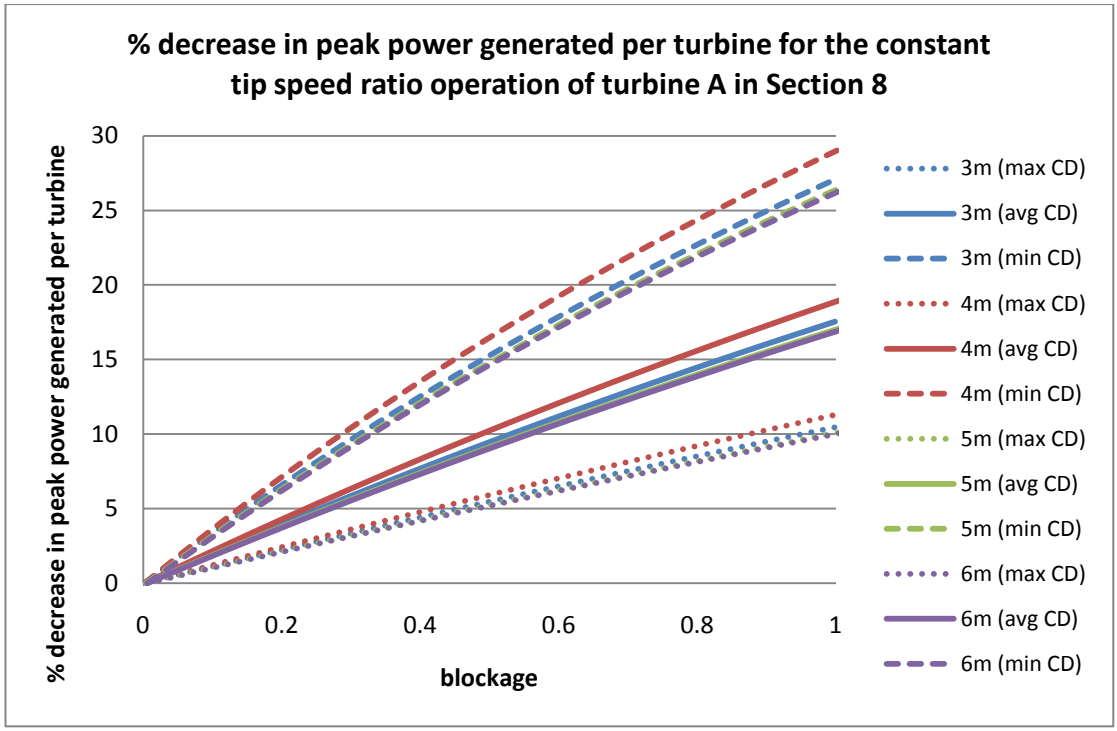

Figure 3.57- Percentage decrease in peak power generated per turbine for the constant tip speed ratio operation of turbine A in section 8

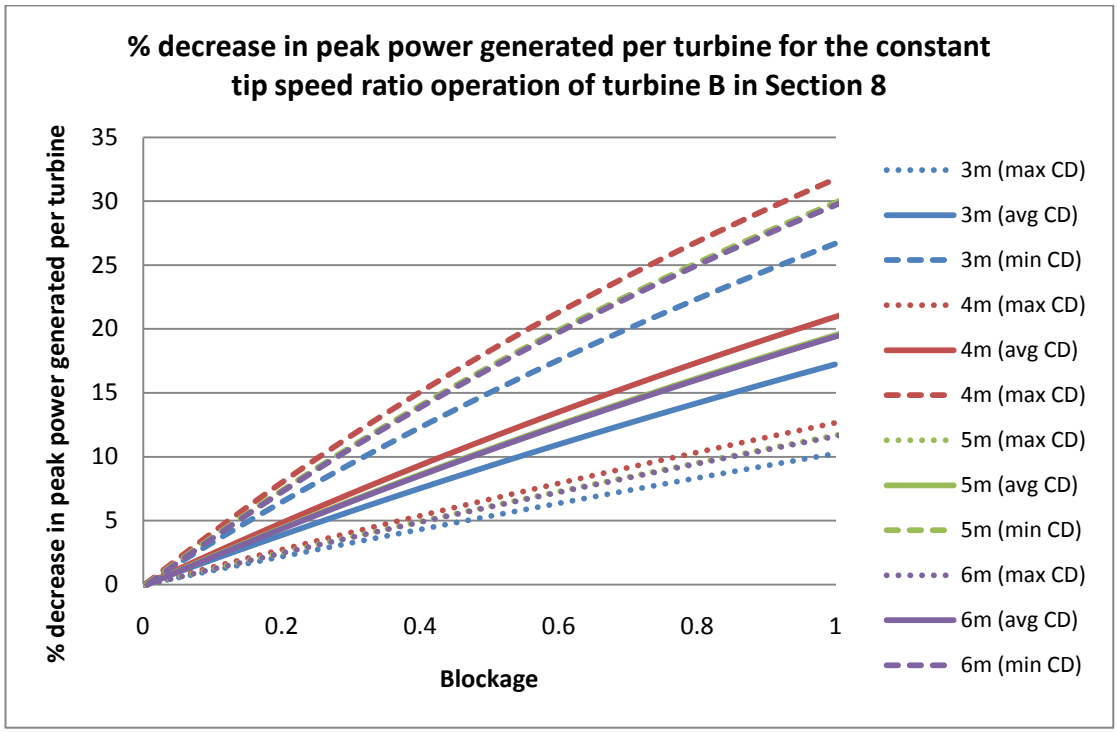

Figure 3.58- Percentage decrease in peak power generated per turbine for the constant tip speed ratio operation of turbine B in section 8

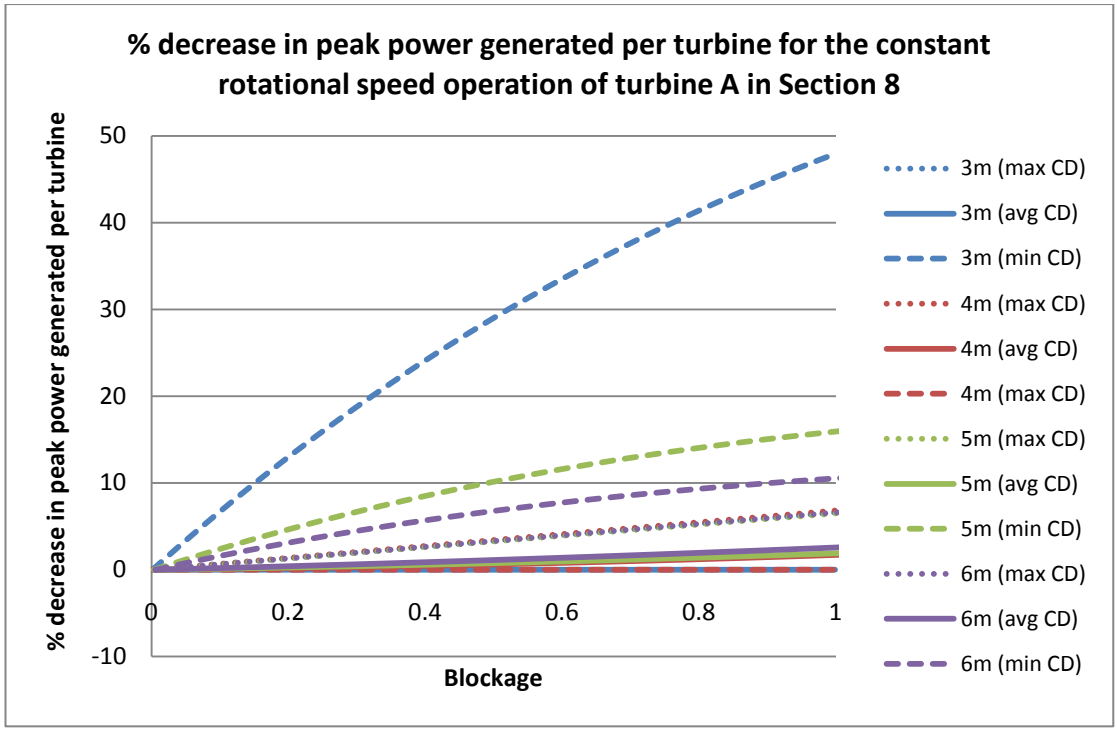

Figure 3.59- Percentage decrease in the peak power generated per turbine for the constant rotational speed operation of turbine A in section 8

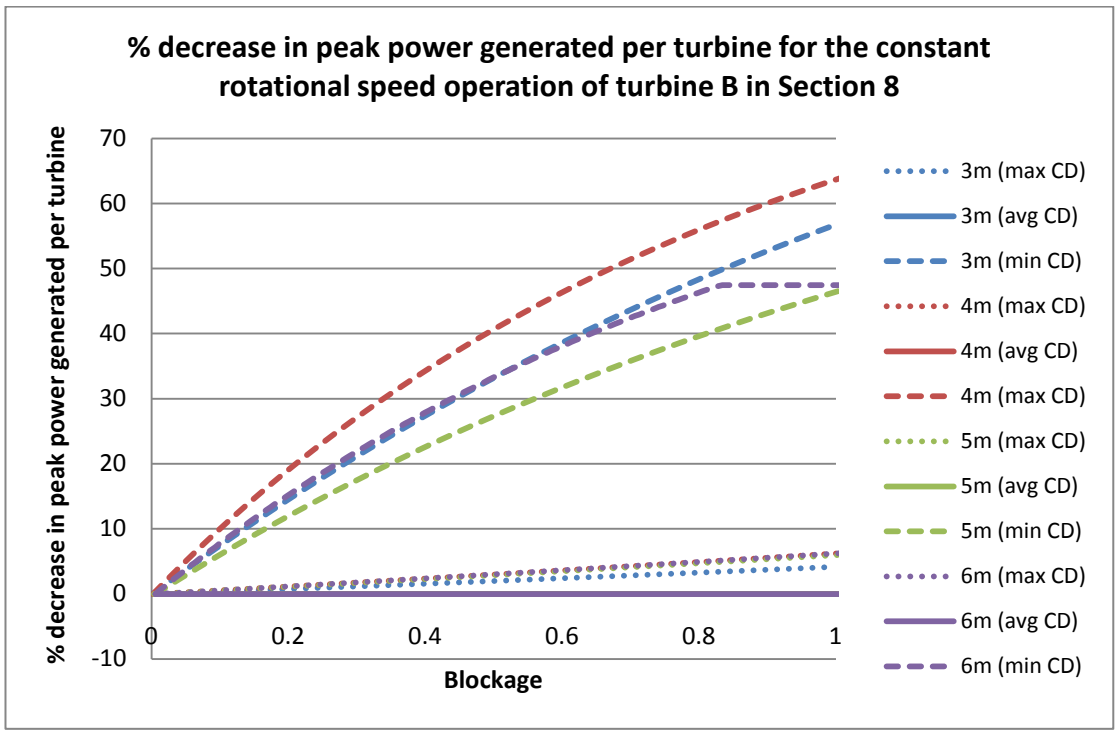

Figure 3.60- Percentage decrease in peak power generated per turbine for the constant rotational speed operation of turbine B in section 8

Figure 3.61, Figure 3.62, Figure 3.63 and Figure 3.64 show how increasing the number of turbines installed in section 8 affects the utilisation factor. For the constant tip speed ratio operation of the turbine the trends in utilisation factor are the same for sections 8 and 11. When the constant rotational speed operation of the turbines is considered there are some differences in the trends in the utilisation factor in the two sections. This is again due to the tuning of the turbines.

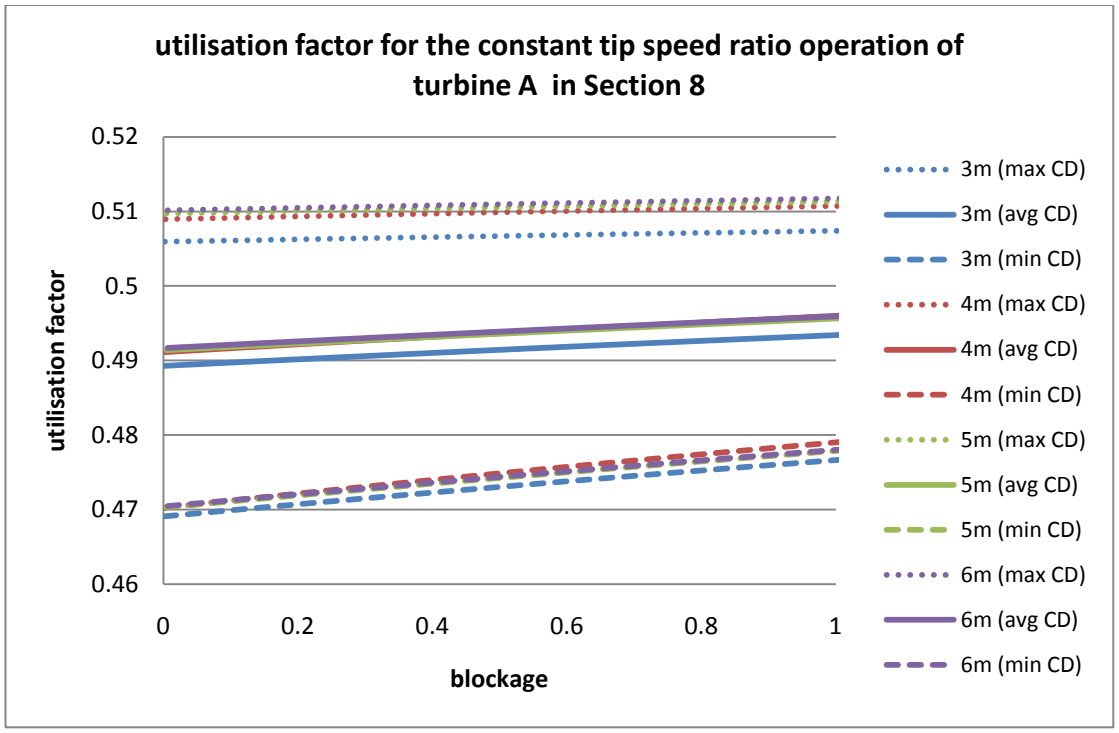

Figure 3.61- The effect of the number of turbines installed on the utilisation factor for the constant tip speed ratio operation of turbine A in section 8

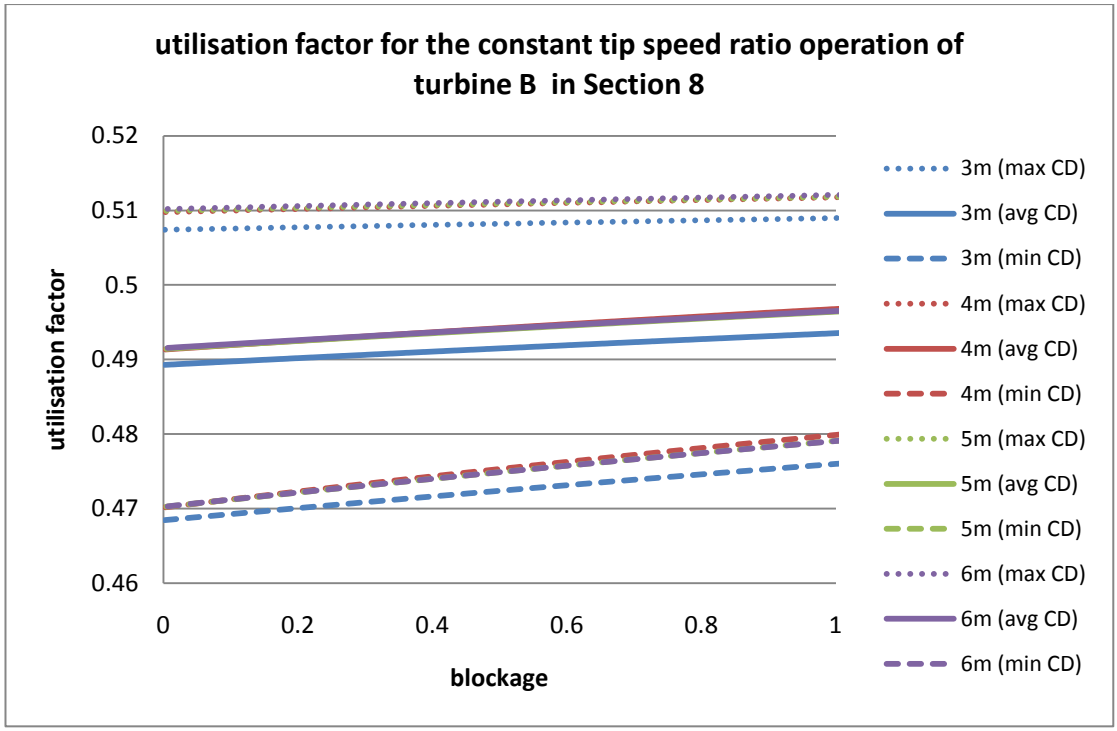

Figure 3.62- The effect of the number of turbines installed on the utilisation factor for the constant tip speed ratio operation of turbine B in section 8

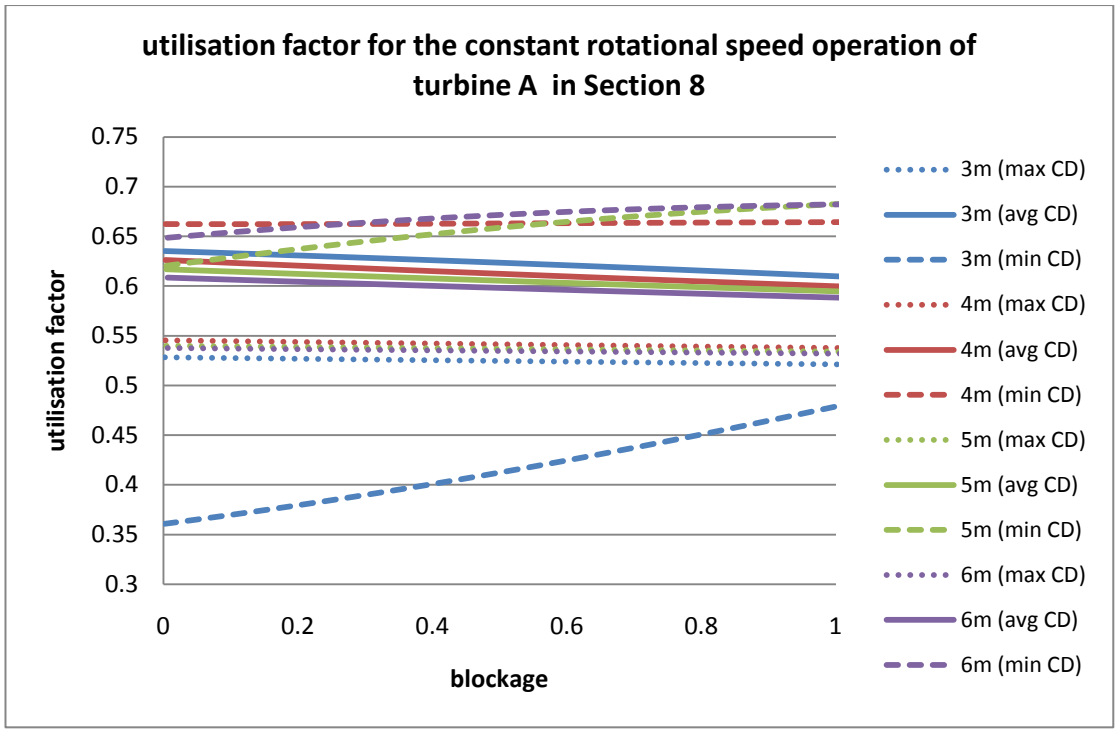

Figure 3.63- The effect of number of turbines installed on the utilisation factor for the constant rotational speed operation of turbine A in section 8

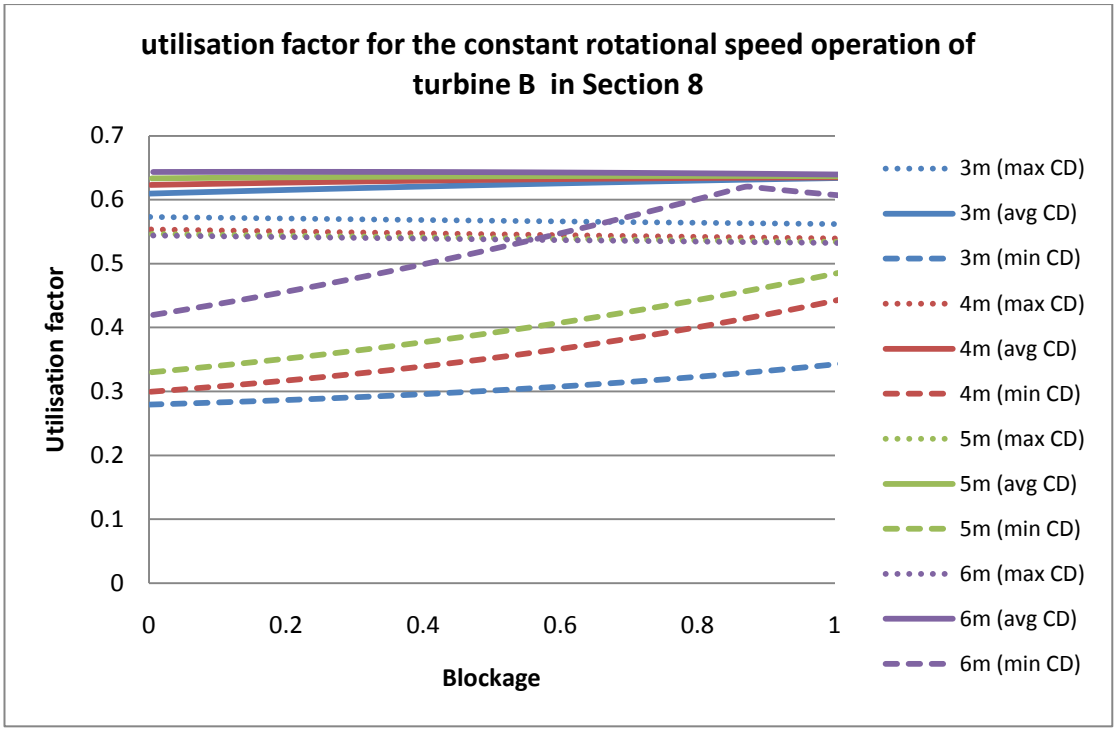

Figure 3.64- the effect of number of turbines installed on the utilisation factor for the constant rotational speed operation of turbine B in section 8

Figure 3.65, Figure 3.66, Figure 3.67 and Figure 3.68 show the effect of increasing the number of turbines installed in the channel on the percentage decrease in energy capture per turbine per tidal cycle. The percentage decrease in energy capture has been calculated using Equation 54. For the constant tip speed ratio operation of the turbines the trends in percentage decrease in energy capture are the same in sections 8 and 11. In section 8, however, the percentage decrease in energy capture is typically larger than that in section 11. The difference is greatest for the drag coefficient calculated from the maximum peak volume flow rate (minimum channel drag coefficient). For the constant rotational speed operation of the turbines there are some differences in the trends shown in sections 8 and 11. This is once again due to the tuning of the turbines.

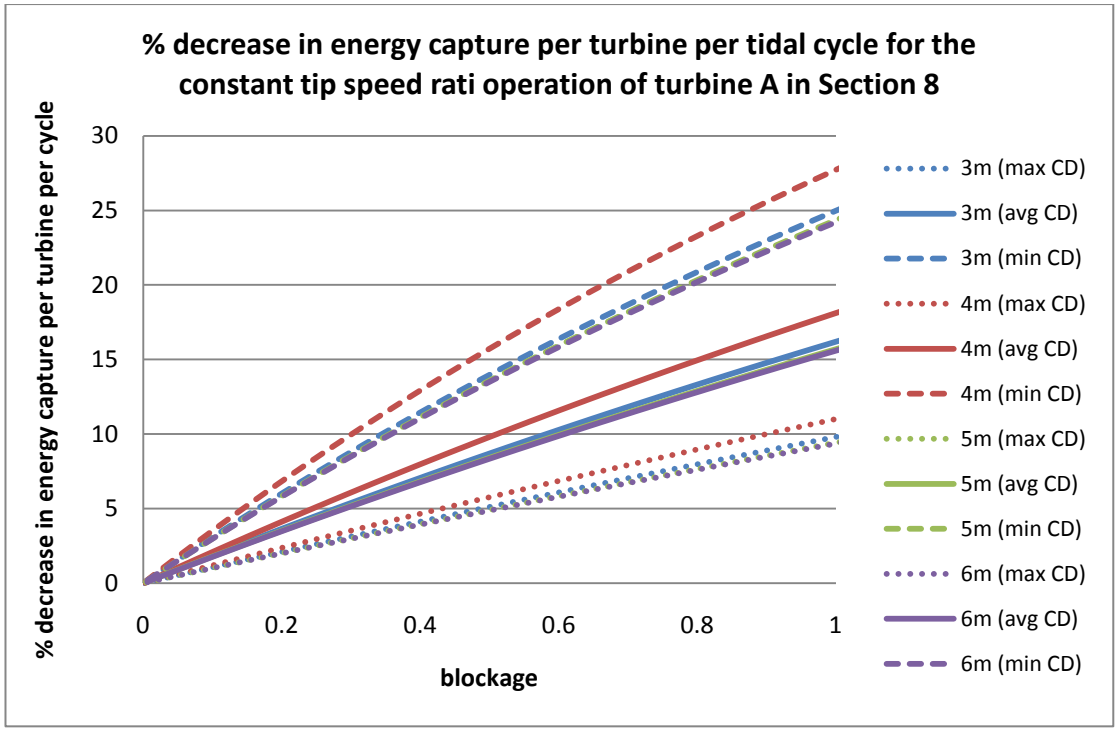

Figure 3.65-Effect of number of turbines on the percentage decrease in energy capture per turbine per tidal cycle for the constant tip speed ratio operation of turbine A in Section 8

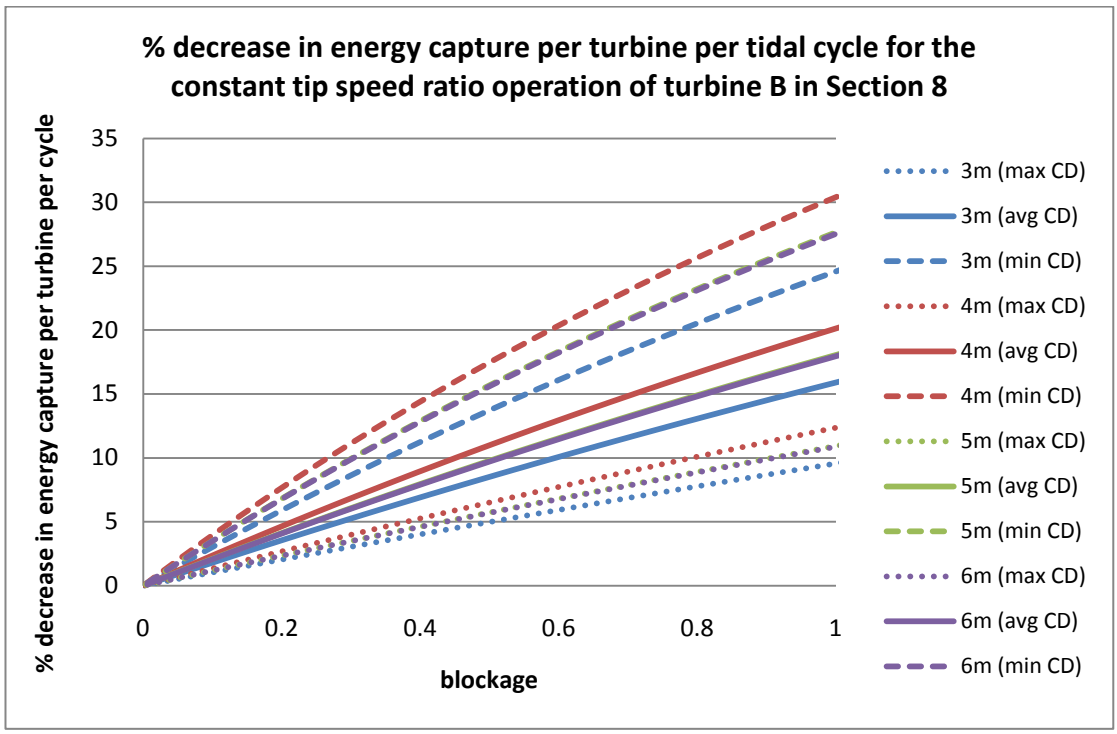

Figure 3.66-Effect of number of turbines on the percentage decrease in energy capture per turbine per tidal cycle for the constant tip speed ratio operation of turbine B in Section 8

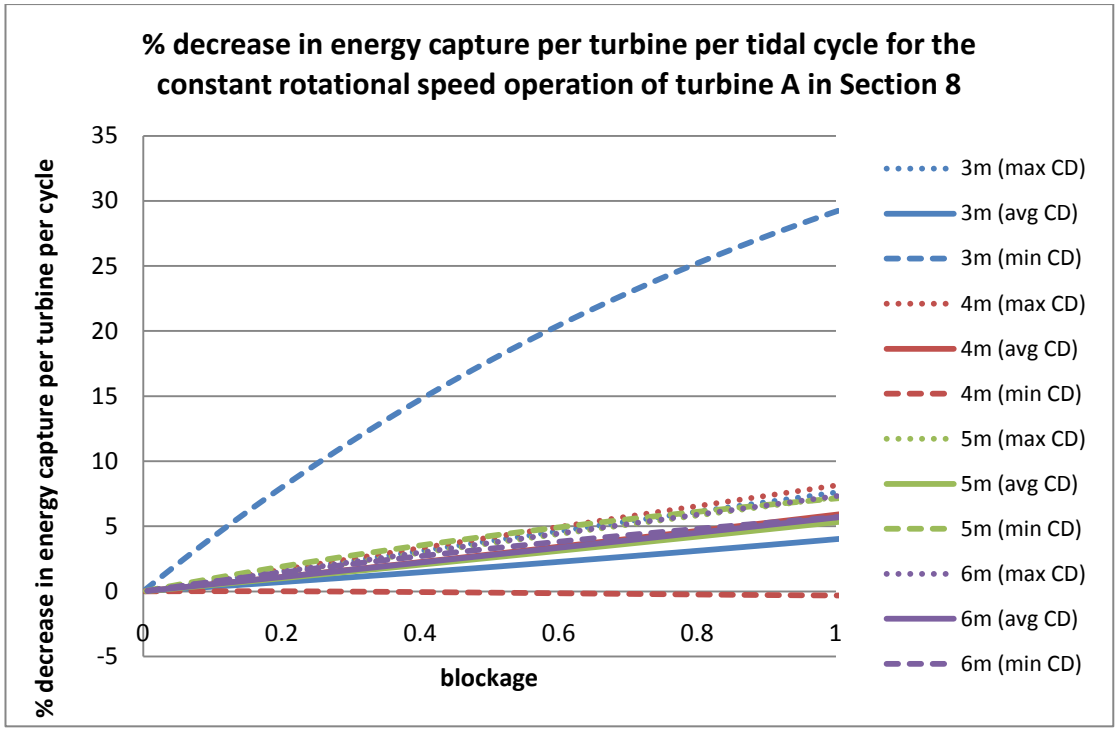

Figure 3.67-Effect of number of turbines on the percentage decrease in energy capture per turbine per tidal cycle for the constant rotational speed operation of turbine A in Section 8

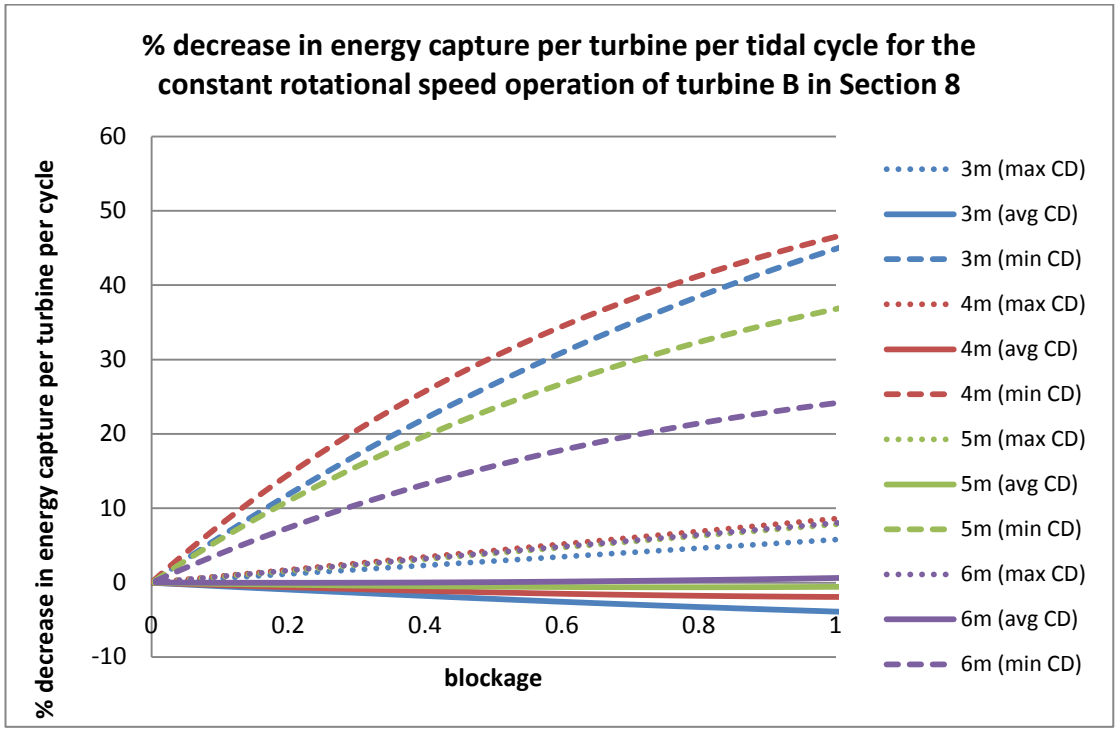

Figure 3.68-Effect of number of turbines on the percentage decrease in energy capture per turbine per tidal cycle for the constant rotational speed operation of turbine B in Section 8

Turbines in other sections

The effects of installing turbines in the other sections of the channel were also explored. Table 3. 16 gives maximum number of turbines of each radius that could be installed in each section without the blockage exceeding 1. Note, once again, that it would not be possible to install this number of horizontal axis turbines in each section without the swept areas overlapping.

Table 3. 16- Maximum number of turbines of each diameter that could be installed in each section

section	A [m^2]	number of turbines for complete blockage of section for turbine radius:			
		3m	4m	5m	6m
1	44058	1558	876	560	389
2	36040	1274	716	458	318
3	35099	1241	698	446	310
4	25300	894	503	322	223
5	26148	924	520	332	231
6	27185	961	540	346	240
7	25716	909	511	327	227
8	18656	659	371	237	164
9	19531	690	388	248	172
10	23813	842	473	303	210
11	21685	766	431	276	191
12	24031	849	478	305	212
13	21380	756	425	272	189
14	24138	853	480	307	213
15b	23875	844	474	303	211
16b	27301	965	543	347	241
17b	37350	1320	743	475	330
18b	40285.63	1424	801	512	356

Table 3.17, Table 3.18, Table 3.19 and Table 3.20 show the percentage decrease in peak volume flow rate for the maximum number of turbines that could be installed in each section for the different designs and modes of operation of turbine. For the constant rotational speed operation of turbine A the undisturbed flow speed in sections 1, 2, 3, 17b and 18b does not reach the cut in speed of the turbine.

It can be seen from Table 3.17, Table 3.18, Table 3.19 and Table 3.20 that, for the constant tip speed ratio operation of the turbines, the greater the area of the section, the smaller the percentage decrease in peak volume flow rate. This is because the larger the area of the section, the slower the flow and the less energy the turbines can extract from the flow. The more energy extracted by the turbines, the larger the effect on the peak volume flow rate in the channel. For the constant rotational speed operation of the turbines larger channel areas typically result in smaller decreases in peak volume flow rate although there are also some instances where the tuning of the turbine is improved in slower flow speeds and so more energy is extracted and there is a greater impact on the peak volume flow rate. It can be seen from the tables that, even with complete blockage of one section of the channel, the effect on the flow is small.

Table 3.17- Percentage decrease in peak volume flow rate for complete blockage of each section and constant tip speed ratio operation of turbine A

Section	% decrease in peak volume flow rate											
	R=3m			R=4m			R=5m			R=6m		
	min. $\dot{V}$ C_{Dc}	average $\dot{V}$ C_{Dc}	max. $\dot{V}$ C_{Dc}	min. $\dot{V}$ C_{Dc}	average $\dot{V}$ C_{Dc}	max. $\dot{V}$ C_{Dc}	min. $\dot{V}$ C_{Dc}	average $\dot{V}$ C_{Dc}	max. $\dot{V}$ C_{Dc}	min. $\dot{V}$ C_{Dc}	average $\dot{V}$ C_{Dc}	max. $\dot{V}$ C_{Dc}
1	1.4	2.6	4.3	1.4	2.6	4.3	1.4	2.5	4.2	1.4	2.5	4.2
2	1.8	3.1	5.2	1.8	3.1	5.2	1.7	3.1	5.1	1.7	3.1	5.1
3	1.8	3.2	5.4	1.8	3.2	5.3	1.8	3.2	5.2	1.8	3.1	5.2
4	2.5	4.4	7.3	2.5	4.4	7.2	2.5	4.3	7.1	2.5	4.3	7.1
5	2.4	4.3	7.1	2.4	4.3	7.0	2.4	4.2	6.9	2.4	4.2	6.9
6	2.3	4.1	6.8	2.3	4.1	6.8	2.3	4.1	6.7	2.3	4.0	6.6
7	2.5	4.4	7.2	2.5	4.3	7.1	2.4	4.3	7.0	2.4	4.3	7.0
8	3.4	5.9	9.6	3.4	5.9	9.5	3.3	5.8	9.3	3.3	5.7	9.3
9	3.3	5.7	9.2	3.2	5.6	9.1	3.2	5.5	9.0	3.2	5.5	8.9
10	2.7	4.7	7.7	2.7	4.7	7.6	2.6	4.6	7.5	2.6	4.6	7.5
11	2.9	5.1	8.4	2.9	5.1	8.3	2.9	5.0	8.2	2.9	5.0	8.1
12	2.6	4.7	7.6	2.6	4.6	7.6	2.6	4.5	7.4	2.6	4.5	7.4
13	3.0	5.2	8.5	3.0	5.2	8.4	2.9	5.1	8.3	2.9	5.1	8.2
14	2.6	4.6	7.6	2.6	4.6	7.5	2.6	4.5	7.4	2.6	4.5	7.4
15b	2.7	4.7	7.7	2.7	4.7	7.6	2.6	4.6	7.5	2.6	4.6	7.5
16b	2.3	4.1	6.8	2.3	4.1	6.7	2.3	4.0	6.6	2.3	4.0	6.6
17b	1.7	3.0	5.1	1.7	3.0	5.0	1.7	3.0	5.0	1.7	3.0	4.9
18b	1.6	2.8	4.7	1.6	2.8	4.7	1.5	2.8	4.6	1.5	2.7	4.6

Table 3.18- Percentage decrease in peak volume flow rate for complete blockage of each section and constant tip speed ratio operation of turbine B

Section	% decrease in peak volume flow rate											
	R=3m			R=4m			R=5m			R=6m		
	min. $\dot{V}$ C_{Dc}	average $\dot{V}$ C_{Dc}	max. $\dot{V}$ C_{Dc}	min. $\dot{V}$ C_{Dc}	average $\dot{V}$ C_{Dc}	max. $\dot{V}$ C_{Dc}	min. $\dot{V}$ C_{Dc}	average $\dot{V}$ C_{Dc}	max. $\dot{V}$ C_{Dc}	min. $\dot{V}$ C_{Dc}	average $\dot{V}$ C_{Dc}	max. $\dot{V}$ C_{Dc}
1	1.4	2.5	4.2	1.6	2.9	4.9	1.6	2.9	4.9	1.6	2.9	4.9
2	1.7	3.1	5.1	2.0	3.6	5.9	2.0	3.6	6.0	2.0	3.6	5.9
3	1.8	3.2	5.3	2.1	3.7	6.0	2.1	3.7	6.1	2.1	3.7	6.1
4	2.5	4.3	7.1	2.9	5.0	8.1	2.9	5.1	8.2	2.9	5.0	8.2
5	2.4	4.2	6.9	2.8	4.8	7.8	2.8	4.9	8.0	2.8	4.9	8.0
6	2.3	4.1	6.7	2.7	4.7	7.6	2.7	4.7	7.7	2.7	4.7	7.7
7	2.4	4.3	7.0	2.8	4.9	8.0	2.8	5.0	8.1	2.8	5.0	8.1
8	3.3	5.8	9.4	3.8	6.6	10.5	3.9	6.7	10.7	3.8	6.6	10.7
9	3.2	5.6	9.0	3.7	6.3	10.1	3.7	6.4	10.3	3.7	6.4	10.3
10	2.6	4.6	7.5	3.0	5.3	8.5	3.1	5.4	8.7	3.0	5.3	8.6
11	2.9	5.0	8.2	3.3	5.7	9.2	3.4	5.8	9.4	3.3	5.8	9.4
12	2.6	4.6	7.5	3.0	5.2	8.5	3.0	5.3	8.6	3.0	5.3	8.6
13	2.9	5.1	8.3	3.4	5.8	9.4	3.4	5.9	9.6	3.4	5.9	9.5
14	2.6	4.5	7.4	3.0	5.2	8.4	3.0	5.3	8.6	3.0	5.3	8.5
15b	2.6	4.6	7.5	3.0	5.2	8.5	3.1	5.3	8.7	3.0	5.3	8.6
16b	2.3	4.0	6.7	2.7	4.6	7.6	2.7	4.7	7.7	2.7	4.7	7.6
17b	1.7	3.0	5.0	2.0	3.5	5.7	2.0	3.5	5.8	2.0	3.5	5.7
18b	1.5	2.8	4.6	1.8	3.2	5.3	1.8	3.2	5.4	1.8	3.2	5.3

Table 3.19- Percentage decrease in peak volume flow rate for complete blockage of each section and constant rotational speed operation of turbine A

Section	% decrease in peak volume flow rate											
	R=3m			R=4m			R=5m			R=6m		
	min. $\dot{V}$ C_{Dc}	average $\dot{V}$ C_{Dc}	max. $\dot{V}$ C_{Dc}	min. $\dot{V}$ C_{Dc}	average $\dot{V}$ C_{Dc}	max. $\dot{V}$ C_{Dc}	min. $\dot{V}$ C_{Dc}	average $\dot{V}$ C_{Dc}	max. $\dot{V}$ C_{Dc}	min. $\dot{V}$ C_{Dc}	average $\dot{V}$ C_{Dc}	max. $\dot{V}$ C_{Dc}
1	0	2.3	4.4	1.1	2.6	4.5	1.2	2.6	4.4	1.1	2.5	4.3
2	0	3.2	5.1	1.7	3.3	5.1	1.8	3.2	5.0	1.7	3.2	5.0
3	0	3.3	5.2	1.8	3.3	5.1	1.8	3.3	5.0	1.8	3.3	5.0
4	2.6	4.1	5.6	2.6	4.1	5.4	2.6	4.0	5.4	2.5	4.0	5.4
5	2.5	4.1	5.6	2.5	4.0	5.5	2.5	4.0	5.4	2.5	4.0	5.4
6	2.4	4.0	5.6	2.4	4.0	5.4	2.4	3.9	5.4	2.4	3.9	5.4
7	2.6	4.1	5.6	2.6	4.0	5.4	2.5	4.0	5.4	2.5	4.0	5.4
8	3.1	4.3	5.2	3.1	4.2	5.3	3.0	4.1	5.1	3.0	4.1	5.1
9	3.1	4.3	5.3	2.6	3.7	4.6	3.0	4.2	5.2	3.0	4.2	5.2
10	2.7	4.2	5.5	2.7	4.1	5.4	2.7	4.1	5.4	2.7	4.1	5.4
11	2.9	4.3	5.4	2.9	4.2	5.3	2.8	4.2	5.3	2.8	4.1	5.3
12	2.7	4.2	5.5	2.7	4.1	5.4	2.7	4.1	5.4	2.6	4.1	5.4
13	2.9	4.3	5.4	2.9	4.2	5.3	2.9	4.2	5.3	2.9	4.2	5.3
14	2.7	4.2	5.5	2.3	3.5	4.6	2.7	4.1	5.4	2.6	4.1	5.4
15b	2.7	4.2	5.5	2.7	4.1	5.4	2.7	4.1	5.4	2.7	4.1	5.4
16b	2.4	4.0	5.6	2.4	4.0	5.5	2.4	3.9	5.4	2.4	3.9	5.4
17b	0	3.1	5.0	1.6	3.2	5.0	1.7	3.1	4.9	1.6	3.1	4.9
18b	0	2.8	4.8	1.4	2.9	4.8	1.5	2.9	4.7	2.1	4.2	6.8

Table 3.20- Percentage decrease in peak volume flow rate for complete blockage of each section and constant rotational speed operation of turbine B

Section	% decrease in peak volume flow rate											
	R=3m			R=4m			R=5m			R=6m		
	min. $\dot{V}$ C_{Dc}	average $\dot{V}$ C_{Dc}	max. $\dot{V}$ C_{Dc}	min. $\dot{V}$ C_{Dc}	average $\dot{V}$ C_{Dc}	max. $\dot{V}$ C_{Dc}	min. $\dot{V}$ C_{Dc}	average $\dot{V}$ C_{Dc}	max. $\dot{V}$ C_{Dc}	min. $\dot{V}$ C_{Dc}	average $\dot{V}$ C_{Dc}	max. $\dot{V}$ C_{Dc}
1	0.9	2.4	4.3	0.8	2.7	5.0	1.2	3.0	5.2	1.4	3.2	5.3
2	1.5	3.1	5.0	1.7	3.7	5.7	2.0	3.9	5.8	2.1	3.9	5.8
3	1.6	3.2	5.1	1.8	3.8	5.8	2.1	3.9	5.8	2.2	4.0	5.8
4	2.5	4.1	5.6	3.0	4.6	5.7	3.1	4.6	5.6	3.1	4.5	5.7
5	2.4	4.0	5.6	2.9	4.5	5.7	3.0	4.5	5.7	3.0	4.5	5.7
6	2.3	4.0	5.6	2.8	4.5	5.8	2.9	4.5	5.8	2.9	4.5	5.8
7	2.5	4.1	5.6	2.9	4.5	5.7	3.0	4.6	5.7	3.0	4.5	5.7
8	3.1	4.3	5.1	3.4	4.3	5.7	3.4	4.2	5.6	3.4	4.2	5.4
9	3.0	4.3	5.2	3.4	4.3	5.5	3.4	4.3	5.4	3.4	4.3	5.3
10	2.7	4.2	5.6	3.1	4.6	5.5	3.2	4.6	5.5	3.2	4.5	5.5
11	2.9	4.3	5.5	3.3	4.5	5.4	3.3	4.5	5.3	3.3	4.5	5.3
12	2.6	4.2	5.6	2.0	2.9	3.6	3.2	4.6	5.5	3.2	4.5	5.5
13	2.9	4.3	5.4	3.3	4.5	5.4	3.4	4.5	5.3	3.3	4.5	5.3
14	2.6	4.2	5.6	3.1	4.6	5.6	3.2	4.6	5.5	3.2	4.6	5.6
15b	2.7	4.2	5.6	3.1	4.6	5.5	3.2	4.6	5.5	3.2	4.6	5.5
16b	2.3	3.9	5.6	2.8	4.5	5.8	2.9	4.5	5.8	2.9	4.5	5.8
17b	1.4	3.0	4.9	1.6	3.5	5.7	1.8	3.7	5.7	2.0	3.8	5.7
18b	1.2	2.7	4.7	1.2	3.2	5.4	1.6	3.4	5.5	1.8	3.5	5.6

Table 3.21, Table 3.22, Table 3.23 and Table 3.24 show the percentage decrease in energy capture per turbine per tidal cycle for complete blockage of each section for the different designs and modes of operation of the turbines. It can be seen from these tables that, for the constant tip speed ratio operation of the turbines, there is a significant decrease in the energy capture per turbine when compared with the energy capture calculated from the undisturbed flow speeds in the channel. This indicates that, for large tidal farms, it is important to consider the effect of energy extraction on the flow speeds when estimating the amount of power that will be generated and when tuning turbines to the channel flow conditions. For the constant rotational speed operation of the turbines there is more variation in the percentage decrease in energy capture: some sections show very large decreases for some turbines and estimates of the channel drag coefficient; other sections show an increase in energy capture when compared to the energy capture calculated from the undisturbed values. This is, again due to the tuning of the turbines and emphasises the need to take into account the effect of the turbines on the flow speed when tuning the turbines to the conditions in the channel.

Table 3.21- Percentage decrease in energy capture per turbine per tidal cycle for complete blockage of each section and constant tip speed ratio operation of turbine A

Section	% decrease in energy capture per turbine per tidal cycle											
	R=3m			R=4m			R=5m			R=6m		
	min. $\dot{V}$ C_{Dc}	average $\dot{V}$ C_{Dc}	max. $\dot{V}$ C_{Dc}	min. $\dot{V}$ C_{Dc}	average $\dot{V}$ C_{Dc}	max. $\dot{V}$ C_{Dc}	min. $\dot{V}$ C_{Dc}	average $\dot{V}$ C_{Dc}	max. $\dot{V}$ C_{Dc}	min. $\dot{V}$ C_{Dc}	average $\dot{V}$ C_{Dc}	max. $\dot{V}$ C_{Dc}
1	8.88	8.42	12.67	8.63	8.11	12.31	8.38	7.88	12.03	7.89	7.38	11.55
2	6.27	9.49	14.75	6.02	9.20	14.42	5.85	8.97	14.13	5.80	8.90	14.04
3	6.29	9.67	15.07	6.05	9.39	14.74	5.86	9.15	14.45	5.81	9.10	14.36
4	7.61	12.53	19.60	7.40	12.27	19.29	7.23	12.05	19.01	7.16	11.94	18.85
5	7.43	12.19	19.09	7.22	11.94	18.78	7.02	11.69	18.46	6.98	11.63	18.38
6	7.21	11.81	18.50	6.98	11.53	18.17	6.81	11.32	17.91	6.75	11.23	17.78
7	7.52	12.36	19.35	7.30	12.09	19.03	7.13	11.87	18.74	7.07	11.79	18.62
8	9.79	16.18	24.97	9.60	15.93	24.66	9.40	15.66	24.30	9.31	15.52	24.10
9	9.41	15.56	24.09	9.21	15.30	23.76	9.03	15.05	23.42	8.96	14.94	23.27
10	7.99	13.18	20.59	7.77	12.91	20.26	7.60	12.70	19.98	7.54	12.59	19.83
11	8.63	14.26	22.19	8.42	14.01	21.88	8.25	13.78	21.58	8.17	13.66	21.40
12	7.92	13.07	20.43	7.72	12.82	20.13	7.52	12.56	19.79	7.47	12.49	19.69
13	8.72	14.43	22.45	8.51	14.17	22.12	8.34	13.94	21.81	8.29	13.86	21.70
14	7.89	13.03	20.36	7.68	12.77	20.05	7.50	12.54	19.75	7.44	12.45	19.62
15b	7.97	13.15	20.55	7.75	12.87	20.21	7.57	12.64	19.89	7.53	12.59	19.82
16b	7.19	11.77	18.45	6.97	11.51	18.14	6.79	11.28	17.83	6.74	11.20	17.73
17b	6.29	9.27	14.35	6.05	8.98	14.03	5.86	8.75	13.74	5.82	8.69	13.66
18b	6.63	8.83	13.54	6.38	8.53	13.20	6.18	8.30	12.92	6.14	8.24	12.85

Table 3.22- Percentage decrease in energy capture per turbine per tidal cycle for complete blockage of each section and constant tip speed ratio operation of turbine B

Section	% decrease in energy capture per turbine per tidal cycle											
	R=3m			R=4m			R=5m			R=6m		
	min. $\dot{V}$ C_{Dc}	average $\dot{V}$ C_{Dc}	max. $\dot{V}$ C_{Dc}	min. $\dot{V}$ C_{Dc}	average $\dot{V}$ C_{Dc}	max. $\dot{V}$ C_{Dc}	min. $\dot{V}$ C_{Dc}	average $\dot{V}$ C_{Dc}	max. $\dot{V}$ C_{Dc}	min. $\dot{V}$ C_{Dc}	average $\dot{V}$ C_{Dc}	max. $\dot{V}$ C_{Dc}
1	8.43	8.00	12.23	9.96	9.18	13.82	9.81	9.14	13.88	9.78	9.09	13.81
2	5.92	9.13	14.37	6.81	10.35	16.12	6.78	10.39	16.28	6.74	10.33	16.19
3	5.94	9.31	14.69	6.85	10.57	16.47	6.80	10.61	16.63	6.77	10.56	16.56
4	7.34	12.22	19.25	8.35	13.74	21.41	8.40	13.93	21.76	8.33	13.82	21.60
5	7.15	11.88	18.73	8.13	13.38	20.86	8.16	13.51	21.15	8.12	13.46	21.07
6	6.92	11.49	18.15	7.88	12.94	20.20	7.92	13.10	20.53	7.86	13.01	20.41
7	7.24	12.06	19.00	8.24	13.55	21.12	8.28	13.72	21.46	8.23	13.64	21.35
8	9.55	15.88	24.58	10.78	17.74	27.14	10.91	18.02	27.61	10.82	17.87	27.41
9	9.18	15.27	23.71	10.35	17.06	26.19	10.47	17.33	26.65	10.40	17.22	26.49
10	7.73	12.89	20.24	8.75	14.45	22.44	8.83	14.66	22.84	8.76	14.56	22.69
11	8.37	13.97	21.82	9.48	15.65	24.18	9.58	15.90	24.62	9.49	15.77	24.43
12	7.65	12.77	20.07	8.70	14.35	22.31	8.74	14.51	22.63	8.70	14.45	22.53
13	8.48	14.14	22.08	9.59	15.82	24.44	9.69	16.07	24.87	9.64	16.00	24.76
14	7.63	12.73	20.00	8.67	14.30	22.22	8.72	14.49	22.58	8.66	14.40	22.46
15	7.71	12.85	20.19	8.73	14.41	22.39	8.79	14.59	22.74	8.76	14.55	22.68
16	6.91	11.46	18.09	7.87	12.92	20.16	7.89	13.04	20.44	7.85	12.97	20.34
17	5.93	8.89	13.96	6.86	10.13	15.70	6.80	10.14	15.83	6.77	10.09	15.76
18	6.24	8.43	13.13	7.27	9.62	14.79	7.19	9.62	14.90	7.16	9.58	14.83

Table 3.23- Percentage decrease in energy capture per turbine per tidal cycle for complete blockage of each section and constant rotational speed operation of turbine A

Section	% decrease in energy capture per turbine per tidal cycle											
	R=3m			R=4m			R=5m			R=6m		
	min. $\dot{V}$ C_{Dc}	average $\dot{V}$ C_{Dc}	max. $\dot{V}$ C_{Dc}	min. $\dot{V}$ C_{Dc}	average $\dot{V}$ C_{Dc}	max. $\dot{V}$ C_{Dc}	min. $\dot{V}$ C_{Dc}	average $\dot{V}$ C_{Dc}	max. $\dot{V}$ C_{Dc}	min. $\dot{V}$ C_{Dc}	average $\dot{V}$ C_{Dc}	max. $\dot{V}$ C_{Dc}
1		35.00	16.07	14.62	10.93	13.18	13.87	10.43	12.90	7.92	8.96	12.72
2		14.40	13.48	8.90	10.48	12.40	8.49	10.16	12.55	6.56	9.82	12.65
3		13.65	13.27	8.72	10.45	12.24	8.30	10.16	12.42	6.63	9.91	12.54
4	9.90	10.03	6.54	7.98	9.26	7.32	7.81	9.50	7.70	7.67	9.58	8.04
5	10.50	10.26	7.75	8.02	9.49	8.11	7.79	9.67	8.47	7.61	9.78	8.79
6	11.45	10.51	9.04	8.05	9.70	8.92	7.80	9.86	9.33	7.50	9.94	9.56
7	10.17	10.15	7.15	7.99	9.37	7.71	7.80	9.59	8.09	7.64	9.69	8.42
8	7.60	4.01	29.16	7.03	5.02	-0.26	7.22	5.31	7.12	7.28	5.64	5.68
9	7.85	5.41	17.80	18.43	17.37	12.79	7.43	6.23	4.16	7.50	6.49	3.94
10	9.10	9.46	4.25	7.89	8.73	5.70	7.80	9.03	6.12	7.76	9.13	6.60
11	8.38	8.04	3.32	7.69	7.65	2.80	7.73	7.99	3.79	7.75	8.12	4.41
12	9.19	9.56	4.57	7.91	8.83	5.97	7.78	9.09	6.35	7.75	9.21	6.83
13	8.30	7.75	4.00	7.64	7.45	2.36	7.69	7.78	3.55	7.75	7.95	4.16
14	9.24	9.61	4.74	20.76	21.44	19.34	7.80	9.15	6.48	7.74	9.25	6.94
15	9.12	9.49	4.34	7.89	8.75	5.77	7.78	9.03	6.17	7.77	9.17	6.68
16	11.60	10.54	9.17	8.07	9.75	9.02	7.80	9.87	9.41	7.50	9.96	9.65
17		15.71	13.78	9.26	10.55	12.63	8.84	10.18	12.70	6.52	9.72	12.78
18		20.20	14.55	10.51	10.68	12.95	10.04	10.23	12.86	6.57	9.40	12.87

Table 3.24- Percentage decrease in energy capture per turbine per tidal cycle for complete blockage of each section and constant rotational speed operation of turbine B

Section	% decrease in energy capture per turbine per tidal cycle											
	R=3m			R=4m			R=5m			R=6m		
	min. $\dot{V}$ C_{Dc}	average $\dot{V}$ C_{Dc}	max. $\dot{V}$ C_{Dc}	min. $\dot{V}$ C_{Dc}	average $\dot{V}$ C_{Dc}	max. $\dot{V}$ C_{Dc}	min. $\dot{V}$ C_{Dc}	average $\dot{V}$ C_{Dc}	max. $\dot{V}$ C_{Dc}	min. $\dot{V}$ C_{Dc}	average $\dot{V}$ C_{Dc}	max. $\dot{V}$ C_{Dc}
1	6.47	7.17	11.22	5.92	9.11	14.57	12.94	11.98	16.05	8.48	10.83	16.14
2	5.15	8.43	11.08	6.26	11.06	14.08	9.25	12.59	14.83	7.50	12.55	14.99
3	5.21	8.60	10.79	6.45	11.27	13.72	9.20	12.65	14.42	7.71	12.67	14.60
4	6.71	7.75	-2.46	8.83	9.90	0.04	9.80	10.45	1.54	9.84	10.61	2.85
5	6.58	8.22	-0.22	8.68	10.48	2.18	9.74	11.01	3.52	9.79	11.19	4.67
6	6.39	8.63	2.24	8.43	10.99	4.55	9.69	11.59	5.72	9.64	11.72	6.62
7	6.65	8.00	-1.35	8.75	10.19	1.10	9.78	10.74	2.53	9.83	10.91	3.76
8	5.78	-3.91	44.86	7.41	-1.83	42.97	7.82	-0.54	36.77	7.95	0.59	24.08
9	6.31	-1.48	35.61	8.05	0.51	29.36	8.47	1.67	21.70	8.59	2.66	9.61
10	6.91	6.54	-6.03	9.00	8.50	-3.60	9.77	9.09	-2.06	9.85	9.36	-0.64
11	6.90	3.57	0.14	8.90	5.39	-1.60	9.45	6.18	-2.85	9.53	6.70	-4.09
12	6.88	6.75	-5.62	39.94	39.73	34.70	9.76	9.30	-1.56	9.87	9.56	-0.12
13	6.87	3.00	3.78	8.82	4.81	0.76	9.35	5.64	-1.49	9.46	6.24	-3.85
14	6.86	6.85	-5.40	8.98	8.86	-2.89	9.78	9.42	-1.30	9.87	9.67	0.14
15	6.90	6.60	-5.92	8.99	8.56	-3.47	9.75	9.13	-1.92	9.88	9.43	-0.49
16	6.37	8.67	2.49	8.42	11.06	4.80	9.68	11.64	5.94	9.62	11.78	6.82
17	5.12	8.22	11.35	6.05	10.79	14.48	9.40	12.51	15.30	7.23	12.38	15.46
18	5.24	7.71	11.52	5.69	10.05	14.82	10.11	12.25	15.88	6.95	11.77	16.04

Turbines in multiple sections

In the previous sections turbines have been assumed to only be installed in a single section of the channel at a time. Since future tidal current farms will need to be designed so as to minimise the obstruction they pose to vessels and wildlife, it is likely that future farms will deploy turbines in multiple sections of the channel. This will allow a greater turbine swept area whilst keeping the blockage of any given section of the channel at an acceptably low level. This section considers the effects of installing turbines in multiple sections of the channel.

Since the area of the channel sections varies, different numbers of turbines are needed in each section to produce the same blockage. When investigating the effect of installing turbines in multiple sections, two different scenarios were considered: in the first, the number of turbines installed in each section was the same; in the second the maximum number of turbines that could be installed in each section without the blockage exceeding a given value were used.

Table 3.25 gives the percentage decrease in peak volume resulting from installing 1, 10 and 100 turbines in each section. It can be seen from this table that significant numbers of turbines can be installed in the channel without them having a large effect on the flow. With ten turbines installed in each section (180 turbines installed in the channel) there is a maximum percentage decrease peak volume flow rate of 6.6% which occurs for the constant tip speed ratio of 6m radius turbines of design B. With 100 turbines installed in each section (1800 turbines overall) the maximum percentage decrease in peak volume flow rate is 36.5%, again for the constant tip speed ratio operation of a 6m radius turbine of design B. These numbers of turbines greatly exceed the number of turbines that are likely to be installed in the first farms of tidal turbines.

Table 3.25- Effect of a given number of turbines in each section on the percentage decrease in peak volume flow rate

		turbines per section:	1			10			100		
		turbine radius (m)	% dec in $\dot{V}$ for:			% dec in $\dot{V}$ for:			% dec in $\dot{V}$ for:		
			min. $\dot{V}$ C_{Dc}	average $\dot{V}$ C_{Dc}	max. $\dot{V}$ C_{Dc}	min. $\dot{V}$ C_{Dc}	average $\dot{V}$ C_{Dc}	max. $\dot{V}$ C_{Dc}	min. $\dot{V}$ C_{Dc}	average $\dot{V}$ C_{Dc}	max. $\dot{V}$ C_{Dc}
constant tip speed ratio operation	turbine A	3	0.052	0.096	0.164	0.500	0.920	1.57	4.67	8.18	13.0
		4	0.091	0.167	0.285	0.879	1.60	2.71	6.96	13.2	20.1
		5	0.138	0.254	0.435	1.34	2.43	4.07	6.96	18.5	27.0
		6	0.197	0.363	0.619	1.91	3.43	5.69	6.96	23.9	33.4
	turbine B	3	0.051	0.094	0.161	0.491	0.901	1.53	4.59	8.03	12.8
		4	0.103	0.189	0.322	1.00	1.82	3.05	6.96	14.7	22.1
		5	0.162	0.299	0.511	1.57	2.85	4.75	6.96	20.8	29.8
		6	0.232	0.426	0.727	2.23	4.01	6.60	6.96	26.5	36.5
constant rotational speed operation	turbine A	3	0.002	0.074	0.110	0.002	0.707	1.05	0.002	5.09	9.93
		4	0.089	0.142	0.193	0.867	1.37	1.86	6.96	12.4	16.8
		5	0.137	0.217	0.294	1.33	2.11	2.86	6.96	17.9	24.3
		6	0.194	0.310	0.421	1.88	3.01	4.09	6.96	23.4	31.6
	turbine B	3	0.049	0.082	0.112	0.476	0.785	1.07	4.47	7.34	10.1
		4	0.099	0.154	0.204	0.966	1.50	1.97	6.96	13.6	17.9
		5	0.160	0.240	0.314	1.56	2.35	3.04	6.96	20.1	26.5
		6	0.232	0.345	0.446	2.25	3.37	4.34	6.96	26.6	34.8

Table 3. 26 gives the percentage decrease in peak volume resulting from installing maximum number of turbines in each section for the blockage not to exceed 0.5, 0.25, 0.2, 0.1 and 0.05. The effect of the turbines on the flow is large for a blockage of 0.5, 0.25 and 0.2 of each section. For a blockage of 0.05 in each section the percentage decrease in peak volume flow rate with a maximum percentage decrease in peak volume flow rate of 7.06% which occurs for the constant tip speed ratio operation of a 5m radius turbine of design B for the minimum estimate of average channel drag coefficient. It should be noted that achieving a blockage of 0.5 in all 18 sections of the channel would require a very large number of turbines, greatly in excess of the size of the farms that it is anticipated will be built in the near future.

From Table 3. 26 it can also be seen that the maximum percentage decrease in peak volume flow rate that occurs for the maximum value of the average channel drag coefficient is 6.96%. Above a blockage of 0.20 in each section the % decrease in peak volume flow rate remains steady at this value and does not increase further. This effect can be seen more clearly in Figure 3.69. It is thought that the effect is due to the cut in speed of the turbines. For all of the designs and modes of operation of turbine the same cut in speed is used, except for the constant rotational speed operation of a 3m radius turbine of design A. For this turbine the percentage decrease in peak volume flow rate levels off at a different value: 0.002%. The effect is noticeable for the maximum value of the average channel drag coefficient and not the average or minimum values because the flow speeds for the maximum value of the average channel drag coefficient are slower than for the other values.

Table 3. 26- Effect of a given maximum blockage in each section on the percentage decrease in peak volume flow rate

		blockage per section:	0.5			0.25			0.2			0.1			0.05		
		turbine radius (m)	% dec in $\dot{V}$ for:			% dec in $\dot{V}$ for:			% dec in $\dot{V}$ for:			% dec in $\dot{V}$ for:			% dec in $\dot{V}$ for:		
			min. $\dot{V}$ C_{Dc}	average $\dot{V}$ C_{Dc}	max. $\dot{V}$ C_{Dc}	min. $\dot{V}$ C_{Dc}	average $\dot{V}$ C_{Dc}	max. $\dot{V}$ C_{Dc}	min. $\dot{V}$ C_{Dc}	average $\dot{V}$ C_{Dc}	max. $\dot{V}$ C_{Dc}	min. $\dot{V}$ C_{Dc}	average $\dot{V}$ C_{Dc}	max. $\dot{V}$ C_{Dc}	min. $\dot{V}$ C_{Dc}	average $\dot{V}$ C_{Dc}	max. $\dot{V}$ C_{Dc}
constant tip speed ratio operation	turbine A	3	6.96	25.8	35.7	6.96	15.8	23.5	6.96	13.2	20.08	4.13	7.28	11.7	2.12	3.83	6.33
		4	6.96	25.8	35.6	6.96	15.7	23.4	6.96	13.1	19.97	4.11	7.23	11.6	2.10	3.78	6.25
		5	6.96	25.5	35.3	6.96	15.4	23.1	6.96	12.9	19.68	4.01	7.06	11.3	2.04	3.68	6.08
		6	6.96	25.4	35.2	6.96	15.4	22.9	6.96	12.8	19.56	4.00	7.04	11.3	2.01	3.62	5.98
	turbine B	3	6.96	25.5	35.4	6.96	15.5	23.2	6.96	13.0	19.78	4.06	7.15	11.4	2.09	3.75	6.20
		4	6.96	28.1	38.2	6.96	17.4	25.5	6.96	14.6	21.89	4.67	8.12	12.9	2.40	4.27	7.00
		5	6.96	28.2	38.4	6.96	17.5	25.7	6.96	14.7	22.12	4.67	8.16	13.0	2.39	4.29	7.06
		6	6.96	28.1	38.3	6.96	17.4	25.6	6.96	14.6	21.99	4.66	8.14	12.9	2.35	4.22	6.94
constant rotational speed operation	turbine A	3	0.002	5.09	28.1	0.002	5.09	20.6	0.002	5.09	17.09	0.002	5.09	9.13	0.002	3.04	4.68
		4	6.96	25.5	34.4	6.96	15.0	20.7	6.96	12.4	17.18	4.08	6.61	9.14	2.08	3.38	4.66
		5	6.96	25.4	34.2	6.96	14.9	20.5	6.96	12.3	17.00	4.03	6.49	8.98	2.04	3.31	4.57
		6	6.96	25.1	34.0	6.96	14.7	20.4	6.96	12.2	16.91	3.97	6.46	8.98	1.99	3.25	4.50
	turbine B	3	6.96	24.9	34.2	6.96	14.8	20.9	6.96	12.3	17.33	3.91	6.59	9.27	2.01	3.40	4.75
		4	6.96	27.2	36.7	6.96	16.4	22.3	6.96	13.6	18.40	4.44	7.25	9.73	2.28	3.70	4.96
		5	6.96	28.1	37.3	6.96	16.8	22.4	6.96	13.9	18.50	4.65	7.31	9.67	2.37	3.72	4.91
		6	6.96	28.5	37.5	6.96	16.9	22.5	6.96	13.9	18.50	4.76	7.36	9.70	2.39	3.69	4.84

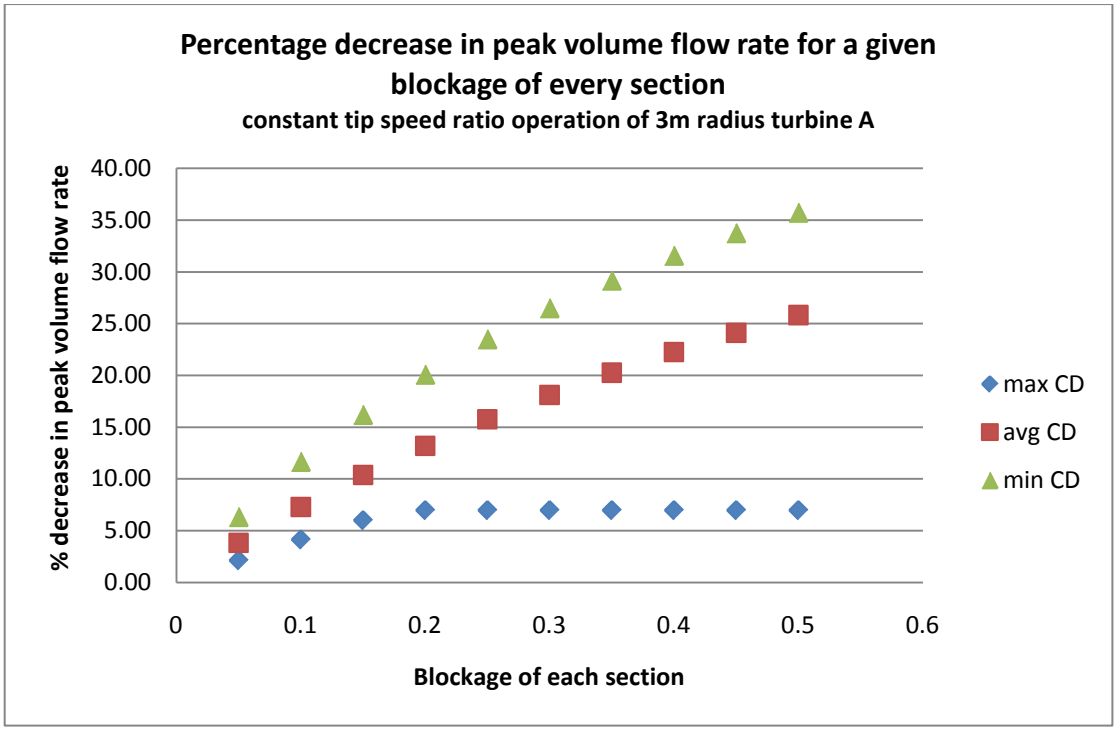

Figure 3.69- Variation in percentage decrease in peak volume flow rate with the blockage of each section for the constant tip speed ratio operation of a 3m radius turbine of design A

The percentage decrease in energy capture is shown in Table 3.27 for a given number of turbines installed in each section and Table 3.28 for a given blockage for each section. From these tables it can be seen that a significant decrease in energy capture occurs for numbers of turbines or levels of blockage that have relatively small effects on the peak volume flow rate. Despite significant decreases in energy capture occurring at lower numbers of turbines or levels of blockage than significant decreases in peak volume flow rate, the effects still may not be noticeable for the sizes of farms of turbines that it is anticipated will be installed in the near future.

Table 3.27- Effect of a given number of turbines in each section on the percentage decrease in energy capture per cycle

		turbines per section:	1			10			100		
		turbine radius (m)	% decrease in energy capture per cycle (kWh/cycle) for:			% decrease in energy capture per cycle (kWh/cycle) for:			% decrease in energy capture per cycle (kWh/cycle) for:		
			min. $\dot{V}$ C_{Dc}	average $\dot{V}$ C_{Dc}	max. $\dot{V}$ C_{Dc}	min. $\dot{V}$ C_{Dc}	average $\dot{V}$ C_{Dc}	max. $\dot{V}$ C_{Dc}	min. $\dot{V}$ C_{Dc}	average $\dot{V}$ C_{Dc}	max. $\dot{V}$ C_{Dc}
constant tip speed ratio operation	turbine A	3	0.11	0.27	0.47	0.96	2.56	4.42	7.28	20.86	32.84
		4	0.18	0.46	0.80	1.61	4.37	7.50	9.02	31.03	46.81
		5	0.26	0.70	1.23	2.39	6.54	11.13	9.08	40.03	57.89
		6	0.37	0.99	1.74	3.30	9.10	15.28	9.11	47.55	66.30
	turbine B	3	0.10	0.26	0.46	0.93	2.50	4.33	7.06	20.42	32.33
		4	0.20	0.52	0.91	1.82	4.93	8.43	8.98	33.65	50.16
		5	0.31	0.82	1.44	2.77	7.61	12.89	9.08	43.50	61.88
		6	0.44	1.17	2.04	3.79	10.55	17.60	9.13	50.61	69.70
constant rotational speed operation	turbine A	3	0.01	0.08	0.23	0.01	0.71	2.18	0.01	3.55	14.36
		4	0.16	0.27	0.20	1.47	2.60	2.00	8.38	22.19	21.37
		5	0.25	0.43	0.40	2.24	4.14	3.88	8.48	31.66	34.55
		6	0.34	0.62	0.57	3.07	5.97	5.65	8.59	39.89	46.10
	turbine B	3	0.08	0.09	0.33	0.70	0.89	3.03	5.51	9.05	16.23
		4	0.17	0.21	0.50	1.59	2.12	4.35	8.28	20.22	20.75
		5	0.29	0.37	0.60	2.65	3.68	5.07	8.74	31.72	29.29
		6	0.41	0.56	0.54	3.65	5.56	4.57	8.78	40.94	40.17

Table 3.28- Effect of a given maximum blockage in each section on the percentage decrease in energy capture per cycle

		blockage per section:	0.5			0.25			0.2			0.1			0.05		
		turbine radius (m)	% decrease in energy capture per cycle (kWh/cycle) for:			% decrease in energy capture per cycle (kWh/cycle) for:			% decrease in energy capture per cycle (kWh/cycle) for:			% decrease in energy capture per cycle (kWh/cycle) for:			% decrease in energy capture per cycle (kWh/cycle) for:		
			min. $\dot{V}$ C_{Dc}	average $\dot{V}$ C_{Dc}	max. $\dot{V}$ C_{Dc}	min. $\dot{V}$ C_{Dc}	average $\dot{V}$ C_{Dc}	max. $\dot{V}$ C_{Dc}	min. $\dot{V}$ C_{Dc}	average $\dot{V}$ C_{Dc}	max. $\dot{V}$ C_{Dc}	min. $\dot{V}$ C_{Dc}	average $\dot{V}$ C_{Dc}	max. $\dot{V}$ C_{Dc}	min. $\dot{V}$ C_{Dc}	average $\dot{V}$ C_{Dc}	max. $\dot{V}$ C_{Dc}
constant tip speed ratio operation	turbine A	3	9.85	51.17	69.74	9.63	36.33	53.16	9.53	31.56	47.21	6.76	18.89	29.93	3.85	10.36	17.13
		4	9.64	50.32	69.06	9.39	35.62	52.48	9.28	30.94	46.59	6.56	18.48	29.46	3.72	10.08	16.76
		5	9.58	49.78	68.59	9.33	35.08	51.91	9.21	30.42	45.99	6.38	18.01	28.84	3.60	9.78	16.32
		6	9.55	49.58	68.38	9.29	34.86	51.65	1.25	24.25	41.12	6.34	17.93	28.73	3.53	9.60	16.05
	turbine B	3	9.71	50.39	69.17	9.46	35.63	52.53	9.34	30.92	46.59	6.55	18.45	29.44	3.72	10.10	16.81
		4	9.62	52.33	71.54	9.39	38.37	55.78	9.29	33.57	49.96	4.62	18.11	30.27	4.14	11.29	18.64
		5	9.60	52.41	71.71	9.37	38.55	56.11	9.28	33.75	50.29	7.18	20.51	32.48	4.13	11.31	18.75
		6	9.60	52.27	71.56	9.36	38.36	55.89	9.25	33.54	50.04	7.15	20.45	32.39	4.06	11.12	18.46
constant rotational speed operation	turbine A	3	0.01	4.32	30.84	0.01	4.27	25.02	0.01	4.25	21.71	0.01	4.17	13.74	0.01	1.45	4.80
		4	9.04	43.28	49.91	8.98	27.93	29.64	8.96	23.57	24.18	6.32	13.06	12.17	3.56	6.78	5.97
		5	9.11	43.83	51.47	9.02	28.31	31.18	8.99	23.91	25.68	6.28	13.20	13.31	3.53	6.85	6.73
		6	9.16	43.47	51.81	8.97	28.20	31.67	8.89	23.85	26.15	6.10	13.24	13.63	3.38	6.78	6.78
	turbine B	3	8.15	34.87	39.11	7.93	21.12	23.73	7.82	17.48	20.60	5.27	9.22	13.98	2.96	4.66	8.91
		4	9.03	41.66	46.02	8.88	26.55	26.57	8.81	22.15	22.27	4.44	8.86	8.92	3.75	6.02	8.25
		5	9.39	44.70	48.45	9.31	28.84	27.04	9.29	24.11	22.16	7.25	12.95	12.38	4.14	6.58	7.03
		6	9.39	44.86	48.32	9.18	29.30	26.09	9.11	24.59	20.83	7.14	13.34	10.49	4.03	6.70	5.49

3.5.2.5 Case study results in context

Scottish Power Renewables is currently working on a project which aims to install an array of ten turbines in the Sound of Islay. The turbines will have a radius of 11m and will be installed between sections 11 and 13 of the channel (102). In order to allow comparison with the case study results it has been assumed that all 10 turbines will be installed in section 11. This gives a blockage of 0.18.

The turbines that will be used in the Scottish renewable farm have variable pitch blades. The example turbines used in the model had fixed pitch blades, so they are not directly comparable with the turbines that will be used in the farm. Despite this, it is thought that the model results can give an idea of the order of magnitude of the effects of the turbines on the channel and the reduction in performance due to the decrease in flow speed. The discrepancy between the farm turbines and the example turbines will be greatest when the power generated by the turbines is considered. The example turbines were not well tuned for the channel and so were frequently operating at quite a low power coefficient. The farm turbines are expected to operate more efficiently. Since the drag force on the blade contributes to the retarding force acting on the flow as well as the lift force, the effect on the flow of a turbine operating at a low power coefficient will be more similar to that of a turbine operating at a higher power coefficient than if the power output of the two turbines was compared directly.

Table 3.29 gives the percentage decrease in peak volume flow rate for the level of blockage equivalent to these ten turbines installed in section 11. The example turbines used in the calculation caused a 0.5-2% decrease in peak volume flow rate so, unless the performance of the turbines proposed for the farm is very different to the example turbines, the proposed farm is not expected to have a large effect on the peak volume flow rate in the channel.

Table 3.29- Percentage decrease in peak volume flow rate for blockage equivalent to the ten proposed Scottish Power renewables turbines in section 11

		turbine radius (m)	% decrease in peak volume flow rate for:		
			min. $\dot{V}$ C_{Dc}	average $\dot{V}$ C_{Dc}	max. $\dot{V}$ C_{Dc}
constant tip speed ratio operation	turbine A	3	0.55	0.99	1.67
		4	0.55	0.98	1.66
		5	0.54	0.96	1.63
		6	0.53	0.96	1.62
	turbine B	3	0.54	0.97	1.63
		4	0.62	1.11	1.87
		5	0.63	1.13	1.91
		6	0.63	1.13	1.90
constant rotational speed operation	turbine A	3	0.54	0.79	0.99
		4	0.53	0.77	0.98
		5	0.52	0.76	0.97
		6	0.52	0.76	0.97
	turbine B	3	0.53	0.79	0.99
		4	0.61	0.82	0.99
		5	0.61	0.81	0.98
		6	0.61	0.82	0.98

Table 3.30 gives the percentage decrease in energy capture per turbine per tidal cycle for the level of blockage equivalent to these ten turbines installed in section 11. It is harder to draw conclusions about the percentage decrease in energy capture of the proposed turbines as it there are likely to be significant differences between the performance of the example turbines and the farm turbines. However looking at the data in Table 3.30 it seems likely that the percentage decrease in energy capture per turbine per cycle is likely to be 5% or less. This magnitude of decrease is unlikely to have a significant impact on the economics of the project.

Table 3.30- Percentage decrease in energy capture per turbine per cycle for blockage equivalent to the ten proposed Scottish Power Renewables turbines in section 11

		turbine radius (m)	% decrease in energy capture per turbine per cycle (kWh per turbine per cycle) for:		
			min. $\dot{V}$ C_{Dc}	average $\dot{V}$ C_{Dc}	max. $\dot{V}$ C_{Dc}
constant tip speed ratio operation	turbine A	3	1.66	2.86	4.74
		4	1.61	2.80	4.66
		5	1.58	2.75	4.58
		6	1.57	2.74	4.55
	turbine B	3	1.61	2.80	4.64
		4	1.83	3.17	5.24
		5	1.85	3.23	5.36
		6	1.84	3.21	5.33
constant rotational speed operation	turbine A	3	1.58	1.44	0.78
		4	1.45	1.39	0.37
		5	1.46	1.45	0.61
		6	1.46	1.48	0.72
	turbine B	3	1.29	0.53	1.07
		4	1.68	0.85	0.34
		5	1.78	1.01	-0.18
		6	1.79	1.13	-0.70

3.5.2.6 Case study results discussion

Applying the extended model to the Sound of Islay has demonstrated that it is likely that significant numbers of turbines could be installed in the Sound of Islay before they have a significant effect on flow through the channel. For the complete blockage of any one section of the channel there was a maximum percentage decrease in peak volume flow rate of 10.7% which occurs for the complete blockage of section 8 for the channel drag coefficient calculated from the maximum peak volume flow rate and the constant tip speed ratio operation of 5 or 6m radius turbine of design B. Currently there is insufficient data to define a threshold above which the reduction in the flow speed will have a significant effect on the physical and biological processes however it seems likely that tidal stream

farms of the size that are likely to be installed in the next 10-20 years are unlikely to have a significant effect on the flow in the channel.

Whilst the effects on the peak volume flow rate tended to be small for reasonable levels of blockage, the effects on the power generated by the turbines tended to be larger. However at the levels of blockage anticipated for initial developments of tidal current farms, failing to take into account the effects of energy extraction on the performance of the turbines is unlikely to significantly affect the economics of the farm in this channel.

The calculations carried out were only for the peak spring current speeds. Future work should be carried out to establish if different trends are observed if the channel is modelled over the entire spring-neap cycle.

3.6 Summary

In Garrett and Cummins' model a parameter, λ, was used to calculate the resistive force due to the turbines. This parameter is related to the number of turbines and their location along the channel, but it does not allow these to be quantified. The extended model allows the effect of a number of turbines of a given design placed at various sections of the channel to be calculated. This has been achieved by changing the manner in which turbine drag is represented. The manner in which natural friction is represented has also been changed in the extended model. This is to allow a more commonly used definition of the drag coefficient of the channel to be used.

The extended model presented above allows the effect of turbines on the flow in a channel to be estimated. This can be used as part of the environmental impact assessment for proposed tidal stream power farms. One of the limitations of using this model to predict the impact of a farm on the flow is that it assumes that the surface elevation at the ends of the channel is unaltered by the presence of the turbines. At some sites and for

high levels of energy extraction the surface elevation at the ends of the channel may be affected by the installation of turbines in the channel. Changes to the surface elevation at the ends of the channel could cause flooding or affect populations of flora and fauna which live in the intertidal zone.

The extended model has confirmed that the impact of installing tidal stream devices at sites with a high drag coefficient will have less impact on the flow than installing the same number of devices at a site with a lower drag coefficient. The energy capture predicted by the extended model is lower than the energy capture calculated from the undisturbed channel flow speeds. The magnitude of the decrease in energy capture depends on the mode of operation of the turbines and the extent to which they alter the flow speeds in the channel. This effect will not be significant for single prototype turbines but it will start to have a noticeable and increasing effect as the number of turbines installed increased. For a farm of 1000 turbines decreases in energy capture of over 50% were observed.

3.6.1 Recommendations for future work

The extended model is based on a large number of assumptions: both those made in Garrett and Cummins model and the additional assumptions introduced through the change in the manner by which turbine drag was represented. As with any simple model used to describe a complex system, the accuracy with which the model describes the behaviour of the system depends on the validity of the simplifying assumption. A number of ways in which the model could be developed to improve its accuracy are considered below.

In the model it was assumed that the water levels at either end of the channel were unchanged by changes to the flow in the channel caused by the presence of turbines. For high levels of energy extraction this may not be the case. This has been demonstrated by Polangye et al (103) who developed a one dimensional model in which the tidal forcing can change in response to energy extraction. The limitations of assuming the tidal

forcing remained constant were also shown by Karsten et al (53) who modelled the Minas Passage using a both a numerical model and modified version of Blanchfield's model (47). For high levels of energy extraction the results from the two models diverged and the assumption that the tidal amplitude did not change was found to be the main reason for this. Thus it has been demonstrated that high levels of energy extraction have the potential to alter the tidal regime not just in the channels where the extraction takes place but also in the ocean outside these channels. This means that high levels of energy extraction have the potential to have far reaching environmental effects and so developing the model so the model should ideally be modified so that it can consider these changes.

The extended model applies only to channels connecting two large bodies of water. Some sites, such as the Sound of Islay, can clearly be described as a channel. Other sites, such as the Pentland Firth are a much harder to describe as a single channel. Analytical models similar to that of Garret and Cummins have been developed by Blanchfield for a channel connecting a small basin to the open ocean (47) and Atwater for a split channel (94). These models could be extended in the same way that Garret and Cummins model was extended to allow it to predict the effects of energy extraction on the flow and the power generated. This would greatly extend the number of sites which could be modelled. There are sites where the flow is accelerated around a headland, such as Portland Bill which clearly cannot be defined as channels. This type of site has been modelled using numerical models but analytical models have yet to be developed for this type of site. As such it would be harder to develop models for predicting the effects of energy extraction on turbine performance for these sites.

The flow in the model was assumed to be one dimensional with the velocity constant across any given section of the channel. Tidal currents however are three dimensional and vary with depth and horizontal position. Polagye (103) states that in narrow channels which are suitable sites for tidal turbines the currents are to the first order one-dimensional

with only limited vertical and lateral variation. However an ADCP survey carried out at 4 sites in the Admiralty Inlet in the Puget Sound (Washington, USA) found there to be significant differences in the flow speeds at the four sites (104). The sites were arranged in two pairs with each pair of sites having roughly the same along channel coordinate. The proximity of the site to the headland was found to affect the strength of the currents more than the along channel position. This indicates that the bathymetry of a site can cause significant variations in the flow speed across a given section. There was also found to be significant variation in flow speed with depth, due to the boundary layer. Variation of flow speed across the channel section and depth will cause the power capture of turbines installed at a given section to vary with the position in which they are installed. Since the power generated varies with velocity cube, small variations in flow speed can cause large variations in the amount of power generated. Tidal sites also typically exhibit large scales of turbulence (105) which will further affect the performance of the turbines although the fatigue loads are likely to be affected by the turbulence than the performance. The assumption of one dimensional flow does not allow the effects of spatial and turbulent variations in flow speed on performance to be taken into account. Whether this will have a significant effect on the accuracy of the predictions of the model will depend on the magnitude of the spatial and turbulent variations in flow speed at the site under consideration.

Other limitations of the model relate to the use of BEM theory to predict the forces applied to the flow by the turbines. The model assumes that, at any given section of the channel, the flow is uniform and as such requires the turbines to cover the entire cross section of the section of the channel where they are installed. The BEM model assumes individual, isolated turbines which cause local variations in the flow speed. In particular the BEM model assumes that the slower moving wake region behind each turbine does not mix with the faster moving flow outside the wake. This does not occur. Instead turbulent mixing occurs between the flow in the wake and the flow outside the wake, until the flow is once more uniform.

The turbulent mixing generates heat, and so is a further source of energy loss. If the length over which the turbines cause non-uniform velocity is short in comparison to the length of the channel, it is acceptable to use the BEM model to represent the turbines. However, even in these cases, the energy loss due to turbulent mixing is still not taken into account. Draper's model (95) takes into account turbulent mixing and so the model could be made more accurate by extending the BEM model to take into account turbulent mixing in a similar manner.

Chapter 4 The effect of blockage on tidal turbine performance

One of the major differences between the operation of wind turbines and the operation of tidal turbines is the extent to which the flow is constrained. The flow through a wind turbine is constrained by the ground but it is free above and to the sides of the turbine. The flow through a tidal turbine is constrained between the channel bed and the free surface. In narrow channels the side walls of the channels may also have an effect. These differences are likely to affect the performance of the turbine and hence limit the applicability of aerodynamic models to tidal turbines.

In order to investigate whether or not the channel boundaries are likely to have an effect on turbine performance three simple models with different boundary conditions are presented below. The first is the classic aerodynamic model in which the flow is unbounded; the second models a flow that is constrained by rigid boundaries on all sides; and in the third the flow is constrained by rigid boundaries on three sides and a free surface on the fourth. The deformation of the free surface can vary along the length of the channel but is constant across the width of the channel for any given section.

Whelan et al have also considered the effect of blockage on tidal turbine performance (41,42). They used actuator strip theory to calculate the blockage effect due to the free surface for an array of tidal stream turbines. This allowed them to develop a correction to the wake induction factor for use in Blade element momentum codes. The deforming boundary model outlined below is based on the same theory as Whelan et al's model however a different solution method is used. The graphical solution method used here provides greater understanding as it shows how the variation of momentum and blade element forces with actuator disc velocity combine to determine the performance of the turbine. A case study is also presented below, which allows the significance of the

blockage effects to be understood when considering realistically sized devices in actual tidal channels.

4.1 Modelling (106)

The models are based on the blade element momentum theory model with adjustments made for the differences in downstream pressure and flow area caused by the different boundary conditions. In blade element momentum models the force acting on the turbine blades is related to the change in the fluid momentum. The notation used in the models is shown in Figure 4.1. It should be noted that the pressures are taken to be the absolute pressure plus the hydrostatic pressure.

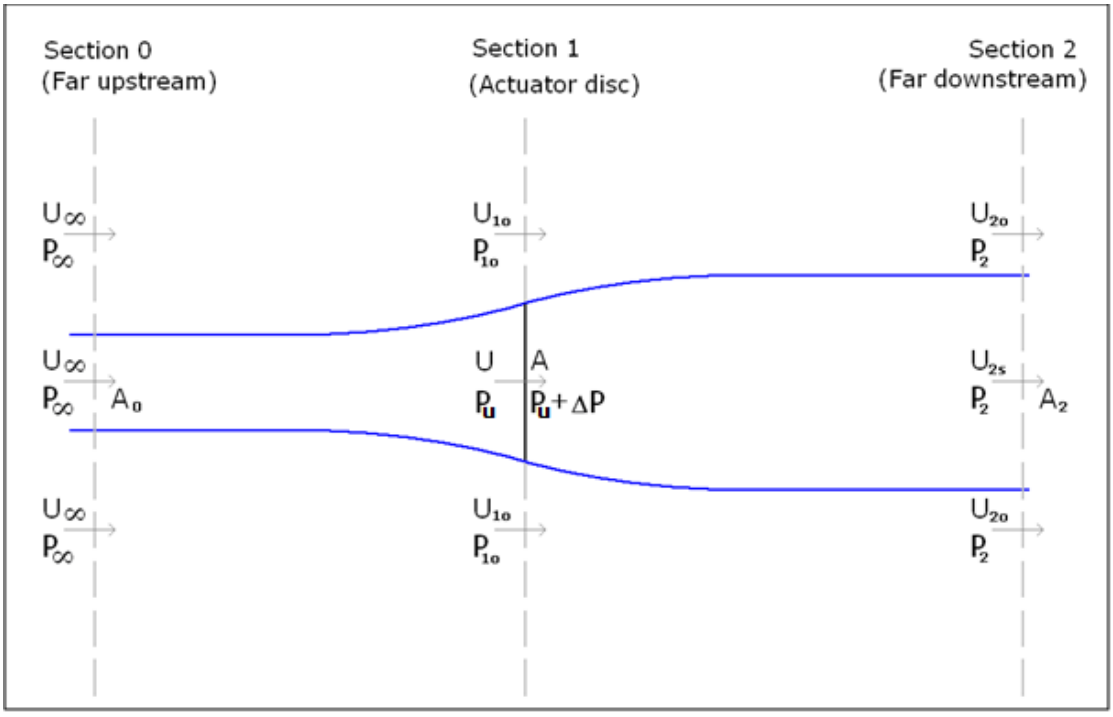

Figure 4.1- Definition of flow velocities and pressures

In this diagram three different sections are given. Sections 0 and 2 are far upstream and downstream of the actuator disc and at these sections the flow is in equilibrium. At these sections the pressure of the flow inside the streamtube is equal to the pressure of the flow outside the streamtube. Depending on the boundary conditions used, the pressure and velocity of

the flow outside the streamtube may be equal at all three sections or it may vary. This is why separate symbols have been assigned to the pressure and velocity of the flow outside the streamtube at the three sections.

4.1.1 Aerodynamic model

The aerodynamic model used is the blade element momentum model described in Section 2.3.

4.1.2 Rigid boundaries model

The flow in a tidal channel is more constrained than the free flow assumed in the aerodynamic model. The simplest constrained flow to model is a flow constrained on all sides by rigid boundaries. This is equivalent to model testing in a closed section wind tunnel where blockage effects can increase the performance of a turbine (107). For an open channel flow in a uniform channel, the channel area can be taken to be constant if the Froude number is small which is typically the case for tidal channels (52). The assumption of constant cross sectional area simplifies the modelling since the cross sectional area of the channel is known at all sections.

Applying Bernoulli's equation in the valid regions yields an expression for the pressure change across the actuator disc.

$$\Delta P = P_2 - P_\infty + \frac{1}{2}\rho\left(U_{2s}^2 - U_\infty^2\right)$$

Equation 55

Applying Bernoulli's equation along the surface gives:

$$P_\infty + \frac{1}{2}\rho U_\infty^2 = P_2 + \frac{1}{2}\rho U_{2o}^2$$

Equation 56

Rearranging to make $P_2 - P_\infty$ the subject gives:

$$P_2 - P_\infty = \frac{1}{2}\rho\left(U_\infty^2 - U_{2o}^2\right)$$

Equation 57

Substituting Equation 57 into Equation 55 gives:

$$\Delta P = \frac{1}{2}\rho\left(U_{2s}^2 - U_{2o}^2\right)$$

Equation 58

The pressure change across the actuator disc can be related to the force acting on the actuator disc by:

$$\Delta P = \frac{T}{A}$$

Equation 59

Combining Equation 58 and Equation 59 gives:

$$T = \frac{1}{2}\rho A\left(U_{2s}^2 - U_{2o}^2\right)$$

Equation 60

Conservation of mass gives:

$$AU = A_2 U_{2s}$$

Equation 61

$$\left(hz - A_2\right)U_{2o} = hzU_\infty - AU$$

Equation 62

Where:

h is the depth of the channel

z is the width of the channel

Equation 61 and Equation 62 allow Equation 60 to be expressed in terms of the far downstream streamtube area and the velocity of the flow through the actuator disc:

$$T = \frac{1}{2}\rho A\left[\left(\frac{Au}{A_2}\right)^2 - \left(\frac{hzu_\infty - Au}{hz - A_2}\right)^2\right]$$

Equation 63

Applying conservation of linear momentum to the flow gives:

$$T = A_2\rho u_{2s}(u_{2s} - u_\infty) + (hz - A_2)\rho u_{2o}(u_{2o} - u_\infty) + hz(P_2 - P_\infty)$$

Equation 64

Substituting Equation 57, Equation 61 and Equation 62 into this expression gives:

$$T = \rho Au\left(\frac{Au}{A_2} - u_\infty\right) + \rho\left(\frac{hzu_\infty - Au}{hz - A_2} - u_\infty\right)(hzu_\infty - Au) + \frac{1}{2}\rho yz\left(u_\infty^2 - \left(\frac{hzu_\infty - Au}{hz - A_2}\right)^2\right)$$

Equation 65

Equation 63 and Equation 65 can be used to calculate the thrust force acting on the actuator disc (T) for a given value of actuator disc velocity (u).

Another equation for T in terms of u can be obtained by summing the axial forces acting on the blade elements. Usually in a blade element model the velocity of the flow through the disc varies with radial position, with each blade element having a different velocity at the disc. The derivation of Equation 63 and Equation 65, however, assumes that the velocity is constant across the entire disc. In order to equate the equation for T in terms of u given by these equations with an expression for T in terms of u from the blade element forces, it must be assumed that the velocity is constant across the actuator disc when calculating the blade element forces. The use of the average actuator disc velocity to calculate

the blade element forces instead of the actual velocity for each blade element will reduce the accuracy of the blade element forces calculated.

An additional iterative procedure is needed to find the tangential interference factor for each blade element. The calculation procedure outlined in Figure 4.2 can be used to calculate the sum of the thrust forces acting on the blade elements for any given values for the u and tip speed ratio. The blade element forces vary with tip speed ratio but are independent of channel area.

Plotting the variation of T with u from both the momentum equations and the blade element equations allows a solution to be found for T and u for a given values of tip speed ratio and the ratio of channel area to turbine actuator disc area. An example of a plot of blade element forces and momentum forces is shown in Figure 4.3. Once u is known, the power coefficient of the turbine can be calculated using Equation 11, Equation 12 and Equation 13.

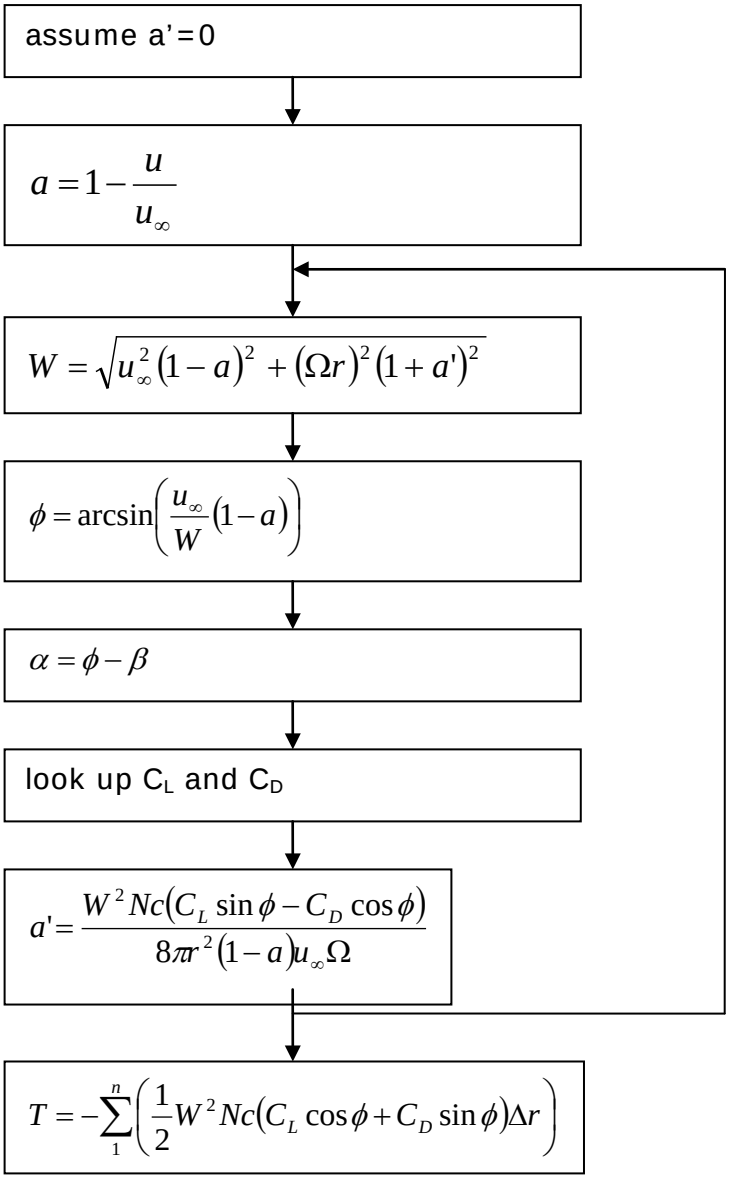

Figure 4.2- Iterative calculation procedure used to find the thrust force acting on the actuator disc from the blade element forces

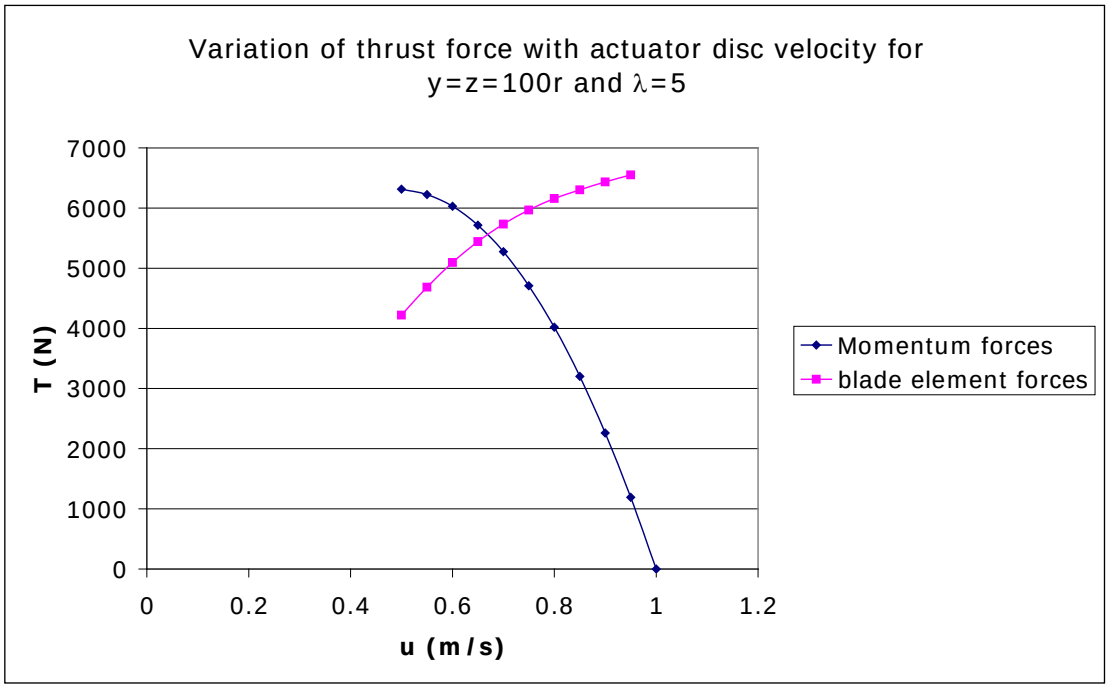

Figure 4.3- Example of graphical solution for T and u

4.1.3 Deforming free surface model

The difference in surface elevation of the far upstream and downstream sections may be negligible, however a major shortcoming of the rigid boundaries model presented above is that it does not accurately represent the pressure distribution in an open channel flow. In an open channel the pressure at the interface between the flow and the air is atmospheric. In the rigid boundaries model the pressure at the surface in the far downstream region was not equal to atmospheric pressure. By allowing the free surface to deform, a more realistic far downstream pressure distribution can be modelled.

Applying Bernoulli's equation in valid regions of the streamtube gives:

$$\Delta P = \rho g \Delta y + \frac{1}{2}\rho\left(u_{2s}^2 - u_\infty^2\right)$$

Equation 66

Substituting Equation 59 into Equation 66 gives:

$$T = \rho g A \Delta y + \frac{1}{2}\rho A\left(u_{2s}^2 - u_\infty^2\right)$$

Equation 67

Bernoulli's equation applied along the surface yields:

$$\frac{1}{2}\rho\left(u_\infty^2 - u_{2o}^2\right) = \rho g \Delta y$$

Equation 68

Applying conservation of linear momentum gives:

$$T = A\rho u\left(u_{2s} - u_\infty\right) + \left(zh - A_o\right)\rho u_\infty\left(u_{2o} - u_\infty\right) - \frac{1}{2}\rho g z\left(h^2 - \left(h + \Delta y\right)^2\right)$$

Equation 69

Continuity:

$$\left(hz - A_o\right)u_\infty = \left(z\left(h + \Delta h\right) - A_2\right)u_{2o}$$

Equation 70

$$u_\infty A_o = uA$$

Equation 71

$$uA = u_{2s} A_2$$

Equation 72

Substituting the continuity equations into Equation 67, Equation 68 and Equation 69 gives:

$$\Delta y = \frac{1}{2g}\left[u_\infty^2 - \left(\frac{hzu_\infty - uA}{z\left(h + \Delta y\right) - A_2}\right)^2\right]$$

Equation 73

$$T = \rho g \Delta y A + \frac{1}{2}\rho A\left[\left(\frac{uA}{A_2}\right)^2 - u_\infty^2\right]$$

Equation 74

$$T = A\rho u\left(\frac{uA}{A_2} - u_\infty\right) + \left(zh - \frac{uA}{u_\infty}\right)\rho u_\infty\left(\frac{zhu_\infty - uA}{z(h+\Delta y) - A_2} - u_\infty\right) - \frac{1}{2}\rho g z\left(h^2 - (h+\Delta y)^2\right)$$

Equation 75

This system of equations can be solved to give the variation of T with u. An iterative procedure was used to find the variation of Δy with A_2 from Equation 73 and these values used in the numerical solution of Equation 74 and Equation 75. The blade element forces and the value of u which satisfies both the blade element and momentum equations can be calculated in the manner described in the rigid boundaries section.

4.1.4 Model results

A 4m diameter turbine of design B has been used in these models. The rigid boundaries and deforming boundary models were applied to square channels with side lengths of 4R, 10R, 20R, 100R and 10000R. These results are plotted with the curve from the aerodynamic model in Figure 4.4. The maximum power coefficient for two of the curves in Figure 4.4 is greater than the Betz limit (0.593). The Betz limit is derived for a turbine in free flow so for cases where blockage is significant the maximum power coefficient can actually exceed the Betz limit. The two curves which exceed the Betz limit are for cases where the ratio of turbine area to channel area is high and so the blockage effect is large.

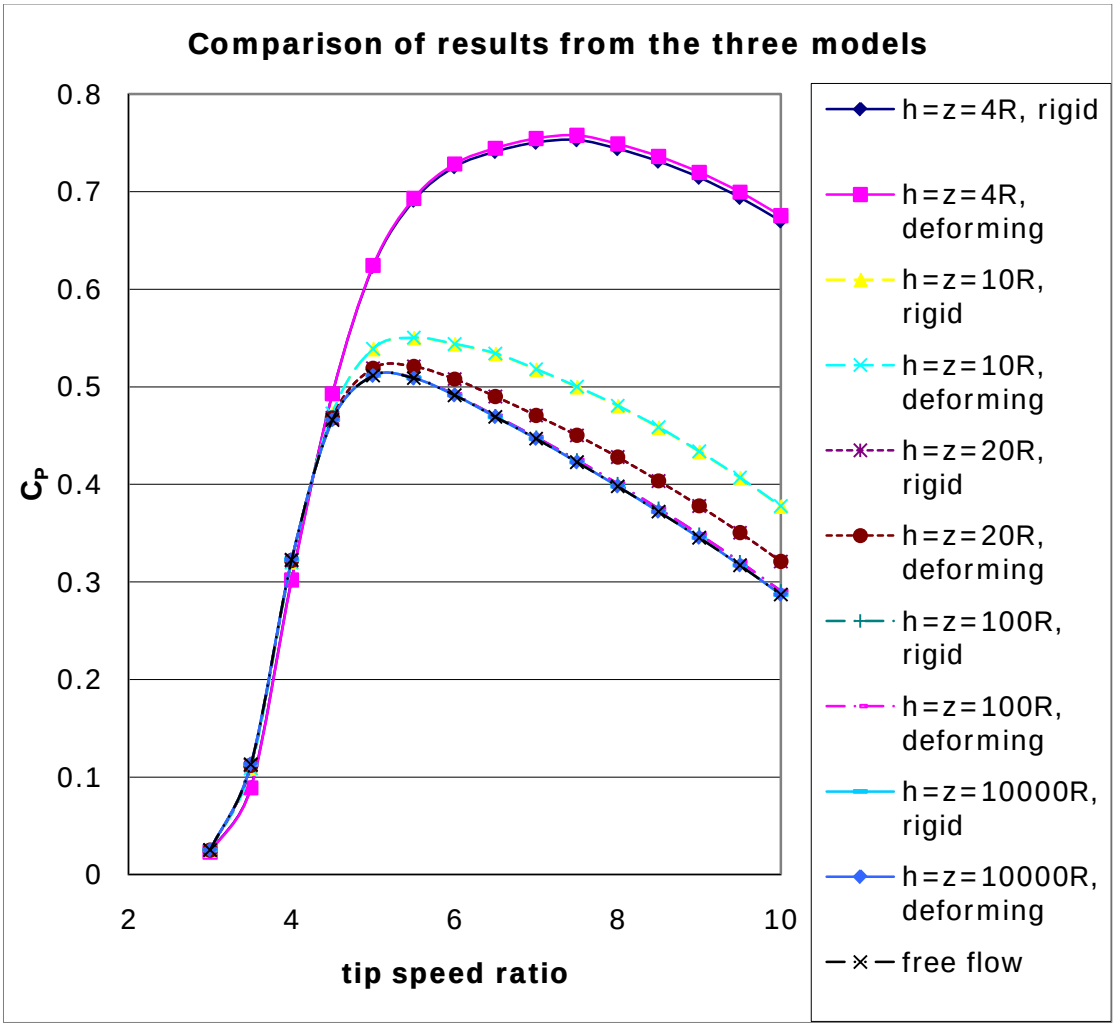

Figure 4.4- Comparison of results from the three models

It can be seen from Figure 4.4 that the difference in the results from all three models decreases as the channel area is increased. The difference between the deforming free surface and rigid boundaries models and the free flow model is very small for the channels with h=z=100r (A/hz= 0.000314) and h=z=1000r (A/hz=0.0000000314). The curves for these data series overlay each other in the graph. The results from the deforming free surface and rigid boundaries models are very similar. The difference between the two data sets is only apparent for the smallest channels.

For the smaller channel areas the peak of the power coefficient curve is shifted up and to the right. For tip speed ratios less than 4 the power coefficient values calculated using the rigid boundaries and deforming free

surface models are below those of the free flow model. In this region, the region before the power coefficient of the free flow starts to peak, the results are less dependant on channel area.

4.1.4.1 Case study- Sound of Islay

In order to allow the effects of blockage on performance to be compared with the effects of energy extraction on performance, the models developed in this chapter will also be applied to the Sound of Islay. The Sound of Islay is described in section 3.5.2. The models have been applied to section 11 of the channel. This section has a width of 900m and a cross sectional area of 21685m^2.

In the models a channel with a rectangular cross section of width 900m and depth 24m (the average depth of the channel at the section) was used to represent the section. The Seagen device installed in Stranford Lough has two 16m diameter rotors (108). This section has a depth of three times the radius of the Seagen device.

The models have been applied to rotors with diameters of 16m and 12m. For the 16m diameter rotor h=3r and z≈112r and for the 12m diameter rotor h=4r and z=150r. Figure 4.5 and Figure 4.6 show the deforming free surface model results plotted with the free flow results for a number of channel widths for channel depths of 3r and 4r. From Figure 4.5 it is apparent that for a 16m diameter turbine, the results have not converged to those of the free flow model for a channel width of either 800m or 1200m. Since the curve for a 900m wide channel will lie between the 800m and 1200m wide channel curves, the use of an aerodynamic model to represent a 16m diameter turbine in this section would lead to errors in the predicted performance. Similarly for the 12m diameter rotor the deforming free surface model for a 900m wide channel has not converged to the free flow model and so an aerodynamic model does not accurately represent this case either.

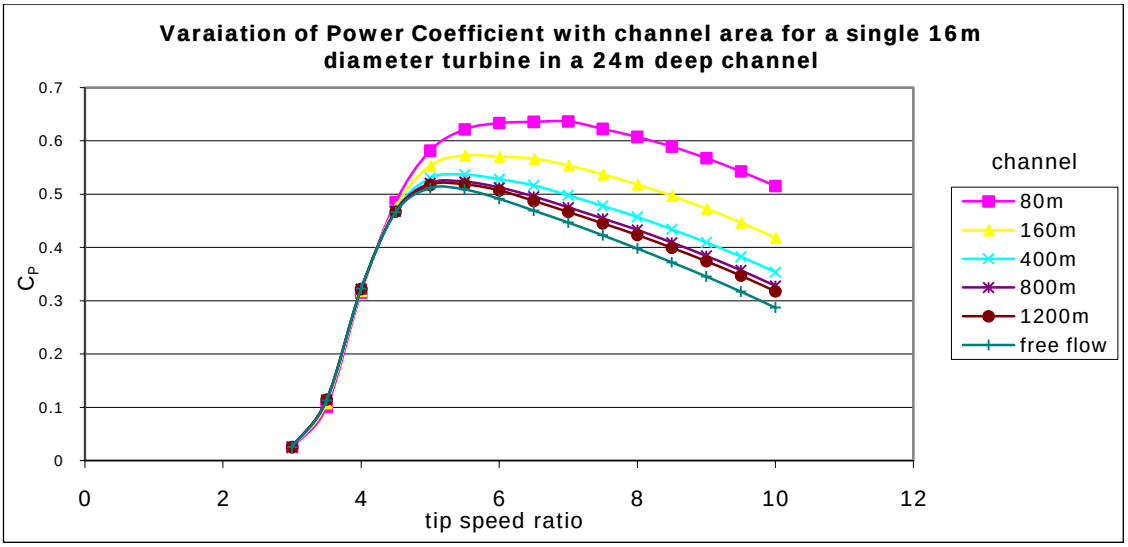

Figure 4.5- Variation of power coefficient with channel area for 16m diameter turbine

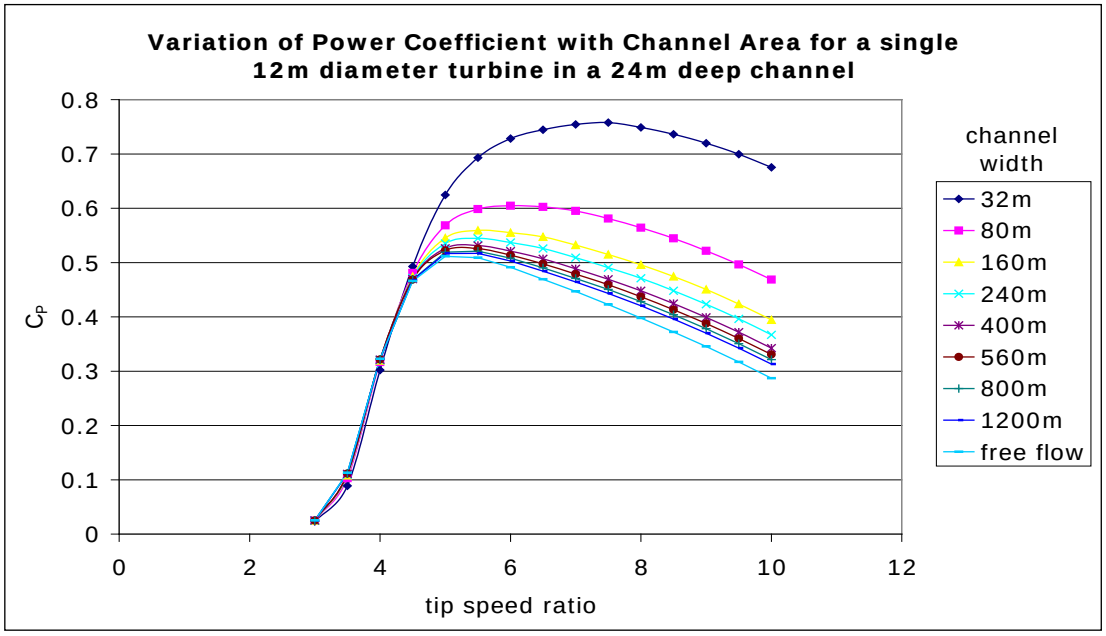

Figure 4.6- Variation of power coefficient with channel area for h=4r

4.1.5 Discussion

Three models have been presented which predict the performance of turbines in flows with different boundary conditions. The model with rigid boundaries was found to give similar results to the model in which the free surface could deform by a constant height over the width of the channel

except for channels which were very small in relation to the turbine. The results from the rigid boundary and deforming free surface models converged towards those from the free flow model as the size of the channel was increased. The difference between the results from all the models was greatest at the higher tip speed ratios. When the deforming free surface model was applied to a single realistically sized turbine in a section of a real tidal channel it was found that there was a significant difference between the results of this model and the free flow model, implying that the use of aerodynamic models to represent tidal turbines will lead to errors. It is also unlikely that only a single device would be installed in a channel, so the ratio of channel area to device area will be even smaller and the difference between the two models even more pronounced.

The models presented here are very simple models and have a number of limitations. The models assumed that the tidal channels were uniform and rectangular and that the flow was frictionless. In the deforming boundary model it was assumed that the deformation of the free surface was constant across the width of the channel. These conditions do not occur in actual tidal channels, so none of the models can be used to accurately predict the performance of a turbine. However the models do demonstrate that the boundary conditions used in a model do have a significant effect on the results for realistically sized devices and channels, even if they cannot accurately quantify the effect of the boundaries.

4.2 Comparison of effects of blockage and energy extraction on turbine performance in the Sound of Islay

Models that investigate the effects of energy extraction on performance and the effects of blockage on performance have been applied to the Sound of Islay. From the results from the model of the effects of energy extraction on the performance it was concluded that a very large number of turbines could be installed in the channel before they had a significant

effect on the flow. A significant decrease in the amount of power generated was predicted for smaller numbers of turbines but this number of turbines still greatly exceeded the blockage expected for farms that will be developed in the near future. The blockage model, however, showed noticeable differences in performance, even for single turbines. Ideally models used to predict the performance of turbines in the initial farms of turbines would consider both the effects of blockage and energy extraction on the performance of the turbines. However since the effects of blockage are much more apparent at the scale expected for initial farms, it is more important that the models take into account the effects of blockage than the effects of energy extraction.

Both of the models are based on a large number of assumptions so, whilst they are demonstrating that energy extraction and blockage have an effect on the performance, they are unlikely to be predicting the effects exactly. This suggests that it may not be worth spending a lot of money designing and building highly tuned turbines since it cannot be predicted with accuracy how farms of turbines will affect the flow or how the level of blockage will affect the performance of these turbines. The investment in ensuring that the turbines are highly tuned is unlikely to be paid back in increased energy capture, given the uncertainties in the effects of the farm on the flow and on performance and, hence, in accurately predicting what flow conditions the turbines will actually encounter.

4.3 Experimental investigation

In order to provide verification of the modelling results, experiments into the effects of blockage on tidal turbine performance were carried out. Turbine simulators were used in the experiments instead of rotating models. Turbine simulators were selected due to the difficulties associated with using rotating models in small test facilities outlined in Chapter 2.

4.3.1 Experimental set up

The experiments have been performed using the flow table at The Robert Gordon University. This facility is 3m x 2m x 0.3m and has a maximum flow speed of 1m/s. The force acting on the simulator was measured using a 600g capacity Teda Huntleigh single point load cell and the flow speed measured using a Nixon Flowmeters Streamflo probe. The Streamflo probe can measure velocities between 5 and 150cm/s (109). The probe operates by measuring the modulations in a signal caused by the blades of the rotor passing by a gold tip wire in the stem of the probe. The flow speed was calculated from the number of pulses occurring each second.

The load cell is attached to the turbine simulator in the manner shown in Figure 4.7. The vertical board which the load cell is mounted on is clamped to a beam across the flow tank and positioned so that the disc is at the desired position in the flow and the desired depth below the surface. The probe used to measure the velocity is mounted to a second beam across the flow tank. This allows the flow speed at various positions relative to the disc to be measured.

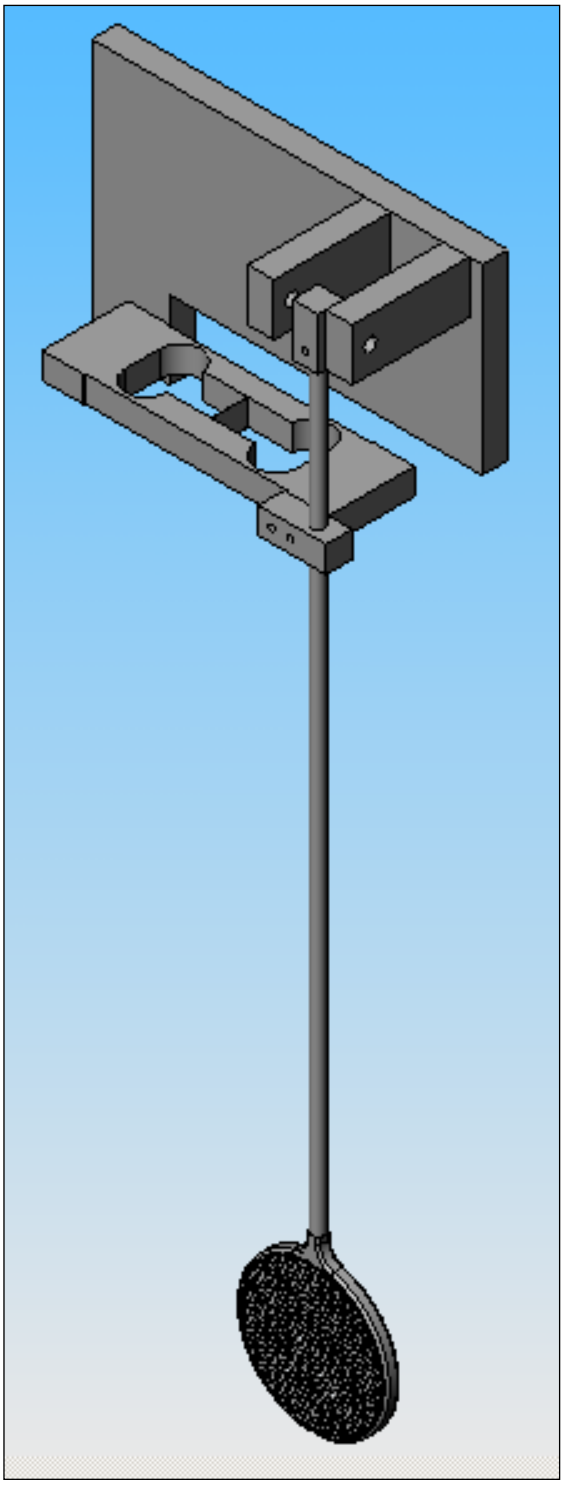

Figure 4.7- Turbine simulator and load cell

The turbine simulator consisted of a mesh disc in an aluminium frame. The frame was welded to the rod which transmitted the force acting on the simulator to the load cell. The corners of the frame were rounded off in order to reduce the drag force acting on the frame. The mesh disc had

a diameter of 50mm, a thickness of 1.2mm and an open area of 62%. Initially mesh with an open area of 47% was used, but the flow speeds behind this disc were too small to measure with the available instrumentation. Using a disc with a larger open area increased the flow speeds in the wake of the disc.

A foam partition was used to change the width of the channel in which the turbine simulator was tested. The partition ran the full length of the flow table. It was held in place using beams running across the width of the table and clamped to the upper rim of the table.

4.3.2 Scaling

In experiments with turbine simulators Froude number similarity needs to be observed but it is generally accepted that a discrepancy between the model and full scale Reynolds number is acceptable so long as both the model and full scale Reynolds numbers lie within the same turbulence classification (66).

Tests were carried out for water depths of 10cm and 15cm at flow speeds between 25 and 30cm/s. This corresponds to Froude numbers between 0.21 and 0.30. An example of a full scale channel with these Froude numbers is a 20m deep channel with flow speeds between 2.9m/s and 4.2m/s.

4.3.3 Test procedure

Initially the flow speed distribution in the flow tank was mapped without the disc in the water. The flow in the tank was found to vary considerably with position. Figure 4.8 and Figure 4.9 show the variation of flow speed with distance along and across the tank at a number of different depths.

These tests were repeated for a number of pump pressures and water depths and the flow was found to be vary considerably with position and depth for all cases. The variation of undisturbed flow speed with position and depth needs to be taken into account when designing the test procedure.

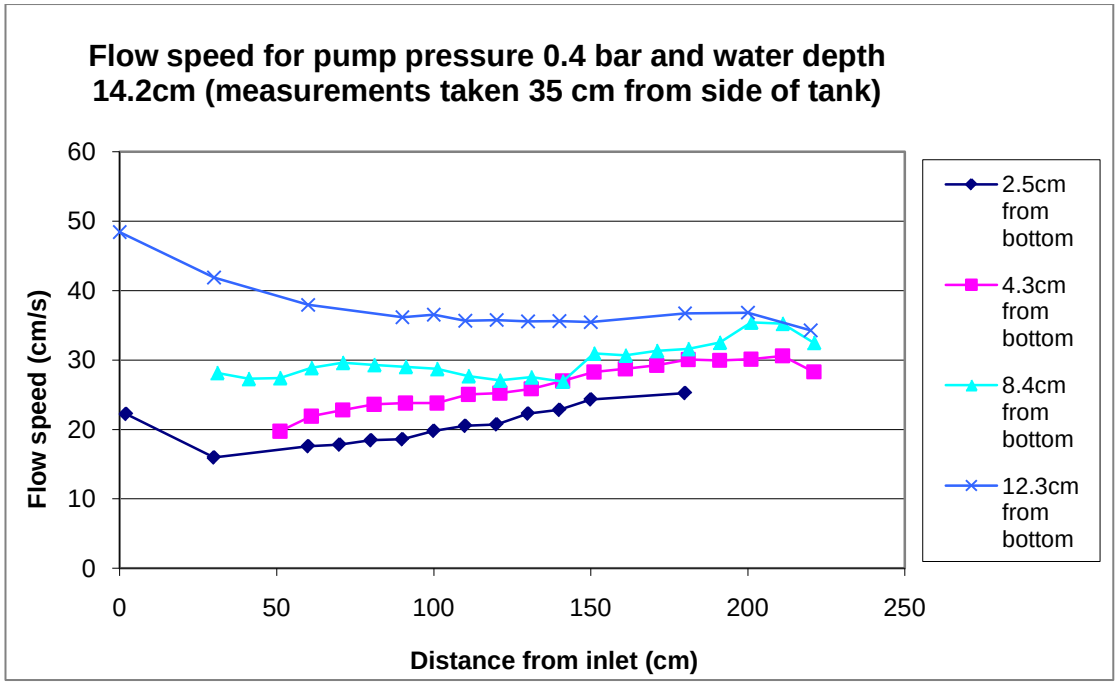

Figure 4.8- Variation of flow speed with distance from inlet

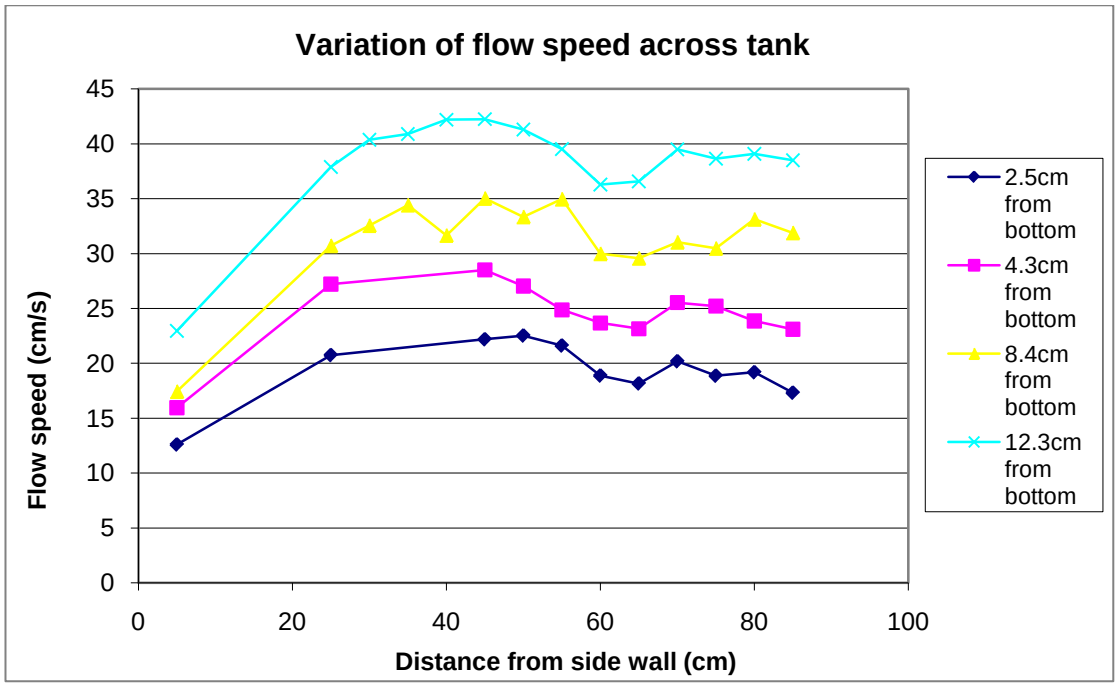

Figure 4.9- Variation of flow speed with distance from side wall of tank

The load cell was calibrated by clamping the plate to which the load cell was mounted to a horizontal surface and placing weights on the centre of the perforated disc. This allowed the relationship between the force acting on the disc and the voltage output of the load cell to be determined. The intercept of the voltage-force curve was obtained by positioning the perforated disc in the desired test position in the tank and measuring the voltage output of the load cell while the water in the tank is stationary. The calibration readings were carried out at a number of different times during the day. There was a very slight variation in the gradient of the curve and a much larger variation in the intercept over the course of the day. The slight variation in the gradient of the curve will be due to slight deviations in the positioning of the weights from the centre of the disc. The variation of the intercept over the course of the day was due to temperature effects.

In order to reduce the uncertainty in the results caused by the non-uniform flow and varying intercept of the calibration curve the following test procedure was devised:

1. Turbine simulator in position in tank, no flow, no flow probe. 3 data sets of force readings to find zero load voltage output for calibration.
2. Turbine simulator in position in tank, flow, no flow probe. 3 data sets of force readings to find force acting on simulator at given flow speed.
3. Turbine simulator in position in tank, no flow, no flow probe. 3 data sets of force readings to find zero load voltage output for calibration.
4. Turbine simulator in position in tank, flow, flow probe 20mm upstream of turbine simulator and level with centre of turbine simulator. 3 data sets of flow speed and force for use in estimating the flow speed through the disc.

5. Turbine simulator in position in tank, flow, flow probe 23mm downstream of turbine simulator and level with centre of turbine simulator. 3 data sets of flow speed and force for use in estimating the flow speed through the disc.
6. Turbine simulator removed from tank, flow, flow probe in plane which disc was previously in. 3 data sets of flow speed for each of the positions shown in Figure 4.10 for use in estimating the free-stream speed of the flow.

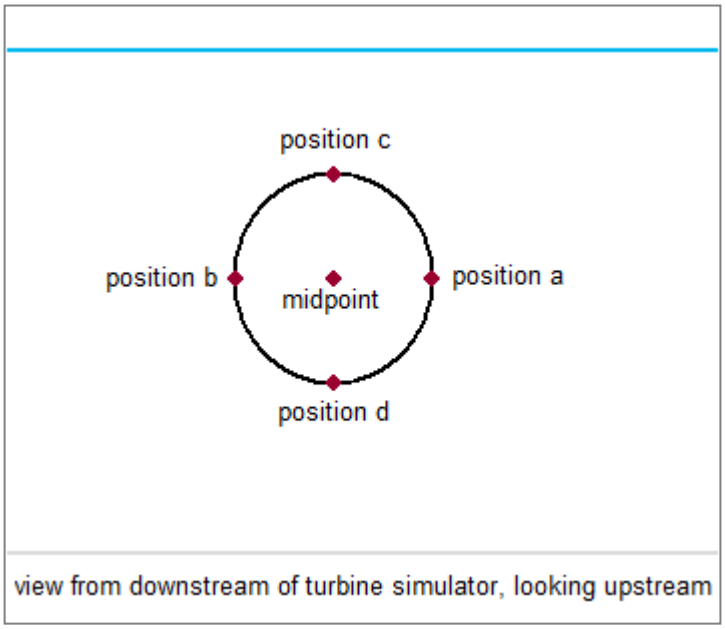

Figure 4.10- Definition of positions for flow sensor

4.3.4 Results

In order to determine how the channel width is affecting the energy extracted by the turbine simulator, the free-stream flow speed, flow speed through the disc and force acting on the disc need to be known. The power generated by the turbine simulator is assumed to be the product of the force acting on it and the velocity of the flow through it (see section 2.2). The free stream velocity is needed to calculate the power in the undisturbed stream, which is used to calculate the power coefficient.

The Streamflo probe does not allow the direct measurement of the speed at the disc. Instead flow speed measurements were made either side of the disc. Linear interpolation was used to estimate the flow speed at the disc from the measurements made either side of the disc. In the streamtube model of a turbine, the flow speed varies in the manner shown in Figure 4.11. Since the speed of the flow through the disc will vary in this manner, estimating the disc velocity from linear interpolation should be reasonably accurate so long as the measurement points are sufficiently close to the disc.

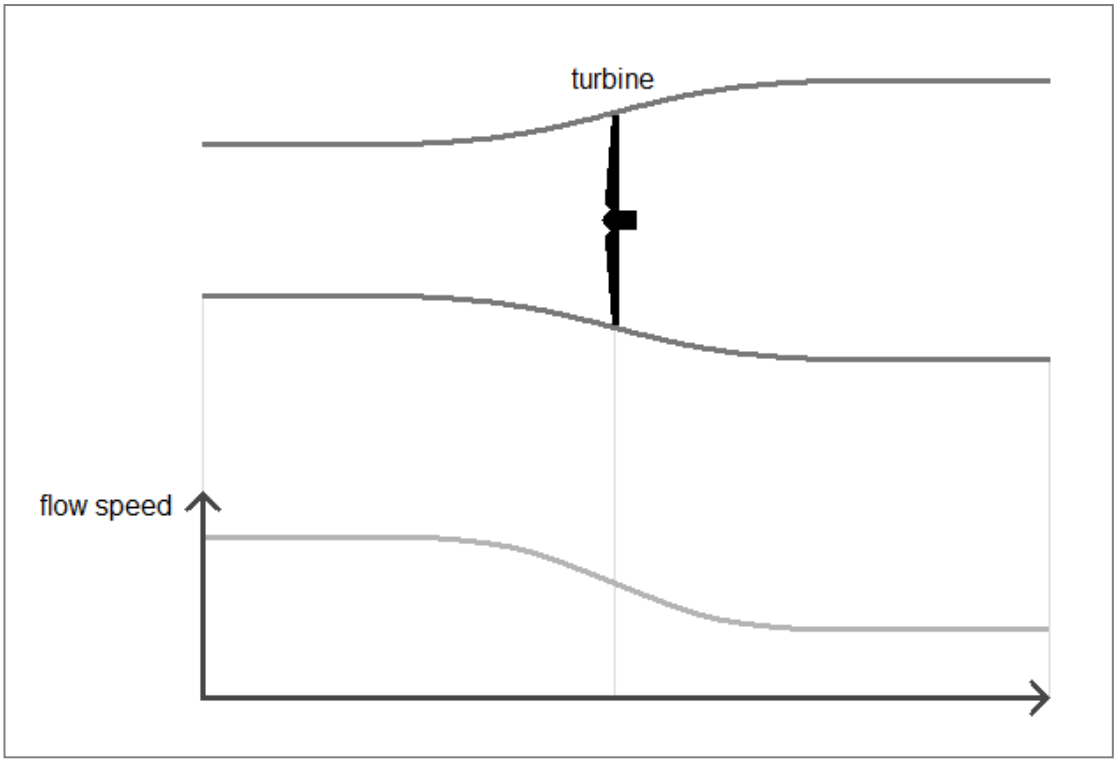

Figure 4.11- Variation of flow speed in streamtube for actuator disc model

In order to establish the free-stream velocity, speed measurements were taken without the turbine simulator in the water. The measurements were taken at a number of points which would be located on the disc, if the disc were in position. The free-stream velocity was taken to be the average of these velocities. This method of calculating free stream velocity was chosen in order to reduce the errors introduced by the non-uniform flow in the tank. If the flow is uniform, the free-stream velocity could be

measured at a point sufficiently far upstream of the disc for the disc to have no effect. Since the flow is non-uniform, it is the undisturbed flow speed through the disc area which is needed for power coefficient calculations. Use of the far upstream velocity would lead to errors since it is not representative of the undisturbed flow speed at the disc.

The intercept used in conversion of the logged values of load cell output was taken to be the average of the no-flow data sets taken either side of the load measurement. The gradient of the calibration curve remained constant over the testing period, so this did not need to be changed for each force reading in the same manner that the intercept did.

Initially tests were carried out for a number of widths of channel with a water depth of 150mm. Figure 4.12 shows how the power generated by the turbine simulator varied with channel width. As the channel width is increased, the blockage decreases and there should be a corresponding decrease in power generated. This trend is not apparent in Figure 4.12. Figure 4.13 shows the variation of free-stream velocity with channel width. Power is proportional to velocity cubed, so the variation of free-stream velocity shown in Figure 4.13 is sufficient to cause significant variations in the power generated by the turbine simulator and hence, the trend expected due to blockage is not apparent.

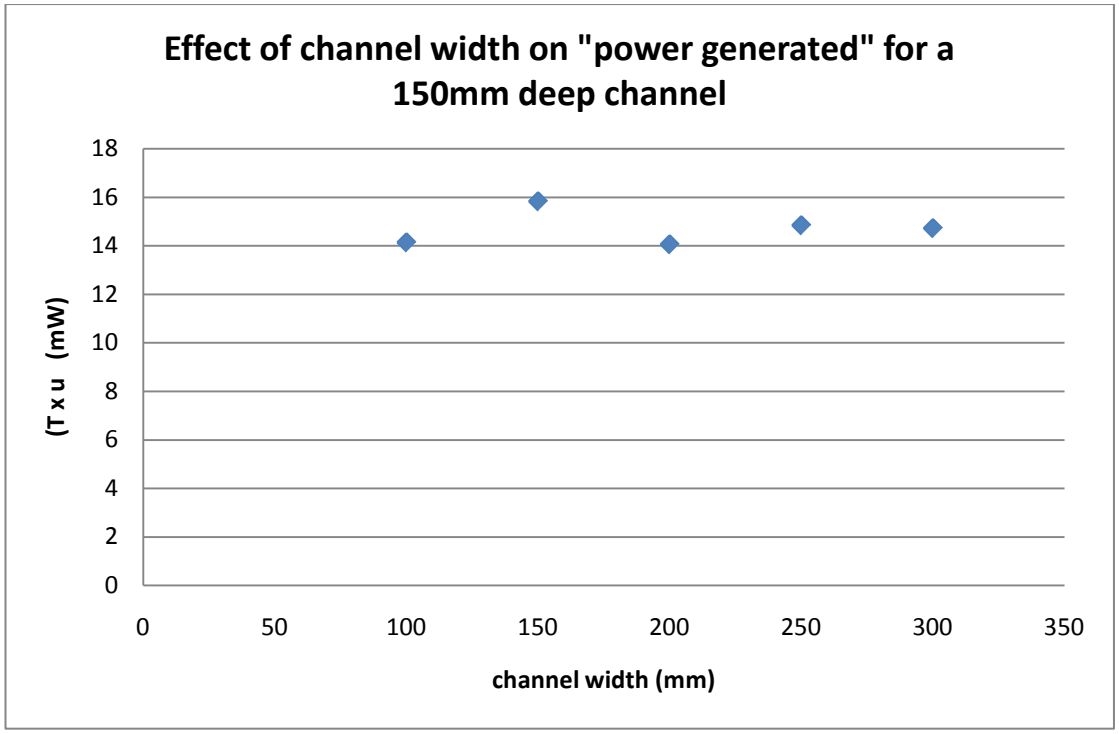

Figure 4.12- Effect of channel width on power generated for a 150mm deep channel

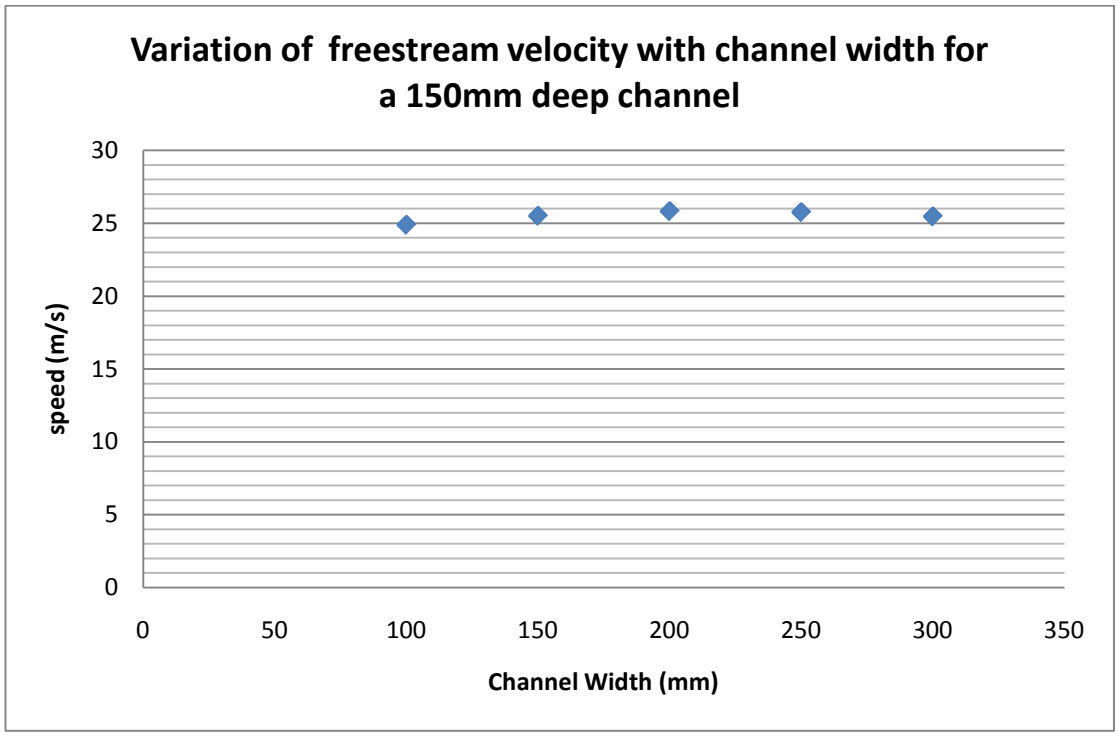

Figure 4.13- Variation of free-stream velocity with channel width for a 150mm deep channel

Further tests were carried out at an increased flow speed in a channel with a 100mm water depth. The depth of the channel was decreased so that the effects of blockage would be more apparent. The tests were carried out at a faster flow speed so that the variations in velocity would have proportionally less effect. Figure 4.14 shows how the power generated by the turbine simulator varied with channel width. The scatter of the results is greater than for the 150mm deep channel. Once again, there is not an pronounced trend between channel width and power generated.

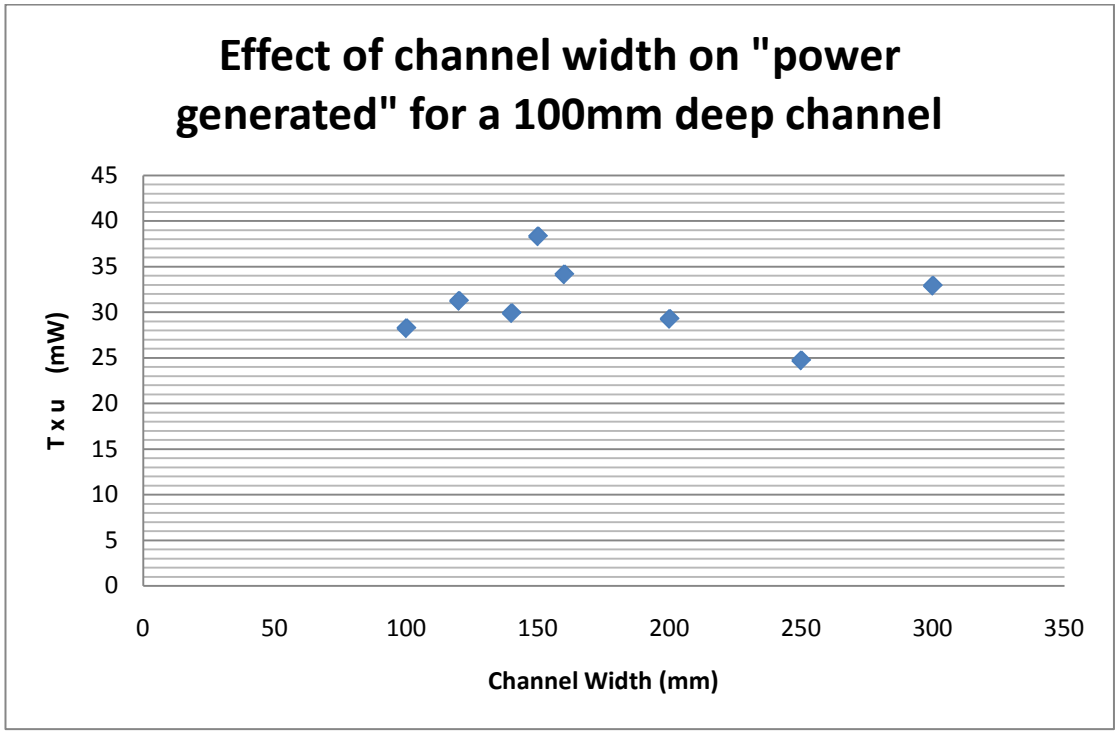

Figure 4.14- Effect of channel width on power generated for a 100mm deep channel

In order to compare the relative effects of free-stream velocity variation for the 100mm and 150mm deep channels, a graph of free-stream velocity/ maximum free-stream velocity was plotted (Figure 4.14). It can be seen from this graph that there is very little difference in the magnitude of variation of the two data sets. This implies that the effect of the variation of free-stream velocity on the power generated will be of similar magnitude for the 100mm deep channel results as it was for the 150mm channel results.

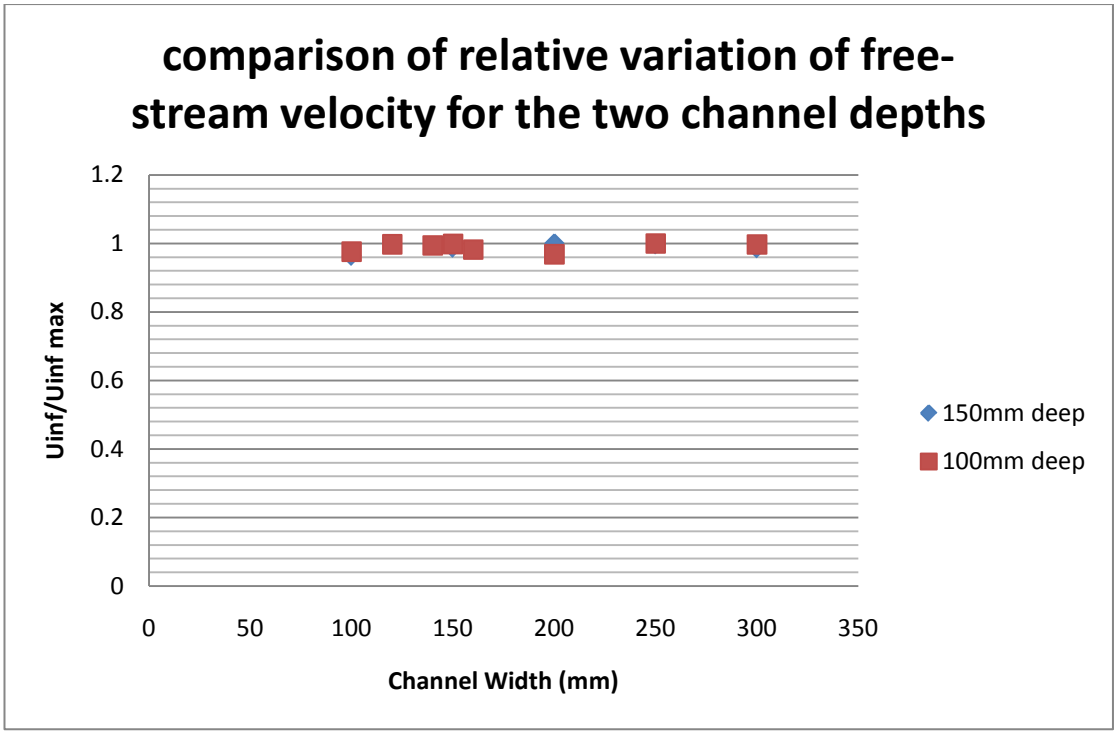

Figure 4.14- Comparison of the relative variation of free-stream velocity for the two channel depths

In Figure 4.15 the variation of power coefficient with channel width is plotted for both depths of flow. The power coefficients shown in this graph are all higher than the Betz limit, implying that blockage is affecting the performance of the turbine simulator. Least squares regression was used to fit a linear trend line to both sets of C_p results. Both of these trend lines have a negative gradient. Whilst this is insufficient evidence demonstrate conclusively how power coefficient increases with blockage, it does indicate that as the blockage increases, the power coefficient increases.

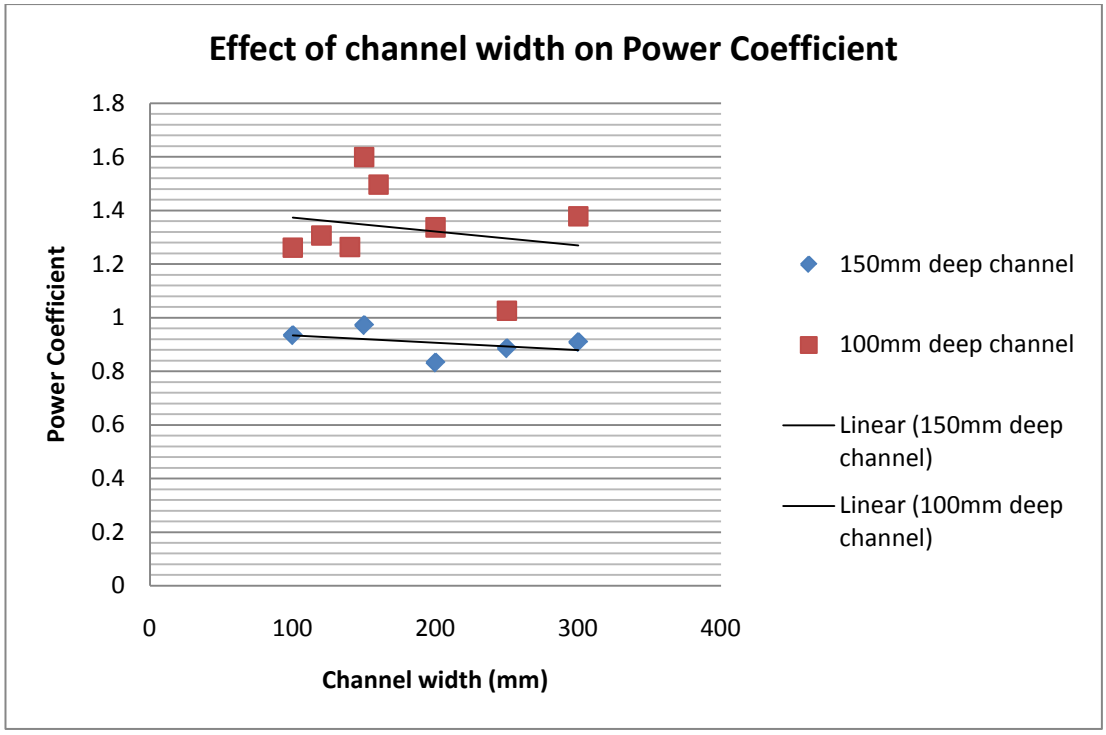

Figure 4.15- Effect of channel width on power coefficient

4.3.5 Discussion

The experimental results do not clearly demonstrate the relationship between blockage and performance. This is thought to be due to the variation of the free-stream velocity with channel width caused by the non-uniform flow in the tank. Using the rigid boundaries model, modelling results were generated for comparison with the experimental results.

For the model to be applied, the dimensions and flow speeds needed to be scaled up from the flow table scale to full size. Using the flow table speeds and dimensions directly in the model leads to unrealistic results. This is because Froude number similarity was maintained in the experiments but Reynolds number similarity was not. As discussed in Chapter 2, it is not feasible to maintain Reynolds number similarity for experiments in small test facilities. For turbine simulators this discrepancy in Reynolds number is acceptable as long as both the model and full scale Reynolds number lie within the same turbulence classification (66). At the Reynolds numbers at which the experiments were carried out, the turbine would be stalled.

Using full scale dimensions and flow speeds in the model allows realistic blade element forces to be predicted. The modelling results can then be converted back to the experiment scale using Froude number similarity. In the modelling a full scale channel with a depth of 24m was used. The equivalent full scale dimensions and speeds for the experimental dimensions and speeds are given in Table 4.1. The design of turbine used in the model was Turbine B, operating at optimum tip speed ratio and hub pitch angle.

Table 4.1 Full scale dimensions and speeds corresponding to experimental dimensions and speeds

	Experimental	full scale
depth of flow	0.1m	24m
turbine radius	0.025m	6m
maximum channel width	0.3m	72m
minimum channel width	0.1m	24m
maximum free-stream velocity	0.2907m/s	4.503m/s
minimum free-stream velocity	0.2816m/s	4.362m/s

The model was used to calculate T, u, power generated and Cp for the maximum and minimum free-stream velocities at both the minimum channel width and the maximum channel width. The results are not directly comparable with the experimental results because the performance of the turbine used in the model will differ from the performance of the turbine simulator. The modelling results do however give an indication of the maximum scatter which is possible due to the variation in free-stream velocity. Figure 4.16 shows the experimental and modelling results for the power generated by the turbine. The power generated has been divided by the maximum power generated for each data set in order to allow comparison between the sets.

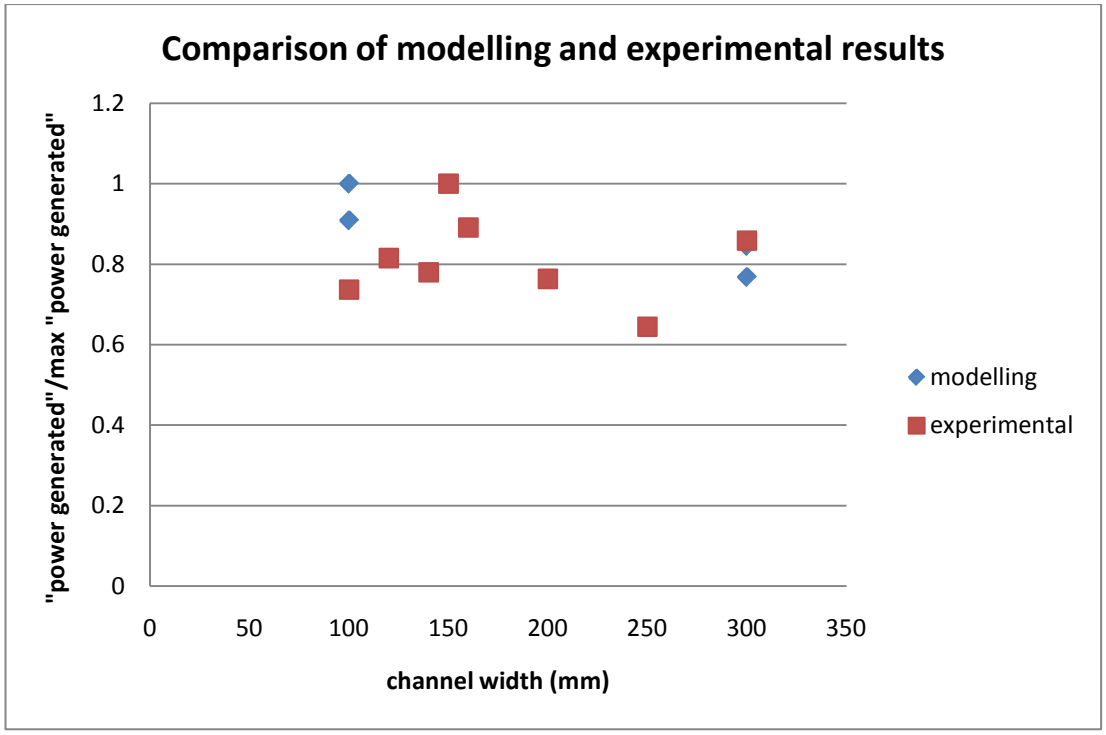

Figure 4.16- Comparison of experimental and modelling results

It can be see from Figure 4.16 that the scatter of the experimental data set is greater than the scatter which would result from the variation in free-stream velocity measured. The gradient of a linear trend line fitted to the experimental data is, however, within the range predicted by the modelling data. This implies that the experimental results could show the same trend as was predicted by the model. The high level of scatter in the experimental results is due to the significant variations in flow speed with position in the flow table. Since the undisturbed flow speed was calculated from the measured flow speed at a limited number of points corresponding to positions on the turbine simulator, and the velocity at these points was found to vary considerably, the estimates of free-stream velocity contain a high degree of uncertainty. This explains why the scatter of the experimental data fell outside the bounds predicted by the modelling results.

4.4 Summary

Modelling suggests that blockage will have a significant effect on the performance of turbines. Experiments were carried out to investigate the effect of blockage on the performance of a turbine simulator. The power coefficient values measured in the experiments were much higher than the Betz limit, so blockage was obviously affecting the performance. The experimental results were, however, unable to provide verification of the modelling results due to the high level of uncertainty in the experimental results. The uncertainty in the experimental results was due to the limitations of the test facility, in particular the significant variation of flow speed with position.

Chapter 5 The effects of boundary proximity on tidal turbine performance

The models developed in the previous chapter do not take into account the distance between the turbine and the free surface. Akwensivie (43) demonstrated using CFD modelling that the geometry of the wake of a turbine changed with distance of the turbine from the surface. This change in wake geometry also implies a change in turbine performance. Bahaj et al carried out towing tank tests with the rotor at two different depths (35). The performance of the rotor at the shallower depth was found to be lower than the performance of the rotor at the deeper depth. These results demonstrate that the surface proximity has an effect on the performance of the turbine, but do not provide enough information to allow the effect to be quantified. In order to gain a deeper understanding of how the performance varies with surface proximity the performance numerical modelling has been carried out. In this investigation the turbine was situated at a number of different positions relative to the free surface for a range of inflow conditions.

5.1 CFD Solution

Simulations were carried out using the commercial CFD package Fluent. In these simulations the turbine was represented by a porous disc. It was felt that the limitations of using an actuator disc rather than a rotating turbine were far outweighed by the increase in the simplicity of the case to be simulated. The multiphase flow model used to visualise the deformation of the free surface was the volume of fluid (VOF) model. The calculations which were carried out were for 2D cases.

5.1.1 Fluent

Fluent has two types of solver: a pressure based solver and a density based solver. For both of these solvers a finite volume discretisation method is used but the approach used to linearize and solve the discretised equations varies depending on which solver is used. Both the solvers are capable of solving a wide variety of flows but the pressure based solver was originally developed for incompressible or mildly compressible flows whereas the density based solver was developed for compressible flows. The pressure based solver has been selected for use in these simulations.

5.1.1.1 Porous jump

The porous jump model in Fluent allows a thin "membrane" with known pressure drop characteristics to be modelled. This model is 1D and so is simpler and more robust and yields better convergence than the porous media model. The pressure change across the porous jump is determined using Equation 76.

$$\Delta p = -\left(\frac{\mu}{\alpha_m} u + C_2 \frac{1}{2} \rho u^2 \right) \Delta m$$

Equation 76

where:

$\Delta p =$ pressure change across the porous jump

$\mu =$ laminar fluid viscosity

$\alpha_m =$ permeability of the medium

$u =$ velocity normal to the porous face

$C_2 =$ pressure jump coefficient

$\rho =$ fluid density

$\Delta m =$ thickness of medium

In Chapter 2 an equation was presented that relates the pressure drop across a porous gauze to the resistance coefficient of the gauze. This equation is:

$$\Delta p = -\frac{1}{2}\rho k u^2$$

Equation 6

Equating these two expressions gives:

$$-\left(\frac{\mu}{\alpha}u + C_2\frac{1}{2}\rho u^2\right)\Delta m = -\frac{1}{2}\rho k u^2$$

Equation 77

if there is to be a direct correlation between Equation 76 and Equation 6 then the $-\frac{\mu}{\alpha}u\Delta m$ term must be equal to zero. $-\frac{\mu}{\alpha}u\Delta m \to 0$ as $\alpha \to \infty$ so for the Δm values used in the simulations, α values of the magnitude of $1.00\text{x}10^{10}$ reduce this term to a magnitude where it will have no effect on Δp. This allows the constant C_2 to be written in terms of k (Equation 78).

$$C_2\Delta m = k$$

Equation 78

5.1.1.2 VOF model

Fluent has a number of models for multiphase flows. The VOF model has been selected as it is the most appropriate for free surface flows. The VOF model is a surface tracking technique (110). The VOF model uses a single set of momentum equations and the volume fraction of each fluid in each cell is tracked throughout the entire domain.

5.1.2 Simulation set up

The simulations were carried out for a 2D case. The 2D case was chosen as it is simpler and faster to model than a 3D case and so it provides a valuable learning environment in which the user can become familiar with the models used and boundary and grid requirements of the simulation. The 2D case also allows more direct comparison with the results from the analytical models. In the analytical model of the effect of blockage on performance the turbine, the deflection of the free surface was assumed to be uniform across the whole channel. This is equivalent to assuming that the flow is two dimensional.

The turbulence model used in the simulations was the k-ω SST model. This model was selected for the reasons given in Chapter 1.

Initially the behaviour of a 0.8m long porous jump in an unbounded flow was investigated. The computational domain was bounded on 3 sides by a pressure outlet and the fourth side was a mass flow inlet. These simulations showed that the size of the elements, particularly on the porous jump, and the position of the boundaries had a significant effect on the results. The velocity along a horizontal line running from inlet to outlet through the centre of the porous jump was found to be a good indication of whether the solution had converged.

In the multiphase model, at the inlet, the water depth was set to 2m, the mass flow rate of water was set to 3992.8 kg/s and the mass flow rate of air was set to 0kg/s. This corresponded to a water flow speed of 2m/s. The length of the porous jump was again 0.8m.

The multiphase model was initially run with $C_2=0$. This gave a flow with constant free surface level. The velocity of the flow was also constant except for a thin boundary layer attached to the wall boundary.

The computational domain used in the simulations is shown in Figure 5.1. The length of the domain is 80m and the porous jump is situated 10m from the inlet. When the behaviour of the porous jump in an unbounded flow was studied, it was found that a 120m domain length was needed before the position of the boundaries stopped having an effect on the results. For the multiphase model for domain lengths of over 100m problems develop with the simulations with the water flowing up the side of the inlet.

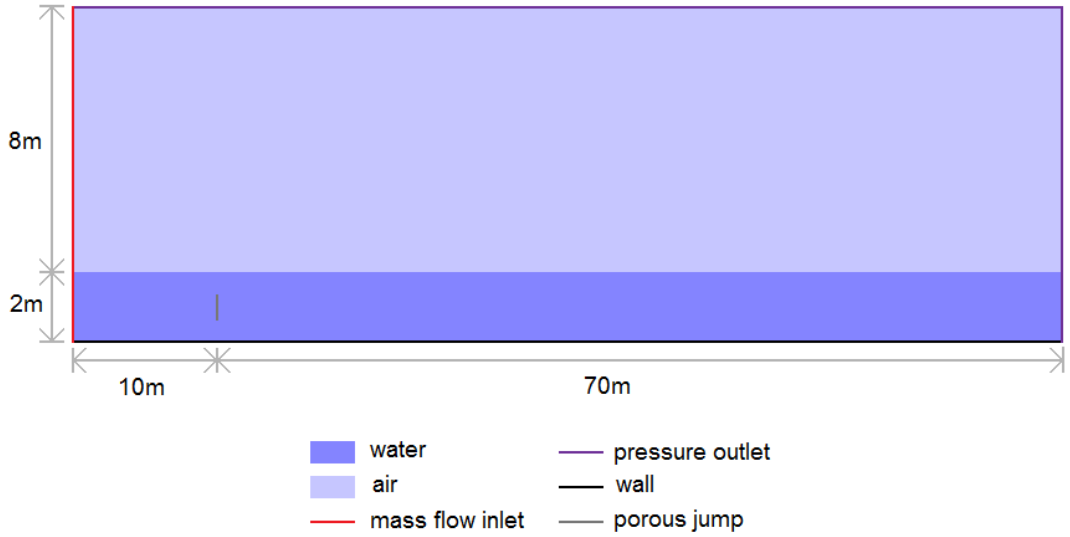

Figure 5.1- Computational domain used in simulations

Figure 5.2 shows the effect of domain length on the axis velocity for a centrally placed disc. It can be seen from this graph that changing the domain length affects the velocity recovery, but does not affect the velocity change from upstream of the disc to the minimum velocity after the disc. This indicates that the domain length should not have a large effect on the power extracted by the disc. An 80m domain length was chosen for the simulations as this gave a good compromise between accurately modelling the wake recovery behind the disc and computational efficiency.

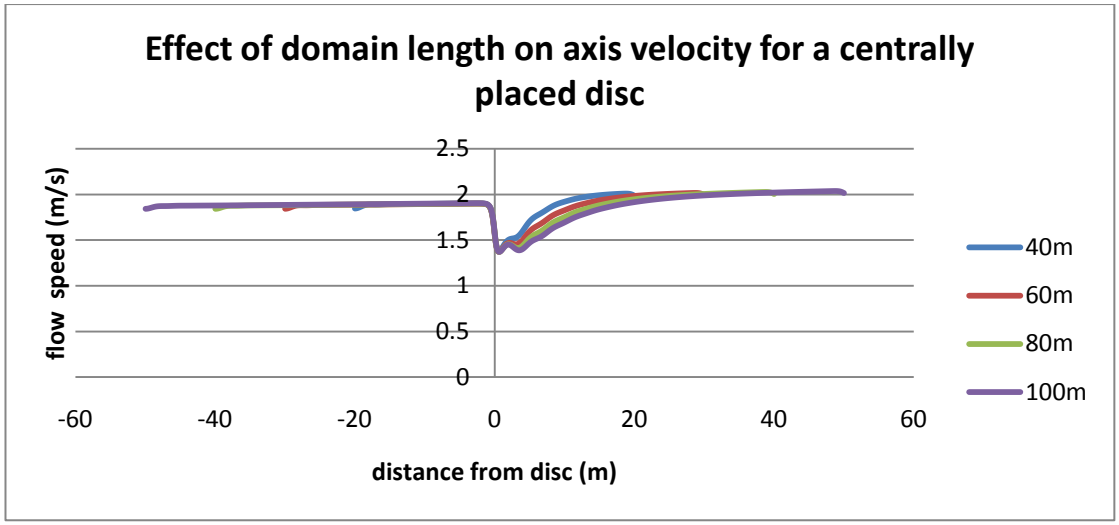

Figure 5.2- Effect of domain length on axis velocity for a centrally placed disc

Whilst the length of the domain does not affect the pressure change across the disc, the position of the disc relative to the inlet does have an effect. Figure 5.3 shows how the pressure change across the disc varies with the ratio of disc position to domain length. As the distance from the inlet to the disc increases, there is an increase in the pressure change across the disc. This increase in pressure change with disc position can be explained by considering how the flow speed along the disc axis varies with disc position. Figure 5.4 shows that as the distance between the inlet and the disc increases there is a slight increase in the velocity upstream of the disc. This suggests that any disc position will give acceptable results if the appropriate upstream velocity is used. Apart from one anomalous data point for the 80m domain and one anomalous data point from the 100m domain, the results from all the domain lengths lie along the same line. This confirms that the domain length does not affect the pressure change across the disc. In the simulations the disc has been placed 10m from the inlet.

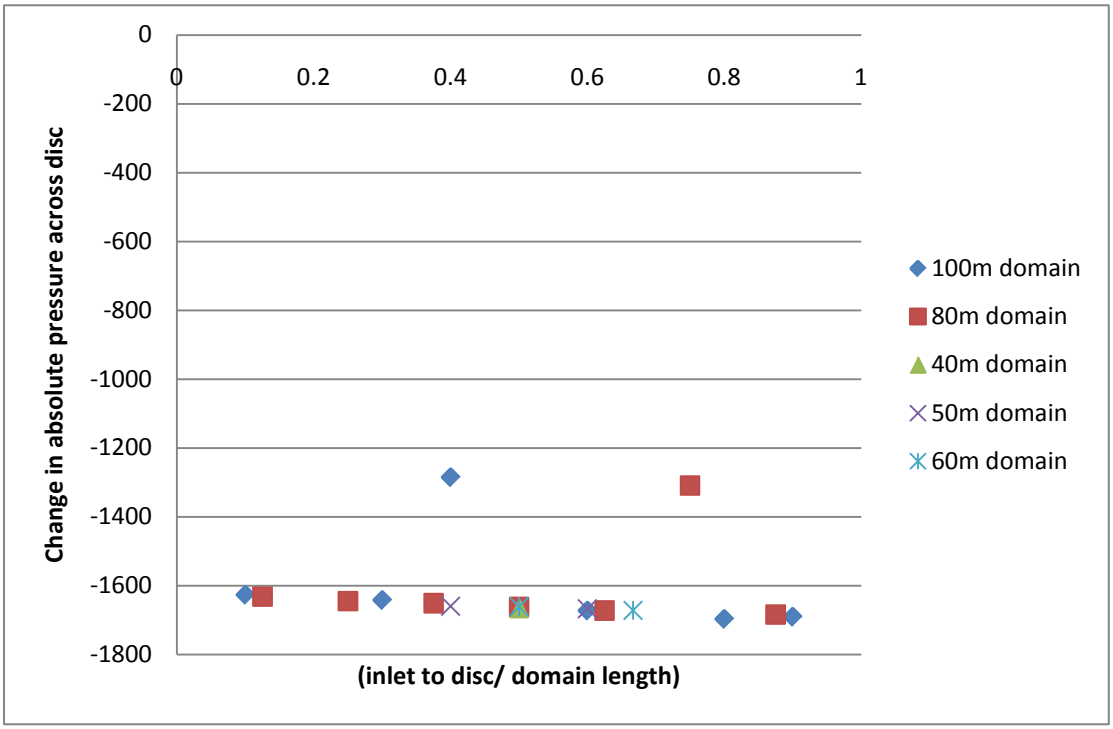

Figure 5.3- Effect of inlet position on pressure change across disc

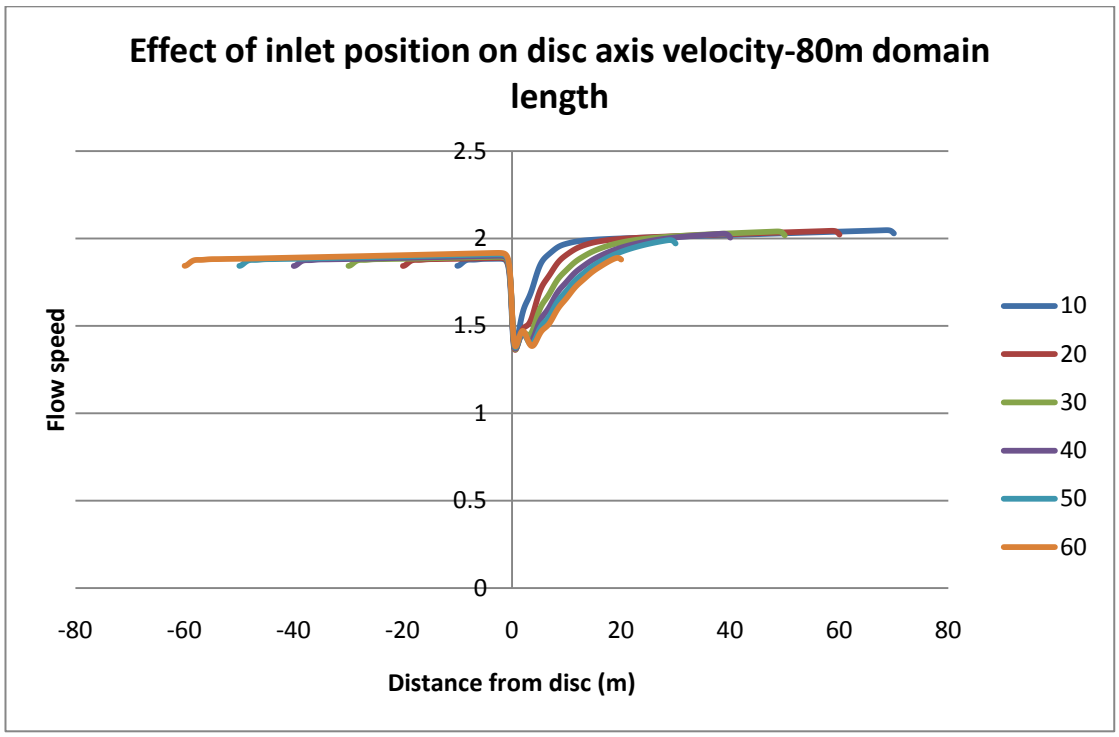

Figure 5.4- Effect of inlet position on disc axis velocity for 80m domain length

The regions in which the element size has the greatest effect are those close to the disc and those close to the free surface. In order to reduce

the computational time, the domain has been split into a number of regions with different mesh sizes. This allows small elements to be used in regions where the element size has a large effect on the results and larger elements to be used elsewhere. The different mesh zones and the element sizes used in these zones are shown in Figure 5.5. The size of the elements in the region close to the disc was determined by carrying out simulations in a domain with a uniform element size. The effect of element size on the pressure change across the disc is shown in Figure 5.6. Once the appropriate size for the element in the region close to the disc had been determined, the region was zoned. The results from the zoned region were compared with those from the region with a uniform element size. The results from the two simulations were found to be very similar so the solution was deemed to be independent of the grid size for the chosen element sizes in the zoned region.

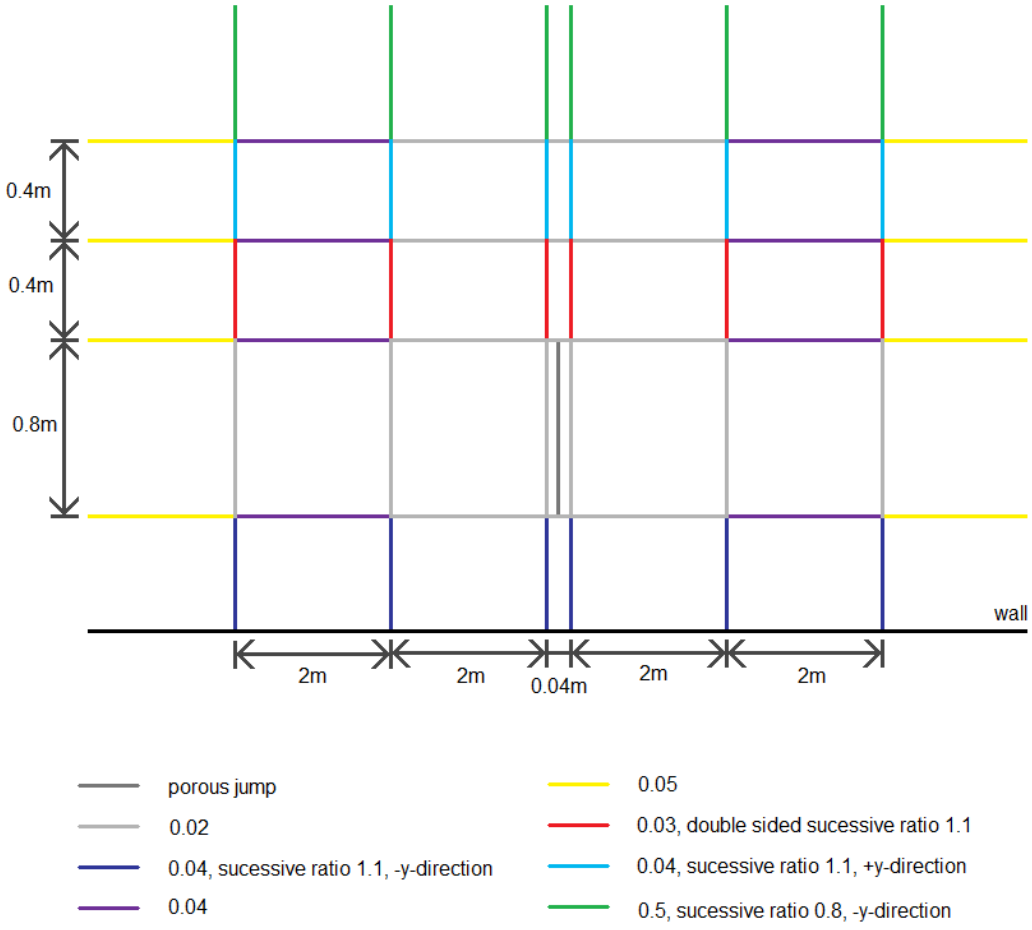

Figure 5.5- Element sizes in mesh zones

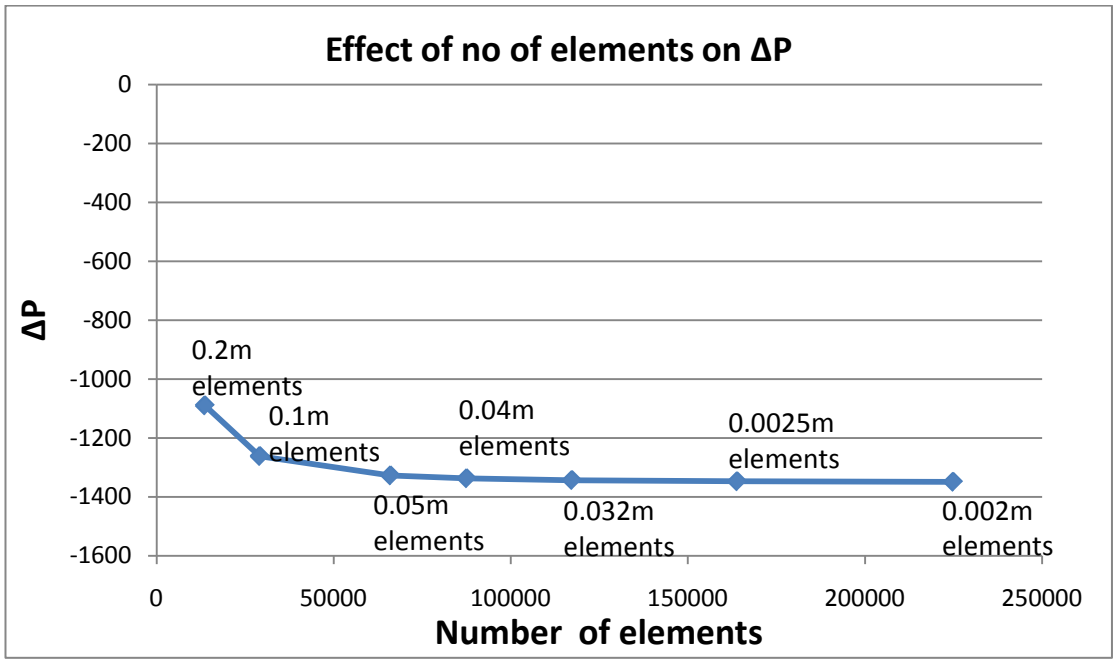

Figure 5.6- Effect of size of elements on disc on pressure change across disc

5.1.3 Results

Simulations were run for a range of pressure drop coefficients between 1 and 20. This corresponded to power coefficient values between 0.036 and 0.47 for the porous region in an infinite flow. For each pressure drop coefficient simulations were run with the disc in 10 different positions ranging from the base of the disc being positioned 0.1m from the channel bed and the top of the disc being positioned 0.2m from the free surface.

Simulations were also carried out for simulations in an all water 120m by 80m zone with a pressure outlet replacing the wall boundary. The disc was placed at the middle of the zone in the y direction and two thirds of the way along the zone in the x direction. In the initial tests carried out to investigate boundary and grid dependence this domain size and disc position was found to give a reasonable representation of disc performance in an infinite zone. These simulations were carried out in order to obtain a baseline value for the performance with which the

channel results could be compared. The performance of the disc in this zone is equivalent predicting the performance of a turbine using an aerodynamic model.

The simulations yielded results for the absolute pressure at points on the front side of the porous region and at points with the same y-positions on the downstream side of the porous region. The velocity at points with the same y-positions mid way between the front and back sides of the porous region were also obtained. This allowed the pressure difference across the disc at each y position to be calculated. Multiplying the pressure difference at each y-position by the velocity through the disc at that y-position and integrating over the area of the disc allows the power per unit width generated by the disc to be calculated. Simpson's rule was used to carry out this numerical integration. Simpson's rule approximates the curve between the points using a series of quadratic curves (97).

The power coefficient was calculated from the power generated per unit width using Equation 79. The variation of power coefficient with porous region position is shown in Figure 5.7. The dashed lines in Figure 5.7 show the unbounded flow values of the power coefficient for each value of the pressure drop coefficient. It can be seen from this graph that the variation of power coefficient with position is small. The highest power coefficients were observed when the porous zone was placed roughly halfway between the channel bed and the undisturbed free surface position. The power coefficient of the discs in the channel was significantly higher than the power coefficient of the disc in the unbounded flow for a pressure drop coefficient of 20. For the lower pressure drop coefficients there was less difference between the channel and unbounded power coefficients. For a pressure drop coefficient of 10 the channel power coefficients were slightly higher than the unbounded value and for a pressure drop coefficient of 5 the unbounded value fell between the maximum and minimum channel values. Figure 5.8 shows how power coefficient divided by maximum power coefficient varies with porous jump position for each pressure drop coefficient. For each porous jump position, the maximum power coefficient

for that position was used. Plotting the results in this manner allows the effect of disc position on performance of the different pressure drop coefficients to be compared.

$$C_P = \frac{power\ per\ unit\ width}{0.5\rho_{water}\ u_\infty^3\ l}$$

Equation 79

Where:

l is the height of the porous region

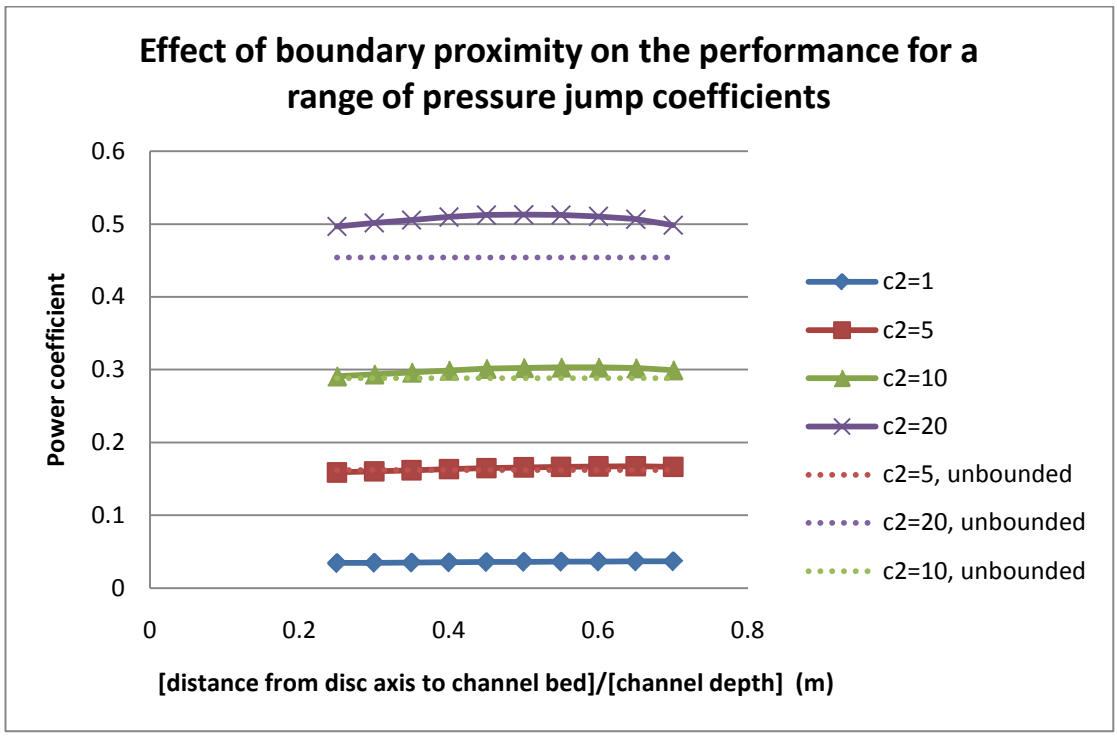

Figure 5.7- Effect of boundary proximity on performance

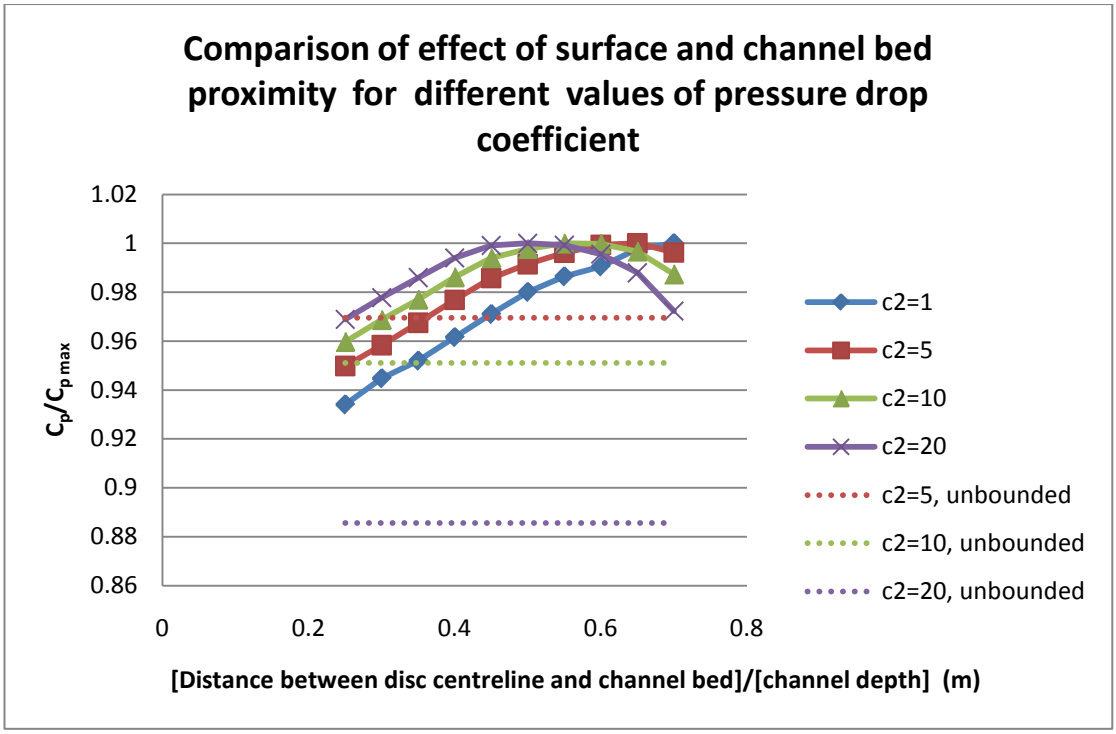

Figure 5.8- Comparison of effect of surface and channel bed proximity for different values of pressure drop coefficient

It can be seen from Figure 5.8 that the power coefficient increases as the distance from the channel bed is increased and decreases again as the free surface is approached. The point at which the power coefficient peaks is dependant on the magnitude of the pressure drop coefficient. The position of the peak shifts towards the right as the pressure drop coefficient decreases. For the simulations in which the pressure drop coefficient is 1, the peak is outside the data range. To the left of the peak the power coefficient increases in a roughly linear manner whereas to the right of the peak the decrease is better described by a quadratic relationship. In order to gain a more detailed understanding of these differences the variation of the free surface profile and flow speed throughout the domain were investigated.

Figure 5.9 shows the variation of the velocity along a line parallel to the channel bed which passes through the mid point of the porous jump region for a pressure drop coefficient of 20. The other pressure drop coefficients show similar trends with the magnitude of the velocity change across the disc decreasing as the pressure drop coefficient decreases. It

can be seen from Figure 5.9 that the velocity upstream of the porous region is below 2m/s, the desired free-stream velocity for the simulations. After the porous jump the velocity increases to a velocity which is higher than the velocity upstream of the porous jump region. There is also a slight variation in the magnitude of the velocity at all points along the length of the domain between the different porous region positions. In Figure 5.10 the variation flow speed has been plotted in just the region close to the porous disc in order to allow this effect to be seen more clearly.

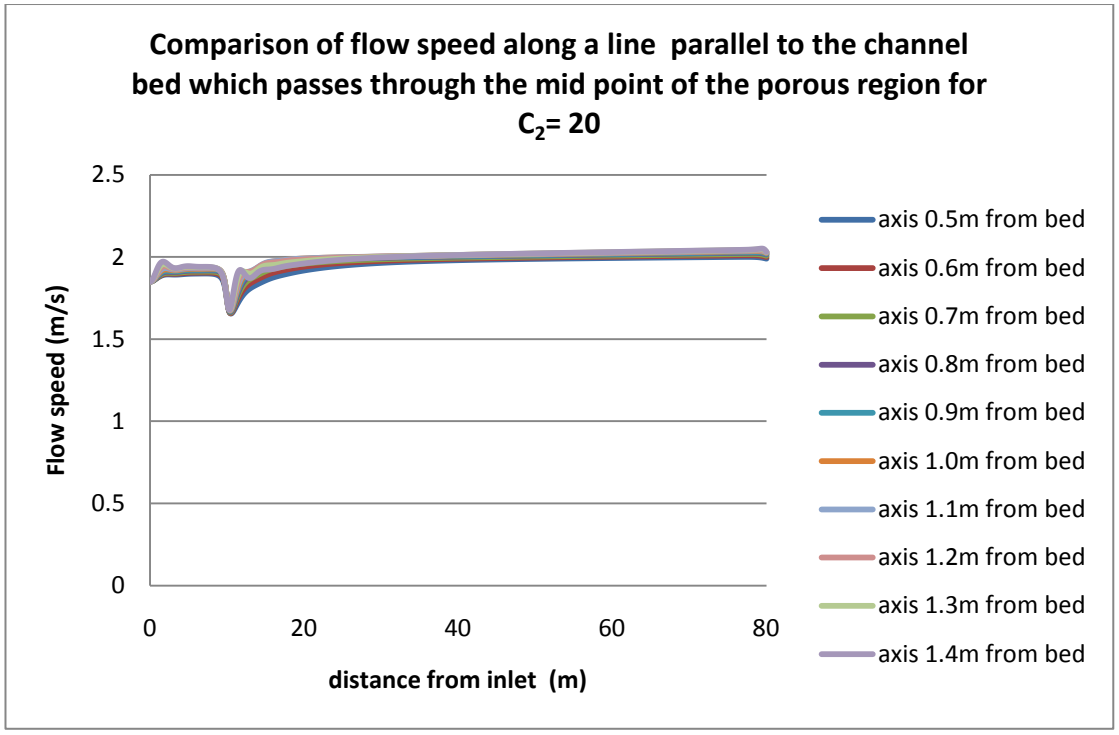

Figure 5.9- Comparison of flow speed along a line parallel to the channel bed which passes through the mid point of the porous region

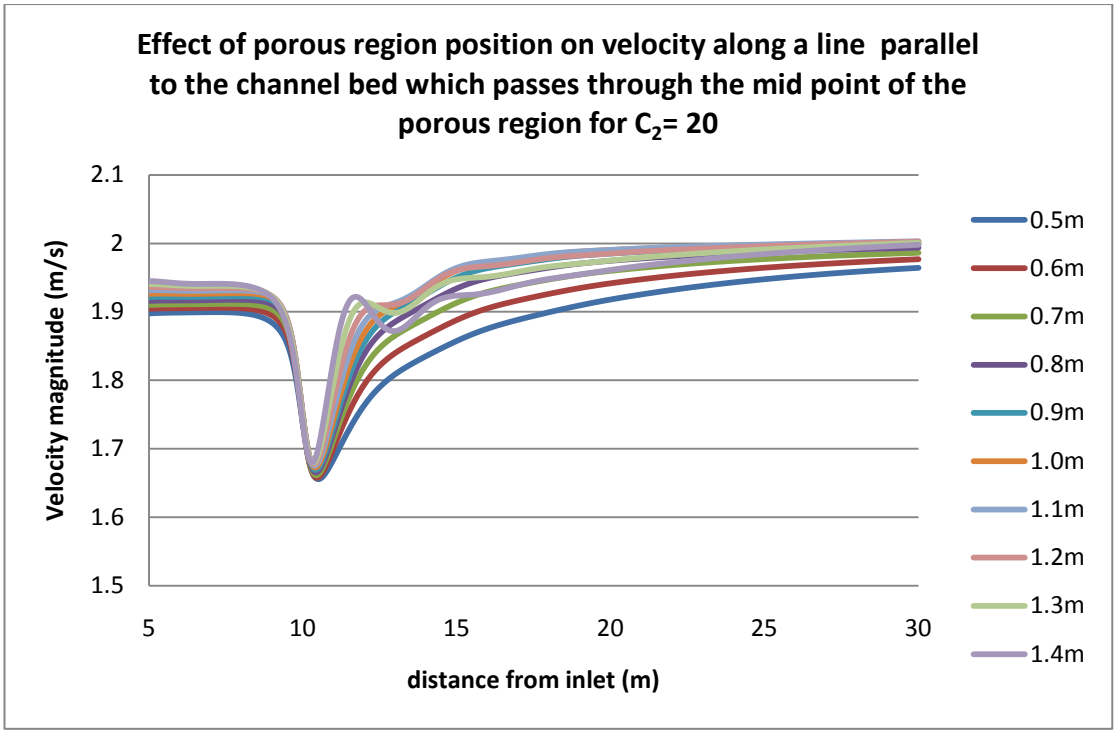

Figure 5.10- Effect of porous region position along the length of the domain

It can be seen from Figure 5.10that as the distance from the channel bed to the mid point of the porous region is increased, the free-stream velocity also increases. Since the power coefficient values were all calculated using a free stream velocity of 2m/s, the change in power coefficient with position may be due to this difference in free-stream velocity. The region of the graph where the velocity varies the least with the distance from the inlet is approximately centred around 7m from the inlet. This allows the velocity at 7m to be used as an estimate for the free-stream velocity. Figure 5.11 shows how the velocity varies over the height of the porous region 7m downstream of the inlet. This graph indicates that the free-stream velocity varies with the position of the disc and that there is also a significant variation in free-stream velocity over the height of the disc region for all disc positions.

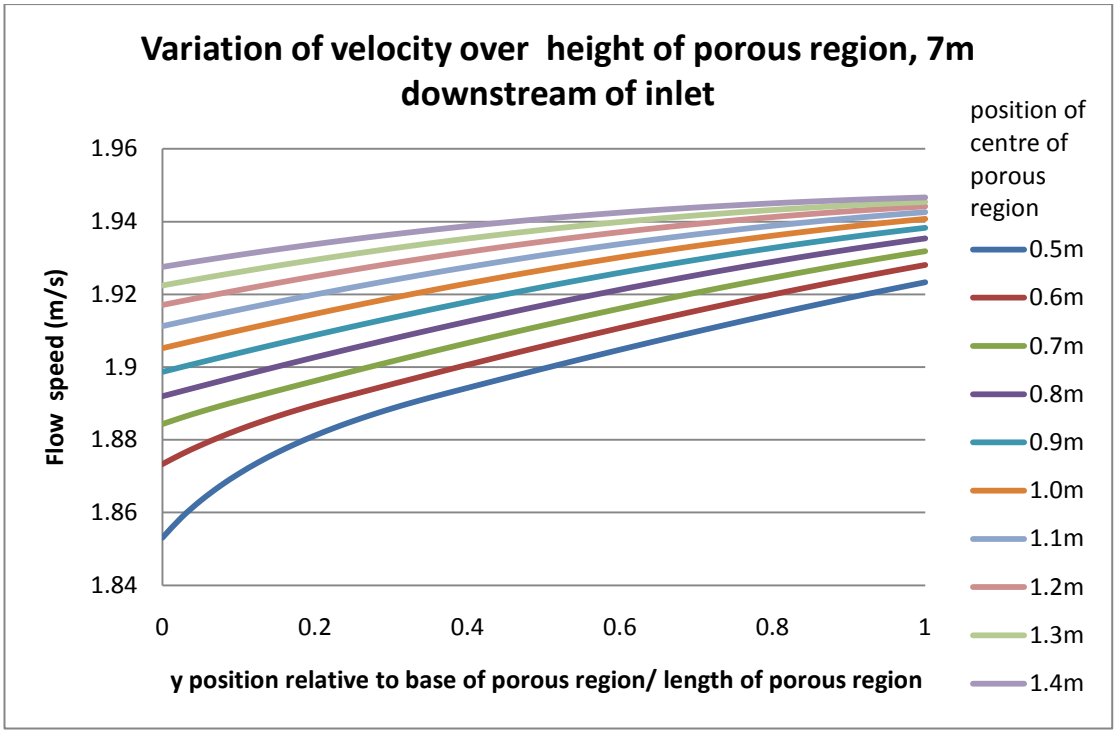

Figure 5.11- Variation in flow speed over height of disc for a range of disc positions

Since the velocity varies significantly, both over the height of the disc and with disc position, the power coefficient values calculated using a constant speed of 2m/s will not accurately reflect the power coefficient at which the turbine simulator was operating. For a free-stream velocity which varies with y position, the power in the undisturbed stream can be calculated using Equation 80. The flow speeds 7m from the inlet have been shown to give an adequate representation of the free-stream velocity, so revised values for the power coefficient can be calculated using these values. Since the free-stream velocity is known at a number of evenly spaced points over the height of the disc, numerical integration using Simpson's rule was used to calculate the power in the undisturbed flow.

$$\text{power in undisturbed flow through turbine area, per unit width} = \frac{1}{2}\rho \int_{y0}^{yL} {u_\infty}^3 \, dy$$

Equation 80

Figure 5.12 shows how performance varies with boundary proximity for power coefficient values calculated from the flow speeds at 7m. Comparison of Figure 5.7 and Figure 5.12 indicates that calculating the

power coefficient using the correct free-stream velocity increases the power coefficient values slightly and changes the manner in which the power coefficient varies with boundary proximity. Calculating the power coefficient using the correct free-stream velocity values also raises all of the channel power coefficients above the corresponding unbounded flow power coefficients. The trends can be seen more clearly in Figure 5.13 where the variation of $C_P/C_{p\ max}$ with actuator disc position has been plotted. It can be seen from Figure 5.13 that the power coefficient decreases as the distance from the channel bed increases. The rate of the decrease becomes more rapid once the turbine position is above the mid point of the channel depth. As the pressure drop coefficient is increased the percentage difference between the maximum and minimum power coefficients also increases.

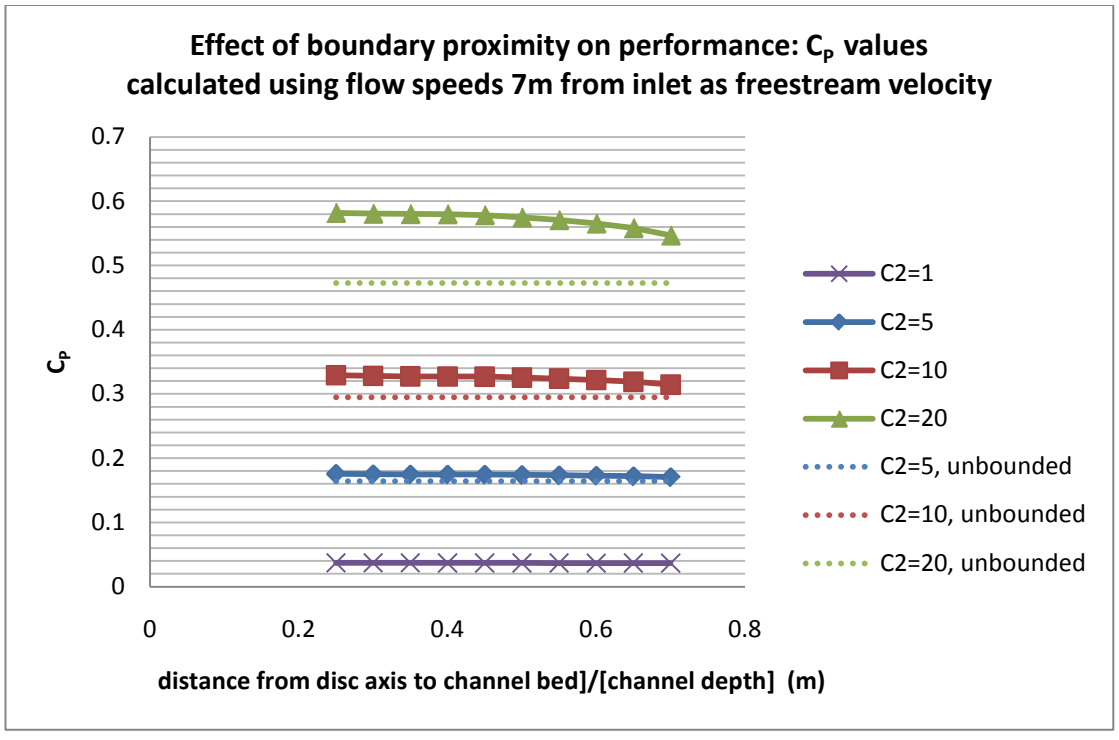

Figure 5.12- Effect of boundary conditions on performance, using revised C_p calculation

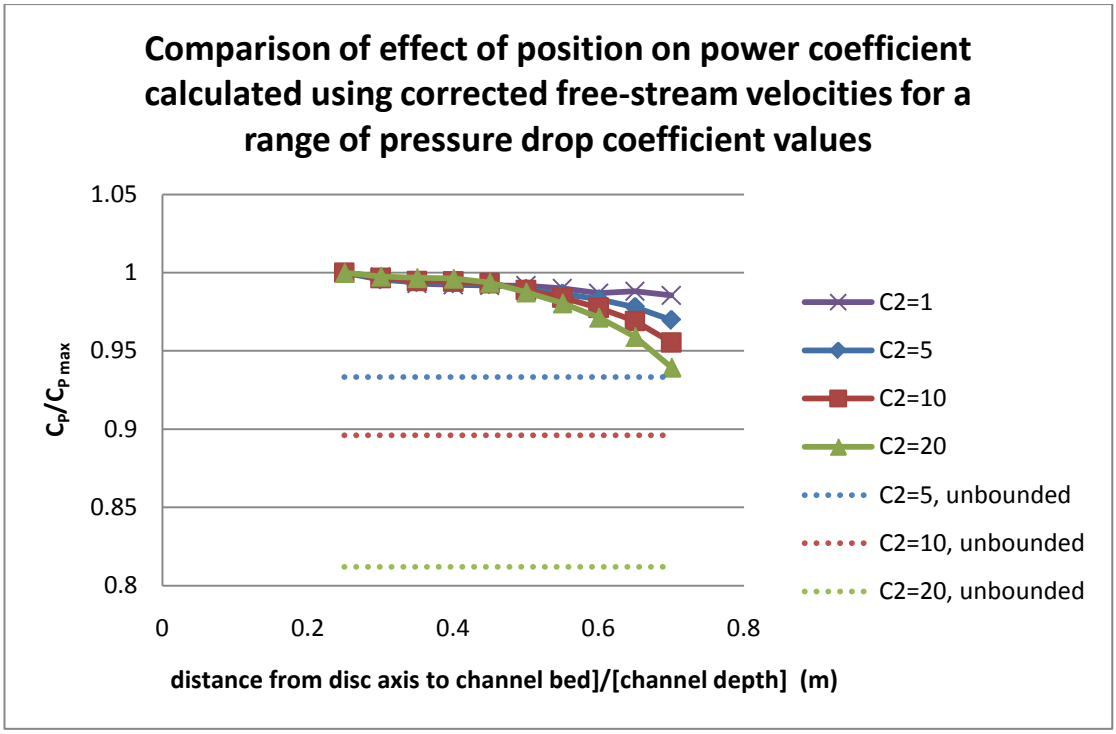

Figure 5.13- Comparison of the effect of position on power coefficient calculated using the corrected free-stream velocities for a range of pressure drop coefficients

As well as inducing velocity changes, the porous region also induces changes in the elevation of the free surface. Figure 5.14 shows how the free surface elevation varies with along channel position for a pressure drop coefficient of 20. The other pressure drop coefficients show similar trends, with the magnitude of the elevation change reducing as the pressure drop coefficient is reduced. It can be seen from Figure 5.14 that the magnitude of the deflection at a given point depends on the position of the porous region.

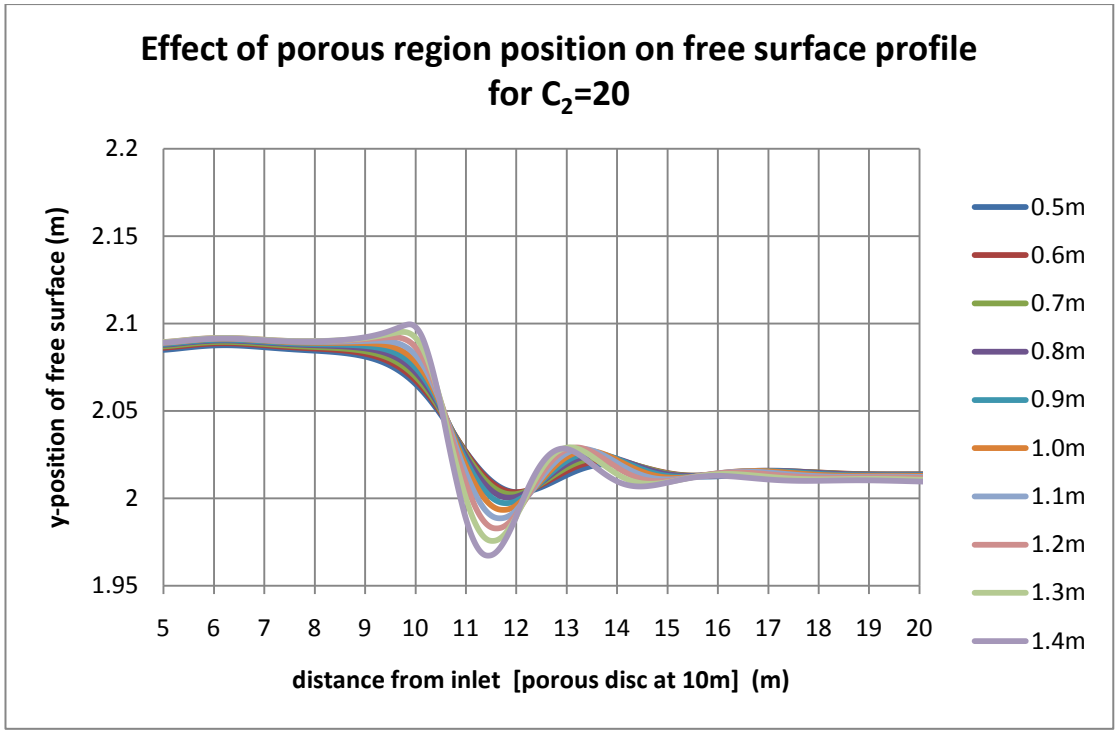

Figure 5.14- Effect of porous region position on free surface profile

In order to see if the change in performance is related to the surface deflection, ways of measuring the change in surface position are needed. Three different quantities were identified as measures to quantify the magnitude of the free surface deflection. These are the change in elevation between the far upstream (7m) and far downstream (20m) regions; the difference between the maximum and minimum free surface elevations; and the difference between the far upstream and maximum free surface elevations.

The difference between the far upstream and far downstream free surface elevations is the overall change in static head caused by the presence of the porous region. Figure 5.15 shows the variation in head drop with porous region position for a number of pressure drop coefficients between 1 and 20. It can be seen from Figure 5.15 that there is an almost linear increase in overall head drop with distance from the channel bed for each value of the pressure drop coefficient. As the pressure drop coefficient is increased, the rate of increase of head drop with porous region position also increases. The larger the pressure drop coefficient, the greater the amount of energy which is extracted from the flow. So extracting more

energy from the flow causes the free surface to deflect by a greater amount.

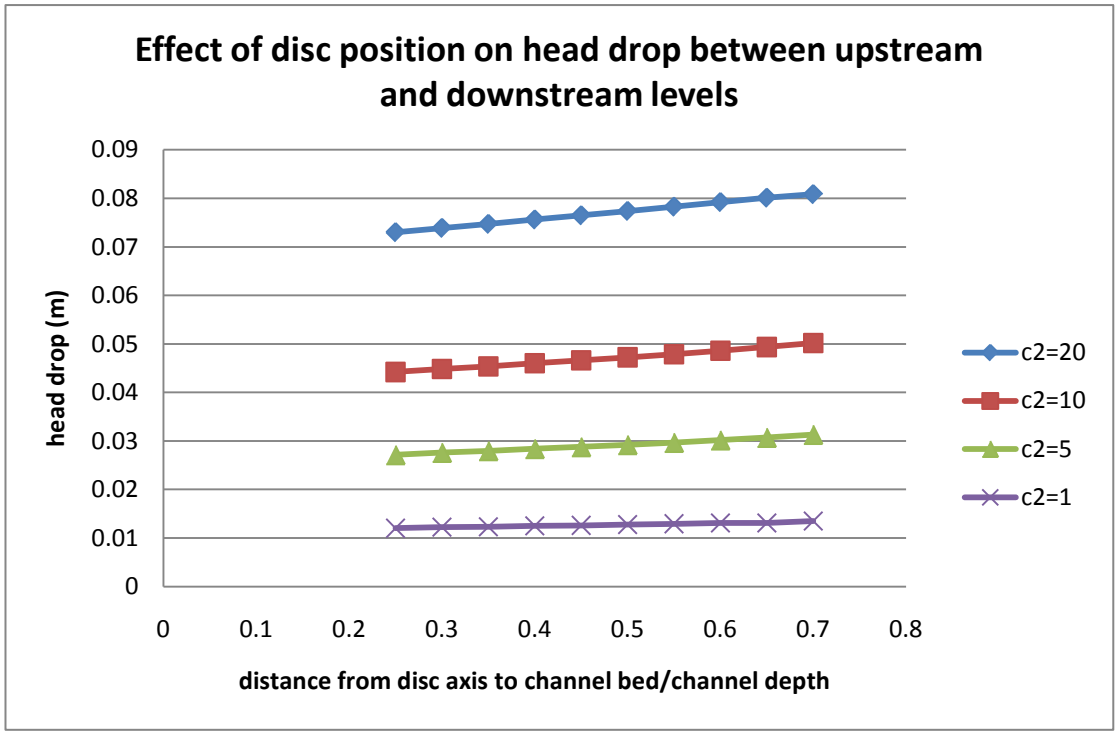

Figure 5.15- Effect of disc position on head drop between far upstream and downstream levels

It can be seen from Figure 5.14 that the difference between the maximum and minimum free surface elevations is greater than the difference between the far upstream and downstream surface levels. The difference between the maximum and minimum free surface levels also varies more with porous region position than the difference between the far upstream and downstream levels. The relationship between porous region position and the difference between the maximum and minimum free surface elevations is shown more clearly in Figure 5.16. The difference between the maximum and minimum free surface elevations is smallest when the porous region is closest to the channel bed and increases as the porous region approaches the free surface. Unlike the overall change in head drop for which the rate of increase in head drop is approximately constant, the rate of increase in maximum head drop increases as the free surface is approached. This change in the rate of increase in maximum head drop is again greatest for the higher pressure drop coefficients: the cases where the energy extracted from the flow is higher.

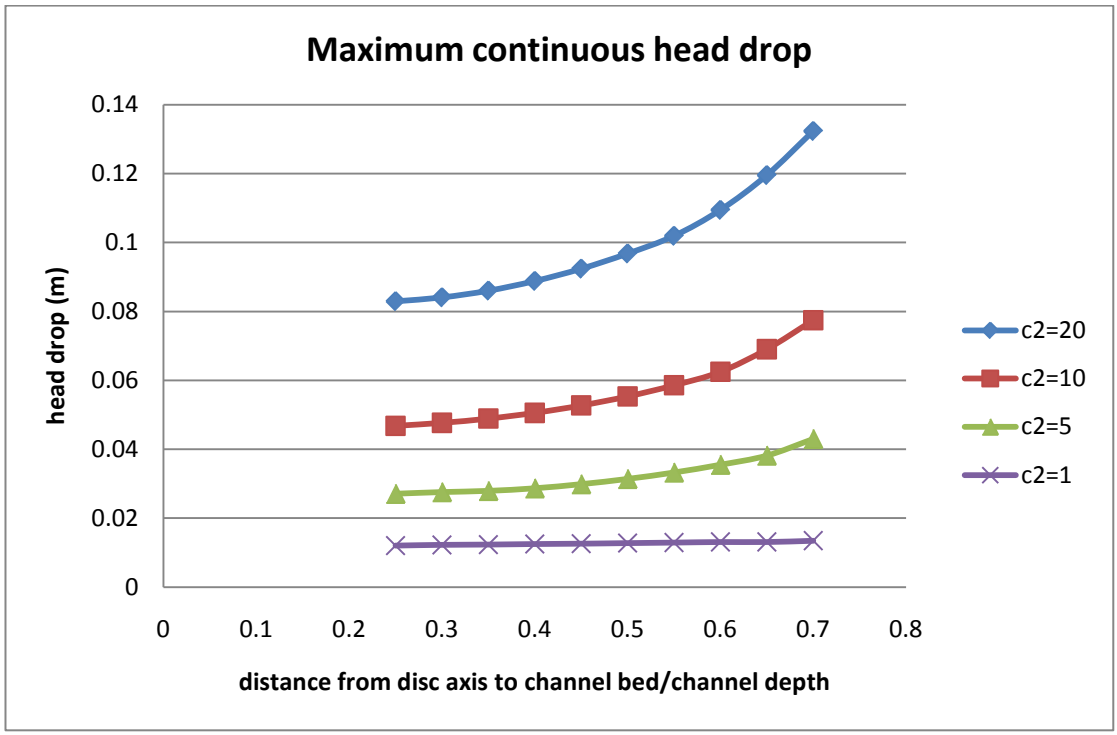

Figure 5.16- Effect of disc position on difference between maximum and minimum free surface elevations

From Figure 5.14 it can also be seen that, for the porous region positions closest to the free surface, there is an increase in free surface level above the far upstream value which occurs a short distance upstream of the porous region. This is shown more clearly in Figure 5.17. It can be seen from Figure 5.17 that the position above which there is an increase in free surface elevation between free stream conditions and the disc gets further away from the surface as the pressure drop coefficient is increased. For the lowest pressure drop coefficient studied, C_2 =1, the far upstream surface level is the maximum for all the disc positions for which simulations were carried out. At a pressure drop coefficient of 1 only very tiny amounts of energy are being extracted from the flow. This means that at this pressure drop coefficient, the disc would have to be much closer to the free surface to cause an increase in free surface elevation upstream of the disc than the positions at which the other pressure drop coefficients start to demonstrate this effect.

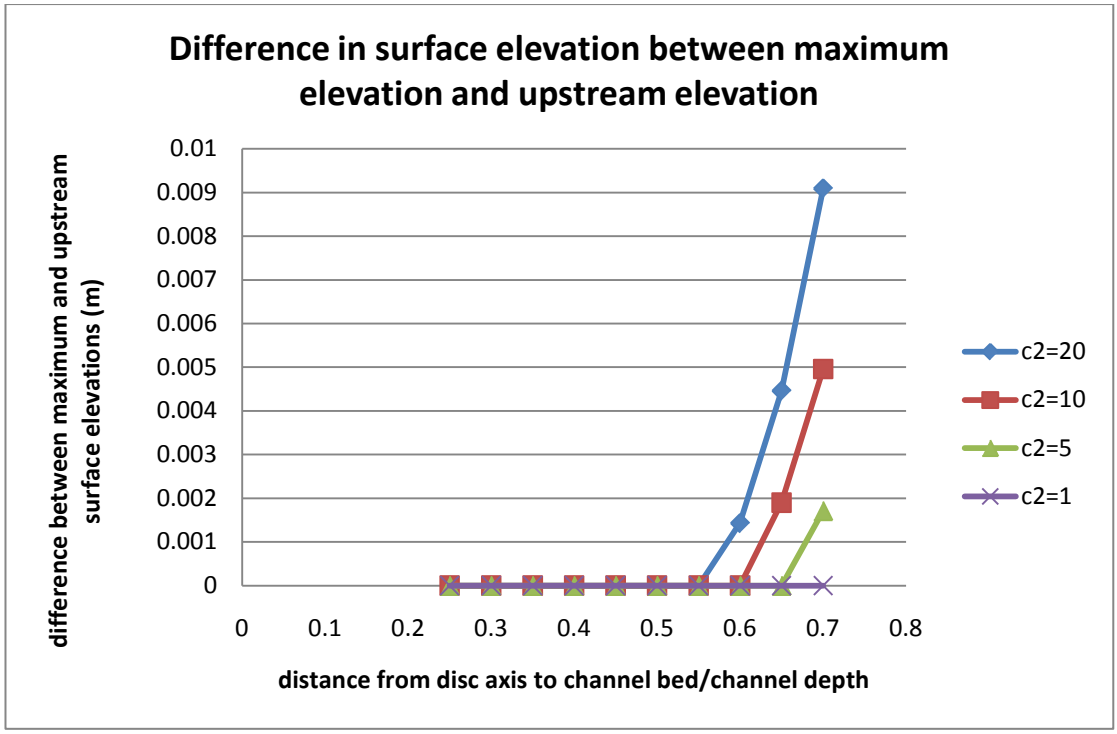

Figure 5.17- Effect of disc position on the difference between maximum and upstream surface elevations

Through Figure 5.14, Figure 5.15, Figure 5.16 and Figure 5.17 it has been demonstrated that the position of the disc affects the amount by which the free surface deflects. These Figures also demonstrated that the greater the pressure drop coefficient of the disc, the greater the effect on the free surface. This demonstrates that the position of the disc has an effect on the flow and that the magnitude of the effect depends on the amount by which the disc affects the flow. It does not, however, explain why the power coefficient of the disc varies with position in the manner shown in Figure 5.13. To do this, an understanding of why the position of the disc affects its effect on the free surface and how the changes in free surface level are affecting the flow is needed.

The changes in free surface elevation are likely to affect both the path and speed of the fluid particles. This is best demonstrated by looking at how the geometry of the streamlines of the flow through the disc is affected by the position of the disc. Since the flow is steady, the pathlines of the flow are identical to the streamlines of the flow. The pathlines for the flow through the disc are shown in Figure 5.18 for the centre of the disc

positioned 1.4m above the channel bed, in Figure 5.19 for a position of 0.5m and Figure 5.20for the case representative of the disc in an infinite flow. The full figures including the key to the pathline shading can be found in the Appendix. The two grey vertical lines seen in each of these figures are 3m upstream and downstream of the disc. The start and end points of the grey lines have the same y positions as the start and end points of the disc. This allows the area of the streamtube upstream, downstream and at the disc to be compared.

The pathlines shown in Figure 5.20 are symmetrical with the streamtube expanding by the same amount above and below a line through the centre point of the disc. This symmetry is not present for the two channel cases shown in Figure 5.18 and Figure 5.19, those for a disc close to the free surface and the channel bed respectively. For the disc positioned close to the free surface the entire wake is shifted downwards by a significant amount. For the case where the disc is positioned close to the channel bed the deviation from the symmetrical wake seen in Figure 5.20 is less than that seen for the disc positioned close to the free surface. When the disc is positioned close to the channel bed the top half of the wake expands slightly more than the lower half of the wake. In Figure 5.21 the upper and lower streamlines through the disc have been plotted for three disc positions: the disc close to the surface, close to the channel bed and the disc mid way between these positions. The downward shift of the wake in the position closest to the surface is very apparent in this figure. The disc

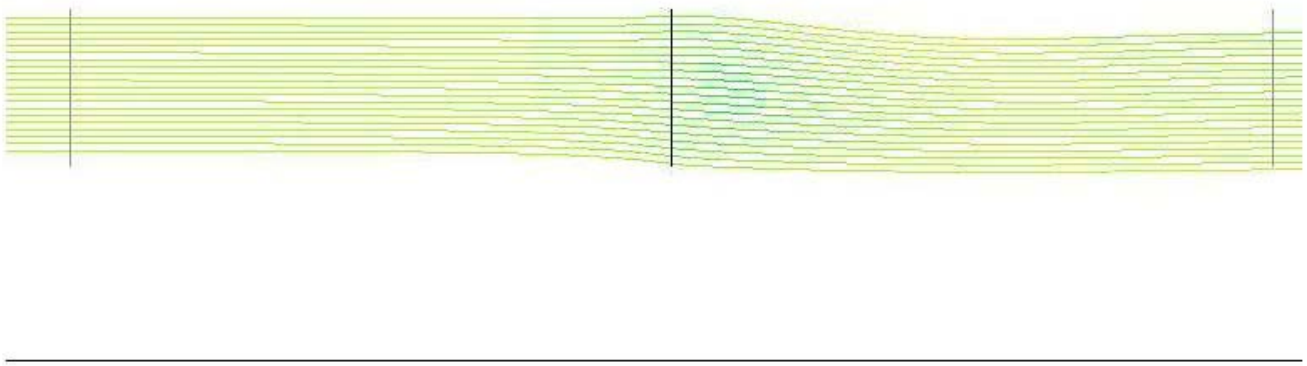

Figure 5.18- Pathlines for flow through the disc, with the centre of the disc 1.4m above the channel bed

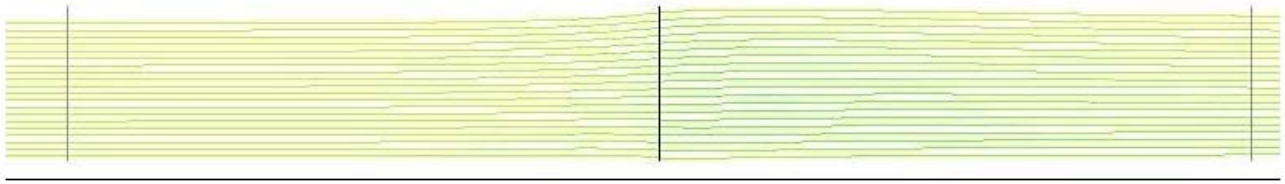

Figure 5.19- Pathlines for flow through the disc, with the centre of the disc 0.5m above the channel bed

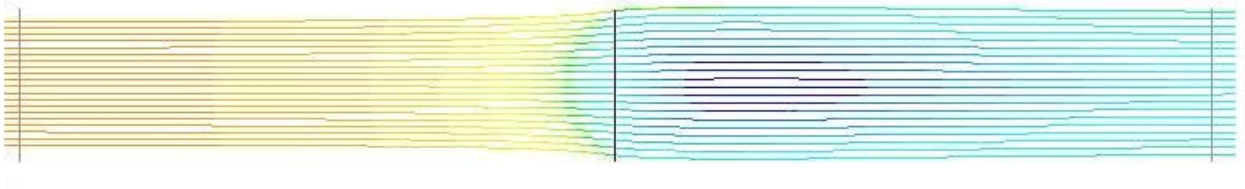

Figure 5.20- Pathlines for flow through disc in unbounded flow

in the middle position also shows a downward shift in the wake, but this is smaller than that for the turbine closest to the surface.

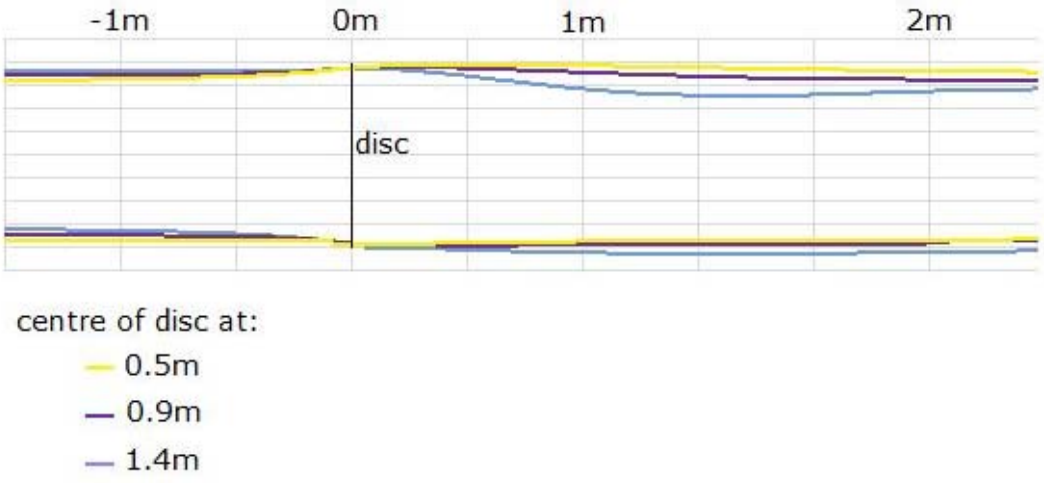

Figure 5.21- Comparison of upper and lower streamline shaped for 3 disc positions in a channel

Disc position has been shown to affect the path of the fluid particles passing through the disc. The wake of the disc in all positions in the channel was found to deviate from the symmetrical wake formed when the disc was placed in a very large water filled domain. It is likely that the asymmetry of the wake will affect the velocity distribution in the streamtube enclosing the disc. The pressure drop across the disc, and hence the power generated by the disc, depends solely on the velocity of the flow through it since the pressure drop coefficient is constant for any given simulation. Thus it is the effect of the asymmetry of the wake on the velocity distribution which is of interest. Figure 5.22 shows the velocity distribution on the disc for disc positions 0.5, 0.9 and 1.4m from the channel bed and for the disc in an unbounded flow. Since the free stream velocity varies with vertical position, the disc velocity has been plotted as a percentage of the free-stream velocity. The reduction in velocity is much greater for the disc in the unbounded flow than for the discs in the channel. This is to be expected as the power generated by the disc in the unbounded flow is lower than the power generated by the disc

in any position in the channel and power is directly proportional to the velocity through the disc cubed.

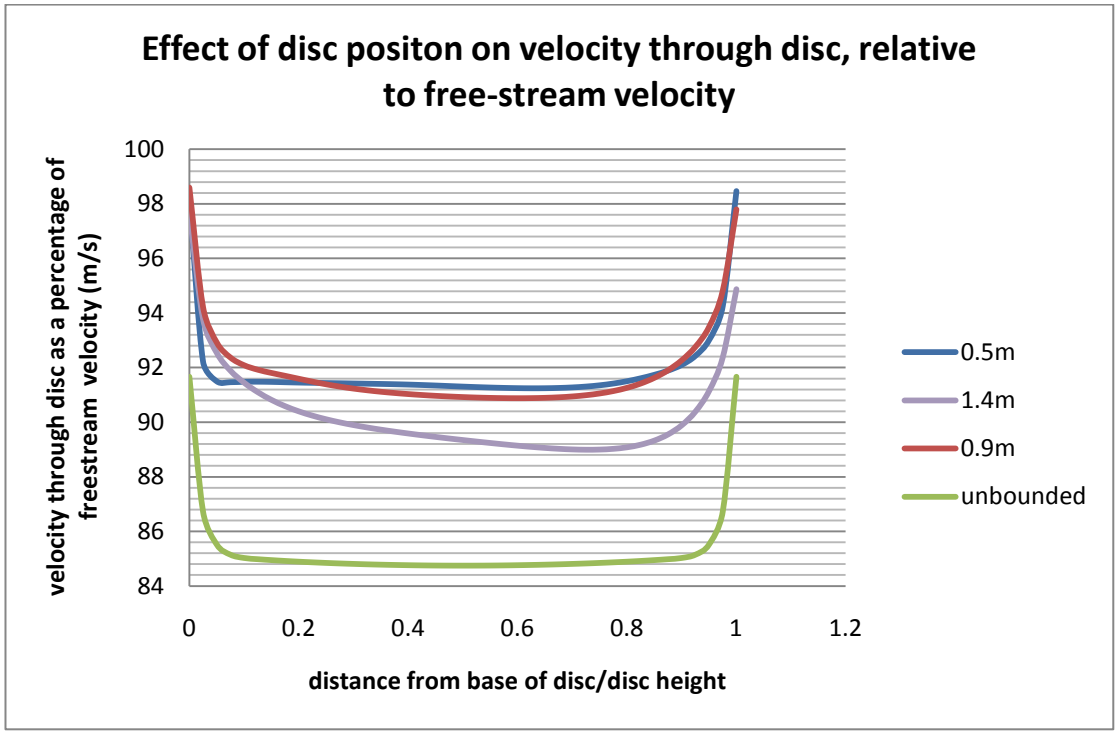

Figure 5.22- Effect of disc position on the velocity through the disc, relative to the free-stream velocity

Figure 5.22 also shows that the velocity distribution on the disc is symmetrical for the disc in the unbounded flow but is not symmetrical for the any of the disc positions in the channel. The streamtube surrounding the disc in the unbounded flow was symmetrical but those for discs in the channel were not, suggesting that asymmetry in streamtube surrounding the disc is linked to asymmetry in the distribution of the velocity through the disc. The distribution of the velocity through the disc in the 0.5m position is closest to that of the disc in the unbounded flow and this is the position for which the streamtube was the least asymmetrical.

For the disc in the unbounded flow the velocity through the disc is constant over most of the disc with small regions as each end of the disc is approached where the velocity recovers rapidly towards the free-stream velocity. For the discs in the channel there is no region of constant velocity instead, outside the recovery regions at the ends of the disc, the

velocity reduces with increasing disc y position. The rate of reduction increases as the position of the disc approaches the surface. The regions over which the velocity recovery takes place are larger for the discs in the channel. The exception to this is the lower end of disc positioned 0.5m from the channel bed for which the recovery takes place over a shorter distance than is shown by the disc in the unbounded flow.

So it has been demonstrated that as the position of the disc is moved toward the surface, the average velocity through the disc is decreased with a resulting decrease in power. As the position of the disc is moved towards the surface the amount by which the free surface deflects from its original flat state and the asymmetry of the streamtube enclosing the disc increase. Since the velocity distribution of the flow through the disc becomes less symmetrical as the disc position approaches the surface it is thought that the change in power with position is related to the free surface deflection and changes in streamtube shape.

In the streamtube model the flow speed outside the streamtube is constant for a given x position. The viscous flow modelled in the computational studies of the effect of disc position on performance is capable of supporting velocity gradients. This means that the effect of the disc on the flow speed outside the streamtube enclosing the rotor decreases as the distance from the streamtube increases. This can be seen in Figure 5.23 which shows how the velocity varies with y-position for a number of x positions for a disc with a pressure drop coefficient of 10 operating in an unbounded flow. The two grey dotted lines in this graph indicate the y positions of the top and the bottom of the disc. Since the streamtube enclosing the rotor has a smaller area than the area of the disc upstream of the disc, the velocity profile 1m upstream of the disc is clearly indicating that the flow speed outside the streamtube enclosing the disc is affected to a greater extent close to the streamtube.

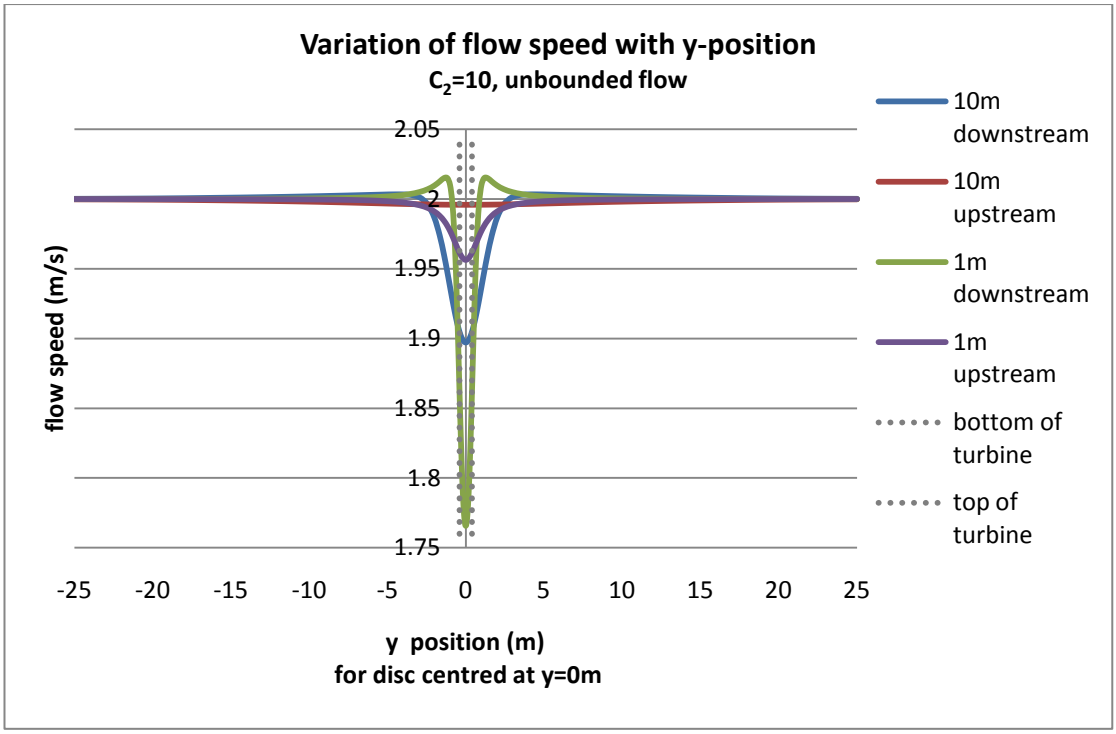

Figure 5.23- Variation of flow speed with y-position

Since the effect of the disc on the flow decreases with the distance away from the disc, the further away from the surface the disc is located, the smaller the effect it will have on the free surface elevation.

5.2 Verification of numerical model results

Experiments were carried out in the towing tank at the Acre Road Hydrodynamics Facility (University of Strathclyde). Unfortunately, due to problems with the test system, the turbine only operated in brake state and so the results were not comparable with the results from the numerical model. Since there are also no published experimental data with which the results from the numerical model can be compared, it has not been possible to validate the numerical model. Further experimental work is needed to confirm that the trends predicted by the numerical model actually occur.

5.3 Summary

The numerical modelling work has demonstrated that the position of the turbine relative to the boundaries affects its performance. It has not,

however, been possible to validate the model. Further experimental work is needed to confirm the effect of the proximity of the free surface and sea bed on turbine performance.

The power coefficient of the turbine was found to decrease as the distance from the channel bed was increased. Comparison of the numerical channel results with simulations carried out in an all water region which was sufficiently large for the boundaries not to have an effect showed that blockage was having a significant effect, improving the performance of the turbine in the channel. The performance was higher in the channel than in the unconstrained flow for all turbine positions.

When using these results to determine the optimum position above the channel bed in which to install turbines it is worth noting that the turbine position in which the power coefficient is highest is not necessarily the position in which it will generate the most power. The turbine operates most efficiently close to the channel bed, but in this position the flow speed is lower and so the power generated is less. This suggests that the turbine may be better positioned further up the water column. This position is the best position for the turbine from a design point of view as it places it outside both the boundary layer and the wave zone. Positioning the turbine outside the boundary layer and the wave zone reduces the fatigue load on the blades since the variation in flow speed between the top and bottom of the turbine swept area is much smaller.

Chapter 6 Discussion and Conclusions

The main aim of this project was to demonstrate whether the aerodynamic performance prediction models developed for wind turbines can be applied to tidal turbines. The literature review identified two differences between wind and tidal turbines which needed further investigation. The first was the proximity of the boundaries to the turbine and the second was the effect of energy extraction on the available resource. A range of experimental, analytical modelling and numerical modelling work was carried out to investigate how these differences affected the performance of tidal turbines. The results from this work have shown that the differences between wind and tidal turbines have the potential to have a significant effect on their performance. This has demonstrated that aerodynamic models are not directly applicable to tidal turbines.

One of the major differences between wind and tidal power is the effect of energy extraction on the resource. Installing tidal current turbines at a site will reduce the flow speeds at the site. The literature contains a number of analytical models which allow the effect of energy extraction on volume flow rate through the site to be investigated. In these models the turbines are represented by additional drag turbines and are assumed to be ideal. The power generated by an ideal turbine is assumed to be equal to the rate of loss of energy by the flow. Real turbines generate less power than ideal turbines since not all of the energy extracted from the flow is converted to a useful form. A model was needed which used real turbines instead of ideal turbines in order to investigate how the change in flow speeds caused by the installation of turbines affected the performance of the turbines. This was achieved by extending one of the analytical models to include elements of BEM theory.

Applying the extended model to a case study of a simple rectangular channel revealed a number of interesting results. In the undisturbed state the average drag coefficient of the channel was found to be related to the peak volume flow rate through the channel and to the time lag between

maximum head difference and maximum flow speed. The average drag coefficient of the channel needs to be known in order to apply the model. Being able to estimate the average drag coefficient from either the peak volume flow rate or the time lag between maximum head difference and maximum flow speed is advantageous since these quantities are easier to measure than the drag coefficient of the channel.

Comparison of the energy capture predicted by the extended model and the energy capture calculated from the undisturbed flow speeds has demonstrated that the magnitude of the difference is dependent on the number of turbines. For individual turbines the difference between the energy capture calculated from the undisturbed flow speeds and the energy capture calculated using the extended model is negligible. As the number of turbines is increased the difference increases. Reductions in energy capture of over 50% were calculated for farms of 1000 turbines.
The drag coefficient of the channel was found to affect the magnitude of the change in the flow at a site due to the presence of turbines. If the channel in which the turbines are to be installed has a high drag coefficient, the turbines will have less of an effect on the flow than if the channel has a lower drag coefficient. This is significant because it indicates that more turbines can be installed at some sites than others if the change in flow speeds is to be kept below a certain level.

The extended model was also applied to the Sound of Islay case study. It was found for this channel that very large numbers of turbines could be installed before there was a substantial decrease in the peak volume flow rate in the channel. However without further data on how much the flow speeds in a channel can be altered without affecting the physical and biological processes in the channel, it is not possible to state at what point the changes in flow speed caused by the tidal turbines becomes significant. It is thought that the sizes of farms that are likely to be installed in the channel in the foreseeable future are unlikely to be large enough to have a significant effect on the flow in the channel, but further ecological data is needed to confirm this. A noticeable decrease in the

energy captured by the turbines is apparent for smaller numbers of turbines than cause a noticeable decrease in the peak volume flow rate in the channel. Again, however, it is thought that for the sizes of farm that are likely to be installed in the channel in the near future, the decrease in energy capture will be small.

The extended model could be used in the planning of tidal current turbine farms. It allows the turbine design and number of turbines to be optimised for maximum power capture at a site. It also allows the effects of the turbines on the flow at a site to be estimated. This could form part of the environmental impact assessment for the farm. Knowledge of the effect of the farm on the flow speeds will allow assessment of whether this will be sufficient to adversely affect processes such as sediment transfer.

The extended model is based on a large number of assumptions. These may limit its applicability to actual tidal sites. Not all strong tidal flows occur in channels. The Sound of Islay can be described by the model but other sites such as Portland Bill, where the flow is round a headland, cannot. Another assumption which might limit the applicability of the model to actual channels is the assumption that the cross sectional area does not vary with time. For many tidal channels the change in surface elevation over the tidal cycle may lead to significant changes in cross sectional area. The accuracy with which the extended model will predict the effect of turbines on the flow will depend on how well the assumptions made in the model correspond to the conditions at the site.

The BEM model used in the extended model predicts the performance of an isolated turbine in an infinite fluid. This model needs to be extended so that it can take into account the effects of blockage. Blockage has been shown to have a significant effect on the performance of turbines so not taking account blockage effects will lead to errors. There are also some discrepancies between the assumptions made about the effect of the turbines on the flow speeds for the BEM model and the channel model. It is thought that this will not be significant if the length over which the

turbines cause the flow speeds to vary over the channel section is short in comparison to the length of the channel.

To date no large farms of turbines have been installed and so there is no experimental data which can be used to verify the output of the model. Without this data it is impossible to say with any certainty that the model accurately describes the behaviour of a tidal channel.

Both the ratio of turbine area to channel area and the proximity of the turbine to the free surface and channel bed have been found to affect turbine performance. The effects of blockage on tidal turbine performance were investigated using analytical modelling and flow table experiments. The effects of surface and sea bed proximity on turbine performance were investigated using CFD modelling.

The three analytical models used in the investigation of blockage each assumed different boundary conditions. The first model had the infinite flow domain assumed by the aerodynamic model, the second model had rigid boundaries and in the third the free surface level could vary with along channel position. Of the three models, the third model best represents the conditions encountered in tidal channels. These models were applied to rectangular channels. Applying these models to rectangular channels and the Sound of Islay demonstrated that the performance of realistically sized devices operating in these channels would differ significantly from that predicted by aerodynamic models.

The effects of blockage increased the power generated by the turbines. The effects of blockage, and hence power generated, will be greatest when the percentage of the cross section of the channel swept by turbines is high. This can be achieved by installing a number of turbines across the cross section and by using turbines with a diameter which is a large percentage of the water depth. Both of these approaches present problems. If the turbine diameter is a large percentage of the water depth the blades pass through the wave zone and the boundary layer near the

sea bed. The changes in velocity due to the waves result in fluctuating forces which will cause problems with fatigue of the blades. The boundary layer also has the potential to cause fluctuating loads since the flow in the boundary layer will typically be turbulent. Installing large numbers of turbines across the cross section of the channel is not practical since this would interfere with the passage of vessels and marine life. Careful design will be needed to maximise the performance of the turbines whilst minimising impact on shipping and marine life and minimising problems due to unsteady loads. This cannot be achieved using an aerodynamic model, since aerodynamic models cannot take into account the effects of blockage.

The analytical models developed to investigate the effects of blockage have a number of limitations. They assume that the channels are uniform and rectangular and that the flow is frictionless. These assumptions are not met by actual tidal channels. As such, there will be differences between the effects of blockage in actual channels and the effects of blockage predicted by the model. It is thought that the models give a sufficiently accurate representation of the performance of a turbine in a channel to indicate that blockage will have a noticeable effect on performance, even if they cannot accurately quantify the effects of blockage. The test facility used in the experimental investigation of the effects of blockage was found to be insufficiently uniform to be used to generate results with a low enough degree of uncertainty to allow trends to be identified. If the effects of blockage on turbine performance are to be accurately quantified, further experimental investigation is needed, using a more suitable test facility.

The assumption of frictionless flow used in the models developed to predict the effects of blockage on performance prevents these models from being able to take into account the effects of the proximity of the turbine to the boundaries. Numerical modelling was used to investigate the effects of boundary proximity on turbine performance.

Based on the numerical modelling results, it was found that the performance of the turbine was greatest in the position closest to the channel bed. Whilst the turbines operated most efficiently in this position, the power generated was actually greatest approximately mid way up the water column. This is due to the boundary layer caused by the channel bed. The mid water column position is ideal from an engineering perspective since it places the turbine outside the boundary layer and wave zone regions in which the velocity varies with position, increasing the fatigue loads.

In order to verify that the numerical model is correctly predicting the variation of performance with turbine position, experimental work is needed. It is thought that the use of a 2D domain and a turbine simulator in the computational models instead of a rotating turbine in a 3D channel will affect the magnitude and rate of decrease of the power coefficient. Of particular interest is how differences in the near wake of a turbine simulator and a rotating turbine affect surface deformation. Experimental investigation of this would confirm whether the numerical model results accurately describe the behaviour of an actual turbine.

All of the analytical and numerical modelling work carried out indicated that aerodynamic models do not accurately represent tidal turbines. The effect of turbines on the flow speed at a site was found to reduce the amount of power generated whilst the effects of blockage were found to increase it. The ratio of turbine area to channel area was not the only factor which determined the effect of the boundaries on turbine performance. The position of the turbine relative to the boundaries has also been shown to have an effect. The combined impact of these effects will depend on the design and geometry of the turbines, the number of turbines installed and the site where they are installed. As such it is not possible to comment on whether aerodynamic models under or over predict the performance of turbines.

It should also be noted that aerodynamic models and the models for tidal turbines developed from the aerodynamic models in this project assume that the flow is uniform. Tidal flows are typically highly turbulent and non-uniform so the assumption of uniform flow will lead to errors. Accurate models of tidal turbine performance will need to take into account these effects.

Performance prediction models are essential to the development of the tidal current power industry. The models which are currently being used have been demonstrated to, at best, only give a rough estimate of the amount of the amount of power that can be generated. This means that tidal current power will not be able to reach its full potential using these models. New models for tidal turbine performance prediction need to be developed. For new models to be developed more experimental data from sea trials is needed. This data is necessary to verify the output of the models.

6.1 Conclusions

- Installing a large number of turbines at a site reduces the power captured by each turbine
- The magnitude of the effect of installing turbines on the flow, and thus the power capture per turbine, depends on the drag coefficient of the site as well as turbine design
- There will typically not be a noticeable reduction in power capture for single turbines or small farms of turbines
- Blockage will increase the performance of tidal turbines above that predicted by aerodynamic models
- Blockage is significant even for single turbines, as was demonstrated by the Sound of Islay case study
- The position of the turbine relative to the free surface and channel bed affects its performance
- The power coefficient decreases as the height of the turbine above the channel bed increases

- The power generated by the turbine was found to be greatest approximately mid way between the channel bed and free surface
- For all of the areas investigated, the differences between wind and tidal turbine caused turbine performance to differ significantly from the performance predicted by the aerodynamic model
- New models which take into account the differences between wind and tidal turbine operation need to be developed

Chapter 7 References

(1) McCombes T, Johnstone C, Grant A. Unsteady wake modelling for tidal current turbines. *Renewable Power Generation, IET.* 2011; 5(4):299-310.

(2) Jahromi MJ, Maswood AI, Tseng K-. Long Term Prediction of Tidal Currents. *Systems Journal, IEEE.* 2011; 5(2):146-155.

(3) Defne Z, Haas KA, Fritz HM. Numerical modeling of tidal currents and the effects of power extraction on estuarine hydrodynamics along the Georgia coast, USA. *Renewable Energy.* 2011; 36(12):3461-3471.

(4) Yang B, Lawn C. Fluid dynamic performance of a vertical axis turbine for tidal currents. *Renewable Energy.* 2011; 36(12):3355-3366.

(5) Vennell R. Estimating the power potential of tidal currents and the impact of power extraction on flow speeds. *Renewable Energy.* 2011; 36(12):3558-3565.

(6) Akwensivie F. *In the Wake of a Marine Current Turbine.* [MSc thesis on the Internet]. Energy Systems Research Unit, University of Strathclyde; 2004 .

(7) ANSYS. [ID: 110]. *ANSYS FLUENT 12.0 Theory Guide.*

(8) Brooks DA, Baca MW, Lo Y-. Tidal Circulation and Residence Time in a Macrotidal Estuary: Cobscook Bay, Maine. *Estuarine, Coastal and Shelf Science.* 1999; 49(5):647-665.

(9) Croft A, Davison R, Hargreaves M. *Engineering Mathematics.* 3rd Edition ed. : Pearson Education; 2001.

(10) Atwater JF, Lawrence GA. Regulatory, design and methodological impacts in determining tidal-in-stream power resource potential. *Energy Policy.* 2011; 39(3):1694-1698.

(11) Atwater JF, Lawrence GA. Power potential of a split tidal channel. *Renewable Energy.* 2010; 35(2):329-332.

(12) Bahaj AS, Myers LE, Thomson MD and Jorge N. Characterising the Wake of Horizontal Axis Marine Current Turbines. Characterising the Wake of Horizontal Axis Marine Current Turbines. *Proceedings of the 7th European Wave and Tidal Energy ConferenceID: 76.* ; 2007.

(13) Bahaj AS, Batten WMJ, McCann G. Experimental verifications of numerical predictions for the hydrodynamic performance of horizontal axis marine current turbines. *Renewable Energy.* 2007; 32(15):2479-2490.

(14) Bahaj AS, Molland AF, Chaplin JR, Batten WMJ. Power and thrust measurements of marine current turbines under various hydrodynamic flow conditions in a cavitation tunnel and a towing tank. *Renewable Energy.* 2007; 32(3):407-426.

(15) Bahaj AS, Molland AF, Chaplin JR, Batten WMJ. Power and thrust measurements of marine current turbines under various hydrodynamic flow conditions in a cavitation tunnel and a towing tank. *Renewable Energy.* 2007; 32(3):407-426.

(16) Bahaj AS, Myers LE. Fundamentals applicable to the utilisation of marine current turbines for energy production. *Renewable Energy.* 2003; 28(14):2205-2211.

(17) Barltrop N, Varyani KS, Grant A, Clelland D, Pham XP. Investigation into Wave-Current Interactions in Marine Current Turbines. *Proceedings of the Institution of Mechanical Engineers Part A: Journal of Power and Energy.* 2007; 221.

(18) Bathurst GN, Weatherill J, Strbac G. Trading Wind Generation in Short Term Energy Markets. *IEEE Transactions on Power Systems.* 2002; 17(3).

(19) Batten WMJ, Bahaj AS, Molland AF, Chaplin JR. The prediction of the hydrodynamic performance of marine current turbines. *Renewable Energy.* 2008; 33(5):1085-1096.

(20) Batten WMJ, Bahaj AS, Molland AF, Chaplin JR. The prediction of the hydrodynamic performance of marine current turbines. *Renewable Energy.* 2008; 33(5):1085-1096.

(21) Batten WMJ, Bahaj AS, Molland AF, Chaplin JR. Experimentally validated numerical method for the hydrodynamic design of horizontal axis tidal turbines. *Ocean Engineering.* 2007; 34(7):1013-1020.

(22) Batten WMJ, Bahaj AS, Molland AF, Chaplin JR. Hydrodynamics of marine current turbines. *Renewable Energy.* 2006; 31(2):249-256.

(23) Black and Veatch. [ID: 94]. *Tidal Stream Energy- Resource and Technology Summary Report.* 2005.

(24) Blanchfield J, Rowe A, Wild P and Garret C. The Power Potential of Tidal Streams Including a Case Study for Masset Sound. The Power Potential of Tidal Streams Including a Case Study for Masset Sound. *Proceedings of the 7th European Wave and Tidal Energy ConferenceID: 103.* ; 2007.

(25) Blanchfield J, Garrett C, Wild P, Rowe A. The extractable power from a channel linking a bay to the opean ocean. *Proceedings of the Institution of Mechanical Engineers, Part A: Journal of Power and Energy.* 2008; 222(3):289-297.

(26) Blunden LS, Bahaj AS. Tidal Energy Resource Assessment for Tidal Stream Generators. *Proceedings of the Institution of*

Mechanical Engineers Part A: Journal of Power and Energy. **2007; 211.**

(27) Blunden LS and Bahaj AS. Effects of Tidal Energy Extraction at Portland Bill, Southern UK, Predicted from a Numerical Model. Effects of Tidal Energy Extraction at Portland Bill, Southern UK, Predicted from a Numerical Model. *Proceedings of the 7th European Wave and Tidal Energy ConferenceID: 50.* ; 2007.

(28) Blunden LS, Bahaj AS. Initial Evaluation of Tidal Stream Energy Resources at Portland Bill, UK. *Renewable Energy.* 2006; 31(2).

(29) Blunden LS, Bahaj AS. Initial evaluation of tidal stream energy resources at Portland Bill, UK. *Renewable Energy.* 2006; 31(2):121-132.

(30) Brooks DA. The tidal-stream energy resource in Passamaquoddy–Cobscook Bays: A fresh look at an old story. *Renewable Energy.* 2006; 31(14):2284-2295.

(31) Bryden I, Melville GT. Choosing and evaluating sites for tidal current development. *Proceedings of the Institution of Mechanical Engineers, Part A: Journal of Power and Energy.* 2004; 218(8):567-577.

(32) Bryden IG, Grinsted T, Melville GT. Assessing the potential of a simple tidal channel to deliver useful energy. *Applied Ocean Research.* 2004; 26(5):198-204.

(33) Bryden IG and Couch SJ. ME1 - Marine energy extraction: Tidal resource analysis. ME1 - Marine energy extraction: Tidal resource analysis. *Marine EnergyID: 100; Compilation and indexing terms, Copyright 2010 Elsevier Inc.; M1: Compendex; T3: Renewable Energy; undefined; undefined; undefined; undefined.* : Elsevier Ltd; 2006. p. 133-139.

(34) Builtjes PJH and Milborrow DJ. Modelling of Wind Turbine Arrays. Modelling of Wind Turbine Arrays. *Proceedings of the Third International Symposium on Wind Energy SystemsID: 77.* ; 1980.

(35) Builtjes PJH and Vermeulen PEJ. Turbulence in Wind Turbine Clusters. Turbulence in Wind Turbine Clusters. *Proceedings of the Fourth International Symposium on Wind Energy SystemsID: 79.* ; 1982.

(36) Builtjes PJH and Vermeulen PEJ. Turbulence in Wind-Turbine Clusters. Turbulence in Wind-Turbine Clusters. *Papers Presented at the Fourth International Symposium on Wind Energy SystemsID: 83.* ; 1982.

(37) Callaghan J. [ID: 6]. *Future Marine Energy.* Carbon Trust; 2006.

(38) Burton T, Sharpe D, Jenkins N, Bossanyi E. *Wind Energy Handbook.* John Wiley & Sons; ID: 11; TY: GEN.

(39) Catalano P, Amato M. An evaluation of RANS turbulence modelling for aerodynamic applications. *Aerospace Science and Technology.* 2003; 7(7):493-509.

(40) Cebeci T, Shao J, Kafyeke F, Laurendeau E. *Computational Fluid Dynamics for Engineers- From Panel to Navier-Stokes Mehods with Computer Programs.* : Springer; 2005.

(41) Defne Z, Haas KA, Fritz HM. GIS based multi-criteria assessment of tidal stream power potential: A case study for Georgia, USA. *Renewable and Sustainable Energy Reviews.* 2011; 15(5):2310-2321.

(42) Department of Energy and Climate Change. [ID: 1]. *The UK Renewable Energy Strategy.* 2009.

(43) Draper S, Houlsby GT, Oldfield MLG and Borthwick AGL. Modelling Tidal Energy Extraction in a Depth-Averaged Coastal Domain. Modelling Tidal Energy Extraction in a Depth-Averaged Coastal Domain. ***Proceedings of the 8th European Wave and Tidal Energy ConferenceID: 62.*** **; 2009.**

(44) Draper S, Houlsby GT, Oldfield MLG, Borthwick AGL. Modelling tidal energy extraction in a depth-averaged coastal domain. ***IET Renewable Power Generation.*** **2010; 4(6):545-554.**

(45) Rourke FO, Boyle F, Reynolds A. Marine current energy devices: Current status and possible future applications in Ireland. ***Renewable and Sustainable Energy Reviews.*** **2010; 14(3):1026-1036.**

(46) Ferziger JH, Peric M. ***Computational Methods for Fluid Dynamics.*** **: Springer; 2002.**

(47) Fraenkel PL. Power from Marine Currents. ***Proceedings of the Institution of Mechanical Engineers Part A: Journal of Power and Energy.*** **2002; 216.**

(48) Freris LL. ***Wind Energy Conversion Systems.*** **: Prentice Hall; 1990.**

(49) Garrett C, Cummins P. Limits to tidal current power. ***Renewable Energy.*** **2008; 33(11):2485-2490.**

(50) Garrett C, Cummins P. The efficiency of a turbine in a tidal channel. ***Journal of Fluid Mechanics.*** **2007; 588:243-251.**

(51) Garrett C, Cummins P. The power potential of tidal currents in channels. ***Proceedings of the Royal Society A: Mathematical, Physical and Engineering Sciences.*** **2005; 461(2060):2563-2572.**

(52) Glauert H. ***The Elements of Aerofoil and Airscrew Theory.*** **: Cambridge University Press; 1947.**

(53) Güney MS, Kaygusuz K. Hydrokinetic energy conversion systems: A technology status review. *Renewable and Sustainable Energy Reviews.* 2010; 14(9):2996-3004.

(54) Harrison ME, Batten WMJ, Myers LE and Bahaj AS. A Comparison Between CFD Simulations and Experiments for Predicting the Far Wake of Horizontal Axis Turbines. A Comparison Between CFD Simulations and Experiments for Predicting the Far Wake of Horizontal Axis Turbines. *Proceedings of the 8th European Wave and Tidal Energy ConferenceID: 75.* ; 2009.

(55) Harwell Laboratory. [ID: 91]. *Tidal Stream Energy Review.* ETSU; 1993.

(56) Hoerner SF. Aerodynamic Properties of Screens and Fabrics. *Textile Research Journal.* 1952; 22(4).

(57) Holmes O. A Contribution to the Aerodynamic Theory of the Vertical Axis Wind Turbine. A Contribution to the Aerodynamic Theory of the Vertical Axis Wind Turbine. *Proceedings of the International Symposium on Wind Energy SystemsID: 18.* ; 1976.

(58) Karsten RH, McMillan JM, Lickley MJ, Haynes RD. Assessment of tidal current energy in the Minas Passage, Bay of Fundy. *Proceedings of the Institution of Mechanical Engineers, Part A: Journal of Power and Energy.* 2008; 222(5):493-507.

(59) Kawase M, Thyng KM. Three-dimensional hydrodynamic modelling of inland marine waters of Washington State, United States, for tidal resource and environmental impact assessment. *IET Renewable Power Generation.* 2010; 4(6):568-578.

(60) Kirke BK. Tests on ducted and bare helical and straight blade Darrieus hydrokinetic turbines. *Renewable Energy.* 2011; 36(11):3013-3022.

(61) Kirke BK. Tests on ducted and bare helical and straight blade Darrieus hydrokinetic turbines. *Renewable Energy.* 2011; 36(11):3013-3022.

(62) Kundu PK. *Fluid Mechanics.* 3rd Edition ed. : Elsevier Academic Press; 2004.

(63) Larsen HC. Summary of a Vortex Theory for the Cyclogiro. Summary of a Vortex Theory for the Cyclogiro. *Proceedings of the Second US National Conference on Wind Engineering ResearchID: 16.* ; 1975.

(64) Marine Current Turbines. [homepage on the Internet]. cited 2008 08]. Available from: http://www.marineturbines.com.

(65) Masters I, Orme JAC and Chapman J. Towards Realistic Marine Flow Conditions for Tidal Stream Turbines. Towards Realistic Marine Flow Conditions for Tidal Stream Turbines. *Proceedings of the 7th European Wave and Tidal Energy ConferenceID: 32.* ; 2007.

(66) Milborrow DJ. The Performance of Arrays of Wind Turbines. *Journal of Industrial Aerodynamics.* 1980; 5.

(67) Mueller M, Wallace R. Enabling science and technology for marine renewable energy. *Energy Policy.* 2008; 36(12):4376-4382.

(68) Munson BR, Young DF, Okiishi TH. *Fundamentals of Fluid Mechanics.* 4th ed. : John Wiley & Sons; 2002.

(69) Myers L, Bahaj AS. Power Output Performance Characteristics of a Horizontal Axis Marine Current Turbine. *Renewable Energy.* 2006; 31(2):197-208.

(70) Myers LE, Bahaj AS. Experimental analysis of the flow field around horizontal axis tidal turbines by use of scale mesh disk rotor simulators. *Ocean Engineering.* 2010; 37(2-3):218-227.

(71) Orme JAC, Masters I, Griffiths RT. Investigation of the Effect of Biofouling on the Efficiency of Marine Current Turbines. *Proceedings of Institute of Marine Engineers.* 2001; .

(72) Owen A, Bryden I. A Novel Graphical Approach for Assessing Tidal Stream Energy Flux in the Channel Islands. *Technical Proceedings of the Institute of Marine Engineering, Science and Technology Part C: Journal of Marine Science and Environment.* 2006; C4.

(73) Paraschivoiu I. Double-Multiple Streamtube Model for Studying Vertical-Axis Wind Turbines. *Journal of Propulsion.* 1988; (4).

(74) Batten WMJ, Bahaj AS, Molland AF, Chaplin JR. Experimentally validated numerical method fo rthe hydrodynamic design of horixontal axis tidal turbines. *Ocean Engineering.* 2007; 34:1089.

(75) Paraschivoiu I. Predicted and Experimental Aerodynamic Forces on the Darrieus Rotor. *Journal of Energy.* 1983; 7.

(76) Paraschivoiu I. Aerodynamic Loads and Performance of the Darieus Rotor. *Journal of Energy.* 1982; 6.

(77) Walker JF. *Wind Energy Technology.* : John Wiley & Sons; 1997.

(78) Nelson V. Chapter 5- Wind turbines. *Wind energy: renewable energy and the environment.* London: CRC; 2009. 5 p. 75-75-101.

(79) Paraschivoiu I, Fraunie P, Beguier C. Streamtube Expansion Effects on the Darrieus Wind Turbine. *Journal of Propulsion.* 1985; 1(2).

(80) Polagye BL, Malte PC. Far-field dynamics of tidal energy extraction in channel networks. *Renewable Energy.* 2011; 36(1):222-234.

(81) Polange B. Limits to the Predictability of Tidal Current Energy. Limits to the Predictability of Tidal Current Energy. *Proceedings of the MTS/IEEE Oceans ConferenceID: 106.* ; 2010.

(82) Ponta FL, Jacovkis PM. A vortex model for Darrieus turbine using finite element techniques. *Renewable Energy.* 2001; 24(1):1-18.

(83) Polange B, Malte P, Kawase M, Durran D. Effect of Large-Scale Kinetic Power Extraction on Time-Dependent Estuaries. *Proceedings of the Institution of Mechanical Engineers Part A: Journal of Power and Energy.* 2008; 222(5).

(84) Pope A, Harper J. *Low-Speed Wind Tunnel Testing.* : John Wiley & Sons; 1966.

(85) Robinson E and Byrne G. Methodology for Modelling Tidal Turbine Characteristics. Methodology for Modelling Tidal Turbine Characteristics. *Proceedings of the IEEE Oceans ConferenceID: 44.* ; 2008.

(86) Roulston MS, Ellepola J, von Hardnberg J, Smith LO. Forecasting Wave Height Probabilities with Numerical Weather Prediction models. *Ocean Engineering.* 2005; 32.

(87) European Commission. [ID: 92]. *The Exploitation of Tidal and Marine Currents.* 1996.

(88) Eggleston DM. Wind Turbine Engineering Design. 1987; .

(89) Fanucci JB and Walters RE. Innovative Wind Machines: The Theoretical Performance of a Vertical Axis Wind Turbine. Innovative Wind Machines: The Theoretical Performance of a Vertical Axis Wind Turbine. *Proceedings of the Vertical Axis Wind Turbine Technology WorkshopID: 15.* : Sandia Laboratoreis Report SAND 76-5586; 1976.

(90) Rumsey CL, Ying SX. Prediction of high lift: Review of present CFD capability. *Progress in Aerospace Sciences.* 2002; 38(2):145-180.

(91) Salter S. Correcting the Under-Estimate of the Tidal-Stream Resource of the Pentland Firth. Correcting the Under-Estimate of the Tidal-Stream Resource of the Pentland Firth. *Proceedings of the 8th European Wave and Tidal Energy ConferenceID: 104.* ; 2009.

(92) Salter S, Taylor JRM. Vertical-Axis Tidal-Current Generators and the Pentland Firth. *Proceedings of the Institution of Mechanical Engineers Part A: Journal of Power and Energy.* 2007; 221.

(93) Saulnier J, Prevosto M, Maisondieu C. Refinements of sea state statistics for marine renewables: A case study from simultaneous buoy measurements in Portugal. *Renewable Energy.* 2011; 36(11):2853-2865.

(94) Scott BE. A Renewable Engineer's Essential Guide to Marine Ecology. A Renewable Engineer's Essential Guide to Marine Ecology. *Oceans 2007 Europe International ConferenceID: 114.*

(95) Sheidahl RE and Klimas PC. [ID: 87]. *Aerodynamic Characteristics of Seven Symmetrical Airfoil Sections Through 180-Degree Angle of Attack for Use in Aerodynamic Analysis of Vertical Axis Wind Turbines.* Sandia National Laboratories; 1981.

(96) Snel H, Houwink R and Bosschers J. [ID: 42]. ***Sectional Prediction of Lift Coefficients on Rotating Wind Turbine Blades in Stall.*** **Energy Research Centre of the Netherlands; 1994.**

(97) Tu J, Yeoh GH, Liu C. ***Computational Fluid Dynamics- A Practical Approach.*** **: Elsevier; 2008.**

(98) Campbell AR, Simpson JH, Allen GL. The dynamical balance of flow in the Menai Strait. ***Estuarine, Coastal and Shelf Science.*** **1998; 46:449-449-455.**

(99) Strickland JH. [ID: 23]. ***The Darrieus Turbine: A Performance Prediction Model using Multiple Streamtubes.*** **Sandia Laboratories; 1975.**

(100) Hagerman G, Polagye BL, Bedard R, Previsic M. ***Methodology for Estimating Tidal Current Energy Resources and Power Production by Tidal In-Stream Energy Conversion (TISEC) Devices (Rev 3).*** **[homepage on the Internet]. 2006 [updated September 29, 2006; cited 2011 11/23]. Available from: http://oceanenergy.epri.com/attachments/streamenergy/reports/TP-001_REV_3_BP_091306.pdf.**

(101) Carbon Trust. ***Tidal streams and tidal stream energy device design.*** **[homepage on the Internet]. London: Carbon Trust; 2006 cited 2011 11/28]. Available from: http://www.carbontrust.co.uk/SiteCollectionDocuments/Various/Emerging%20technologies/Technology%20Directory/Marine/Technical%20guidelines/Tidal%20streams%20%20device%20design.pdf.**

(102) Macdonald A. ***Sound of Islay Tidal Energy Project- Update August 2011.*** **[homepage on the Internet]. Bowmore (UK): Islay Energy Trust; 2011 cited 2012 02/03]. Available from: http://islayenergytrust.files.wordpress.com/2011/08/sound-of-islay-update-august-2011.pdf.**

(103) Strickland JH, Webster BT, Nguyen T. A Vortex Model of the Darrieus Turbine: An Analytical and Experimental Study. *Transactions of the ASME.* 1979; 101.

(104) Sun X, Bryden IG, Jeffrey H, Forehand D. An experimental survey in the wake of a simulated tidal current turbine. *Proceedings of the Institute of Marine Engineering, Science and Technology Part A: Journal of Marine Engineering and Technology.* 2008; (12):13-22.

(105) Sun X, Chick JP, Bryden IG. Laboratory-scale simulation of energy extraction from tidal currents. *Renewable Energy.* 2008; 33(6):1267-1274.

(106) Tulapurkara EG. Turbulence Models for the Computation of Flow Past Airplanes. *Progress in Aerospace Sciences.* 1997; (33).

(107) Sutherland D, Foreman M, Garret C. Tidal Current Energy Assessment for Johnstone Strait, Vancover Island. *Proceedings of the Institution of Mechanical Engineers Part A: Journal of Power and Energy.* 2007; 222.

(108) Taylor GI, Davies RM. The Aerodynamics of Porous Sheets. [ID: 85]. Reproduced In: Batchelor GK, editor. *The Scientific Papers of G I Taylor.* : Cambridge University Press; 1963.

(109) Nixon Flow Meters. *Streamflo Velocity Meter.* [homepage on the Internet]. 2010 Available from: http://www.nixonflowmeters.com/.

(110) Templin RJ. [ID: 22]. *Aerodynamic Performance Theory for the NRC Vertical Axis Wind Turbine.* National Reseach Council of Canada; 1974.

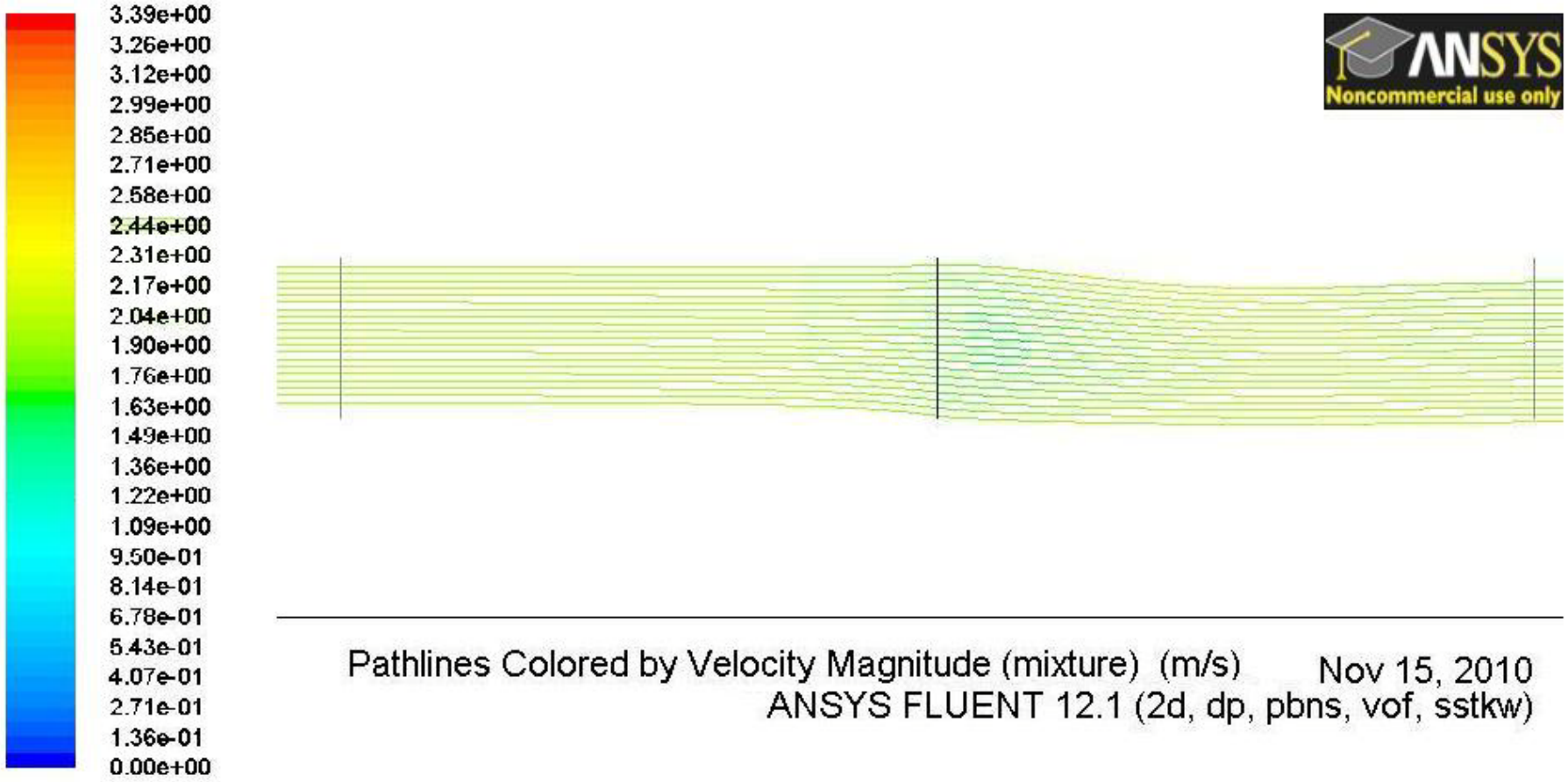

Pathlines for flow through the disc, with the centre of the disc 1.4m above the channel bed

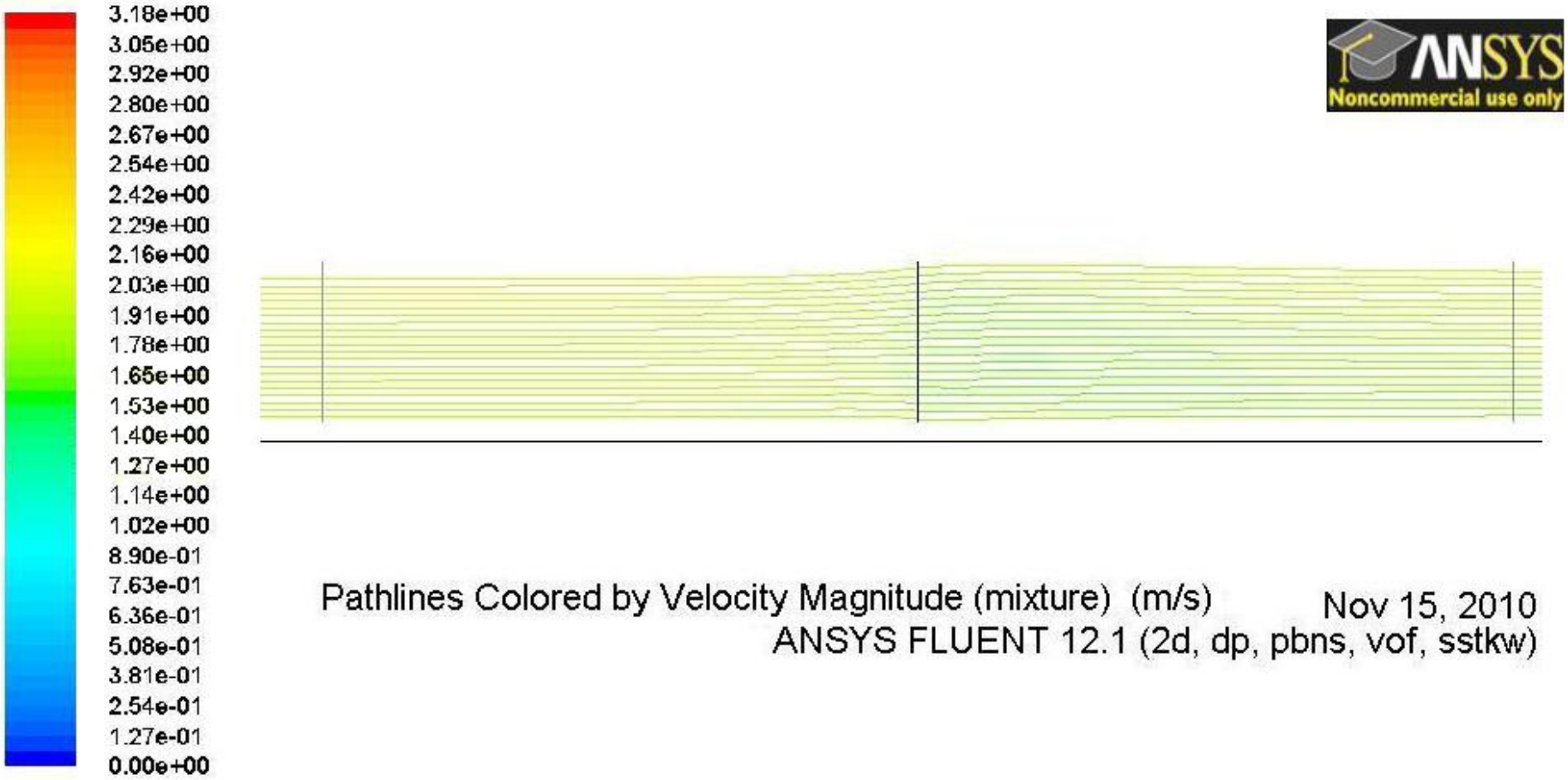

Pathlines for flow through the disc with the centre of the disc 0.5m above the channel bed

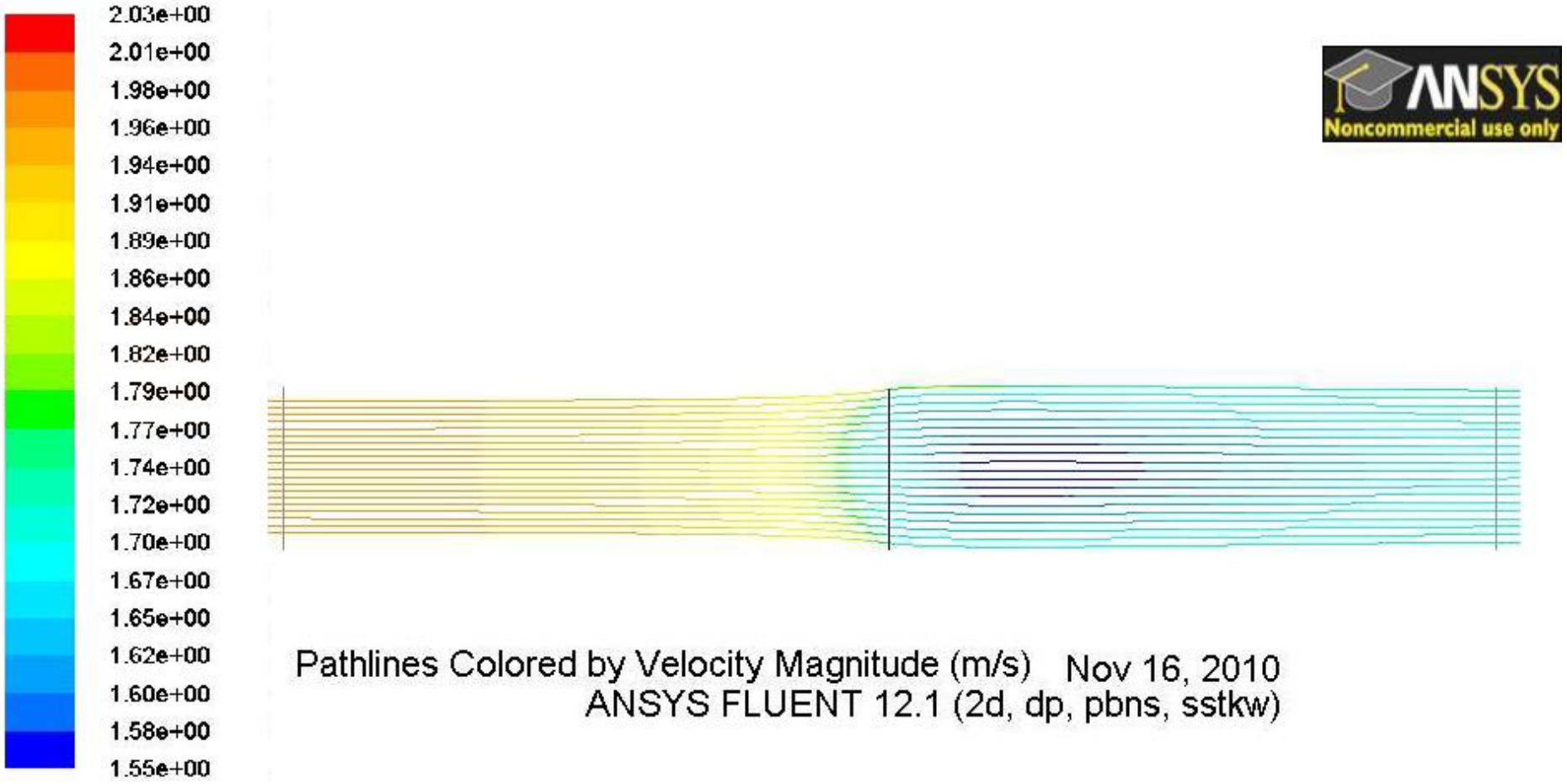

Pathlines for the flow through the disc in an unbounded flow